# Compact Wide Scan-Angle Antennas for Automotive Applications and RF MEMS Switchable Frequency-Selective Surfaces

**by**

**Bernhard Schoenlinner**

A dissertation submitted in partial fulfillment
of the requirements for the degree of
Doctor of Philosophy
(Electrical Engineering)
in The University of Michigan
2004

Doctoral Committee:
Professor Gabriel M. Rebeiz, Chair
Professor Brian Gilchrist
Associate Professor Amir Mortazawi
Associate Professor Christopher S. Ruf
Associate Professor Leo C. Kempel, Michigan State University

To my Parents Theresia and Franz Xaver Schoenlinner

# ACKNOWLEDGEMENTS

Now, that I am approaching the end of my Ph.D. thesis, it is a good time to look back and conclude a period which is a substantial part of my life. The memory is a (frequency?) selective thing. Good memories stay with you and bad ones tend to fade and/or turn into good ones, considering the experience you gain out of it.

My summary must be incomplete - unfortunately - because there are only so many pages to write on and there are so many people I was fortunate to meet and so many experiences to make in a 4 year span of time. Please, anybody forgive me whom I don't give enough reward in these few lines.

First and foremost I would like to thank my advisor Prof. Gabriel Rebeiz. It was a little bit because of him that I decided at all to pursue a Ph.D. degree. I met him when I did my Diplomarbeit at the University of Michigan in summer 1999 as a visiting student and he asked me then - after getting to know each other for a couple of months - to join his group. For me, there are several reasons to do a Ph.D.. The most obvious one is to have a very productive time where you learn a lot and where you learn how to find interesting problems and how to attack and solve them in a scientific and effective way. You want to become an expert in your field. A second reason, to me as important as the first one, is to have an advisor who teaches you more than facts and methods. The German word for advisor is Doktorvater (literally: "doctor father") and it tells that an advisor should teach through his personality and his leadership things that are important in your profession and in life and that you won't find in any engineering book. It was for both reasons that I joined Gabriel's group and I did not regret it for a single minute.

For the time they spent for me and for many valuable suggestions I would like to thank my thesis committee: Prof. Brian Gilchrist, Prof. Amir Mortazawi, Prof. Christopher Ruf, and especially Prof. Leo Kempel. Leo Kempel was another little Doktorvater for me and I would have been in big trouble for not meeting the paper deadline had he not switched on his laptop while making his wife take over the steering wheel on their way to Washington D.C. on a beautiful Saturday afternoon and ran a couple simulations while I was giving instructions on the phone. He was my man for the tricky things with the FSSs.

I would also like to thank Prof. Detlefsen from the Technische Universitaet Muenchen for establishing the contact and supporting my studies abroad.

I would like to thank Jim Ebling from ASL/Takata. That's where all the money came from that supported me. Often, a joint project between university and a company gives rise to tension because they have slightly different goals. Not so in this case. It was a great pleasure to work with and for Jim and also Mike O'Boyle, Mike Schmidlin, and Dennis Rumps.

Doing a Ph.D. with Gabriel is a full time job. I am just thinking about the phone call at 3 o'clock in the morning (!) when he needed a viewgraph for his presentation the following day. And it is rewarding and full of surprises. Maybe only astronomy students can claim they have seen places like Puerto Rico, Hawaii, and New Mexico on scientific journeys, not to mention all the conferences I was allowed to attend in Columbus/Ohio, Seattle, Philadelphia, Paris, London, and Munich.

There is not only a life after the Ph.D. but also during. What would it be without good friends? I would like to thank Josef Kellndorfer, with whom I share being from the same hometown in Bavaria, and his wife Emily. Through miraculous circumstances and coincidences it was actually finally him who was the key to my whole adventure in Ann Arbor. They provided a home for me more than once and they were a constant source of support, good food, and new nice people to meet. It was fun to stick with bavarian traditions and play music and play Schafkopf together with Ursula Jakob, Hans Buegl, Franko Bayer, and Michael Rothe.

Special thanks go also to Martha Perkins. She became a deep friend of mine and I'll miss the early morning swims in Pickerel lake and discussions on her porch with wine and candle light late at night.

I will also miss playing darts at the ABC-bar with a wonderfully mixed group of international actual and former students, among them Ormond McDougald, Nicolas Gilbert, Anne Dievart, Tony Withers, Stephen Sanders, Martin Bader, Simone Abmayr, Jean-Marie Rouillard, Trinh Pham, Isabelle Gerin, Connie Kubisch, Joerg Hoffmann, Jutta Hager, and Sanjay Ravipati.

I am a person who is not satisfied with engineering alone but needs some other activities, too. It was Prof. George Wynarsky who taught me how to prepare properly for long distance runs and who worked out a training schedule for me which finally led me to the successful participation of several marathon races. Training would not have been as much fun if Everett Mayes, Torrey McMillan, and Stephanie Hitztaler had not been my running partners. Thanks also to my faithful "Dances with Dirt"-team Suzanne Harvey, Peter Menard, Wendy Caldwell, Buzz Tourbin, and Kristen Cunningham and my squash partner Richard Altendorfer.

Speaking of dancing: I finally learned how to swing my legs in a ballroom to Waltz, Tango, and Samba music. Thanks to Tudor Stoenescu, Magdalena Stolarczyk, and Sibylle Thies of the University of Michigan Dance Team and Stephen and Susan McFerran, my outstanding teachers.

I satisfied my singing needs in different ensembles in Ann Arbor, the most outstanding of them being the University of Michigan Men's Glee Club and the Ann Arbor Choral Union. I am very thankful to Thomas Sheets and Jerry Blackstone, my conductors and mentors. I am also deeply thankful to Prof. Randall Reid-Smith and David Dillard. Every single singing lesson - first as a private student and then as a regular student - was a special experience.

Work is part of life and life is part of work. I am glad I had such a nice group of Ph.D. students around me. I would like to thank the older students who graduated before me for all the things they taught me, all the advice they gave me, and all the fun that I shared with them. Scott Barker, Leo DiDomenico, Andy Brown (my constant source of stories about ... well who?), Mark Casciato, Jeremy Muldavin (who else can lift 380 lbs on the benchpress?) and his wife Katherine Herrick, Alex Margomeros, Bill Chappell, Dimitrios Peroulis, Yongshik Lee, Ron Reano, Lee Harle, Rick Kindt, Joe Hayden (the lord of the toga parties), Guan-Leng Tan (my very patient lab-mentor), Kiran Nimmagadda

(Gandhi cannot have had a more peaceful mind), Jose Cabanillas (unfortunately they don't sell quadruple espressos in Ann Arbor), Jad Rizk (my housemate for two years), Laurent Dussopt, Tauno Vaha-Heikkila (if there was just a Sauna in Ann Arbor), Noriyo Nishijima, and Abbas Abbaspour-Tamijani (man, what a brain).

I wish good luck to the new generation of Radlab-ers, Michael Chang (where is the next Italian restaurant, please?), Timothy Hancock (after the Oktoberfest I am convinced he has Bavarian genes), Bryan Hung, Kamran Entesari, Chris Galbraith, Carson White, Byung Wook Min, Sang-June Park, and Koen van Caekenberghe. I also value having met Helena Chan (no beer is better than our homebrew) and Phill Grajek (no mountain too high - Mt. Rainier, 14410 ft - no weather too cold - he, Kiran, and me in a tent at 0° F in upper Michigan).

My deep thanks go to my parents, my grandfather, my siblings Irmgard, Markus, and Rupert, their spouses and my nieces and nephews. It is wonderful to be far far away and whenever I go back I feel at home. Thank you for all the support and love.

And Madhavi Krishnan, for her love and care and being there with me.

# TABLE OF CONTENTS

# LIST OF TABLES

# LIST OF FIGURES

**Figure**

# LIST OF APPENDICES

**APPENDIX**

# CHAPTER 1

# Introduction

## 1.1 Pushing Towards Millimeter-Wave Frequencies

Historically, millimeter-wave frequencies (30-300 GHz) have been used mostly for military applications such as radars, imaging and tracking systems, and in scientific areas such as radio-astronomy and more recently, remote sensing of the atmosphere, oceans, and earth. Millimeter-wave frequencies were rarely used for commercial applications for different reasons. Millimeter-wave circuits and devices such as waveguides, diodes, and sources which deliver a lot of power were very expensive or practically not available at all. Also, there was often no need to push frequencies beyond 10 GHz, since wireless communication and data transfer was not well developed. However, new developments and advances in existing technologies, especially over the last 15 years, and inexpensive analysis software for millimeter-wave circuit design on personal computing machines made it possible to develop commercial millimeter-wave circuits.

There are several reasons which make the millimeter-wave range attractive. The antenna size for radar and imaging applications scales proportionally to the wavelength squared. Hence, the antenna size is potentially small as compared to microwave systems. This is a prerequisite for many applications like spaceborne imaging systems, autonomous vehicles in industrial environments or automotive radar systems. Higher operating frequency also leads to antennas with higher gain since gain increases proportionally to the operating frequency squared. Imaging systems like radiometers can achieve higher resolution because smaller beamwidths allow smaller pixel size. For radar systems, a higher gain results in better angular resolution and therefore better target discrimination. Also, degradation due to multipath effects are reduced. This is especially important for automotive applications when used in dense environments such us cities, where not only the surface of the road but also buildings and road deliminations are potential scatterers. Another advantage of moving to higher frequencies is the higher bandwidth which is available. Frequency modulated continuous wave (FM/CW) or pulsed radar systems achieve higher range resolution due to wider bandwidth or alternatively sharper pulses. Furthermore, the Doppler shift increases proportionally with increasing frequency, which improves velocity resolution. Moreover, as the lower microwave region becomes more and more crowded with personal communications and broadcast services, there is a natural need to shift to higher frequencies.

Millimeter-waves are able to penetrate many atmospheric conditions, such as fog, smoke, and dust which are opaque to infrared/optical wavelengths. This characteristic makes millimeter-waves attractive for high-resolution sensor systems which can operate in reduced visibility conditions. Radar applications generally require the maximum feasible detection range; consequently, millimeter-wave radar research and development is concentrated in bands of lower atmospheric attenuation (or "windows") which occur at 35 GHz, 95 GHz, 140 GHz, and 220 GHz (Fig. 1.1). Historically, these frequencies have been attractive for military sensor systems, however, there are currently growing commercial applications in the areas of Intelligent Vehicle Highway systems (IVHS), such as collision avoidance radar and autonomous cruise control, and passive millimeter-wave imaging for aircraft landing. Water vapor and oxygen molecule resonances cause bands of large absorption at 60 GHz, 118 GHz, and 183 GHz. These frequencies can be exploited for short-range, secure communications, and indeed 60 GHz has emerged as an important band for high-bandwidth wireless local-area networks (LANs). Finally, there are a range of millimeter-wave applications in atmospheric remote sensing, radio astronomy, and plasma diagnostics.

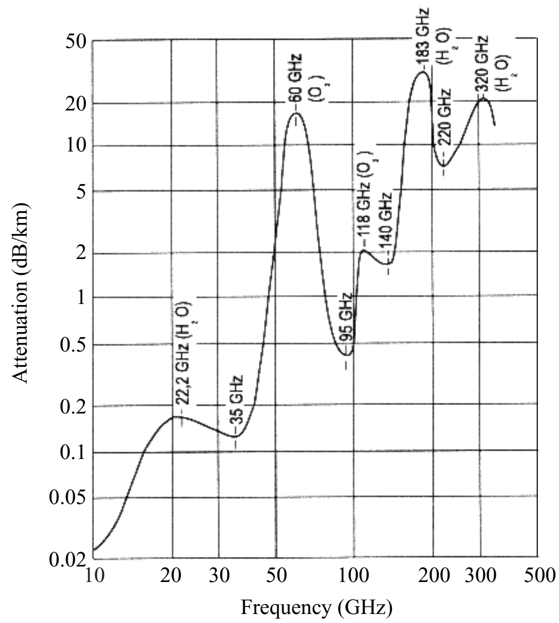


**Figure 1.1: Electromagnetic attenuation due to molecular resonances in the atmosphere.**

## 1.2 Automotive Radar Systems

Besides military applications, there are two major current commercial application areas for millimeter-wave systems: communications and automotive traffic control [1], the latter probably being the area with the greatest immediate commercial interest.

There is already a long history in the development of automotive radar sensors. The first car radars were constructed in the early 1960's in the USA. Beginning in the early 1970's, automotive radar systems have been developed first at 10 GHz [2], soon shifting up to higher frequencies (34 and 50 GHz) [3–5] in the mid 1970's and to 60, 77, and 94 GHz in the 1990's [6]. The frequencies mostly used for automotive radar systems in the present are 24 and 77 GHz.

### 1.2.1 Applications

In the near future, a car could be equipped with a whole range of sensors (Fig. 1.2). Each sensor has advantages and disadvantages, but especially infrared and video sensors

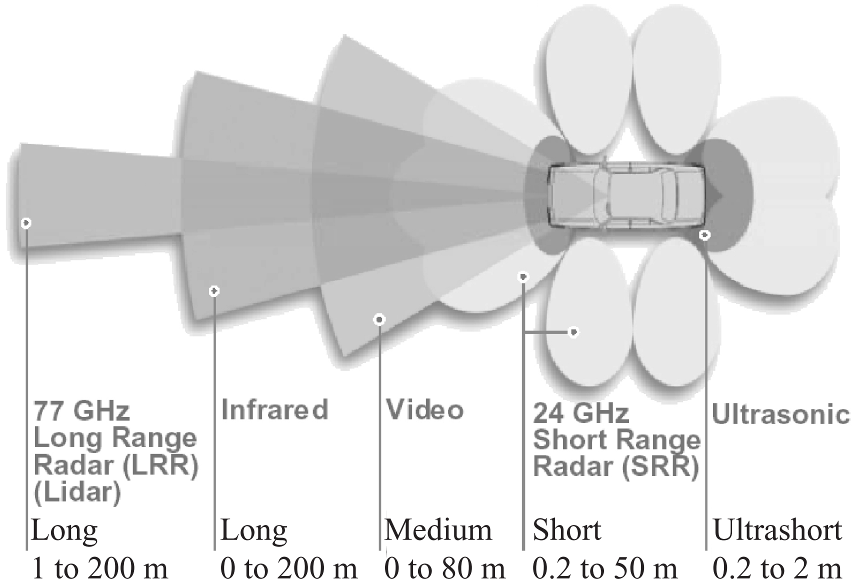


**Figure 1.2: Different types of sensors for automotive applications.**

are limited to certain weather conditions due to the high attenuation in fog, smoke, dust, rain, and snow. Also, radar systems can be placed behind a dielectric radome which works as a protection against the environment and - very importantly - makes it attractive for car designers. The 77 GHz radar system is suitable in ranges up to 200 m, because of its inherent possibility of higher antenna gain antennas in the same physical package as compared to a radar system operating at 24 GHz. For short ranges (up to 50 m), radar systems must be inexpensive because many sensors may be placed on a car. For this kind of application, 24 GHz systems are a better candidate.

There are many possible applications (Fig. 1.3). A 77 GHz system can serve as adaptive cruise control, lane change warning system, front obstacle collision warning and avoidance system, or, further ahead in the future, be essential part in an autonomous driving system. A 24 GHz radar system can be used as parking assistant, pre-crash detection system for front, back, and side impacts, which could release airbags before the actual impact, back-up warning system, assistant in stop and go traffic, blind spot detector, lane change assistant, speed-o-meter, and for road condition recognition.

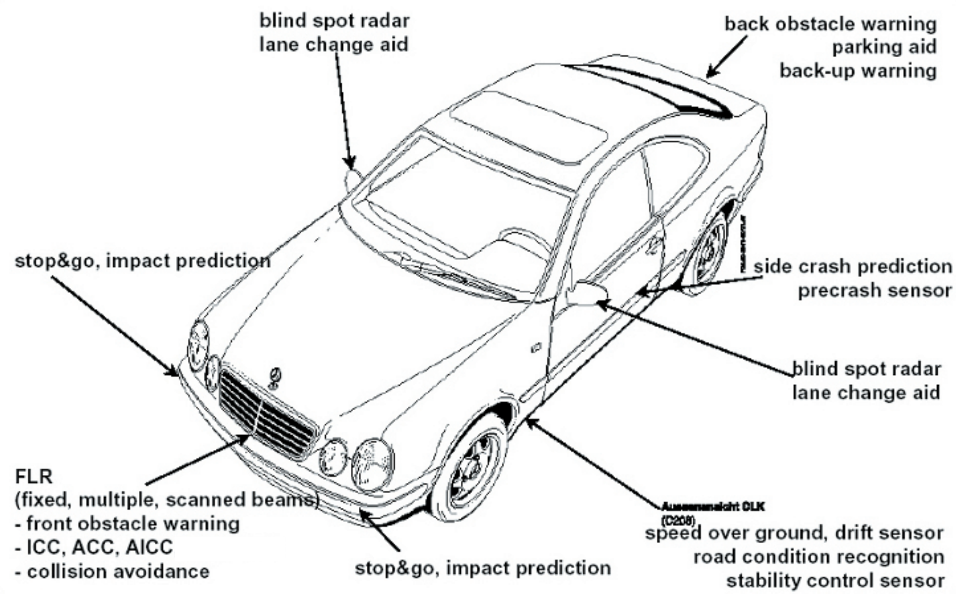


**Figure 1.3: Different applications for automotive radar systems.**

### 1.2.2 Basic Concept of an Automotive Radar System

Almost all automotive radar systems use either FM/CW (Frequency Modulated / Continuous Wave) or are pulse-Doppler radars. FM/CW radars send out a continuous signal with changing frequency. Due to the time delay of the returning signal there is a frequency difference compared to the outgoing signal. Combined with the frequency Doppler-shift, the information of distance and relative speed of the scatterer can be extracted. A pulse-Doppler radar uses short pulses rather than a continuous signal and again, the measured time delay and frequency Doppler-shift contain the desired information. In both cases, the bandwidth is an important system parameter. The higher the bandwidth, the faster the frequency sweep for an FM/CW radar and the shorter a pulse in a pulse-Doppler radar. Both frequency slope and pulse width are directly related to spatial resolution of the target.

Fig. 1.4 shows a basic example of a monostatic pulse-Doppler radar. An oscillator with variable output frequency generates a continuous signal which is sometimes multiplied in frequency, especially for radar systems operating at 77 GHz. A fast switch generates the pulsed signal which is then amplified. This can be achieved with MMIC's (millimeter-wave integrated circuits) in GaAs [7–9], or at 24 GHz in SiGe technology [10,11]. For the duration of the pulse, the 2 switches direct the signal to the antenna. At the time when the scattered

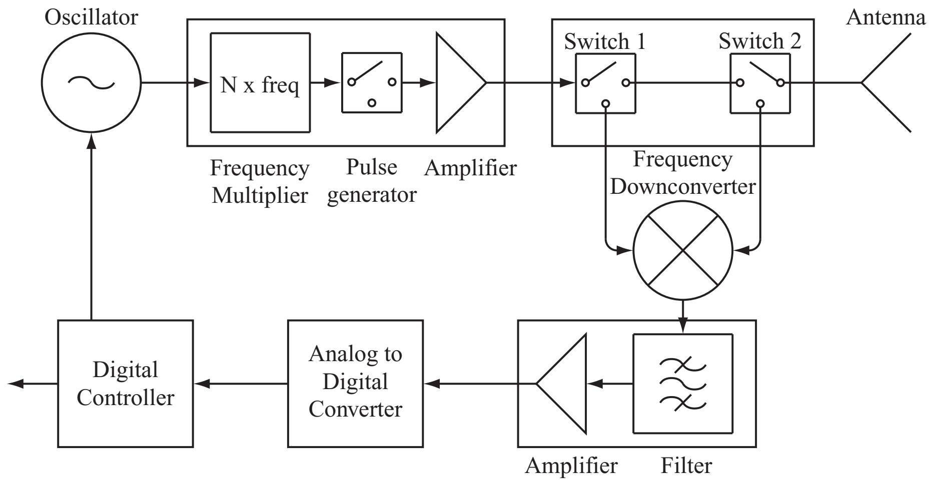


**Figure 1.4: Basic block-diagram of a monostatic pulse-Doppler radar system.**

pulse is received, switch 1 and 2 are such that the signal coming from the oscillator and the received signal will be both directed to the frequency downconverter. The intermediate frequency signal is first filtered and amplified, then converted from the analog to digital domain and sent to a digital signal processing unit and controller. In an FM/CW radar, each of the switches is replaced by couplers and/or isolators, and sometimes, a bistatic solution with only one coupler and two antennas is used.

### 1.2.3 Antennas for Automotive Radar Systems

Radar systems for automotive applications - other than for military or many research applications - operate based on consumer demand. This means that not only good performance, but also economic criterions are important. This includes the cost of production as well as the possibility of integration into a vehicle. For radar units to become standard equipment in most cars, their size has to be small enough to be easily integrated in different parts of a car and the costs have to be decreased dramatically.

The crucial components in terms of costs are the high frequency devices, located in the upper half of Fig. 1.4, including the frequency downconverter. With planar transmission-lines and MMIC (Monolithic Microwave Integrated Circuit) technology it is now possible to avoid waveguides, which are big, heavy, and expensive. Oscillators, frequency up- and downconverters, couplers, and switches can be built on a single chip at comparably low cost. However, at 24 and 77 GHz, low loss phase shifters using diodes or FETs for electronic beamsteering are not available at acceptable cost and will not be in the near future. While there is not many different topologies for the high frequency circuitry, the antenna opens a lot of possibility for cost reduction because there are many different design approaches.

The antenna has to have good performance which includes the radiation pattern of the antenna, namely the $-3$ dB beamwidth and the sidelobe level (which in most systems is required to be below $-14$ dB or even $-20$ dB), as well as the antenna radiation efficiency. The size should be small and the cost of production low. Furthermore, in the next generation systems, the antenna should allow for a very wide scan-angle and at the same time allowing a high angular scan rate (which precludes the use of mechanical scan systems). Different radar systems and applications require different antenna properties, and therefore, the antenna design should be easily adaptable in terms of antenna gain, scan-angle, and operating frequency.

Probably the most challenging requirement to achieve is the wide scan-angle. An interesting solution is to use an overmoded coaxial cable to feed a biconical horn antenna for a 360° field of view [12]. However with this method, only low directivity can be achieved and it is very hard to realize at 77 GHz. At millimeter-wave frequencies, there are two main approaches to building a wide scan-angle antenna for automotive applications:

The first approach is to use one single low-gain antenna and a focusing mechanical rotating reflector or lens. This is a rather simple concept and allows a field of view of $\pm 180°$. Common problems are the low scan rate and therefore long update times. Also, there are usually reliability issues due to the mechanically moving parts.

The second approach uses a number of low-gain antennas at the focal plane of a single lens or reflector [13]. In this multibeam design, scanning is done by switching between the different antenna elements and thus covering the entire field of view. Menzel*et al.* have applied this technique to a planar folded lens/reflector and achieved a $\pm 25°$ field of view with 11 different beams in a very compact design [14]. Ideally, the lens is a sphere because in this case, the focusing properties of the lens are the same regardless of the direction of incidence. However, a uniform sphere is not a perfect lens in the sense that it does not have a single focal point for rays which pass through the center of the lens and rays which are off center. For the lens to have a real focal point, it requires a gradient in its dielectric permittivity: highest in the center and dropping off towards the edges of the lens [15–17]. Such a lens is called a Luneburg lens [18]. However, it is very difficult - if at all possible - to build this lens at millimeter-wave frequencies. Many existing antenna designs therefore use a layered approximation of a Luneburg lens [19] or a focal-plane system with a collimating lens. This system provides ideal focusing properties for a feed antenna placed exactly at the focal point. For off-axis antennas, the radiation pattern is degraded. Hence, the scan-angle is limited and can be improved only by a sophisticated lens design [20–22].

A main problem for multibeam antennas is the switch that addresses the individual elements. Switches using PIN diodes are available but have around 1.5 to 2 dB of loss at 77 GHz. However, a new switch technology is approaching the market which may soon be standard in automotive applications for frequencies of 24 GHz and beyond: RF MEMS (Radio Frequency Micro Electro Mechanical Systems). The superior electrical performance of RF MEMS switches over PIN diode switches in this kind of application has been well demonstrated in the past few years [23, 24, 26–29, 114]. However, reliability issues are still waiting to be solved and only few companies are now coming up with promising packaging techniques which would allow the lifetime of a switch to go beyond 10 years at average use [30–32].

### 1.2.4 Existing Systems

The past decade has seen ever increasing research activities by companies and research institutes in the area of automotive radar systems. With improved technologies, the cost continues to decrease, and it is now compelling for car companies to implement advanced radar systems in upper class vehicles first, but in near future, also as standard equipment in most cars.

At 24 GHz, most existing systems are short-pulsed systems. The cost factor is very important since many sensors may be placed on one car. The leader in radar hardware (other than the antenna) at the moment is M/A-COM, which developed transceiver modules using SiGe. The resolution requirements are widespread depending on the application, and many different antenna solutions exist.

There are many organizations contributing to the 77 GHz field. But most of them are still working on first generation systems and their designs suffer from a narrow field of view (Bosch, Hitachi, Fujitsu-Ten, Siemens, and Autocruise). This is sufficient for adaptive cruise control, but otherwise is very limited in applications. Most companies work with a multibeam system with 3 - 5 beams (RoadEye uses 7 beams) instead of mechanical scanning (Celsius). Some companies try to combine more than one sensor into one single system: Bosch uses a low gain and a high gain sensor, both working at 77 GHz, to double the field of view to $\pm 8°$ and Fujitsu-Ten is using an optical sensor with a field of view of $\pm 20°$ in combination with a 77 GHz sensor. Toyota CRL is in an early phase of developing a wide scan-angle system ($\pm 20°$) using holographic techniques in a novel design. The most mature system at the moment comes from Daimler-Benz using an antenna developed at the University in Ulm / Germany. It is a multibeam system in its second generation, achieving a field of view of $\pm 25°$. However, automotive radar systems with an operating frequency of 77 GHz are still expensive to build. They are still not available except on Daimler-Benz S-class vehicles, and recently on Japanese and Volvo vehicles.

## 1.3 Tunable Frequency-Selective Surface

A frequency-selective surface (FSS) is a periodic surface which is an assembly of identical elements arranged in a one or two-dimensional infinite array [33]. Depending on the type of element, an incoming plane wave will be either reflected (band-stop type element) or transmitted (band-pass type element) completely, as soon as the frequency of the plane wave coincides with the resonant frequency of the elements of the FSS.

The history of FSS goes at least back to the year 1919, when a patent was granted to Marconi and Franklin on a "Reflector for use in wireless telegraphy and telephony" (US patent #1,301,473). This shows that the principle of FSS was known for a long time, but it was only in the mid-1960s that intense study of periodic surfaces got started because of the great potential for military applications. Most work, however, was not widely publicized at that time. Today, FSSs have been studied thoroughly and powerful analytical and numerical simulation tools have been developed. The result is that many different FSS designs have been investigated using a great variety of different elements .

### 1.3.1 Literature Overview

Usually, the frequency at which the FSS elements are in resonance is fixed. However, in certain applications, it would be desirable to be able to change the properties of the circuit over time. This can either mean the complete change of electromagnetic behavior in a certain frequency band, e.g. from pass-band to all-stop behavior (switchable FSS), or the shift of resonance frequency within a certain frequency band (tunable FSS). In the literature, one can find only very little work on switchable or tunable FSSs. The main reason is that in order to change the behavior of an entire FSS, one has to change either the properties of the substrate, or the properties of every single element on the circuit, or the position of the elements relative to each other. Any of these possibilities is in general very difficult to realize.

In the work of Lima *et. al.* [34], the relative permittivity of the substrate is altered by filling a cavity underneath a slot array with a dielectric liquid, thus changing the resonance frequency of the slot elements. Chang *et. al.* [35] printed an FSS on a ferrite substrate, and when biased with a strong magnetic field, a considerable shift in resonance frequency was achieved. Chang *et. al.* [36] used varactor diodes, mounted in different configurations on an FSS circuit with different elements. When biasing the diodes, thus changing their capacitance, a shift in resonance frequency was observed. A similar approach was followed by Stephan *et. al.* [37], who developed a quasi-optical PIN diode switch for millimeter-wave application. At lower frequency, Mias [38] used also varactor diodes to achieve tunability of an FSS. Instead of varactor diodes, Gianvittorio *et. al.* [39] built a dipole array using MEMS technology. The elements could be rotated off the surface of the supporting dielectric substrate by applying a magnetic field, thus changing their effective length and resonance frequency. In a different approach, Lockyer *et. al.* [40] investigated through simulation a double layer FSS with dipoles. By changing the relative position of the two layers, a large tuning range could be achieved. All of the techniques above resulted in marginal results and suffer from either a slow response (mechanical movement), DC power consumption (PIN diodes), or relatively high loss (PIN diodes, varactor diodes).

### 1.3.2 Applications

The most important applications for tunable/switchable FSSs at the present are in the military area. Antennas - as one of the largest scatterer on a military target - can be made "invisible" or missiles with radar systems can be protected against broadband high power jamming that would destroy the sensitive electronics using a switchable FSS. An FSS can also be used as a quasi-optical high power switch at millimeter-wave frequencies. Field effect transistors (FETs), diodes, and especially RF MEMS have only limited power handling capabilities. But by distributing the power over many, possibly thousands of elements, the power handling can be improved dramatically. Other possible applications lie in the field of antenna design. Often it is desirable to use one aperture - e. g. a parabolic reflector - for two or more frequencies. This can be achieved with FSSs used as secondary reflectors in different realizations.

## 1.4 Objective

The antenna in existing automotive radar systems is usually a compromise between low cost, performance, reliability, and size. For example, in a multibeam design, a wide scan-angle can be achieved with a Luneburg lens, but this is very difficult to build at millimeter-wave frequencies. Using a standard focal-plane system with a collimating lens reduces the cost of the lens but is limited to a scan-angle of about $\pm 20^{\circ}$. Also, using a rotating mirror allows the use of only one antenna and no Luneburg lens is required. But the reliability is affected because of mechanically moving parts and the scan rate is too low for many systems.

The objective of the antenna work presented in this thesis is to develop an antenna system for automotive radar applications at 24 and 77 GHz which emphasizes on combining good performance (in particular a sidelobe level of below $-14$ to $-20$ dB) with wide scan-angle (possibly up to 180$\circ$), compactness, reliability and low cost of production.

A second objective of this thesis, as an extension of one aspect of the antenna work, is the design of a switchable frequency-selective surface at Ka-band (26.5 - 40 GHz). Very few attempts have been reported in literature and none of them show good electrical performance as well as high switching speed, low DC-power consumption, relative low cost, extendability to multilayer structures, and the possibility of analog or digital frequency tuning. This thesis aims to fill part of this void.

## 1.5 Overview of Thesis

This thesis presents antennas suitable for automotive applications at 24 and 77 GHz and a switchable frequency-selective surface at 30 GHz. The proper design and characterization of a tapered-slot antenna (TSA) leads to a first design of a wide scan-angle antenna (Chapter 2). This TSA is then used in Chapter 3 as a feed antenna for antenna-lens-systems at 24 and 77 GHz with high gain and wide scan-angle capabilities. For compactness, the system is then extended in Chapter 4 to a dual-frequency design using FSSs. Chapter 5 extends the topic of FSS and presents a switchable FSS using RF MEMS as tuning elements. Comprehensive modelling and design are verified by extensive fabrication and testing of both, the antenna systems and the switchable FSS.

# CHAPTER 2

# Design of Millimeter-Wave Tapered-Slot Antennas

This chapter covers the selection, design, and characterization of a feed antenna suitable for wide scan-angle multibeam systems using a homogeneous spherical lens for automotive radar applications at 24 and 77 GHz. Also, a 24 GHz low-gain wide scan-angle antenna system, based on this feed antenna, is presented.

## 2.1 Feed Antenna for Multibeam System

The best candidates for low-cost applications at 24 and 77 GHz are planar antennas. Also, advances in the past 12 years allow for the design of low-loss circuits and transitions which result in much lower cost than waveguide antennas and components. Planar antennas may be divided into two classes: broadside and endfire antennas. Typical broadside radiating elements are microstrip patches, printed dipoles, and slots [41–45]. All these elements are resonant structures and yield low bandwidth and low gain. For a multibeam antenna system using a spherical lens, an endfire feed antenna is much more suitable. Two possible candidates at millimeter-wave frequencies are planar Yagi-Uda antennas [46–48] and tapered-slot antennas (TSAs) [49].

### 2.1.1 The Tapered-Slot Antenna

The TSA is a traveling-wave antenna. This allows more wideband operation compared to resonant structures (such as Yagi-Uda antennas). The phase velocity $v_{ph}$ is lower than the speed of light $c_0$ (as opposed to leaky-wave antennas with $v_{ph} > c_0$), and the TSA's main beam is in the endfire direction [50]. A basic understanding can be found in Zucker's review [51]. The directivity of a traveling-wave antenna depends mostly on its length and only minimally on its aperture. The aperture has to be larger than $0.5\lambda_0$ to ensure proper radiation and low reflection at the end (opening) of the antenna. Typical numbers for traveling-wave antennas are a directivity of $D \cong 10l/\lambda_0$ for $3\lambda_0 \leq l \leq 8\lambda_0$ and $c/v_{ph} \cong 1.05$ [52], where $l$ is the length of the TSA. For very short TSAs, the input impedance cannot be assumed to be matched to the feeding slotline and considerable reflections may occur. For longer antennas, the coefficient multiplying $l/\lambda_0$ decreases somewhat. For a good estimate of the directivity from measured radiation patterns, it has been found [49] that one needs to take co- and cross-polarized radiation pattern in E, H, and D-plane (45° tilted with respect to E- and H-plane) into account. Traveling-wave antennas are much less susceptable to mutual coupling than resonant antennas, which makes it possible to place them in close proximity to each other without disturbing the radiation pattern much. Also, being a planar antenna, its physical cross-section is very small. Both are important features for multibeam antenna systems as will be seen in Chapter 3. The size of few wavelengths can be physically small at 24 GHz, and especially at 77 GHz.

### 2.1.2 Different Kinds of TSA

An antenna is in principle a transition from a guided wave to an unbounded wave or vice versa. Ideally, this transition occurs without reflections. Looking at a typical TSA, this definition is quite intuitive: the TSA is a slot in a ground plane, supported by a dielectric substrate, which increases in width gradually in a certain fashion. As the width of the slotline increases, the characteristic impedance increases as well, thus providing a smooth transition to the free space characteristic impedance of $120\pi\ \Omega$.

Since 1979, there has been a number of publications that investigated the properties of TSAs with different slotline geometries. The most common types are LTSA (linear tapered slot antenna) [53–56], Vivaldi (exponential tapered slot antenna) [57–59], DETSA (dual exponential tapered slot antenna or bunny-ear radiating element) [60–62], CWSA

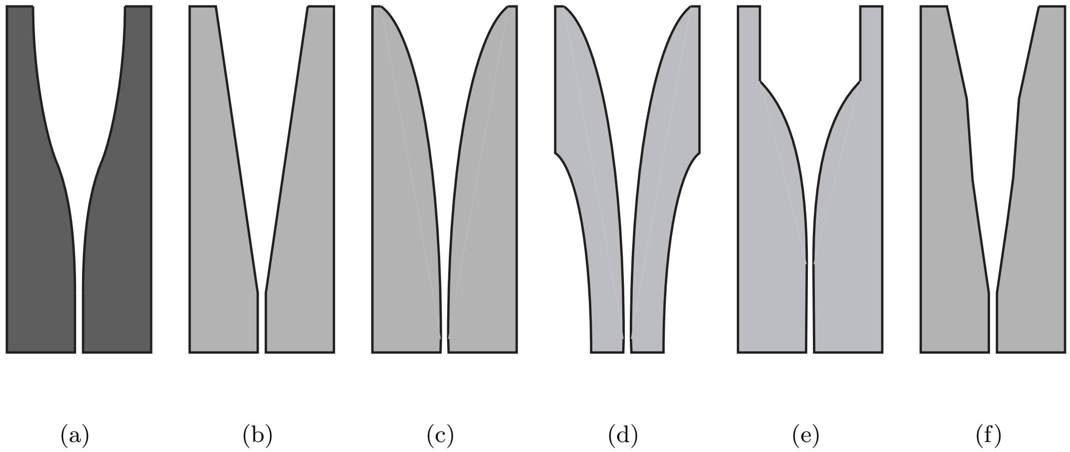


**Figure 2.1: Differently shaped tapered-slot antennas: (a) Fermi-TSA, (b) Linear TSA, (c) Vivaldi TSA, (d) Dual exponential TSA, (e) Constant width slot antenna, (f) Broken Linear TSA.**

(constant width slot antenna) [56,63], BLTSA (broken linear tapered slot antenna) [64–66], and FTSA (Fermi tapered slot antenna) [67,68] (Fig. 2.1).

All these types of TSA show different radiation patterns, also depending on the length and aperture of the slot and the supporting substrate. In general, when compared on the same substrate with the same length and aperture, the beamwidth is smallest for the CWSA, followed by the LTSA, and then the Vivaldi. The sidelobes are highest for the CWSA, followed by the LTSA, and then the Vivaldi [49]. The Vivaldi has theoretically the largest bandwidth due to its exponential structure [52]. The BLTSA shows a wider $-3$ dB beamwidth than the LTSA [67] and the cross-polarization in the D-plane (diagonal plane) is about 2 dB lower compared to LTSA and CWSA [65]. The DETSA has a smaller $-3$ dB beamwidth than the Vivaldi, but the sidelobe level is higher, although for higher frequency, the sidelobes can be suppressed [62]. Also, the DETSA gives an additional degree of freedom in design especially with regard to parasitic effects due to packaging. The FTSA exhibits very low and fairly symmetric sidelobes in the E- and H-plane, but its $-3$ dB beamwidth is larger than the BLTSA [67].

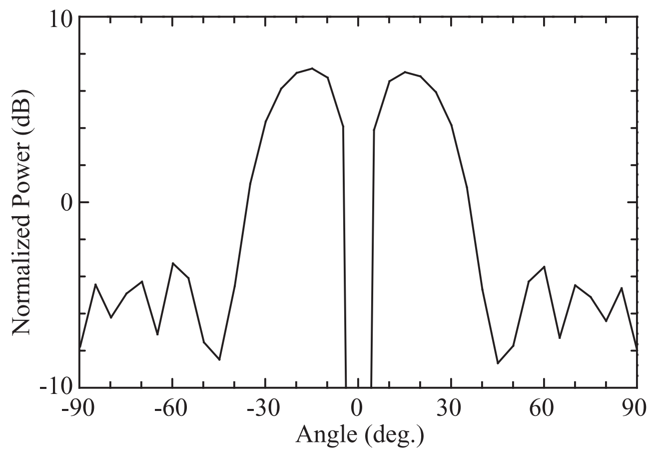


**Figure 2.2: Simulated H-plane radiation pattern with IE3D of an FTSA with length of $5\lambda_0$ and aperture of $0.7\lambda_0$ at 24 GHz on a 381 μm thick RT/Duroid substrate ($\varepsilon_r = 2.2$). The substrate is not truncated.**

### 2.1.3 Electromagnetic Simulation of TSAs

TSAs have been characterized analytically or with numerical methods [69–74]. Full 3-dimensional electromagnetic solvers like HFSS take a long time to complete a simulation run because with a length of 3 to $8\lambda_0$, the simulated structure is electrically large. 2.5-dimensional solvers like IE3D, Momentum, or Sonnet are sufficiently fast, but they cannot include a truncated dielectric layer. This means that one usually omits the dielectric layer which requires the knowledge of the effective dielectric constant in order to scale the circuit accordingly and still, the results will be somewhat inaccurate because the effective dielectric constant changes along the tapered slotline. Another method is to consider the dielectric layer as an infinite sheet, but this alters the simulated far-field radiation patterns in the plane of the substrate (Fig. 2.2) and introduces a sharp pattern null on-axis. Also, 2.5-dimensional solvers have typically difficulties modelling slotlines and simulation results should be carefully examined.

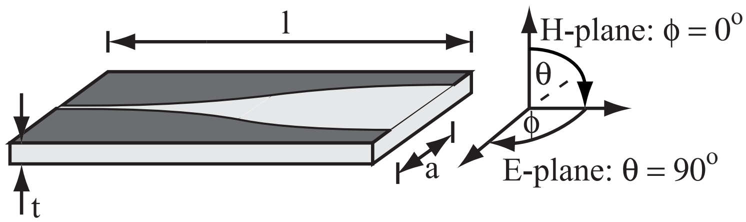


**Figure 2.3: Configuration of an FTSA.**

## 2.2 Design of Tapered Slot Antennas

The design of the feed antennas for this work meets certain constraints. First of all, the length of the TSA should be as short as possible to keep the overall size of the antenna-lens system small. Also, the aperture of the TSA should be small to be able to place many feed antennas around a spherical lens and possibly achieve a $-3$ dB overlap of adjacent beams. As will be seen in Chapter 3, it is discovered that the TSA aperture cannot be larger than $0.7\ \lambda_0$ (for $-3$ dB overlap), and the $-10$ dB beamwidth needs to be within $60°$ to $100°$ (for good coupling efficiency to the spherical lens).

The designed feed antennas are based on the TSA concept of Sugawara *et al.* [67] with a Fermi taper (Fig. 2.3). It provides symmetric radiation patterns and low sidelobe level in both, E- and H-plane, and its aperture is small. The taper of the slotline follows the function:

$$y = \frac{0.5a}{1 + e^{bx+c}} \tag{2.1}$$

where $a$ is the size of the aperture, and $b$ and $c$ are variables. In this work, $b = 2.4/\lambda_0$ and $c = -3$.

A TSA is sensitive to the thickness $t$ and the dielectric permittivity $\varepsilon$ of the supporting substrate. An accepted range for good operation of a TSA has been experimentally determined by Yngvesson *et al.* [52] and is:

$$0.005 \leq t_{eff}/\lambda_0 \leq 0.03 \tag{2.2}$$

where $t_{eff}$ is the effective thickness of the substrate defined as:

$$t_{eff} = t(\sqrt{\varepsilon_r} - 1). \tag{2.3}$$

For substrate thicknesses above the upper bound, the performance of the TSA is degraded by substrate modes, while TSAs on substrates thinner than the lower bound suffer from decreased directivity.

The supporting dielectric substrate for this work is RT/Duroid 5880 with a relative dielectric constant of $\varepsilon_r = 2.2$ because it is relatively inexpensive, has very low dielectric loss (tan $\delta = 0.001$ at 10 GHz), and is easy to manufacture. Its low dielectric constant is favorable for antenna design and allows substrate thicknesses which do not impose a mechanical problem. Also, the commercially available thicknesses of this substrate (127 µm, 254 µm, 381 µm, ...) are suitable for the design of the surrounding microwave/millimeter-wave circuits. Following 2.2, for a relative dielectric constant of 2.2, the limits of the substrate thickness for good operation are $42 \leq t \leq 250$ µm at 77 GHz, and $130 \leq t \leq 800$ µm at 24 GHz.

Since the pattern requirement of the feed antennas (between 60° - 100°) is not very challenging, the design of the TSA is done experimentally by the fabrication and measurement of different TSAs. The following antennas have been fabricated and tested:

- TSAs at 24 GHz with lengths $l$ from 2 to $5\lambda_0$, following exactly the FTSA design of Sugawara. The aperture is fixed at $a = 0.7\lambda_0$ and the substrate thickness is $t = 381$ µm.
- TSAs at 24 GHz with $l = 2.5\lambda_0$, $a = 0.7\lambda_0$, and $t = 381$ µm with different shapes of slotline tapering in an effort to decrease the length of the TSA.
- An FTSA at 77 GHz with $l = 5\lambda_0$, $a = 0.7\lambda_0$, and $t = 127$ µm.

## 2.3 Microstrip Line-to-Slotline Transition

### 2.3.1 Slotline

A slotline is a planar transmission line first proposed by Cohn in 1968 [75]. It is a thin slot in an infinite metallization layer supported by a dielectric substrate on one side (Fig. 2.4(a)). The major electric field component is oriented across the slot in the plane of

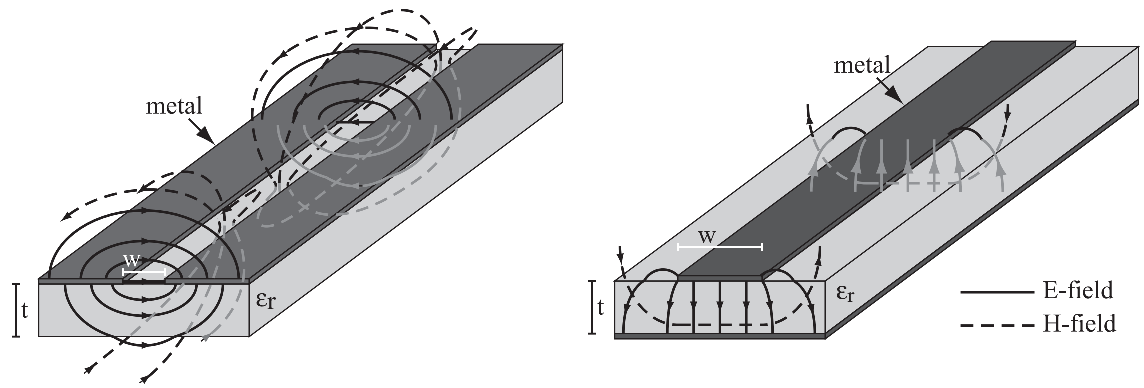


(a) (b)

**Figure 2.4: Configuration and field distribution of (a) slotline and (b) microstrip line.**

the metallization. The magnetic field has a major longitudinal component and therefore, the mode of propagation is almost transverse electric in nature.

The design formulas for the slotline used in this work are presented in Appendix A. The maximum frequency of operation is limited by the cut-off frequency of the first higher surface-wave mode ($TE_1$) [76]:

$$f_{c,TE_1} = \frac{c_0}{4t\sqrt{\varepsilon_r - 1}} \tag{2.4}$$

with $c_0$ being the speed of light in free space. The slotline is a transmission line with a relatively high characteristic impedance, and on a substrate with $\varepsilon_r = 2.2$ and metal thickness of 17 µm, it is impossible to fabricate a slotline with $Z_0 = 50\ \Omega$ with a standard fabrication process due to limitations in the minimum feature size. Therefore, the slotwidth in the antenna feedline is always kept at 100 µm since this is the minimum feature size that can be reliably realized. Table 2.1 gives an overview of the characteristic values of the slotlines used in this work.

A slotline is a two-conductor waveguide with a differential structure. Therefore, in order to transfer a signal from a single-ended source into a slotline, one needs a transformer or, in other words, a transition from an unbalanced transmission line (microstrip) to a balanced

| Frequency of Operation [GHz] | 24 | | 77 | |
|---|---|---|---|---|
| Substrate thickness [μm] | 381 | 254 | 254 | 127 |
| $Z_0$ [Ω] | 112 | 113.3 | 147.6 | 148.7 |
| $\varepsilon_{r,eff}$ | 1.39 | 1.35 | 1.43 | 1.34 |
| $f_{c,TE_1}$ [GHz] | 180 | 269 | 269 | 539 |

**Table 2.1: Characteristic impedance, effective dielectric constant, and cut-off frequency of a slotline with width $w = 100$ μm on a substrate with $\varepsilon_r = 2.2$.**

transmission line (slotline). Possible single-ended structures are waveguides, coaxial cables, coplanar waveguide (CPW) lines, or microstrip lines. Microstrip lines have less loss compared to CPW lines, and are much easier to fabricate on $\varepsilon_r = 2.2$ substrates with a copper layer with a thickness of 17 μm due to the small gaps required in the CPW structures. The other types of guiding structures are not planar and not applicable in this case.

### 2.3.2 Microstrip Line

A microstrip line is a two-conductor transmission line (Fig. 2.4(b)). One conductor is an infinite plane metallization layer acting as the ground plane and the other conductor is a line suspended at a certain distance above the ground plane using a thin dielectric substrate. The presence of the dielectric-air interface modifies the mode of propagation in a microstrip line to a non-TEM hybrid mode ($HE_0$). However, the longitudinal components of the E- and H-field are small and therefore, the departure from TEM behavior is minor and one can generally speak of a quasi-TEM mode. Approximate formulas for the design of microstrip lines are presented in Appendix A [77].

A microstrip line has no lower cut-off frequency since it is a quasi TEM structure. Depending on the geometry, the maximum frequency of operation is limited by the frequency at which significant coupling occurs between the quasi-TEM mode and the lowest order surface-wave spurious mode ($TM_0$), with the cut-off frequency of the next higher surface-wave mode ($TE_1$), or alternatively with the first higher-order mode ($HE_1$) of the microstrip

| $f$ [GHz] | $t$ [µm] | $W$ [µm] | $\varepsilon_{r,eff}$ | $Z_0$ | $f_t$ [GHz] | $f_{c,TE_1}$ [GHz] | $f_{c,HE_1}$ [GHz] |
|---|---|---|---|---|---|---|---|
| 24 | 381 | 300 | 1.74 | 102 | 173 | 180 | 223 |
| 24 | 381 | 1100 | 1.86 | 51.9 | 173 | 180 | 80.7 |
| 24 | 254 | 300 | 1.76 | 84.4 | 259 | 269 | 252 |
| 24 | 254 | 800 | 1.86 | 48.5 | 259 | 269 | 112 |
| 77 | 254 | 300 | 1.78 | 86.0 | 259 | 269 | 252 |
| 77 | 254 | 800 | 1.91 | 50.4 | 259 | 269 | 112 |
| 77 | 127 | 110 | 1.72 | 93.9 | 519 | 539 | 628 |
| 77 | 127 | 400 | 1.85 | 48.2 | 519 | 539 | 224 |

**Table 2.2: Characteristic impedance, effective dielectric constant, and maximum frequency of operation of a microstrip line on a substrate with $\varepsilon_r = 2.2$ and copper thickness of 17 µm.**

line. Significant coupling to the $TM_0$-mode occurs for frequencies higher than [78]:

$$f_t = \frac{c_0}{2\pi t}\sqrt{\frac{2}{\varepsilon_r - 1}\tan^{-1}(\varepsilon_\mathrm{r})}. \tag{2.5}$$

The cut-off frequency of the $HE_1$ mode of the microstrip line is [78]:

$$f_{c,HE_1} \cong \frac{c_0}{\sqrt{\varepsilon_r}(2W + 0.8t)}. \tag{2.6}$$

Table 2.2 gives an overview of the microstrip lines that are used in this work.

### 2.3.3 Microstrip Line-to-Slotline Transition

For a transition between microstrip line and slotline, the slotline is etched into the ground metal layer of the microstrip line and is crossed out of plane by the microstrip conductor in a right angle (Fig. 2.5(a)). The coupling of the fields between microstrip line and slotline occurs through the magnetic field (Figs. 2.4(a) and 2.4(b)). The coupling is strongest when the intersection occurs at a short circuit of the microstrip line (maximum current) and an open circuit of the slotline.

Since short circuits in a microstrip line require via holes, it is easier to terminate the microstrip line in an open circuit $\lambda_g/4$ from the transition intersection, where $\lambda_g$ is the

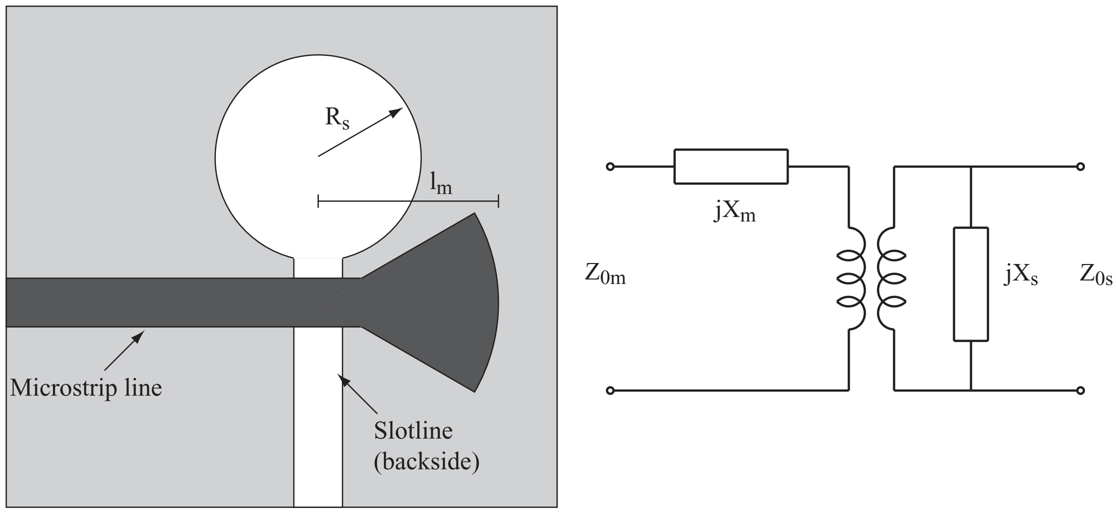


(a) (b)

**Figure 2.5: Schematic (a) and equivalent circuit (b) of the Microstrip line-to-slotline transition.**

guided wavelength in the microstrip line. For a wideband behavior, the termination is a quarter-wave radial stub [79]. Similarly for the slotline, an open circuit requires the ground metal layer to be truncated, which is impractical. Therefore, the slotline is terminated with a short circuit and recessed from the intersection by $\lambda_g/4$, with $\lambda_g$ being the guided wavelength in the slotline. To increase the bandwidth, the quarter-wave termination is realized in a circular disc [80], which is an approximation of an open circuit of a slotline. The larger the radius of the disc the better will be the open-circuit behavior. Theoretically, the circular disc will behave like a resonator. It is observed in [80] that the circular disc is capacitive in nature, and it behaves as an open circuit, as long as the operating frequency is higher than the resonance frequency of the disc resonator.

The microstrip line-to-slotline transition has been analyzed comprehensively by [81–84] and studied experimentally [85]. A transmission line equivalent circuit developed by Chambers [86] is shown in Fig. 2.5(b) with:

$$jX_s = Z_{0s}\frac{jX_{0s} + jZ_{0s}\tan(\theta_s)}{Z_{0s} - X_{0s}\tan(\theta_s)} \tag{2.7}$$

$$jX_m = Z_{0m}\frac{1/j\omega C_{0c} + jZ_{0m}\tan(\theta_m)}{Z_{0m} - \tan(\theta_S)/\omega C_{0c}}. \tag{2.8}$$

where $X_{0s}$ is the inductance of a shorted slotline, $C_{0c}$ is the capacitance of an open microstrip line, $Z_{0s}$ and $Z_{0m}$ are the characteristic impedances of slotline and microstrip line, respectively, and $\theta_s$ and $\theta_m$ represent the electrical lengths of the extended portions of the slotline and the microstrip line, respectively, measured from the center of the intersection.

## 2.4 Fabrication

All circuits described and measured in Chapters 2, 3, and 4 are fabricated on RT/Duroid 5880 substrate with a copper layer of 17 μm thickness on either side. The fabrication process is a one-mask process with one lithography step. First, photo-sensitive resist is spun onto the substrate. Then, the substrate is aligned to a mask and the pattern is transferred by exposure to UV-light. The photosensitive resist is developed and then the exposed areas of the copper are removed in a wet-etching process. Finally, the undeveloped photosensitive resist is removed. The reader is referred to Appendix D for more details about the fabrication process. The minimum feature size in this process is around 70 μm. However, to ensure consistency, all fabricated circuits have features no smaller than 100 μm.

## 2.5 Measurements

### 2.5.1 Radiation Patterns

#### Pattern measurement setup at 24 and 77 GHz

The radiation pattern measurements at 24 and 77 GHz are all done in an anechoic chamber to approximate conditions in free space (Fig. 2.6). Fig. 2.7 shows the schematic of the measurement setup. At 24 GHz, a signal is generated at 12 GHz by a synthesizer, up-converted to 24 GHz using a $\times 2$ multiplier, and amplified to 23 dBm. At 77 GHz, the signal is generated with a Gunn-diode with an output power of 16 dBm. Both signals are transmitted through a standard gain horn antenna with 22 dB of gain. The signal is received by the device under test (DUT). To detect the signal, a planar Silicon Schottky

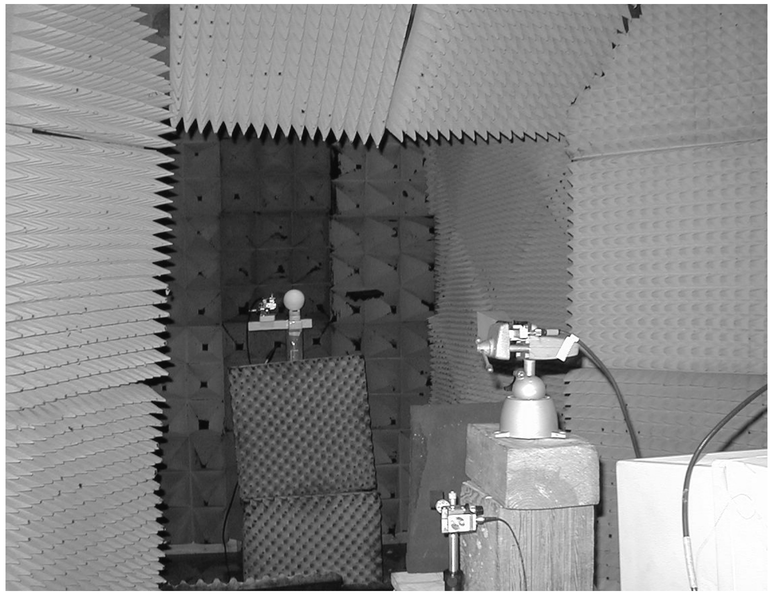

**Figure 2.6: Photograph of the anechoic chamber for radiation pattern measurements at the University of Michigan.**

diode (Metelics MSS 30−148-B10) is mounted with electrically conductive epoxy (H20E, Epoxy Technology) across a gap in the microstrip line (Fig. 2.8). For higher sensitivity, the diode is DC-biased at 20 μA. Two $\lambda/4$-stub filters make sure that there is a current maximum at the location of the diode detector and no leakage into the DC-path. The transmitted signal is amplitude modulated at 1 kHz and the detected video signal is sent to a lock-in amplifier. The signal-to-noise ratio at an integration time of 300 ms is limited by the measurement chamber and the diode responsivity and is around 35 dB. The distance between the transmitting and receiving antenna is around 3 m, satisfying well the far-field condition ($r_{ff} > 2D^2/\lambda_0$, where in the worst case $2D^2/\lambda_0 = 1.32$ m with D $= 13\lambda_0$ for a 50 mm sphere at 77 GHz).

**FTSA at 24 GHz from $l = 2$ to $5\lambda_0$**

The influence of the length of the tapered slot on the radiation pattern is investigated experimentally. The substrate is RT/Duroid 5880 with a thickness of 381 μm and a dielectric constant of $\varepsilon_r = 2.2$. The size of the aperture is found to have little influence on the

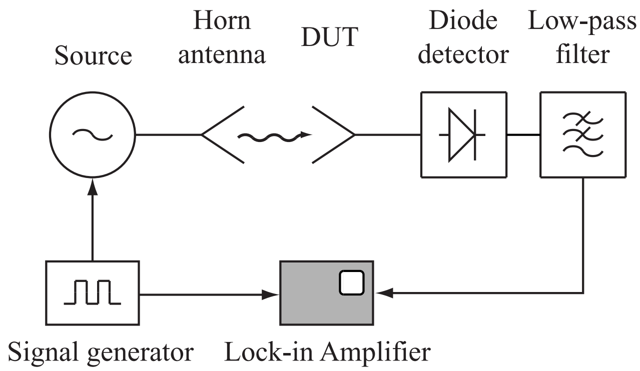


**Figure 2.7: Schematic of the radiation pattern measurement setup at 24 and 77 GHz.**

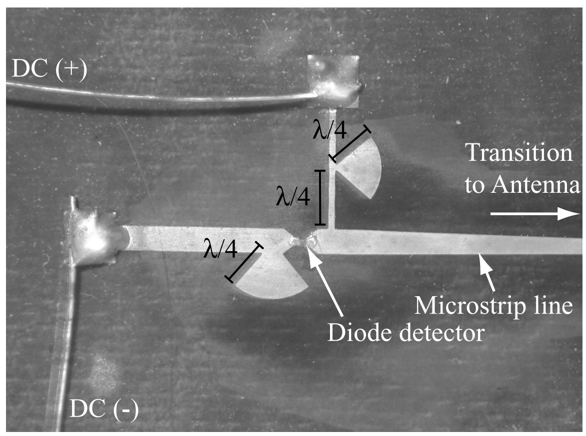


**Figure 2.8: Photograph of the diode detector and filter circuit used for radiation pattern measurement.**

radiation pattern and is fixed at $a = 0.7\lambda_0$. Fig. 2.9 presents the measured E- and H-plane radiation patterns at 24 GHz for co- and cross-polarization for FTSAs with lengths $l = 2$, 3, 4, and $5\lambda_0$. As expected, the gain increases with increasing length (Fig. 2.10). The cross-polarization level is below $-11$ dB throughout all lengths of the FTSA.

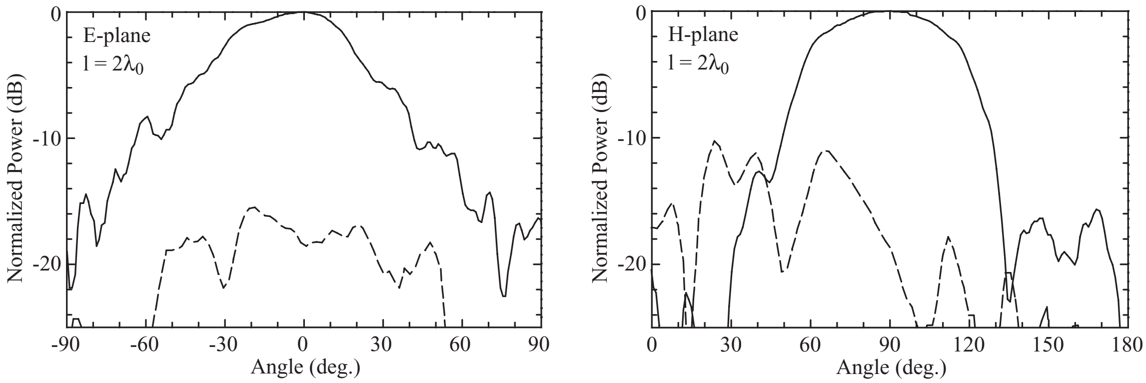
E-plane
l = 2λ0
H-plane
l = 2λ0
Normalized Power (dB)
0
-10
-20
Angle (deg.)
-90
-60
-30
0
30
60
90
0
30
60
90
120
150
180

(a)

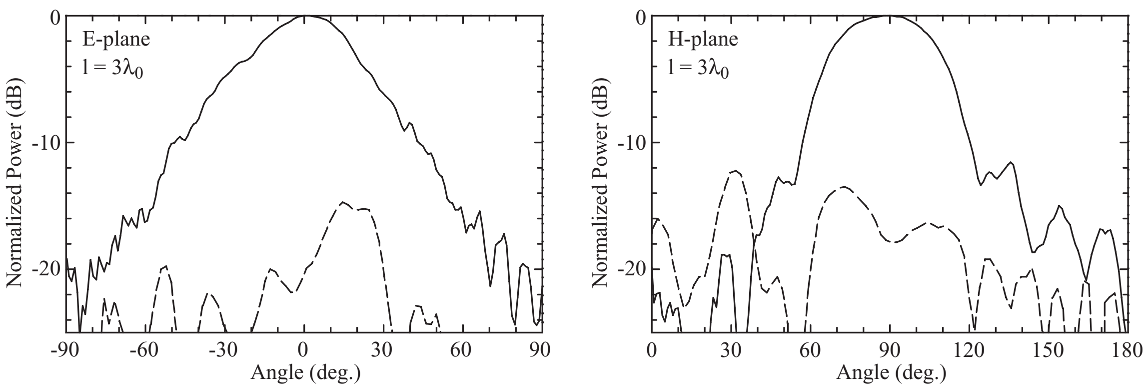
E-plane
l = 3λ0
H-plane
l = 3λ0
Normalized Power (dB)
0
-10
-20
Angle (deg.)
-90
-60
-30
0
30
60
90
0
30
60
90
120
150
180

(b)

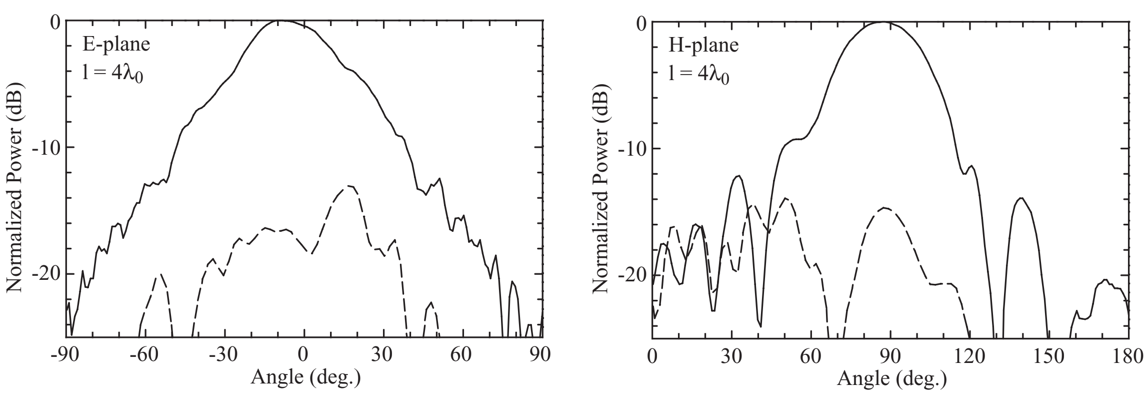
E-plane
l = 4λ0
H-plane
l = 4λ0
Normalized Power (dB)
0
-10
-20
Angle (deg.)
-90
-60
-30
0
30
60
90
0
30
60
90
120
150
180

(c)

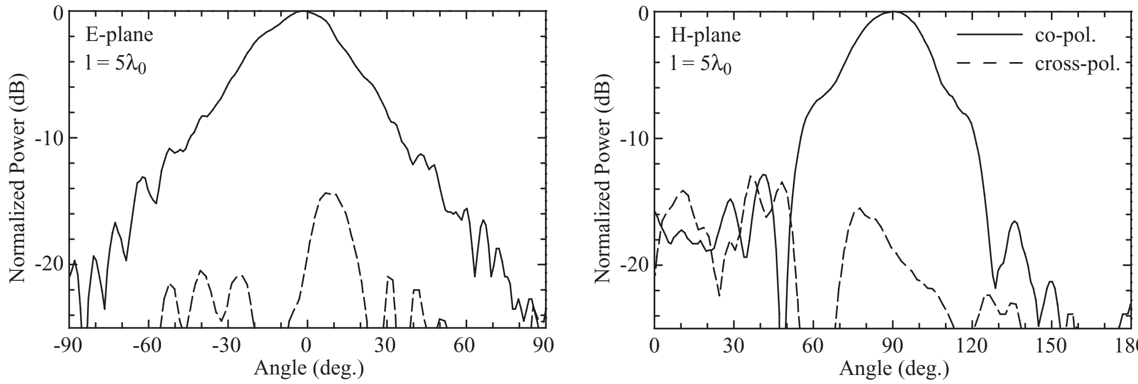


(d)

**Figure 2.9: Measured E- and H-plane radiation patterns of co- and cross-polarization of FTSAs built on 381 μm thick RT/Duroid 5880 substrate with lengths from $l = 2$ to $5\lambda_0$ at 24 GHz: (a) $2\lambda_0$, (b) $3\lambda_0$, (c) $4\lambda_0$, (d) $5\lambda_0$.**

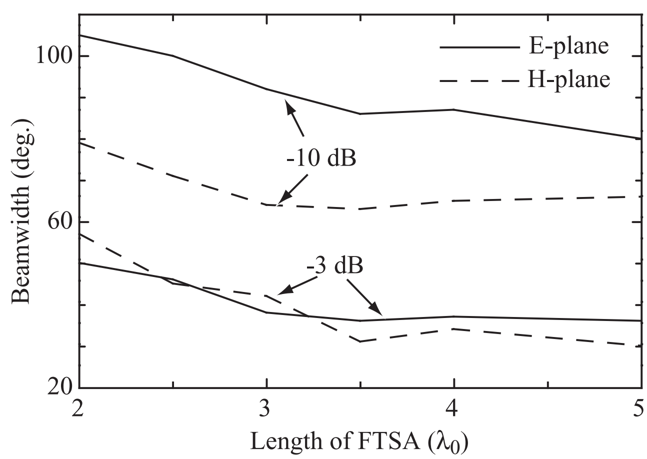


**Figure 2.10: Measured $-3$ and $-10$ dB beamwidths of FTSAs built on 381 μm thick RT/Duroid 5880 substrate with lengths from $l = 2$ to $5\lambda_0$ at 24 GHz.**

### Different TSA designs at 24 GHz with $l = 2.5\lambda_0$

At 24 GHz, the TSAs are rather large and contribute substantially to the overall size of an antenna-lens system. Therefore, different variations of the FTSA are tested in order

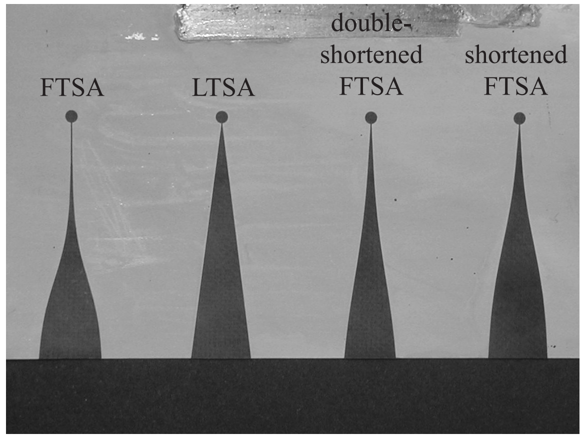


**Figure 2.11: Photograph of four different types of TSA with $l = 2.5\lambda_0$ and $a = 0.7\lambda_0$.**

to find a design which is shorter than the standard FTSA of Fig. 2.3, at the same time, provide the same antenna gain and have symmetric patterns and low sidelobes as well as low cross-polarization. Three designs are investigated (Fig. 2.11):

- A linear tapered-slot antenna (LTSA).
- An FTSA where $1.6\lambda_0$ of the slotline is taken away at the narrow end and then scaled to the desired length. This design will be referred to as *shortened FTSA*.
- An FTSA where $1.6\lambda_0$ of the slotline is taken away at the narrow end and $0.8\lambda_0$ is taken away at the wide end of the slotline. This design will be referred to as *double-shortened FTSA*.

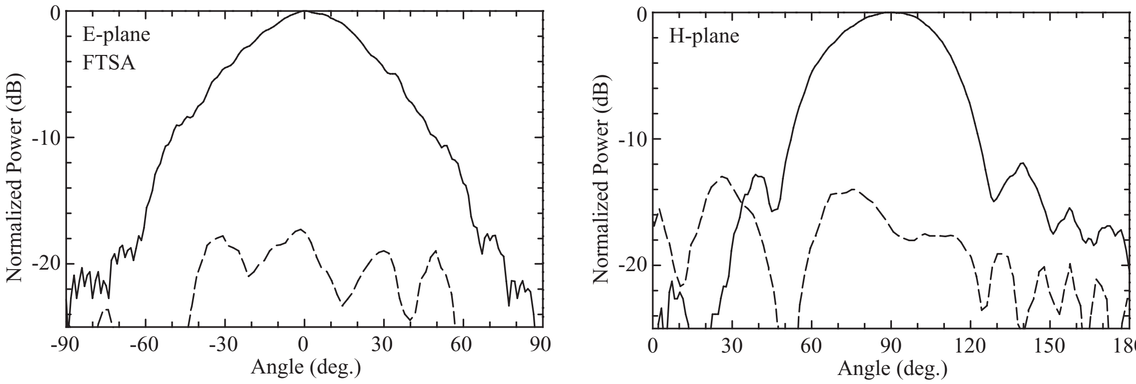
E-plane
FTSA
Normalized Power (dB)
Angle (deg.)
H-plane
Normalized Power (dB)
Angle (deg.)

(a)

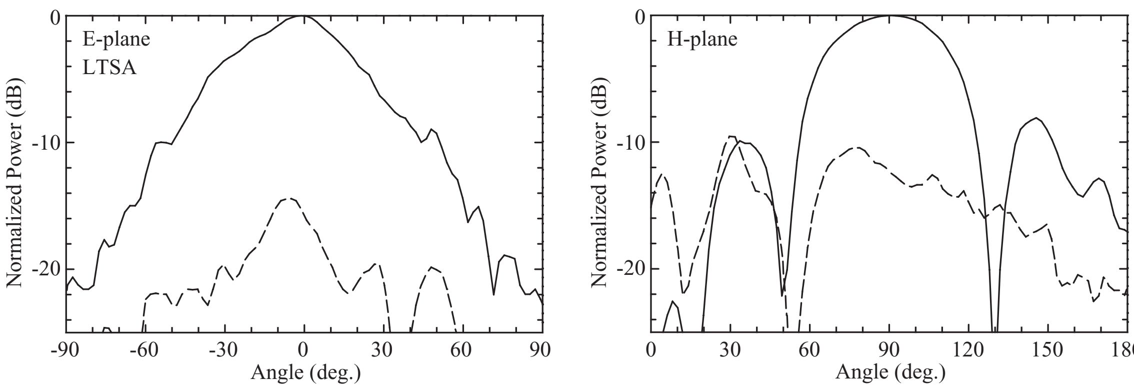
E-plane
LTSA
Normalized Power (dB)
Angle (deg.)
H-plane
Normalized Power (dB)
Angle (deg.)

(b)

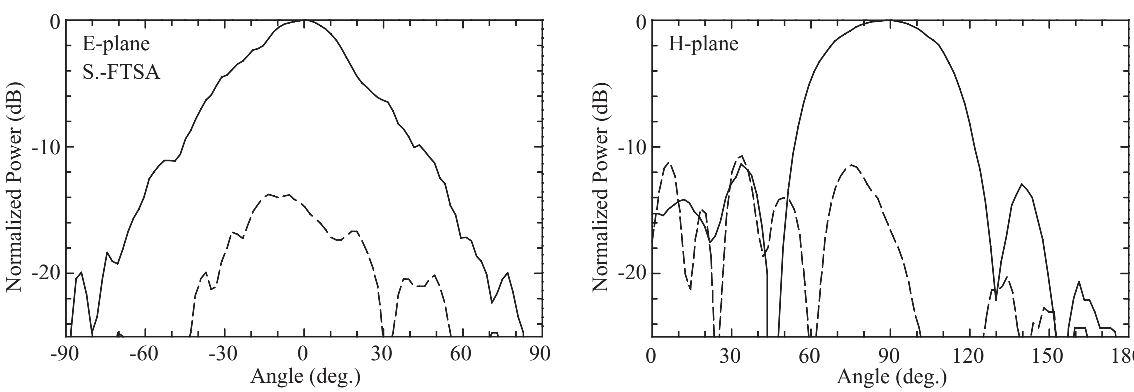
E-plane
S.-FTSA
Normalized Power (dB)
Angle (deg.)
H-plane
Normalized Power (dB)
Angle (deg.)

(c)

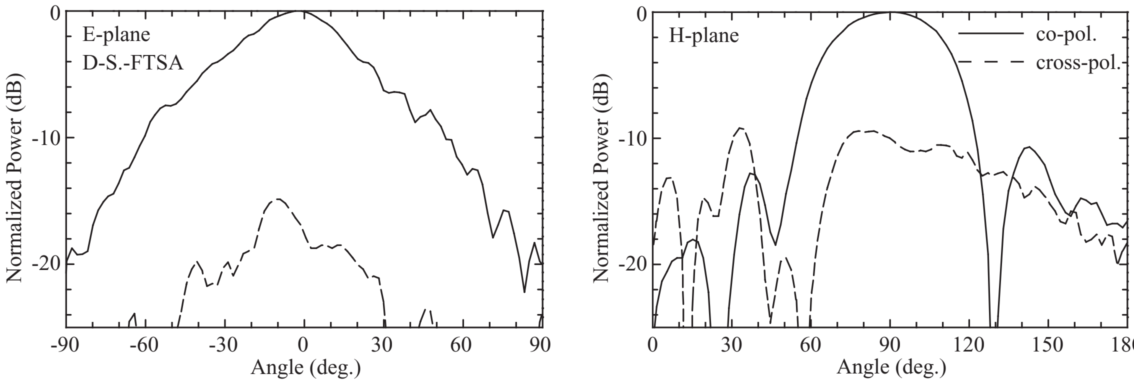


(d)

**Figure 2.12: Measured E- and H-plane radiation patterns of co- and cross-polarization components of four different TSAs fabricated on 381 μm thick RT/Duroid 5880 substrate with length $l = 2.5\lambda_0$ at 24 GHz: (a) FTSA, (b) LTSA, (c) shortened FTSA, (d) double-shortened FTSA.**

Fig. 2.12 shows the measured radiation patterns in E- and H-plane for co- and cross-polarization of these three alternative TSA designs with an overall length of $l = 2.5\lambda_0$. It is clear that the LTSA and the double-shortened FTSA have $-3$ and $-10$ dB beamwidths similar to the FTSA, indicating a similar directivity (Table 2.3). However, both designs show sidelobes of $-10$ dB or higher in the H-plane which is about 4 dB higher than the FTSA. Also, the level of cross-polarization is slightly higher in the E-plane and considerably higher in the H-plane ($\geq -10$ dB as compared to $-13$ dB). The shortened FTSA design shows greater directivity than the FTSA. In the H-plane, the sidelobe level is about 2 dB higher compared to the FTSA and the cross-polarization level is below $-10$ dB.

From these measurements, it is seen that the FTSA is indeed a very good tapered-slot antenna design with symmetric radiation patterns in E- and H-plane, low cross-polarization level and low sidelobes (Sugawara *et al.* have done a good job). The shortened FTSA is not exactly as well-natured but has higher gain which can be a good compromise when size is a critical issue. The LTSA and the double-shortened FTSA are not competitive for the purposes of this work. Fig. 2.13 shows the measured radiation patterns of a $2.5\lambda_0$ shortened

| Beamwidth | −3 dB | | −10 dB | |
|---|---|---|---|---|
| Type of TSA | E-plane | H-plane | E-plane | H-plane |
| FTSA | 46° | 45° | 100° | 71° |
| LTSA | 43° | 47° | 106° | 68° |
| *Shortened* TSA | 38° | 48° | 90° | 68° |
| *Double-shortened* TSA | 44° | 46° | 113° | 68° |

**Table 2.3: Measured −3 and −10 dB beamwidths of four different TSAs built on 381 μm thick RT/Duroid 5880 substrate with $l = 2.5\lambda_0$ at 24 GHz.**

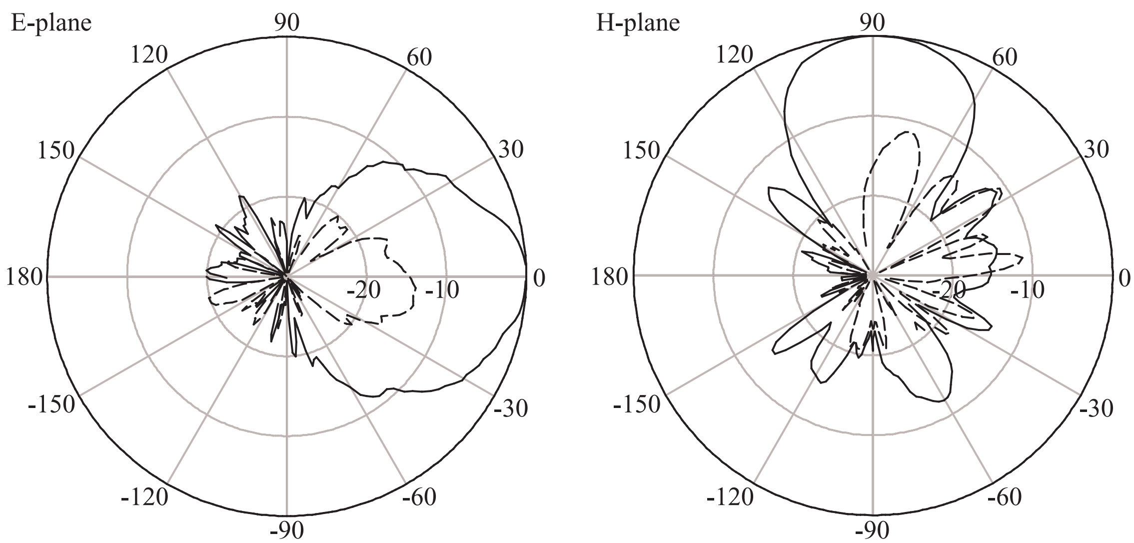


**Figure 2.13: Polar plot of the measured radiation patterns of the $2.5\lambda_0$ shortened FTSA at 24 GHz.**

FTSA at 24 GHz in a polar plot with very good front-to-back ratio.

### Shortened FTSA with $l = 2.5\lambda_0$ st 24 GHz measured from 16 to 27 GHz

In order to verify that the TSA is indeed a wideband antenna, the radiation patterns of the shortened FTSA with a length of $l = 2.5\lambda_0$ at 24 GHz are measured from 16 to 27 GHz

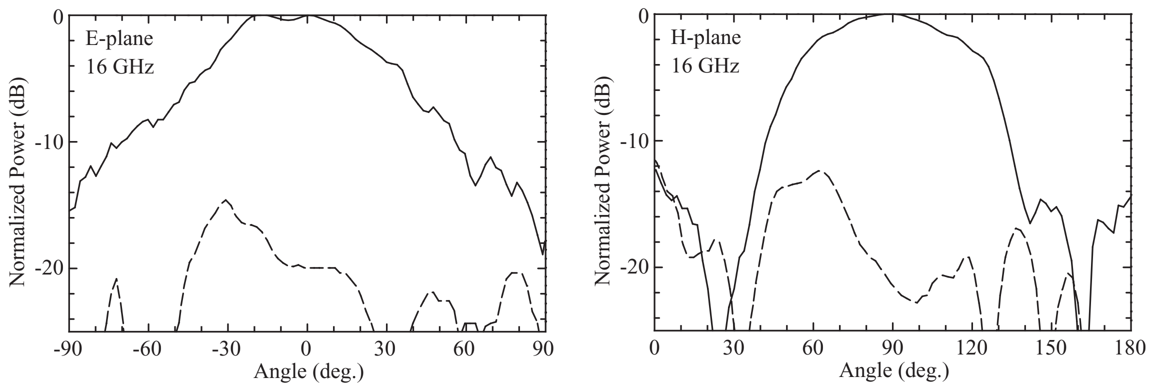


(a)

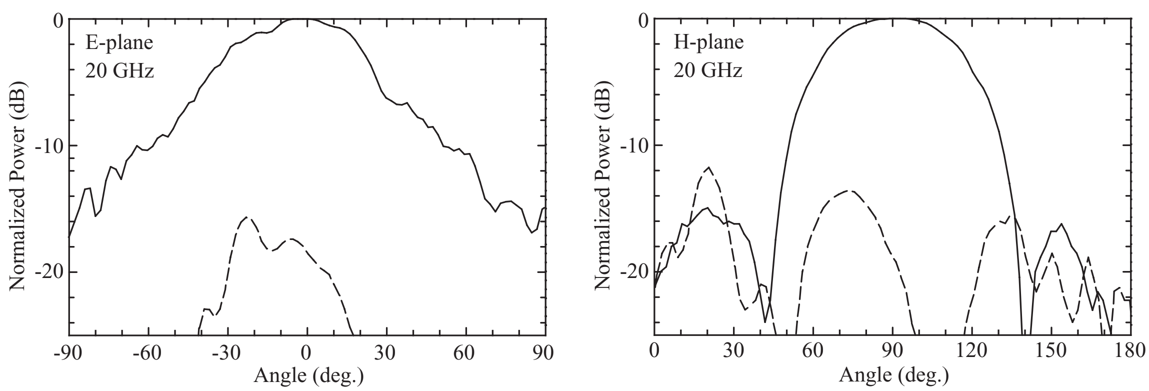


(b)

(Fig. 2.14). The results show that the shortened FTSA design is a very wideband antenna with a cross-polarization level as well as a sidelobe level below $-10$ dB throughout the entire measured frequency range in E- and H-plane. The $-3$ and $-10$ dB beamwidths (Fig. 2.15) are larger for lower frequencies and smaller for higher frequencies, which is expected, since the antenna becomes electrically larger as the frequency of operation increases.

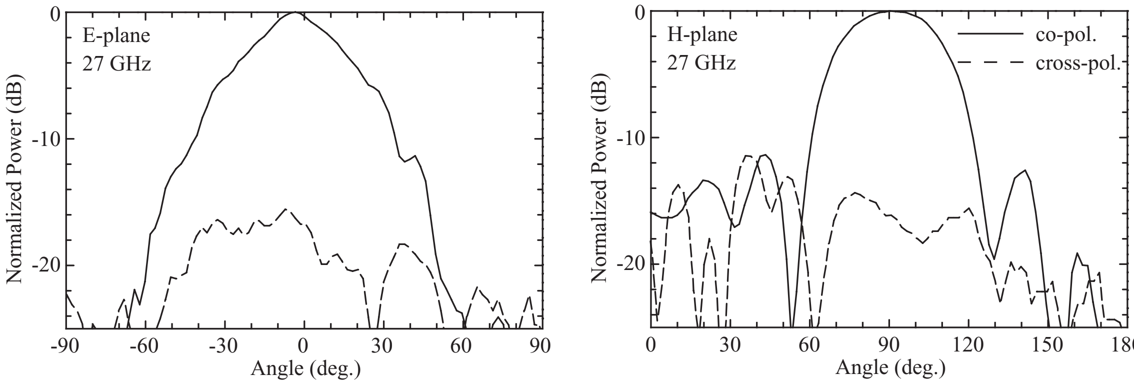


(c)

**Figure 2.14: Measured E- and H-plane radiation patterns of co- and cross-polarization components of the shortened FTSA fabricated on 381 μm thick RT/Duroid 5880 substrate with length $l = 2.5\lambda_0$ at 24 GHz for different frequencies: (a) 16 GHz, (b) 20 GHz, (c) 27 GHz.**

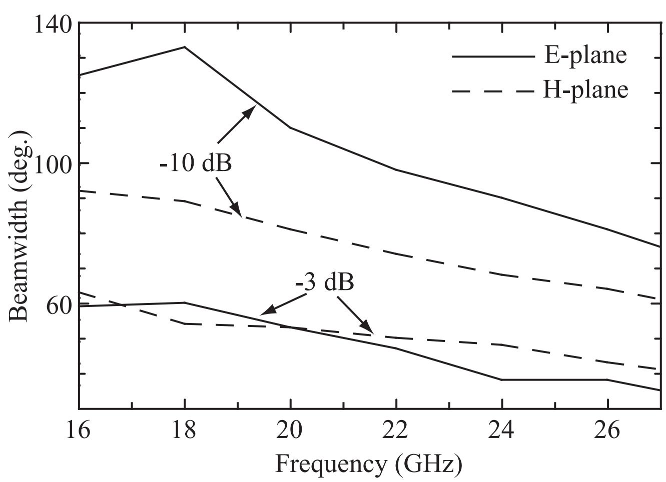


**Figure 2.15: Measured −3 and −10 dB beamwidths of the shortened FTSA fabricated on 381 μm thick RT/Duroid 5880 substrate with length $l = 2.5\lambda_0$ at 24 GHz for different frequencies.**

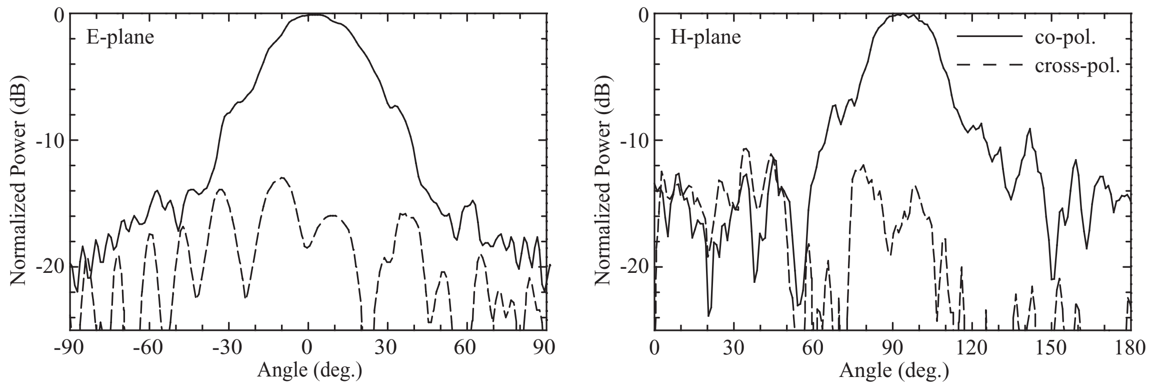


**Figure 2.16: Measured radiation patterns in E- and H-plane of co- and cross-polarization of FTSA built on 127 μm thick RT/Duroid 5880 substrate with lengths of $l = 5\lambda_0$ at 77 GHz.**

### FTSA at 77 GHz with $l = 5\lambda_0$

To verify that the FTSA design works also well at 77 GHz on an $\varepsilon_r = 2.2$ substrate with thickness $t = 127$ μm, an FTSA with length $l = 5\lambda_0$ is fabricated and measured. The radiation patterns are shown in Fig. 2.16. The measured $-3$ dB and $-10$ dB beamwidths are 38° and 76° in the E-plane, and 27° and 70° in the H-plane, respectively. The cross-polarization level is below $-10$ dB as well as the sidelobe level. These results agree very well with the measured radiation patterns of the $5\lambda_0$ long FTSA at 24 GHz on 381 μm thick substrate.

## 2.5.2 Microstrip Line-to-Slotline Transition Measurement

### K and W-band on-wafer measurements

The S-parameter measurements are done using an HP8510 vector network analyzer (VNA) and the Through-Reflect-Line (TRL) on-wafer calibration technique is used to de-embed all the transitions and parasitics from the waveguide or coaxial cable to the CPW probe launchers and the transmission-line itself, up to a predetermined reference plane. The software used is MULTICAL developed by NIST [87] and it calculates the best set of calibration coefficients based on the measured line responses. It allows easy characterization

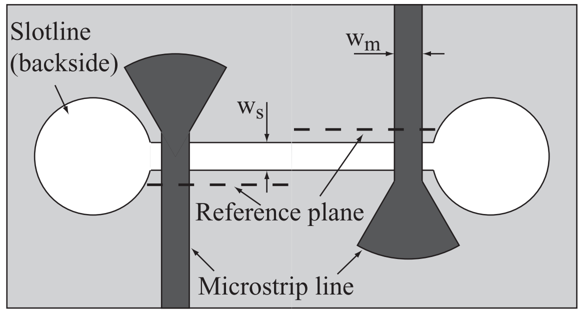


**Figure 2.17: Back-to-back Microstrip line-to-slotline configuration used for S-parameter measurements.**

of the effective dielectric constant and the loss of the calibration lines. According to MULTICAL, the loss of a 50 Ω microstrip line on a 381 µm thick RT/Duroid 5880 substrate at 24 GHz is 0.015 dB/mm and the loss on a 127 µm thick substrate at 77 GHz is 0.06 dB/mm.

### S-Parameter Measurement Results

The characterization of microstrip line-to-slotline transitions for 24 and 77 GHz on different substrates is done in a back-to-back configuration (Fig. 2.17). This makes measurement and calibration much easier. The S-parameter measurement results therefore include two microstrip line-to-slotline transitions and a short section of slotline (2300 µm at 24 GHz and 1100 µm at 77 GHz). Measurements with slotlines of different length indicate that the loss in the slotline is about 0.063 dB/mm at 24 GHz and 0.25 dB/mm at 77 GHz. The reference plane of the measurements is shifted close to the transition to get accurate values. Four microstrip line-to-slotline transitions with a slotline width of $w_s$ = 100 µm are designed and measured at 24 and 77 GHz, on 381, 254, and 127 µm thick substrates with $\varepsilon_r = 2.2$ (Fig. 2.18).

At 24 GHz, the length of the quarter-wave microstrip line stub $l_m$ is 1650 µm and its opening angle is 60°. The circular termination of the slotline has a radius $R_s$ of 685 µm. At 77 GHz, the length of the quarter-wave microstrip line stub $l_m$ is 600 µm with an opening angle of 60°. The radius $R_s$ of the circular termination of the slotline is 250 µm.

24 GHz on 381 µm thick substrate (Fig. 2.18(a)): The width of the microstrip line $w_m$

| Frequency [GHz] | 24 | | 77 | |
|---|---|---|---|---|
| Substrate thickness [µm] | 381 | 254 | 254 | 127 |
| $w_m/w_s$ [µm/µm] | 300/100 | 300/100 | 220/100 | 110/100 |
| Loss per transition [dB] | 0.43 | 0.18 | 0.86 | 0.46 |
| Range of frequency [GHz - GHz] | 12 - 33 | 10 - 27 | 70 - 100 | 70-110 |

**Table 2.4: Summary of microstrip line-to-slotline transitions.**

is 300 µm. The reflection coefficient is below $-10$ dB from 10 to 40 GHz with a small peak of $-9$ dB around 33 GHz. The transmission coefficient is around $-1.0$ dB from 12 to 30 GHz, resulting in an insertion loss of $-0.43$ dB per transition. The drop at 22 GHz is attributed to the fact that at this frequency the two transitions are exactly $\lambda_g/4$ apart from each other. It has been found experimentally that the choice of the widths for microstrip line and slotline is not very critical. Similar results have been achieved for $w_m/w_s$-pairs of 220/200 µm and 220/100 µm.

<u>24 GHz on 254 µm thick substrate</u> (Fig. 2.18(b)): $w_m$ is 300 µm. The reflection coefficient is below $-14$ dB from 10 to 40 GHz. The transmission coefficient is around $-0.5$ dB from 10.5 to 28 GHz with a drop to $-1.0$ dB at 16 GHz. This results in an insertion loss of 0.18 dB per transition. In this design, it has been found experimentally that values for the line widths are more critical and $w_m/w_s$-pairs of 220/200 µm and 220/100 µm show a drop in the transmission coefficient of more than 0.25 dB per transition.

<u>77 GHz on 254 µm thick substrate</u> (Fig. 2.18(c)): With $w_m = 220$ µm, the reflection coefficient is less than $-10$ dB from 70 to 100 GHz. The transmission coefficient is around $-2.0$ dB from 70 to 89 GHz and drops to around $-4.0$ dB at 105 GHz. This results in an insertion loss of 0.86 dB per transition at 77 GHz.

<u>77 GHz on 127 µm thick substrate</u> (Fig. 2.18(d)): The measured reflection coefficient with $w_m = 110$ µm is below $-10$ dB from 70 to 110 GHz. The transmission coefficient is around $-1.2$ dB up to 85 GHz and drops to $-2.8$ dB at 110 GHz. This results in a transmission loss per transition of 0.46 dB at 77 GHz.

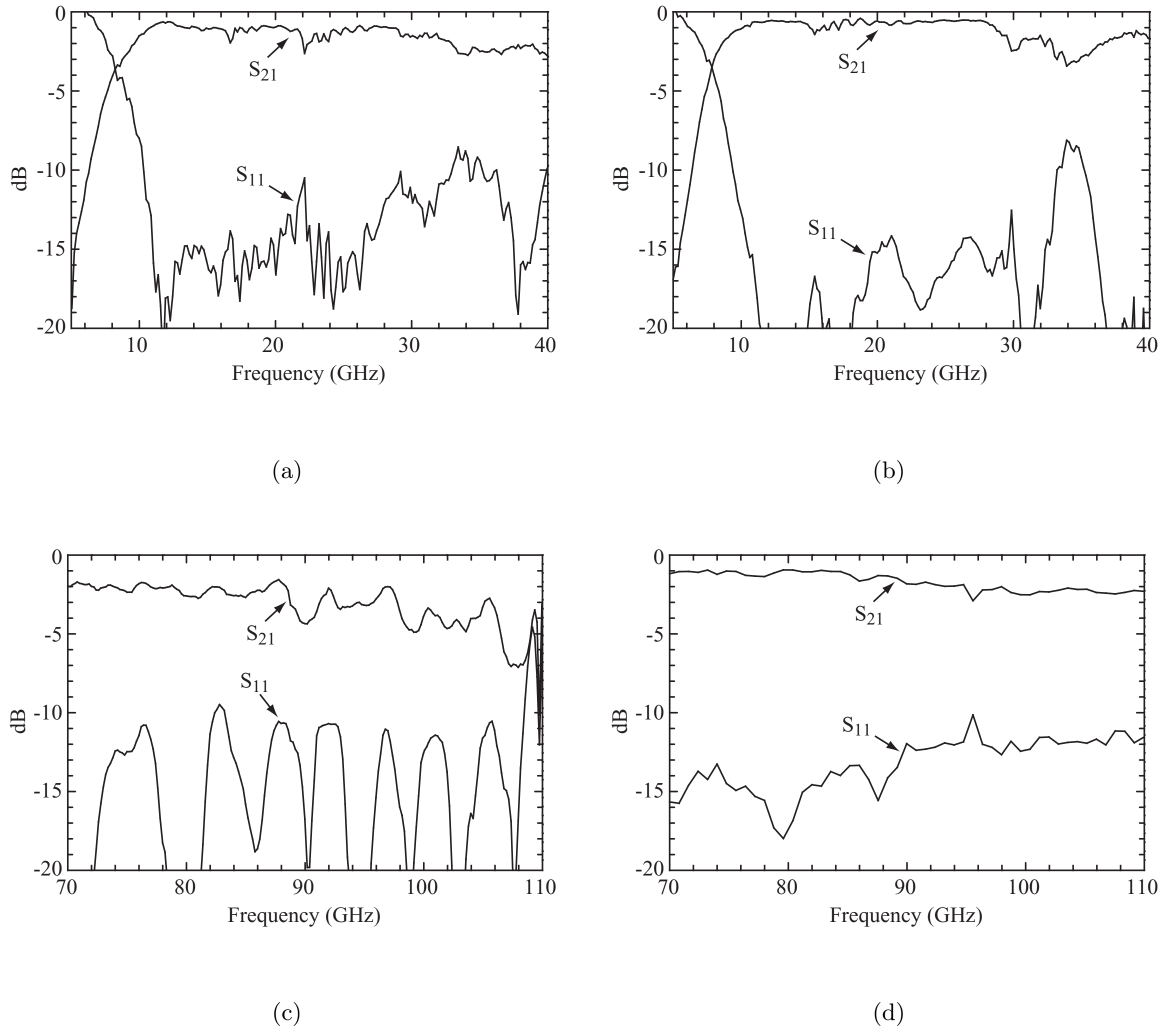


**Figure 2.18: Measured S-parameters of microstrip line-to-slotline transitions on RT/Duroid 5880 substrate designed for 24 GHz on (a) 381 μm substrate and (b) 254 μm substrate and 77 GHz on (c) 254 μm substrate and (d) 127 μm substrate (see Table 2.4 for details).**

### 2.5.3 $S_{11}$ Measurement of TSAs

Knowing that the microstrip line-to-slotline transition works well over a wide frequency band, the reflection coefficient of two different antennas including the transition from microstrip line to slotline is measured:

- a shortened FTSA at 24 GHz with $l = 2.5\lambda_0$ on 381 μm thick substrate.

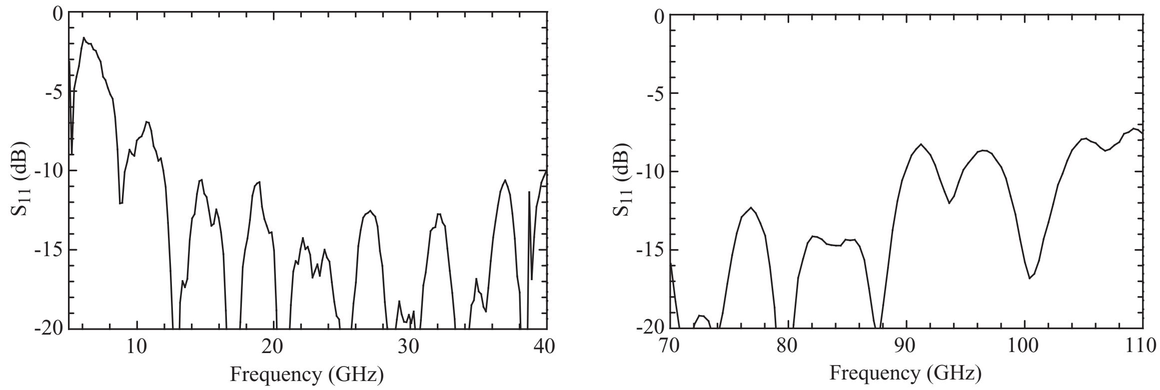


(a) (b)

**Figure 2.19: Measured reflection coefficient of (a) a shortened FTSA with $l = 2.5\lambda_0$ at 24 GHz on a 381 μm substrate and (b) an FTSA with $l = 5\lambda_0$ at 77 GHz on a 127 μm substrate.**

- an FTSA with $l = 5\lambda_0$ at 77 GHz on 127 μm thick substrate.

The reflection coefficient of a shortened FTSA with $l = 2.5\lambda_0$ at 24 GHz is shown in Fig. 2.19(a). With $S_{11}$ better than −10 dB, the antenna with transition from microstrip line-to-slotline is well matched from 11 to 40 GHz. The FTSA with $l = 5\lambda_0$ at 77 GHz (Fig. 2.19(b)) has a reflection coefficient below −12 dB from 70 to 90 GHz. It stays below −8 dB to almost 110 GHz.

### 2.5.4 Absolute Gain Measurement

The absolute gain of different TSAs is measured using the setup shown in Fig. 2.20. A signal is generated and transmitted through an antenna which is placed at a distance $R$ from a receiving antenna. Both antennas are pointed directly at each other. The gain of the tested antenna (DUT) can be calculated if the gain of the other antenna, the transmitted power, and the received power is known, using the Friis transmission formula:

$$\frac{P_r}{P_t} = \frac{G_1 G_2 \lambda^2}{(4\pi R)^2} \tag{2.9}$$

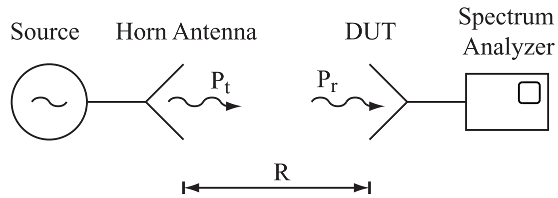


**Figure 2.20: Schematic of the absolute gain measurement setup at 24 and 77 GHz.**

with $P_r$ and $P_t$ being the received and transmitted power, $G_1$ and $G_2$ the gains of the transmitting and the receiving antenna and $R$ the physical separation.

At 24 GHz, a signal at 12 GHz is generated by a synthesizer, doubled in frequency, and amplified. The signal is transmitted through a standard gain horn antenna and received by the tested antenna. The gain $G_1$ is calculated from the measured radiation pattern according to:

$$G_1 = \frac{180^2}{\Theta_{-3dB\_E}\Theta_{-3dB\_H}} \tag{2.10}$$

where $\Theta_{-3dB\_E}$ and $\Theta_{-3dB\_H}$ are the $-3$ dB beamwidths in degrees in E- and H-plane, respectively, and is 21.2 dB at 24 GHz. The output power and received power is measured with a spectrum analyzer. The measured absolute gain of the antenna is de-embedded from the losses in the slotline-to-microstrip line transition and in the microstrip line. At 24 GHz, the measured absolute gain of an FTSA with $l = 5\lambda_0$ and $a = 0.7\lambda_0$, built on a 381 µm thick substrate, is 10.9 dB. It is estimated that this gain is accurate to $\pm 0.75$ dB due to the inaccuracy in 3.30 and in the spectrum analyzer power reading.

## 2.6 Wide Scan-Angle 24 GHz Tapered-Slot Antenna Array

For certain automotive applications like parking aid and military radars, a wide scan angle is desirable and at the same time high resolution is not required. With the tapered slot antennas described in this chapter, a simple, low-cost, and highly reliable antenna system can be designed that suits these applications.

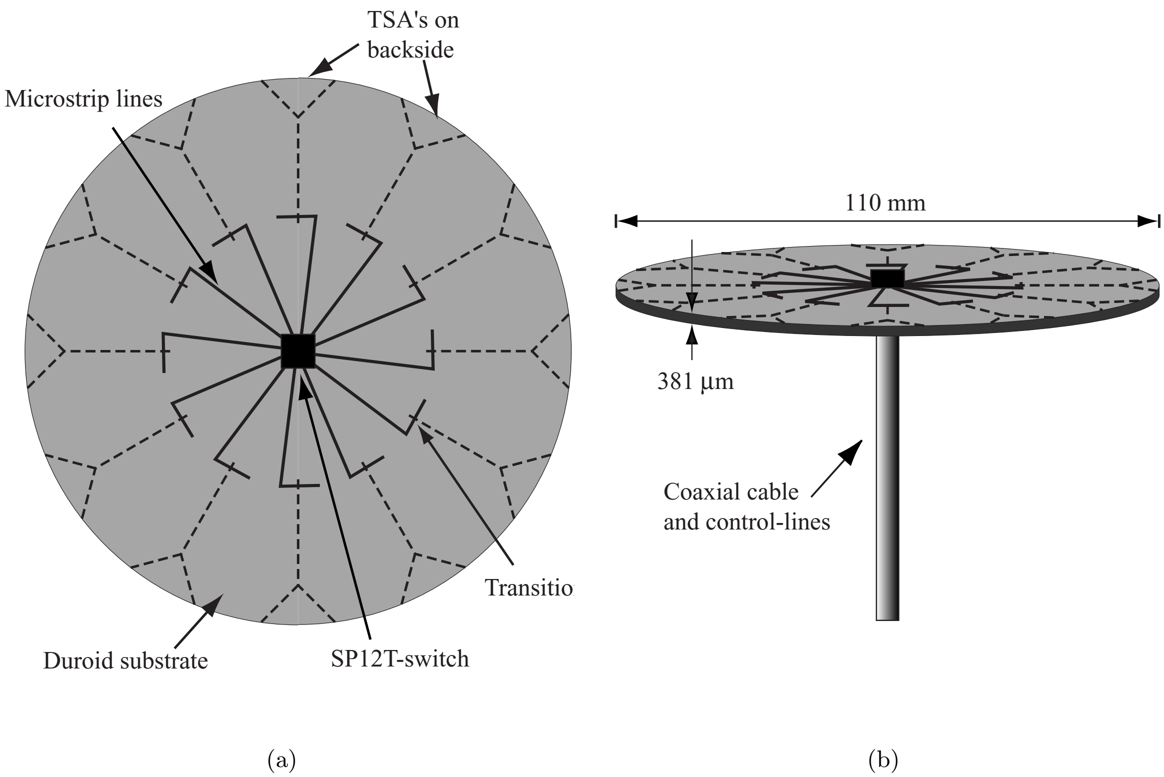


**Figure 2.21: The schematic of a wide scan-angle, low-resolution antenna system: (a) topview, (b) sideview.**

### 2.6.1 Concept

Depending on the desired resolution and cross-over level of adjacent antenna beams, 8 to 16 TSAs can be arranged in a circular fashion (Fig. 2.21). The antennas are pointing outwards, away from the center of the circle. The TSAs can be fed by a coaxial cable which is connected to an SPNT switch-MMIC in the center of the circuit. Beam-scanning of 360° in the horizontal plane is achieved by switching between the different antennas elements.

### 2.6.2 Design Challenges

The main challenge with this antenna system is to minimize the coupling between the antennas which will degrade the radiation patterns. The coupling between the tapered slots is not a critical issue because the TSAs are not very closely spaced. Since the TSAs are pointing outwards, the distance is large especially where the fields are only loosely confined in the wide slots. The main source of coupling is actually in the microstrip feedlines. Coupling is high at the center of the circuit because the switch is a small MMIC and the microstrip lines are very close to each other when connected to the switch. Also, bends in the microstrip line which are necessary for the microstrip line-to-slotline transitions can launch substrate modes when not well designed. Coupling between closely spaced microstrip lines can be reduced by metallic walls between the lines. These can be implemented by embedding the substrate in a metallic support structure with groves for each feed line.

The losses due to bends in the microstrip lines are studied experimentally. Taking a straight line with width $w = 240$ μm ($Z_0 = 100\ \Omega$) as a reference, the transmission coefficient of an equally long line with a 90° bend is measured. On 254 and 381 μm thick substrates, four different bends are investigated:

- a 90° abrupt bend with the corner chamfered such that the slanted edge is $\sqrt{2}w$.
- curved 90° bends with radius $R = 1$, 2, and 3 mm.

On a 254 μm thick substrate, the lowest loss (0.045 dB) at 24 GHz is achieved with the curved 90° bend with $R = 3$ mm (Fig. 2.22). The curved bend with $R = 2$ mm and the abrupt bend contribute about 0.055 dB of loss and the curved bend with $R = 1$ mm has the highest loss with 0.095 dB. Bends on thicker substrate exhibit higher loss because the field lines are less confined under the microstrip line. As a comparison, the transmission of the abrupt bend on 381 μm thick substrate is presented with $S_{21} = -0.13$ dB at 24 GHz.

From these results, an 8-beam antenna array on a 254 μm thick substrate is designed (Fig. 2.23). Since no SP8T switch was available, the radiation patterns are measured with individual diode detectors and a scan angle of only 180° is realized due to the space requirement of the additional circuitry. This, however, eliminates the problem of closely spaced microstrip feedlines. Eight $3\lambda_0$-long shortened FTSAs with an aperture of $a = 0.7\lambda_0$ as antenna elements are placed with an angular distance of 22.5° so as to cover a 180° field of view. The curvature of the microstrip feedlines is kept no smaller than 3 mm. The two circular holes in the substrate are necessary for further investigation presented in Section 2.6.4.

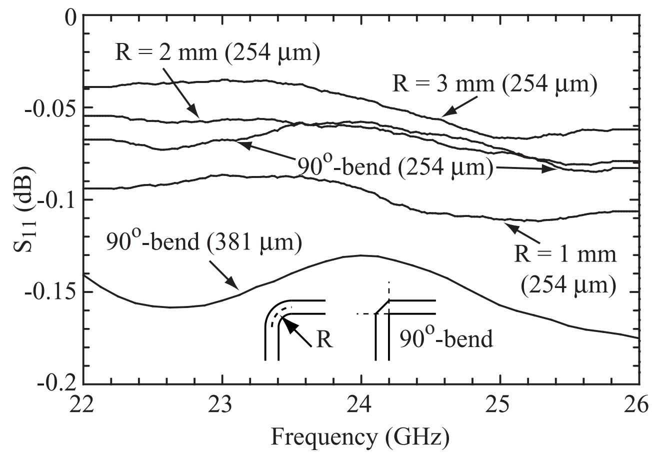


**Figure 2.22: Losses due to bends in 100 Ω microstrip lines on 254 μm thick RT-Duroid 5880 substrate and comparison with 381 μm thick substrate.**

### 2.6.3 Radiation Patterns

The measured E-plane radiation patterns are shown in Fig. 2.24(a). Only the patterns of four antenna beams from 0 to 90° are measured and the data is reflected about 0° to show the ±90° coverage. With a −3 dB beamwidth of 29°, the cross-over of adjacent beams occurs at the −2 dB level and sidelobes of −8 dB are measured at about ±40° off the center of each antenna beam. It is conjectured that the increase in the sidelobe level is due to coupling between the microstrip lines at the feed. The measured H-plane patterns (Fig. 2.24(b)) are similar for all antenna elements. The −3 and −10 dB beamwidths are 31° and 64°, respectively, and there are sidelobes of −12 dB, ±50° off the center of the beam.

To demonstrate the negative effect of coupling through microstrip feedlines, the measured E-plane radiation patterns of a similar array on a 381 μm thick substrate with badly designed feedlines is presented in Fig. 2.25. From this example, the importance of the good design of the microstrip line bends is quite obvious.

### 2.6.4 Gain Improvement with Biconical Reflector

In a slightly different effort as in [88, 89], and to increase the directivity of the antennas and to improve the H-plane radiation pattern while keeping the horizontal dimen-

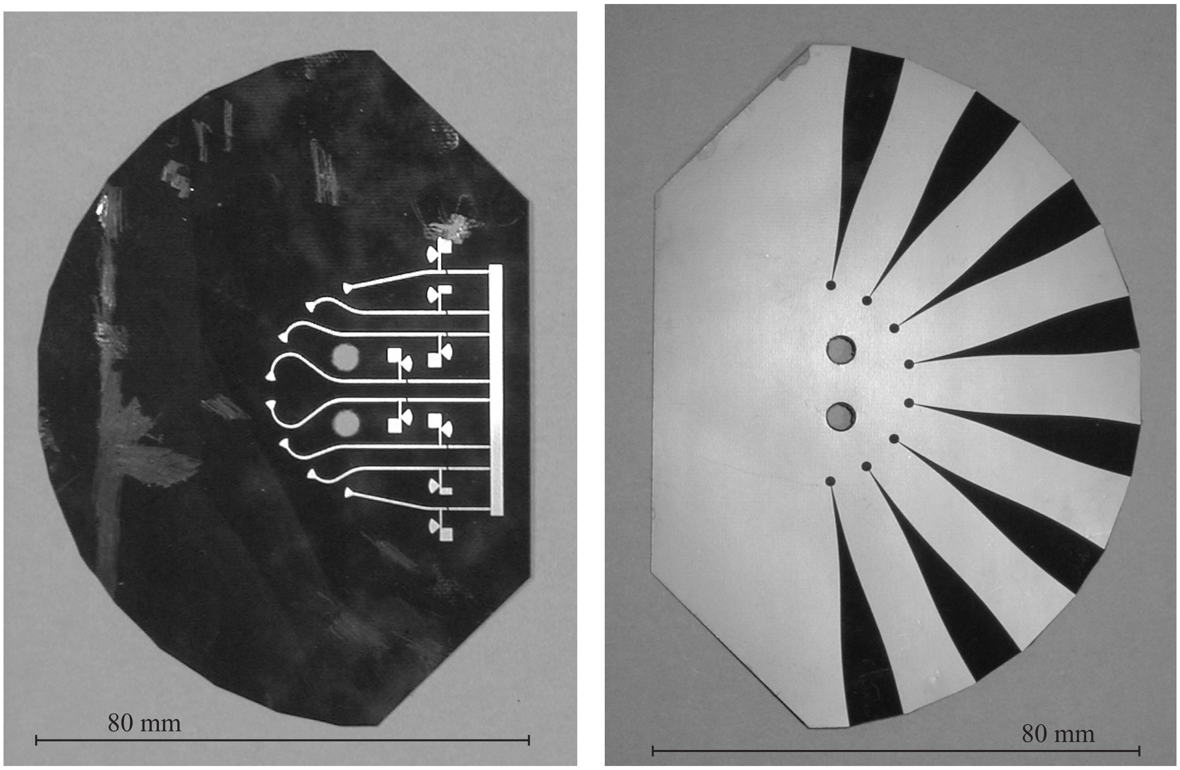


(a) (b)

**Figure 2.23: Photograph of the 24 GHz 180° 8-beam array: (a) feedlines and (b) FTSAs.**

sions the same, a biconical reflector is added to imitate a horn-like antenna in the H-plane (Fig. 2.26) [90]. The opening angle is 50° and the lateral dimensions coincide with the substrate. The measured radiation patterns in E-plane (Fig. 2.27(a)) exhibit a −3 dB beamwidth of 26° and the cross-over of adjacent beams occurs at the −2.5 dB level. The sidelobe level is only −6 dB, and compared to the array without a reflector, the depth of the nulls between main beam and sidelobes is greatly increased. In the H-plane, the −3 and −10 dB beamwidths are 35° and 68°, respectively, and the sidelobe level is below −20 dB. The measured gain is increased by 10%.

It is concluded, that with a biconical reflector on both sides of the antenna array there is no significant improvement in gain achievable while keeping the horizontal dimensions

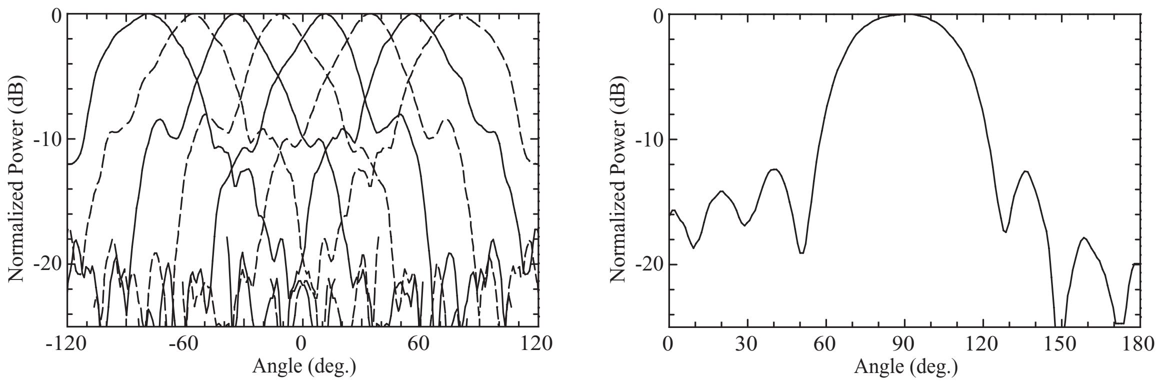


(a) (b)

**Figure 2.24: Measured radiation patterns at 24 GHz of the 180° 8-beam array: (a) E-plane and (b) H-plane.**

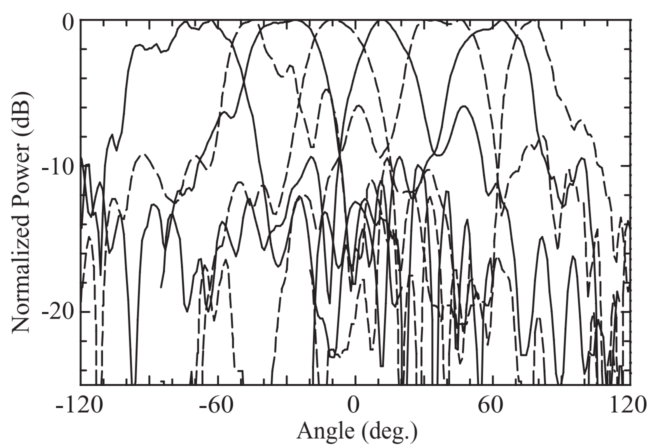


**Figure 2.25: Measured E-plane radiation patterns at 24 GHz of a 180° 8-beam array: the degradation of the pattern is due to coupling through badly designed bends in the microstrip feedlines.**

the same. The improvement in radiation pattern in the H-plane is counteracted by the degradation in the E-plane. The final word is not yet written on TSAs with biconical reflectors and clearly more research is needed for optimal performance.

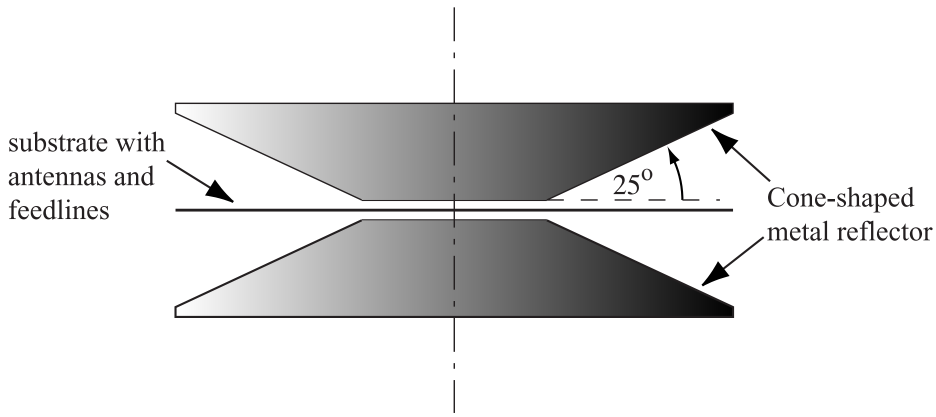


**Figure 2.26: Schematic of the wide scan-angle array with cone-shaped reflectors.**

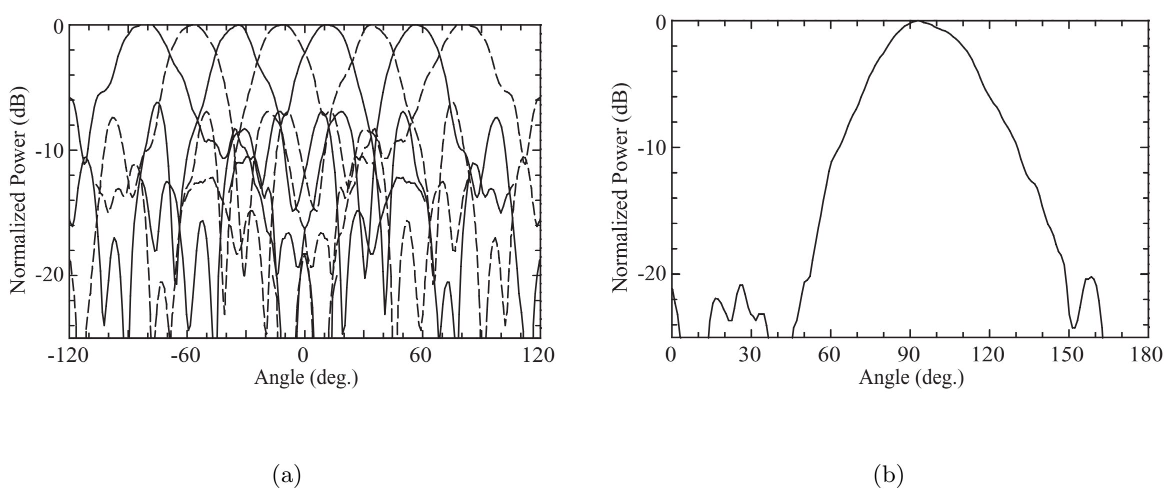


**Figure 2.27: Measured radiation patterns at 24 GHz of the 180° 8-beam array with 25° biconical reflector: (a) E-plane and (b) H-plane.**

# CHAPTER 3

# Wide Scan-Angle Spherical Lens Antennas (24 and 77 GHz)

In this chapter, a theoretical analysis of an antenna lens system using a homogeneous spherical lens is presented. This analysis is done in collaboration with X. Wu and G.V. Eleftheriades at the University of Toronto, Canada. Next, using the results from Chapter 2, such an antenna-lens system is realized and experimentally evaluated. This system is then expanded to different multibeam antenna-lens systems with a measured field of view of up to 180°.

## 3.1 Simulation

### 3.1.1 Simulation Theory

Referring to the conventions in Fig. 3.1, the normalized paraxial focal length of a spherical lens is given by [91]:

$$\frac{\overline{FO}}{R} = \frac{n}{2(n-1)} \tag{3.1}$$

where $n$ is the refractive index of the lens material. The refractive index is connected to the dielectric constant simply through $n = \sqrt{\varepsilon_r}$. However, (3.1) holds true only for rays going through the center of the lens and is approximately true for small angles of $\theta$. For large angles of $\theta$, the deviations are considerable. This is obvious in Fig. 3.1, where the focal length for three different dielectric constants is related to the angle of incidence. The calculation is done using ray-tracing techniques, applying Snell's laws of diffraction.

Equation (3.1) gives also a practical limit of the maximum relative dielectric constant

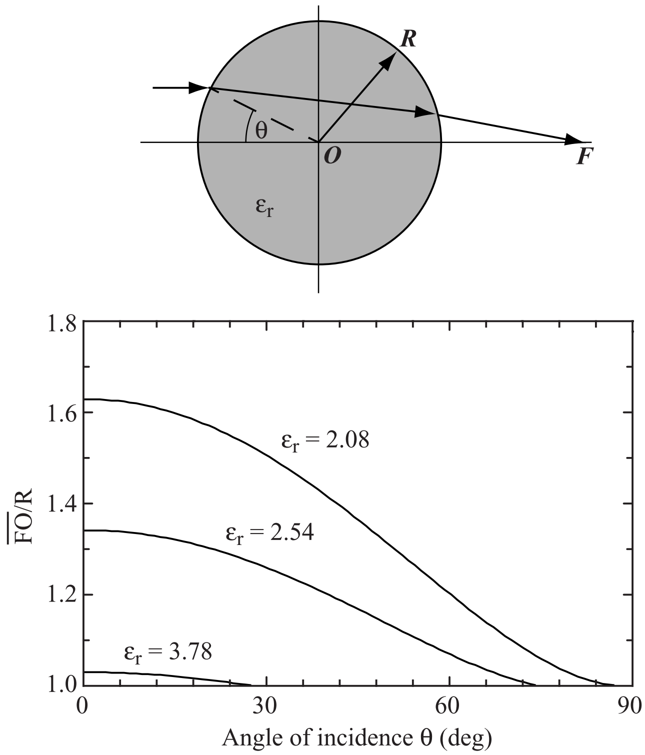


**Figure 3.1: Normalized focal length as a function of the angle of incidence for spherical lenses with different dielectric constants.**

of the lens material. For values greater than 4, the focal point lies within the lens itself and is therefore of no use for this work. The dielectric constants considered in Fig. 3.1 are therefore the three most interesting lens materials at 24 and 77 GHz with values below 4: Teflon ($\varepsilon_r = 2.08$), Rexolite ($\varepsilon_r = 2.54$), and Quartz ($\varepsilon_r = 3.78$). The maximum angle of incidence which guarantees that the normalized focal length be greater than one (in order to ensure that the focus lies outside the lens) is 87°, 74°, and 27° for relative dielectric constants of 2.08. 2.54, and 3.78, respectively. Since it is desirable to have good illumination over an extended portion of the spherical lens, a small dielectric constant material is better suited as the lens material.

Fig. 3.2 shows the ray-tracing from a point source at a distance $d$ from the edge of a Teflon spherical lens. In order to achieve diffraction-limited patterns, which means a maximum directivity, whose limit is given by the size of the aperture (the maximum area of the lens: $A = R^2\pi$), the exit angle $\theta_e$ should be as small as possible for all input angles, $\theta_s$.

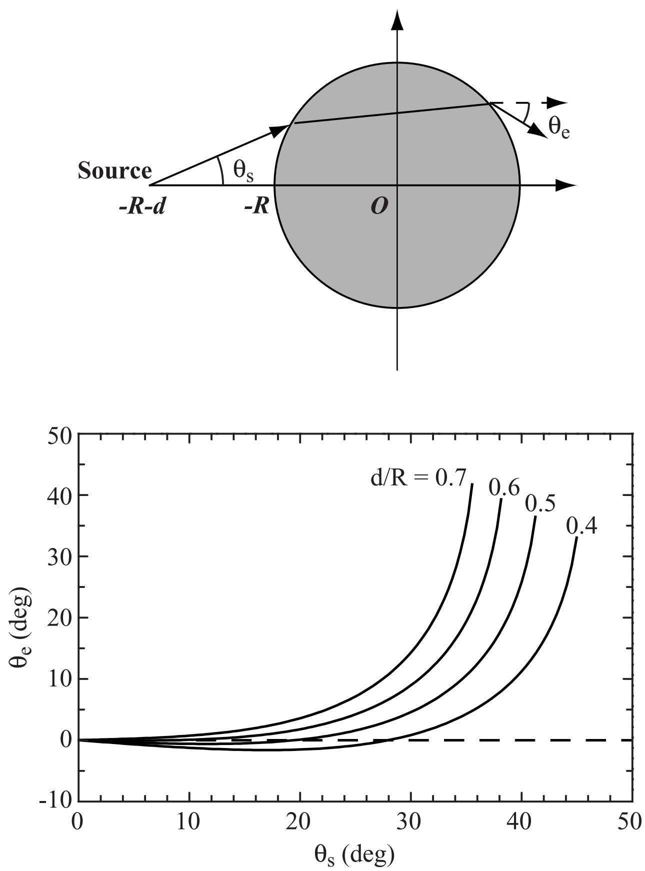


**Figure 3.2: Exit angle $\theta_e$ as a function of the input angle $\theta_s$ for a Teflon spherical lens for different $d/R$.**

This is achieved for $d/R$ between 0.4 and 0.5. Note that the optical paraxial focal position is $d/R = 0.63$ for the Teflon case. From this calculation, it is obvious that the optimal feed position for achieving maximum directivity does not coincide with the paraxial focus.

To calculate the far-field pattern, a universal class of feeds is first chosen with gain patterns defined by:

$$G(\theta) = \begin{cases} 2(m+1)\cos^m\theta & 0 \le \theta \le \pi/2 \\ 0 & \pi/2 < \theta \le \pi \end{cases} \tag{3.2}$$

Assuming that the feed source pattern is $y$-polarized (Fig. 3.3), the incident field pattern can be expressed as:

$$\mathbf{E}^s = \hat{e}_i\sqrt{G(\theta)} \tag{3.3}$$

where $\hat{e}_i$ is a unit vector perpendicular to $\hat{r}$ ($\hat{r}$ is the radial unit vector) and parallel to the plane formed by $\hat{r}$ and $\hat{y}$, and is:

$$\hat{e}_i = (\hat{r} \times \hat{y}) \times \hat{r}/\sin\psi = (\hat{y} - \cos\psi\hat{r})/\sin\psi \tag{3.4}$$

where $\psi$ is the angle between $\hat{r}$ and $\hat{y}$. The electric field components can then be written as:

$$E^s_\theta = (\hat{e}_i \cdot \hat{\theta})|E^s| = \frac{\cos\theta\sin\phi}{\sqrt{1-\sin^2\theta\sin^2\phi}}\sqrt{2(m+1)}\cos^{m/2}\theta \tag{3.5}$$

$$E^s_\phi = (\hat{e}_i \cdot \hat{\phi})|E^s| = \frac{\cos\phi}{\sqrt{1-\sin^2\theta\sin^2\phi}}\sqrt{2(m+1)}\cos^{m/2}\theta \tag{3.6}$$

For a $-10$ dB beamwidth of 80°, $m = 9$ and the directivity is 13 dB.

The geometry of the problem is shown in Fig. 3.3. In this case, each ray encounters two diffractions before escaping out of the spherical lens, i.e. the first one from the source point S to the first trace point P, and then from point P to the second trace point Q (Fig. 3.3). In order to solve the ray tracing problem, first the maximum value of the input angle $\theta_s$ is defined according to:

$$\theta_s \leq \theta_m = \sin^{-1}\left(\frac{R}{R+d}\right) \tag{3.7}$$

The other pertinent angles in Figure 3.3 can then be expressed in terms of $\theta_s$ as follows:

$$\theta_1 = \sin^{-1}\left(\frac{\sin\theta_s}{\sin\theta_m}\right) \tag{3.8}$$

$$\theta_c = \theta_1 - \theta_s \tag{3.9}$$

$$\theta_2 = \sin^{-1}\left(\frac{\sin\theta_1}{n}\right) \tag{3.10}$$

$$\theta' = 2\theta_2 - \theta_c \tag{3.11}$$

The perpendicular and parallel polarization components of the electric field at point Q outside the lens are:

$$E_\perp = E^s_\phi \frac{e^{-jk_0r_1}}{r_1} T_\perp(P) e^{-jk_0nr_2} \cdot DF \cdot T_\perp(Q) \tag{3.12}$$

$$E_\parallel = E^s_\theta \frac{e^{-jk_0r_1}}{r_1} T_\parallel(P) e^{-jk_0nr_2} \cdot DF \cdot T_\parallel(Q) \tag{3.13}$$

where $E^s_\phi$, $E^s_\theta$ are the source field patterns, as found from (3.5) - (3.6). Furthermore, $T_\perp$, $T_\parallel$ are the perpendicular and parallel Fresnel transmission coefficients at points P, Q,

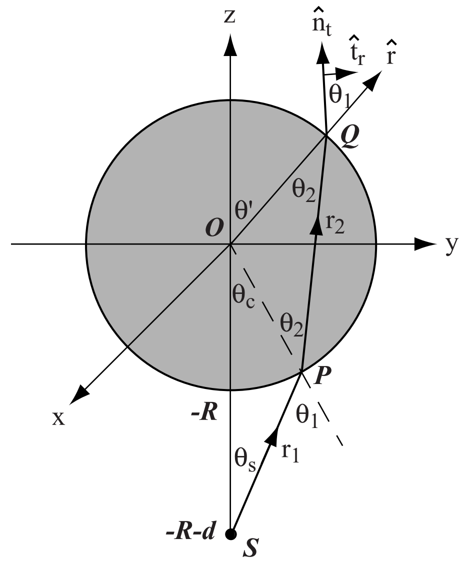


**Figure 3.3: Geometry used for radiation pattern calculation of the antenna-lens system.**

respectively. Also, $r_1$, $r_2$ are the distances from point S to point P, and from point P to point Q, respectively:

$$r_1 = \overline{SP} = R\frac{\sin\theta_c}{\sin\theta_s} \tag{3.14}$$

$$r_2 = \overline{PQ} = 2R\cos\theta_2 \tag{3.15}$$

In addition, $DF$ is the divergence factor which can be calculated for the spherical surface as [92]:

$$DF = \frac{1}{\sqrt{1+\frac{r_2}{R_1}}}\frac{1}{\sqrt{1+\frac{r_2}{R_2}}} \tag{3.16}$$

$$R_1 = n\cos^2(\theta_2)\left(\frac{\cos^2\theta_1}{r_1} - \frac{n\cos\theta_2 - \cos\theta_1}{R}\right)^{-1} \tag{3.17}$$

$$R_2 = \left(\frac{1}{nr_1} - \frac{n\cos\theta_2 - \cos\theta_1}{nR}\right)^{-1} \tag{3.18}$$

The electric and magnetic fields outside the spherical lens can then be represented by:

$$\mathbf{E} = E_{\parallel}\hat{t}_r + E_{\perp}\hat{\phi} \tag{3.19}$$

$$\mathbf{H} = \hat{n}_t \times \mathbf{E}\sqrt{\frac{\varepsilon_\mathbf{0}}{\mu_\mathbf{0}}} \tag{3.20}$$

where $\hat{t}_r$ is the polarization of the parallel transmitted field, $\hat{\phi}$ is the polarization of the perpendicular transmitted field and $\hat{n}_t$ is the direction of propagation of the transmitted field. As before, once the electric and magnetic fields have been found just outside the sphere, the corresponding equivalent electric and magnetic current densities can be calculated as:

$$\mathbf{J} = \hat{r} \times \mathbf{H} = (-E_{\|}\hat{\theta} - \cos\theta_1 E_{\perp}\hat{\phi})\sqrt{\frac{\varepsilon_0}{\mu_0}} \tag{3.21}$$

$$\mathbf{M} = -\hat{r} \times \mathbf{E} = E_{\perp}\hat{\theta} - \cos\theta_1 E_{\|}\hat{\phi} \tag{3.22}$$

In the far-field, the transverse electric field can be calculated using standard diffraction integrals over the closed spherical surface just outside the lens.

### 3.1.2 Spherical-Lens Characterization

The characterization strategy adopted in this work is to determine the optimum ratio $d/R$ in terms of system radiation efficiency. The radius of the spherical lens is fixed to $R = 25$ mm aiming at a system directivity of $D_{sys} = 30$ dB at 77 GHz ($R/\lambda_0 = 6.5$). The system directivity is calculated from:

$$D_{sys} = \frac{4\pi U_{max}}{P_{rad}} \tag{3.23}$$

where $U_{max}$ is the maximum radiation intensity and $P_{rad}$ is the power radiated by the feed pattern. The corresponding system efficiency is defined as:

$$\eta_{sys} = \frac{D_{sys}}{(2\pi R/\lambda_0)^2} \tag{3.24}$$

The system efficiency can be decomposed according to $\eta_{sys} = \eta_r\eta_s\eta_t$, where $\eta_s$ is the spillover efficiency, $\eta_r$ is the reflection efficiency through the spherical lens and $\eta_t$ is the taper efficiency over the spherical lens. The taper efficiency accounts for both, the non-uniform amplitude and phase distribution on the lens. These efficiencies can be calculated by:

$$\eta_s = P_{in}/P_{rad} \tag{3.25}$$

$$\eta_r = P_{tr}/P_{in} \tag{3.26}$$

$$\eta_t = \frac{4\pi U_{max}/P_{tr}}{(2\pi R/\lambda_0)^2} \tag{3.27}$$

where $P_{in}$ and $P_{tr}$ are the incident power on the spherical lens surface and the transmitted power through the spherical lens surface, respectively.

Teflon Lenses: Figure 3.4 presents the simulated system efficiency and its breakdown as a function of $d/R$ for Teflon spherical lenses ($\varepsilon_r = 2.08$). Three different feed patterns with m = 5, 9 and 16 are used corresponding to $-10$ dB beamwidths of 100°, 80° and 60°, respectively. The optimum $d/R$ which yields the best system efficiency is 0.3-0.4, and the corresponding system efficiencies for feed beamwidths of 100°, 80°, 60° are 51%, 54% and 52%, respectively. The maximum system efficiency is achieved with a feed beamwidth of 80° and represents the best compromise between the taper and spillover efficiencies. The reflection efficiency is better than 90% due to the low dielectric constant of the Teflon, indicating that an anti-reflection coating is not necessary for most applications. Note that the 100°-beamwidth antenna results in optimal efficiency at $d/R = 0.3$ due to the rapid decline in its spillover efficiency.

Figure 3.5 shows the $-3$ dB beamwidth and first sidelobe level of the far-field radiation pattern from the Teflon spherical lens. As expected, a wider feed pattern results in a more uniform illumination, leading to a narrower beamwidth and a higher sidelobe level. The focal point of the lens may be defined as the feed point which yields diffraction-limited patterns, that is, a flat phase within the main lobe and a phase reversal in the sidelobes. This is observed at $d/R = 0.5$ for all three cases, and therefore the spherical lens has a shorter focal length for antenna applications than what paraxial optics would predict ($d/R = 0.63$). Another way to determine the diffraction-limited position is to find the position which yields the lowest sidelobe level (Fig. 3.5(b)). However, a lens with the feed placed at the diffraction-limited position does not necessarily imply an optimum efficiency due to the effect of the spillover loss. An excellent compromise between diffraction-limited performance and maximum efficiency is achieved at $d/R = 0.4$ for feed antennas with a $-10$ dB beamwidth of 80°.

The spherical lens does not have a constant focus as seen in Fig. 3.1. As a result, the system efficiency will depend on the radius of the spherical lens since the phase distribution on a spherical surface is different for lenses with different radii. Fig. 3.6 shows the system efficiency of the Teflon spherical lens as a function of $R/\lambda_0$, with the feed placed at $d/R =$

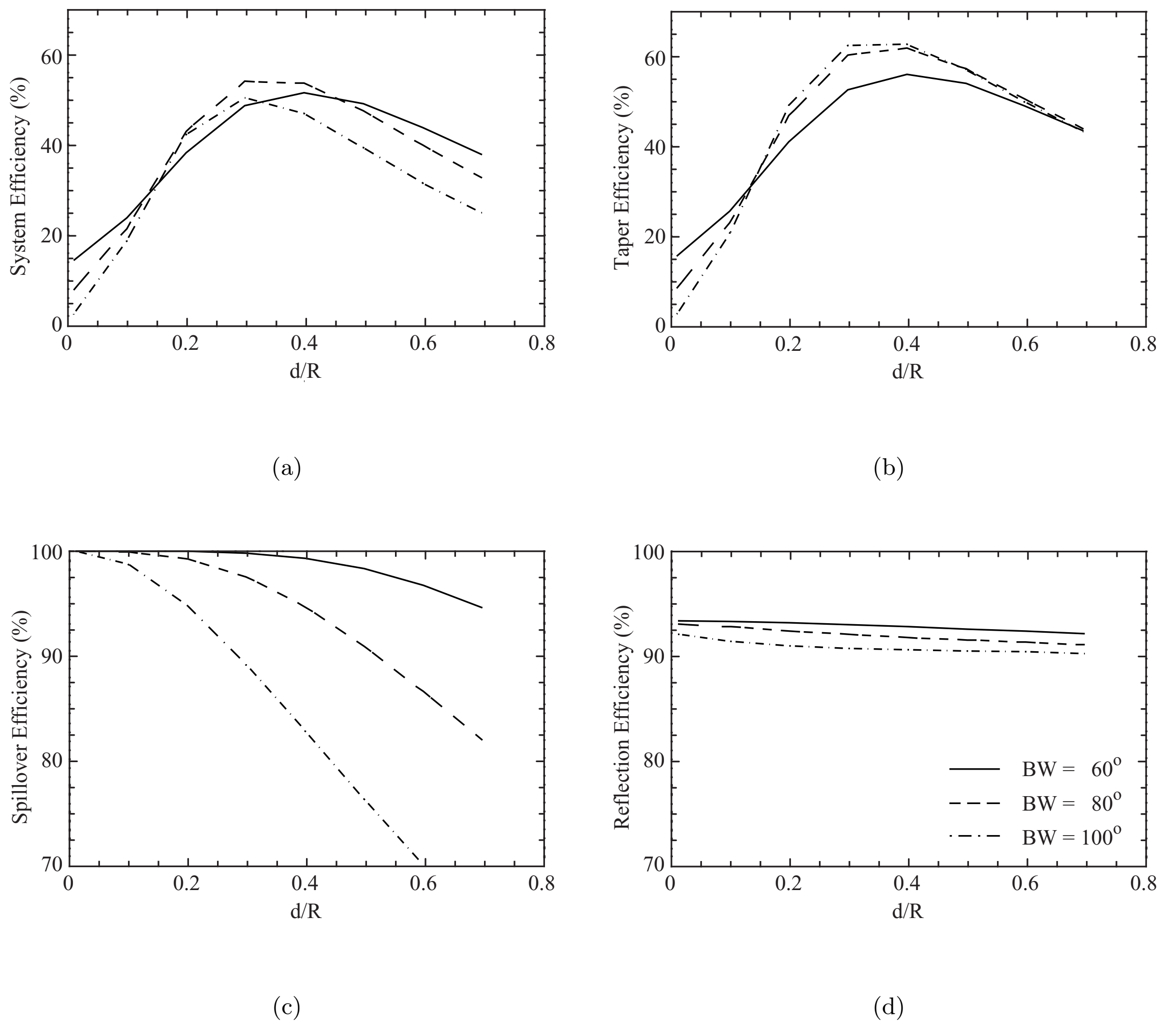


**Figure 3.4: Efficiency breakdown of a Teflon spherical lens for different beamwidths of the feed antenna: (a) overall efficiency, (b) taper efficiency, (c) spillover efficiency, and (d) reflection efficiency.**

0.4. The spillover and reflection efficiencies remain constant with the radius R. It is clear from Fig. 3.6 that Teflon spherical lenses with a diameter larger than 30-40$\lambda_0$ should be avoided [91]. The maximum corresponding gain using a Teflon lens is 36-38.5 dB for a feed beamwidth of 80°.

It is interesting to investigate the effects associated with the phase of the feed pattern. This is especially important for the tapered-slot antenna. For this purpose, an extra phase

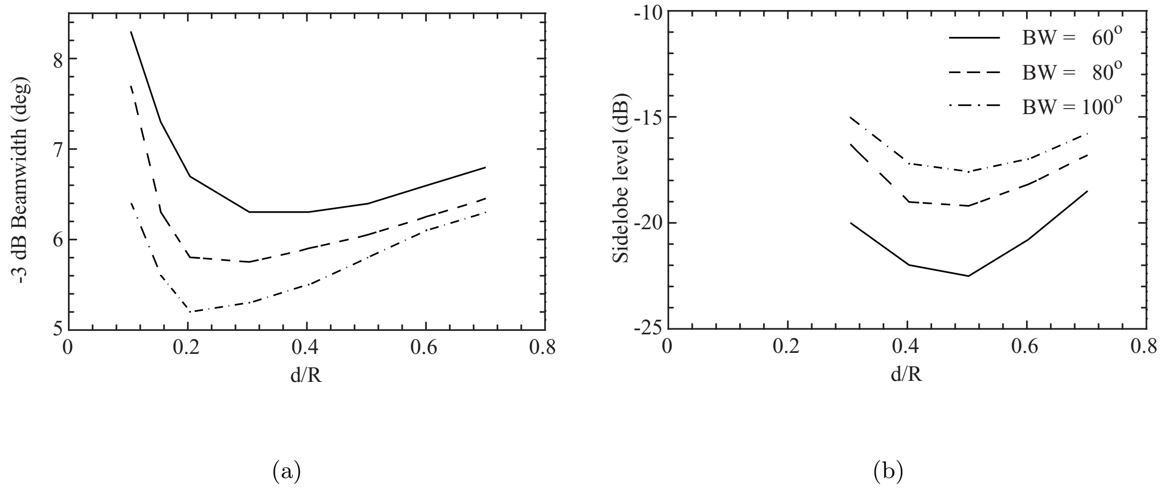


**Figure 3.5: (a) $-3$ dB beamwidth and (b) first sidelobe level as a function of $d/R$ of a Teflon spherical lens for different beamwidths of the feed antenna.**

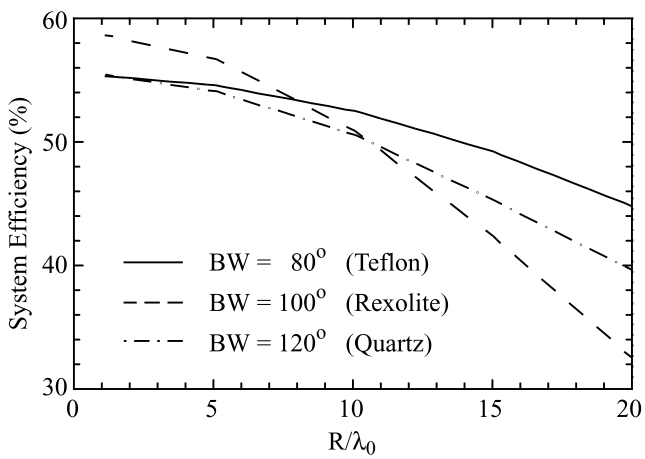


**Figure 3.6: System efficiency as a function of $R/\lambda_0$ of a spherical lens for different materials and their associated optimum feed beamwidth with $d/R = 0.4$ (Teflon), 0.15 (Rexolite), and 0.0 (Quartz).**

distribution is introduced in the feed pattern:

$$E^{s'}_{\theta,\phi} = e^{jA\sin\theta} E^{s}_{\theta,\phi} \tag{3.28}$$

where $E^{s}_{\theta,\phi}$ is defined in (3.5) and (3.6), and $A$ is a constant used to control the phase error.

Figure 3.7 shows the system efficiency, $-3$ dB beamwidth, and the first sidelobe level for an 80° beamwidth feed antenna with various phase errors, $\xi$, defined at the $-10$ dB feed pattern level. Accordingly, the constant $A$ can be written as:

$$A = \xi / \sin \theta_{-10\mathrm{dB}} \tag{3.29}$$

where $\theta_{-10\mathrm{dB}}$ is the elevation angle which corresponds to the $-10$ dB level in the feed pattern.

The spillover and reflection efficiencies are independent of the feed phase. The results clearly indicate that a positive phase distribution of the feed pattern can partly compensate for spherical aberration, leading to a better overall performance. This also results in a reduced optimum feed distance, leading to a more compact system. However, a positive phase distribution does not correspond to any practical feed antenna, since it actually implies a focused beam incident on the lens. Unfortunately, most planar antennas have a negative phase distribution, and should be limited to $\xi = -45°$ if good performance is desired.

Rexolite and Quartz Lenses:

Figures 3.8 and 3.9 show the simulated system efficiency and beamwidth as a function of $d/R$ for a Rexolite spherical lens ($\varepsilon_r = 2.54$). The feed patterns use m $= 3, 5, 9$ corresponding to $-10$ dB beamwidths of 120°, 100° and 80°. The optimum $d/R$ is 0.1-0.2 for the best system efficiency. The reflection efficiency is 0.87-0.90 for all three cases. The corresponding system efficiencies for feed beamwidths of 120°, 100°, 80° are 52%, 55% and 53%, respectively. The diffraction-limited pattern occurs at $d/R = 0.2$ for all feed antennas. Therefore, a position of $d/R = 0.16$-$0.2$ results in excellent performance for a feed beamwidth of 100°, and the Rexolite lens leads to a more compact structure than the Teflon lens. However, it is more expensive to build and has a higher dielectric loss at millemeter-wave frequencies.

Figure 3.10(a) shows the simulated system efficiency for a Quartz spherical lens ($\varepsilon_r = 3.78$), with the feed patterns of 140°, 120° and 100° (m $= 2, 3, 5$). Notice that the focal point is just outside the lens ($d/R = 0$). The optimum system efficiency is 52% for a 120° beamwidth. The reflection efficiency is 78% for the 120° feed pattern. As shown in Fig. 3.10(b), diffraction-limited pattern for all three feed patterns occurs at a position at

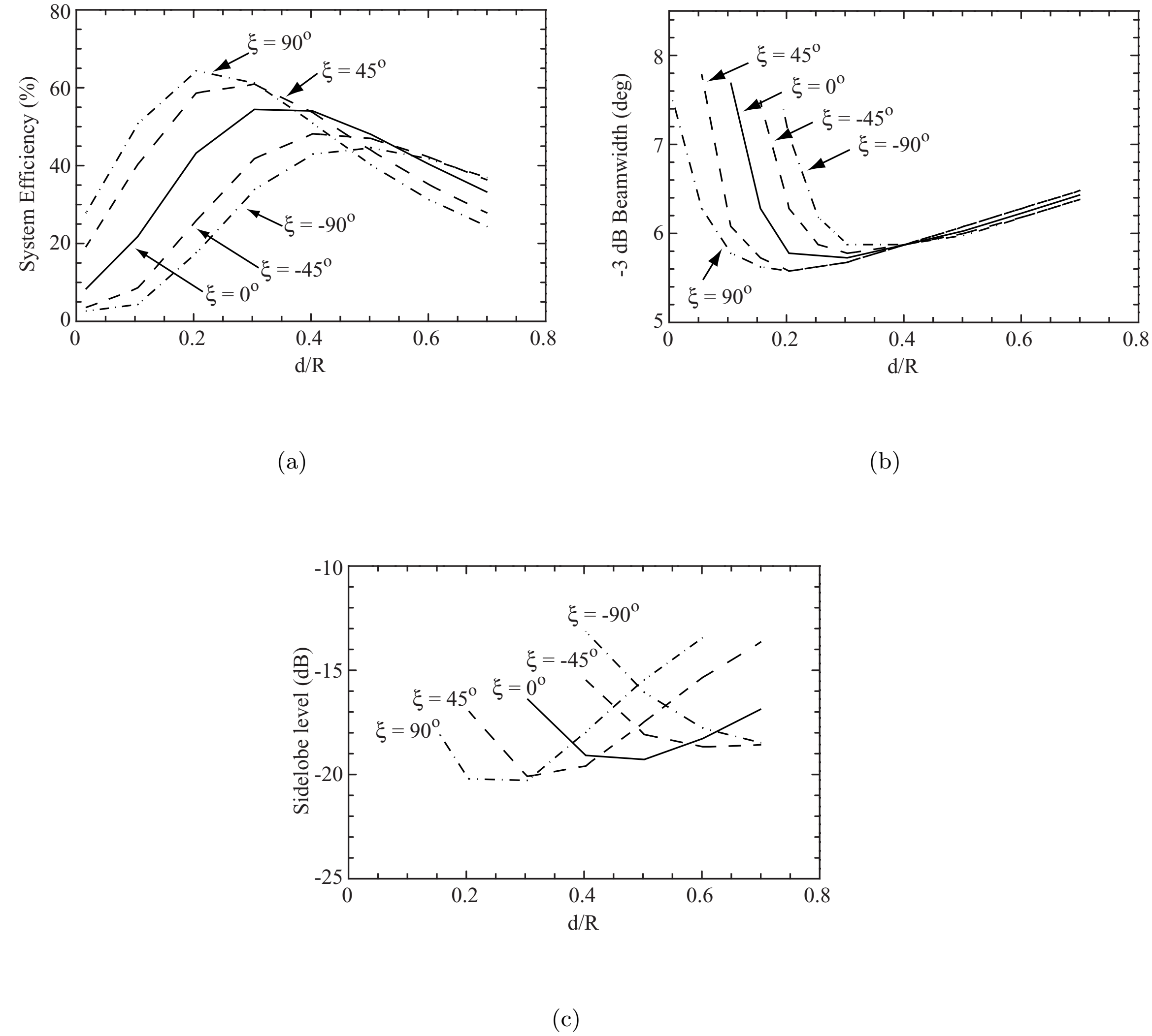


**Figure 3.7: Effects of the phase of the feed pattern on (a) efficiency, (b) −3 dB beamwidth, and (c) sidelobe-level for a Teflon spherical lens and a feed pattern beamwidth of 80°.**

$d/R = 0.0$.

The effects of a phase distribution in the feed pattern for a Rexolite or a Quartz lens are similar to the Teflon lens. The system efficiency can be improved by using a feed with positive phase distribution. However, if a feed antenna with a negative phase distribution is used, then the phase error should be kept at below $-45°$ (Rexolite) and $-90°$ (Quartz) at the $-10$ dB level. Detailed calculations are presented in [93]. Finally, Fig. 3.6 shows that

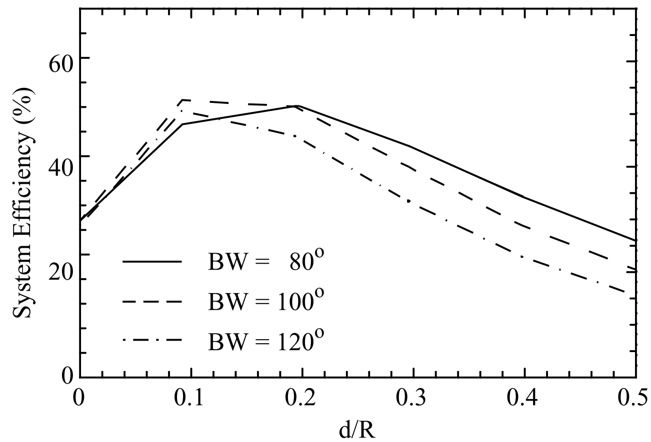


**Figure 3.8: System efficiency of a Rexolite spherical lens as a function of $d/R$ for different beamwidths of the feed pattern.**

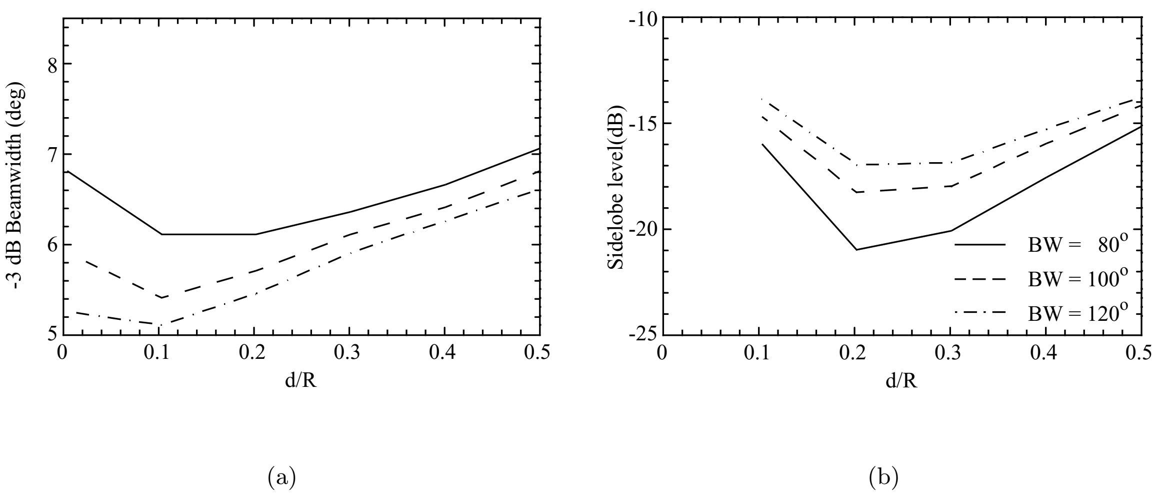


**Figure 3.9: (a) −3 dB beamwidth and (b) first sidelobe-level as a function of $d/R$ of a Rexolite spherical lens for different beamwidths of the feed antenna.**

one can use Rexolite and Quartz lenses up to a maximum of $D/\lambda_0 = 28{-}32$. The system efficiency drops quickly at larger $R/\lambda_0$ due to spherical abberations.

A comparison between Teflon, Rexolite, and Quartz spherical lenses is shown in Table 3.1. All lenses exhibit similar efficiency and beamwidths when well designed. The Quartz lens presents the limiting case ($d/R = 0$), and therefore results in the most com-

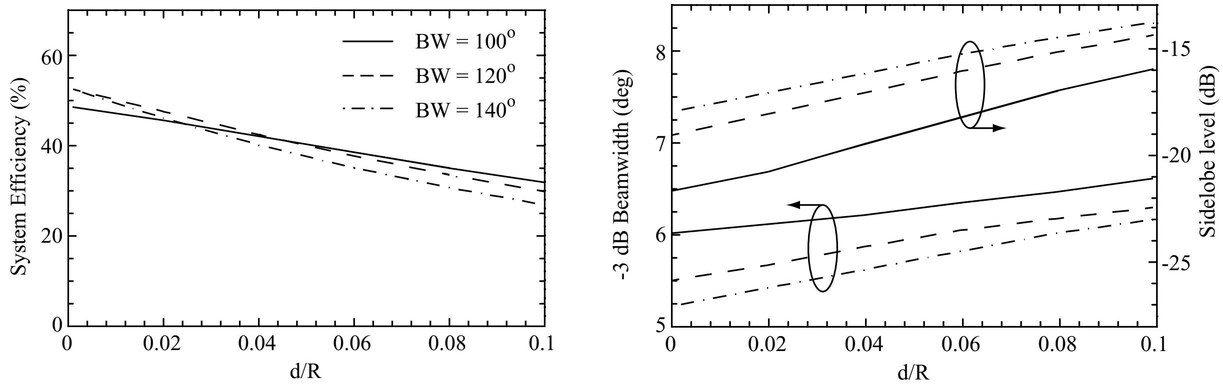


(a) (b)

**Figure 3.10: (a) System efficiency and (b) −3 dB beamwidth and sidelobe level as a function of $d/R$ for a Quartz spherical lens antenna for different beamwidths of the feed antenna.**

| | Teflon ($\varepsilon_r = 2.08$) | Rexolite ($\varepsilon_r = 2.54$) | Quartz ($\varepsilon_r = 3.78$) |
|---|---|---|---|
| Optimum $d/R$ | 0.4 - 0.5 | 0.16 - 0.2 | 0.0 |
| Optimum Feed Beamwidth | 80° | 100° | 120° |
| Efficiency (%) | 54 | 55 | 52 |
| Beamwidth | 5.7° | 5.6° | 5.5° |
| Sidelobe level (dB) | -19 | -18 | -18 |
| Maximum $R/\lambda_0$ | 20 | 14 | 16 |
| Maximum Gain (dB) | 38.5 | 35.4 | 36.6 |

**Table 3.1: Comparison of Teflon, Rexolite, and Quartz spherical lenses. All data is for optimum system efficiency.**

pact system, but is very expensive to produce. A Teflon or Rexolite lens is an excellent compromise for millimeter-wave applications.

When designing a multibeam antenna for radar applications one often wants adjacent antenna beams to overlap at the level of −3 or −6 dB. The achievable −3 dB beamwidth at 77 GHz with a lens diameter of 50 mm in the simulated cases for Teflon, Rexolite, and Quartz, is around 5.5° when placing the feed antennas at the optimum $d/R$. This translates into a distance between adjacent antennas of $0.6\lambda_0$, $0.72\lambda_0$, and $0.9\lambda_0$. This is independent of frequency and is true for other lens sizes, as long as the efficiency is around 50%, since the directivity scales approximately with the aperture size (up to a diameter of about 30 $\lambda_0$). In addition, the physical distance between the lens and the feed antennas may be less than the simulated result, since the calculations refer to the phase center of the feed antennas, which may not coincide with the physical aperture of the feed antennas. Since Rexolite and especially Quartz put a hard constraint on the location of the feed antennas, the best lens material for multibeam systems is Teflon.

## 3.2 TSA with Spherical Teflon Lens

### 3.2.1 Radiation Pattern Measurements

#### Single Feed Antenna with Spherical Teflon Lens

The antenna-lens system is characterized at 77 GHz, using a spherical Teflon lens with $R = 25$ mm ($R/\lambda_0 = 6.42$) and an FTSA with $l = 5\lambda_0$ and an aperture of $a = 0.7\lambda_0$ as feed antenna. This feed antenna is characterized in Chapter 2.5.1 and shows a $-10$ dB beamwidth of around 73°. The lens is fabricated using a standard CNC milling machine, with a surface roughness smaller than $\lambda_0/15$.

When executing the measurements described in this section, it is found that a similar feed antenna designed at 24 GHz has to be placed around 3 mm closer to the lens surface than the 77 GHz antenna in order to achieve comparable results in a similar setup. This is due to the location of the phase center which does not coincide with the aperture of the antenna. It is therefore concluded, that the phase center of the FTSA used in this work is around 1 mm away from the aperture at 77 GHz and 4 mm at 24 GHz (on a scaled model). It is also found experimentally that for apertures larger than $0.7\lambda_0$, the phase center is recessed even more. In the following, the distance $d$ between lens and feed antenna refers to the phase center of the feed antenna and *not* to its aperture location.

The radiation pattern at 77 GHz in the E-plane is first measured versus the distance $d$ between the feed antenna and the lens (Fig. 3.11). For $d = 0.04R$, which means the antenna substrate touches the lens surface, it is quite obvious from the graph that the feed antenna is not at an optimum feed location, and the radiation pattern shows severe ripples in the main lobe. When the FTSA is moved further away from the lens to $d = 0.28R$, a main lobe in the endfire direction becomes clearly visible and it is obvious that the feed antenna is now closer to the optimum feed location. However, sidelobes are still unacceptably high with a $-10$ dB level. At $d = 0.40R$, the sidelobe level drops below $-16$ dB, which is acceptable for automotive radar systems and, drops even further to $-20$ dB for $d = 0.52R$. When the feed antenna is moved even further away from the lens, the sidelobe level rises rather quickly to $-13$ dB for $d = 0.64R$ and $-11$ dB for $d = 0.76R$, and the gain starts to drop. Note, that the radiation patterns are normalized to the result with the highest measured gain (at $d = 0.40R$) and present therefore a true relative comparison of the gain. At $d = R$, the radiation pattern is quite distorted and it is obvious that the feed antenna was moved far away from the optimal feed location.

It is clear that the best feed location is around $d = 0.40 - 0.52R$ which is in agreement with the simulation. The lowest sidelobe level occurs at $d = 0.52R$ and the highest gain is measured at $d = 0.40R$.

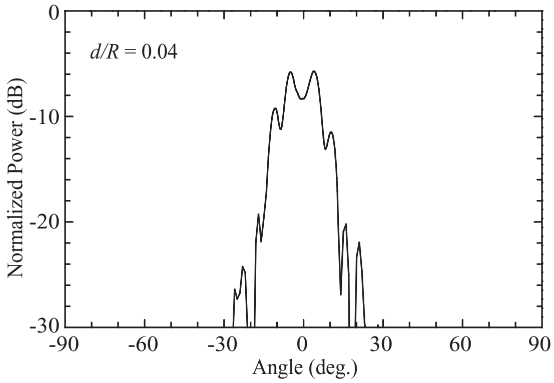

d/R = 0.04
Normalized Power (dB)
0
-10
-20
-30
-90
-60
-30
0
30
60
90
Angle (deg.)


(a)

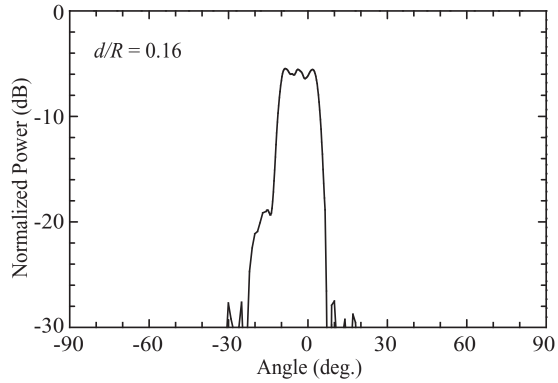

d/R = 0.16
Normalized Power (dB)
0
-10
-20
-30
-90
-60
-30
0
30
60
90
Angle (deg.)


(b)

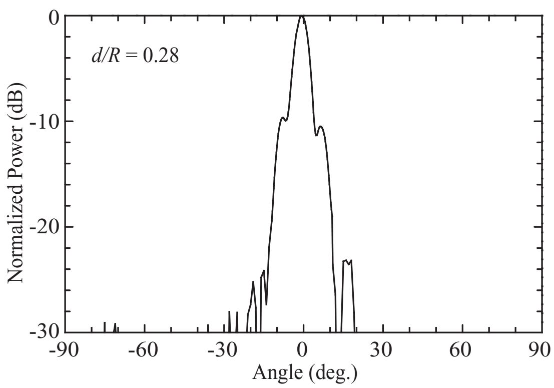

d/R = 0.28
Normalized Power (dB)
0
-10
-20
-30
-90
-60
-30
0
30
60
90
Angle (deg.)


(c)

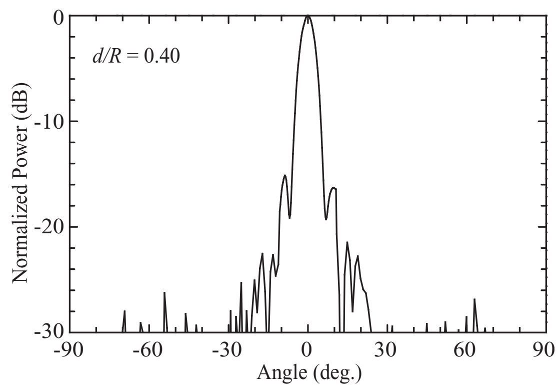

d/R = 0.40
Normalized Power (dB)
0
-10
-20
-30
-90
-60
-30
0
30
60
90
Angle (deg.)


(d)

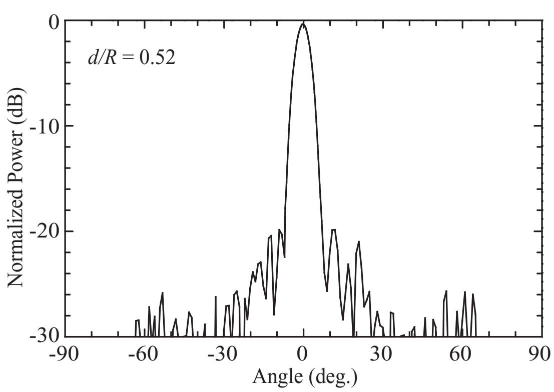

d/R = 0.52
Normalized Power (dB)
0
-10
-20
-30
-90
-60
-30
0
30
60
90
Angle (deg.)


(e)

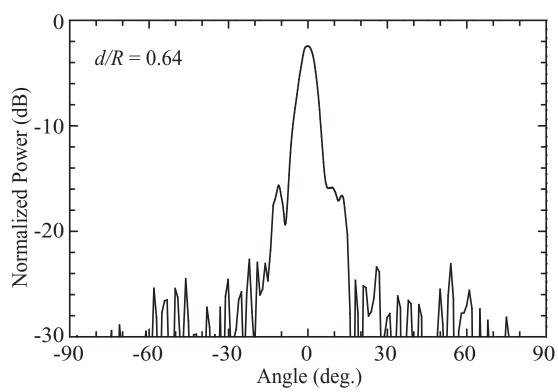

d/R = 0.64
Normalized Power (dB)
0
-10
-20
-30
-90
-60
-30
0
30
60
90
Angle (deg.)


(f)

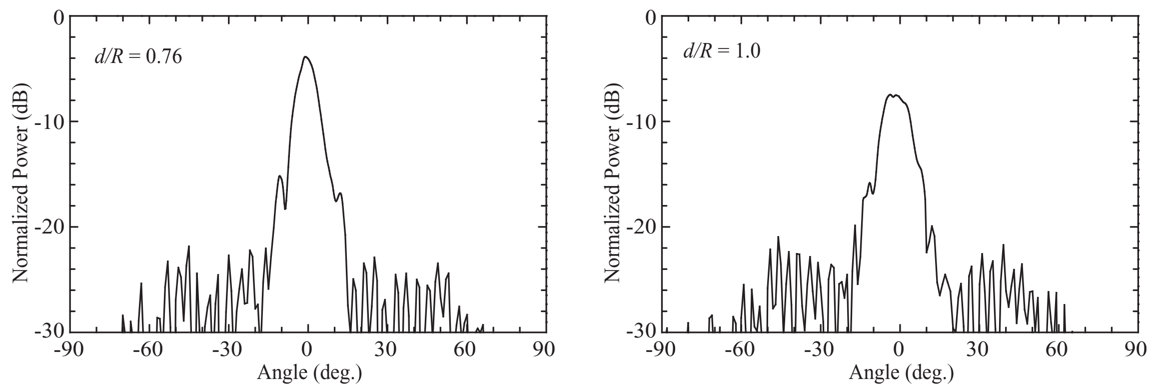


(g) (h)

**Figure 3.11: Measured radiation patterns in E-plane versus distance between feed antenna and spherical Teflon lens with $R = 25$ mm at 77 GHz.**

Next, the measured radiation pattern is directly compared with simulation. The far-field pattern of the tapered slot antenna can be modelled with (3.30) using $m = 10$, which results in a $-10$ dB beamwidth of 75°. As shown in Fig. 3.12, the measurements agree very well with the simulations. Diffraction-limited patterns (deepest nulls) occur at a relative distance $d \simeq 0.52R$, which compares well to the expected value of $d = 0.5R$ (Fig. 3.5). The main beam and the first sidelobe level are accurately predicted for $d/R$ values greater than 0.40. The inaccuracy for small $d/R$ values can be attributed to near-field effects of the feed antennas or to the disturbed feed pattern caused by the proximity of the spherical lens. The disagreement for higher-order sidelobes is due to the approximate feed patterns used and also to the fact that only first order ray-tracing has been taken into account (reflections inside the lens were not taken into account).

The measured E- and H-plane patterns for $d = 0.52R$ are shown in Fig. 3.13. It is seen that the tapered-slot antenna/spherical Teflon lens design results in excellent E- and H-plane patterns, with $-3$ and $-10$ dB beamwidths of 5.5° and 10.6°, respectively, a sidelobe level of $-20$ and $-23$ dB in E- and H-plane, respectively, and cross-polarization levels below $-19$ dB at the diffraction limited position.

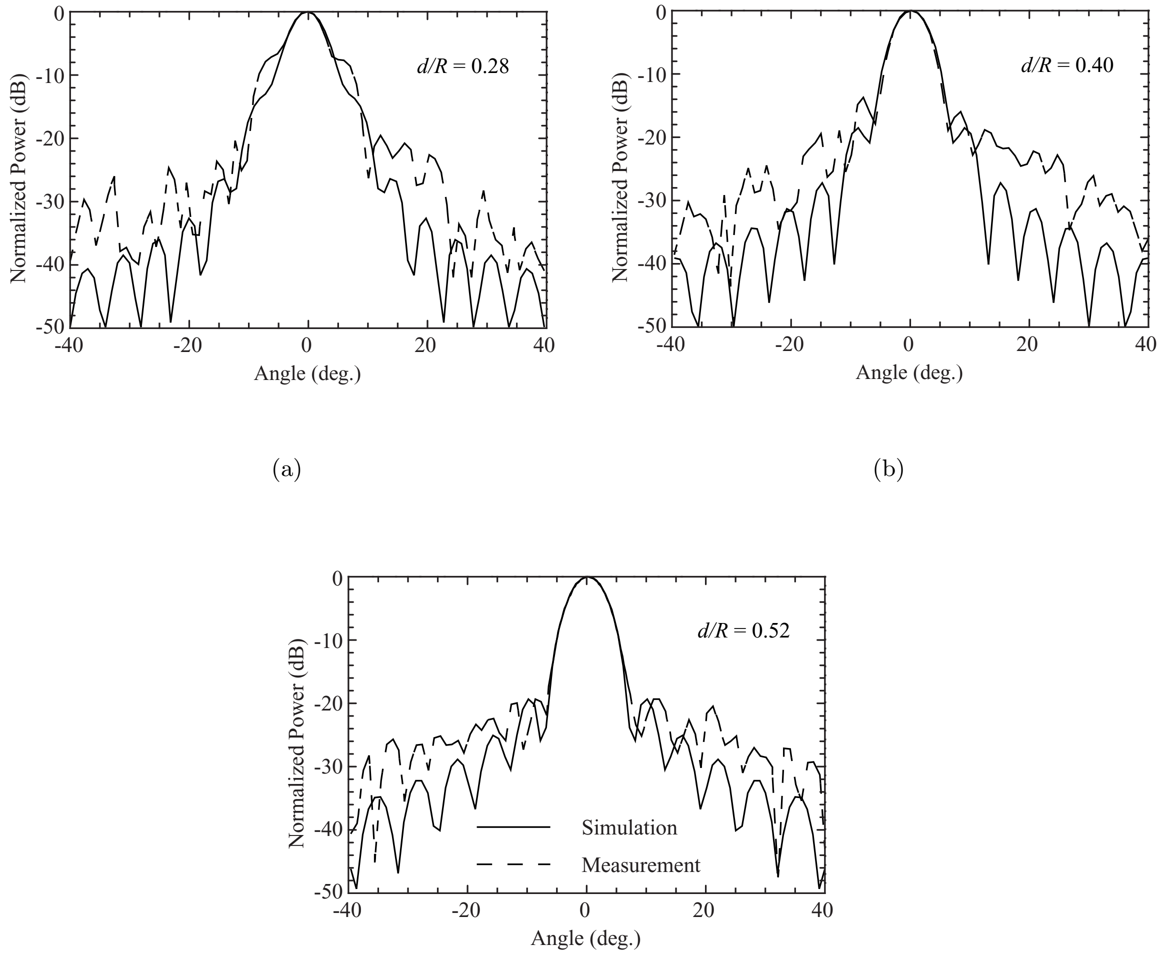


(a) (b)

(c)

**Figure 3.12: Comparison of simulated and measured E-plane radiation patterns at 77 GHz for a Teflon spherical lens with $R = 25$ mm for different $d/R$.**

### Elevation-Scan Measurements

The tapered-slot antenna can be displaced *linearly* in the vertical direction to result in a tilted beam in the elevation direction. The reason for the linear and not radial displacement is that horizontal antenna "cards" can then be used for elevation scanning. The measured patterns (Fig. 3.14) indicate that one can obtain an elevation scan of up to 12° for a displacement of 8 mm while still maintaining excellent patterns. The associated gain loss is

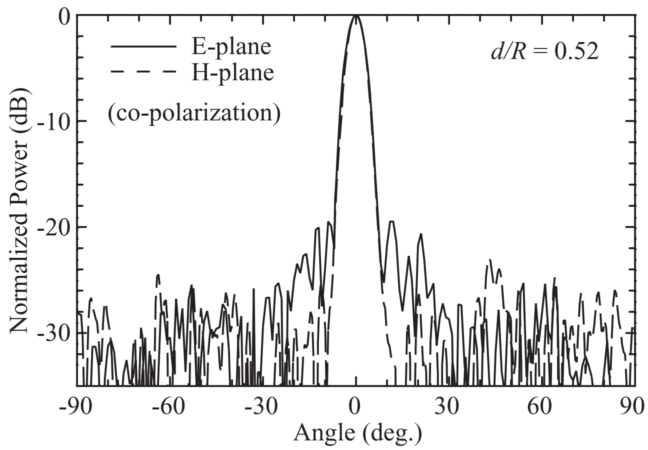


(a)

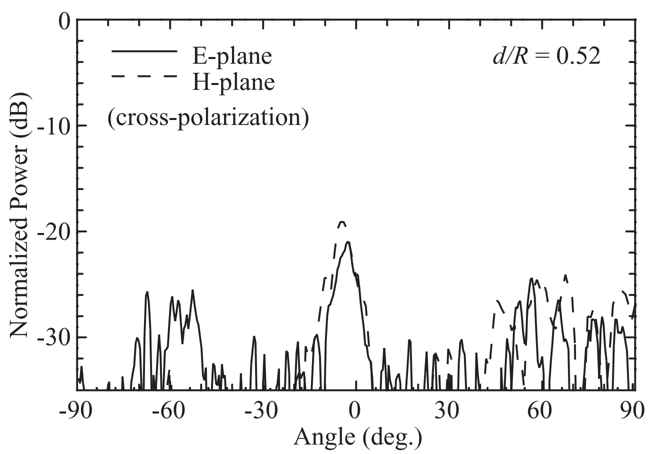


(b)

**Figure 3.13: Measured E- and H-plane patterns at 77 GHz of a Teflon spherical lens with $R = 25$ mm, fed with a tapered-slot antenna: (a) co-polarization, (b) cross-polarization.**

around 2.0 dB. Of course, if the feed antenna is displaced radially in the vertical direction, then the patterns are identical to Fig. 3.13 due to the symmetry of the lens.

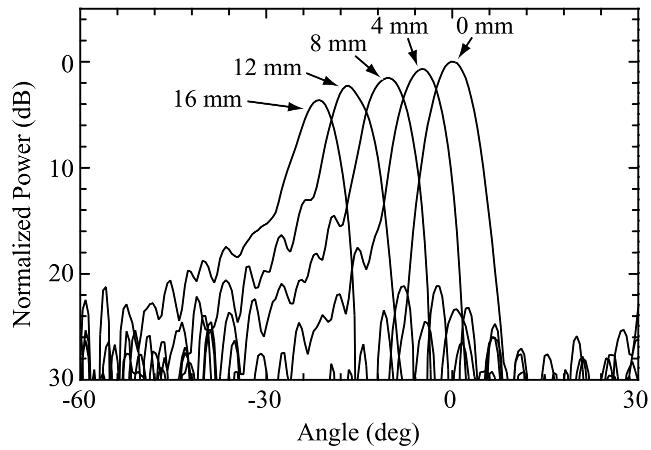


**Figure 3.14: Measured H-plane patterns of single antenna element with Teflon spherical lens as a function of vertical offset of feed antenna with respect to the lens.**

### 3.2.2 Efficiency Measurements

#### Absolute Gain Measurement

The absolute gain versus distance $d$ between feed antenna and spherical lens of the FTSA with $l = 5\lambda_0$ and $a = 0.7\lambda_0$ is measured using a similar setup as described in Section 2.5.4. The transmitted power is generated by a Gunn-oscillator and the received power is detected by a power meter. A well matched transition from microstrip line-to-coaxial cable or waveguide is not available and therefore, the FTSA as feed antenna is replaced by a small pyramidal waveguide horn antenna with a $-10$ dB beamwidth of 70°. The aperture of the horn antenna is $2.7\lambda_0 \times 1.9\lambda_0$ and its radiation pattern (co-polarization) is similar to the pattern of the FTSA (Fig. 2.16). The lens has a radius of 25 mm. The measured absolute gain is highest for $d/R = 0.36$ and is 29.4 dB (Fig. 3.15). The data starts at $d/R = 0.16$ because the distance between lens and feed antenna refers to the phase center of the feed antenna which is not located at the aperture of the horn antenna and therefore, cannot be moved closer to the lens surface. The measured gain can be translated into efficiency by comparison with the maximum gain for a given aperture:

$$G_{max} = \frac{4\pi A}{\lambda_0^2} \tag{3.30}$$

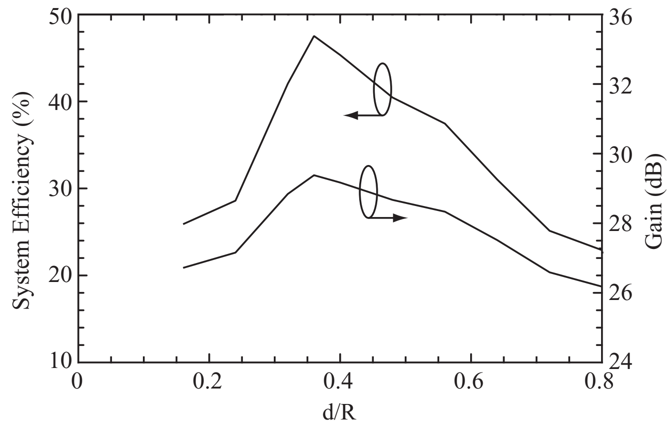


**Figure 3.15: Measured gain and system efficiency of a Teflon spherical lens fed using a small pyramidal horn.**

where $A = \pi R^2$ is the area of the lens. This results in a maximum efficiency of 49%. The measured efficiency agrees fairly well with theory (Fig. 3.15). Differences can be explained by the dielectric loss in the Teflon lens, which is not taken into account in the calculation. The absorption coefficient of Teflon at 77 GHz is around 0.012 Np/cm [94], which results in a loss of around 0.5 dB for a path length of 50 mm. Also, the location of the phase center of the horn may be the reason for additional deviations.

A similar measurement is done at 24 GHz. In this case, a well matched microstrip line-to-coaxial cable transition using Anritsu K110-3 connectors is available. The FTSA ($l = 5\lambda_0$ and $a = 0.7\lambda_0$) is built on a 381 μm thick RT/Duroid 5880 substrate and its gain can be measured directly in combination with a spherical Teflon lens ($R = 23$ mm). The measured antenna gain for a distance $d = 0.5R$ between the FTSA and the lens is 16.0 dB. When taking into account the losses due to the microstrip line-to-slotline transition (0.43 dB), the losses in the 50 mm long microstrip line (0.015 dB/mm), the simulated system efficiency of around 50% (including the dielectric losses in the Teflon lens), the reflection losses in the FTSA (about 0.6 dB), and the maximum gain of 21.2 dB (using 3.30), the simulated gain is therefore $(21.2 - 0.43 - 0.75 - 3.0 - 0.6)$ dB= 16.42 dB and agrees well with the measurement.

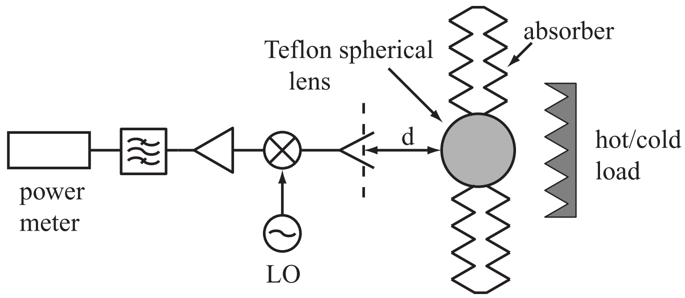


**Figure 3.16: Setup for efficiency measurement using radiometer techniques.**

### Radiometer Efficiency Measurement

The efficiency of the spherical-lens antenna is also measured using radiometer techniques. This technique has been described in [95] and [96] and is accurate to within $\pm 5\%$. With this method, the efficiency of an antenna is derived by presenting a known incident power to the antenna. This is achieved by filling the entire field of view of the antenna with a black-body absorber at a certain temperature (Fig. 3.16). The presented input power is very small and has to be down-converted in frequency and amplified for accurate detection. For calibration, the measurement has to be done at 2 different temperatures of the black-body absorber (hot/cold load) and repeated with an antenna of known efficiency, in this case, a waveguide horn antenna of near 100% efficiency. More details about this measurement are presented in Appendix C. The radiometer method estimates the spillover, dielectric absorption, and reflection loss of the spherical-lens antenna. It does not take into account the taper and phase-loss efficiency since the hot/cold absorber will always couple to the antenna using whatever mode needed for maximum power transfer. It also does not include losses in the TSA with microstrip line, because a small pyramidal waveguide horn is used here.

The measured efficiency is $82 \pm 5\%$. This is in agreement with the calculations of Fig. 3.4: for a beamwidth of 70° and $d/R = 0.4$, the spillover efficiency is 97% and the reflection efficiency is 92%. Together with the dielectric losses in the lens of about 12%, the calculated loss is about 79%.

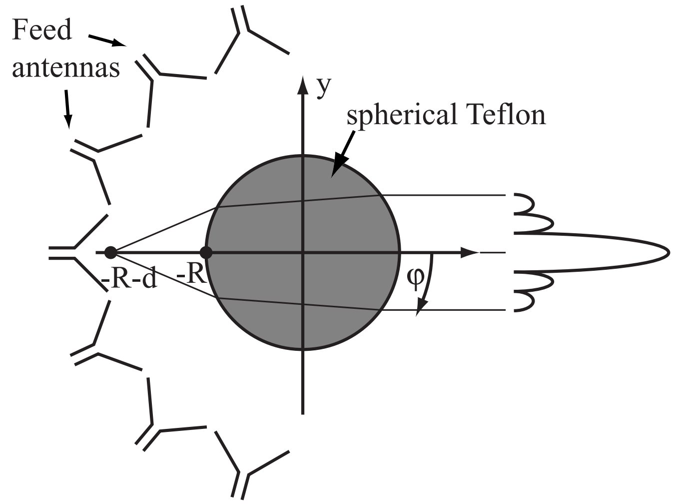


**Figure 3.17: Conceptual drawing of a multibeam antenna system with spherical lens.**

## 3.3 Multibeam Arrays

So far, the antenna-lens system was characterized with a single TSA as the feed antenna and a homogeneous Teflon sphere. The optimal location of the feed antenna with respect to the lens was found, and the radiation pattern, the efficiency, and the absolute gain was calculated and measured.

The next step is to extend this to a multibeam array by placing many feed antennas around the lens (Fig. 3.17). The TSA being a travelling-wave antenna is especially suitable for this application since it has a small aperture, and the mutual coupling between adjacent elements is much smaller than in resonant antennas such as dipoles or slot-antennas.

### 3.3.1 −3 dB Overlap Array with 180° coverage at 77 GHz

An array with 180° field of view is first presented at 77 GHz, where the adjacent beams cross over at the −3 dB point. The feed antennas follow the design in Chapter 2.5.1 with $l = 5\lambda_0$ and an aperture of $a = 0.7\lambda_0$. The FTSAs are fabricated on a 127 μm thick RT/Duroid 5880 substrate and are placed in a semicircular fashion around a spherical Teflon lens of radius $R = 25$ mm at a distance of $d = 13$ mm ($d/R = 0.52$) to the lens. A

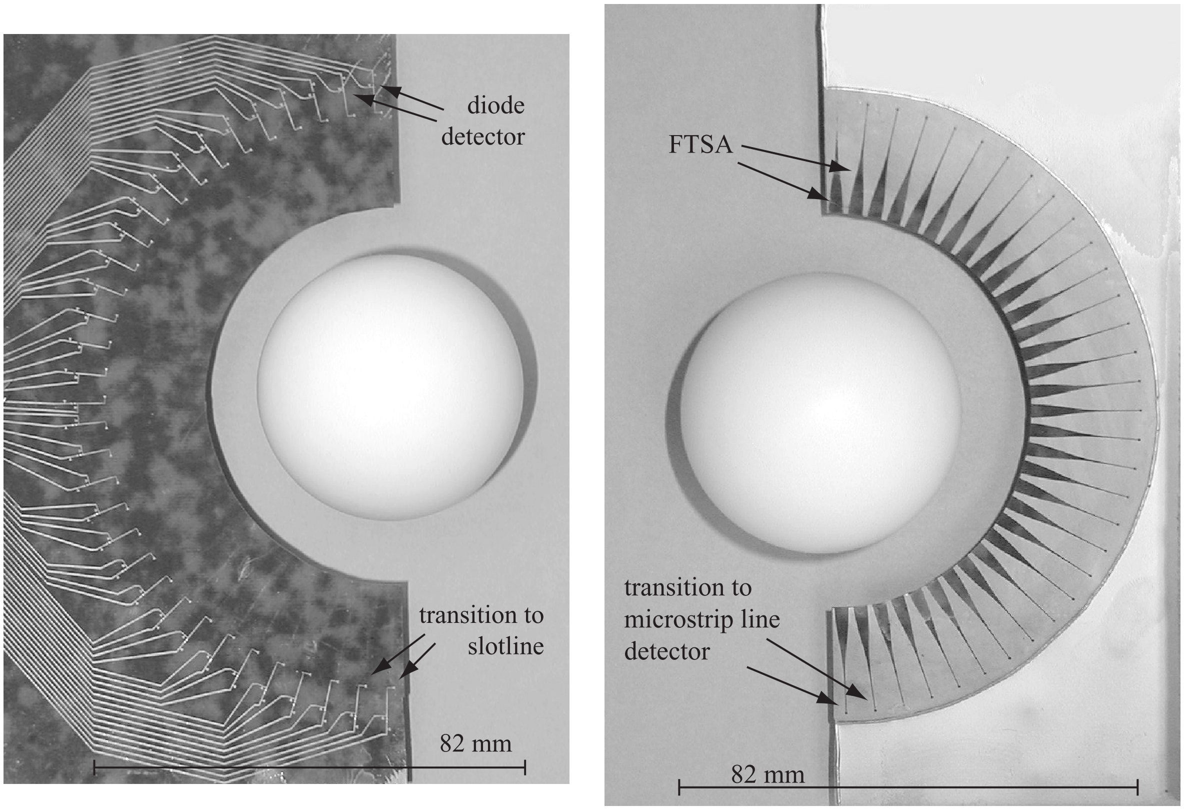


(a) (b)

**Figure 3.18: Photograph of the 33 beam array with Teflon spherical lens resulting in a −3.5 dB cross-over of adjacent beams: (a) frontside with microstrip feed lines and (b) backside with FTSAs.**

photograph of the multibeam array is shown in Fig. 3.18. Each antenna has a transition to microstrip line on the backside and a diode detector. The center-to-center spacing of the TSAs at the aperture is 3.6 mm, which results in a beam scan of 5.5° between any two antenna elements. Since each antenna-lens combination results in a 5.5° beam, the pattern cross-over should occur at the −3 dB level. A total of 33 antennas is needed to cover the 180° scan angle.

The substrate is quite large and thin, and when a large area of the copper is removed in the fabrication process, the substrate is almost like a thin sheet of paper. Therefore, in order to place the feed antennas correctly around the lens, the substrate is mounted

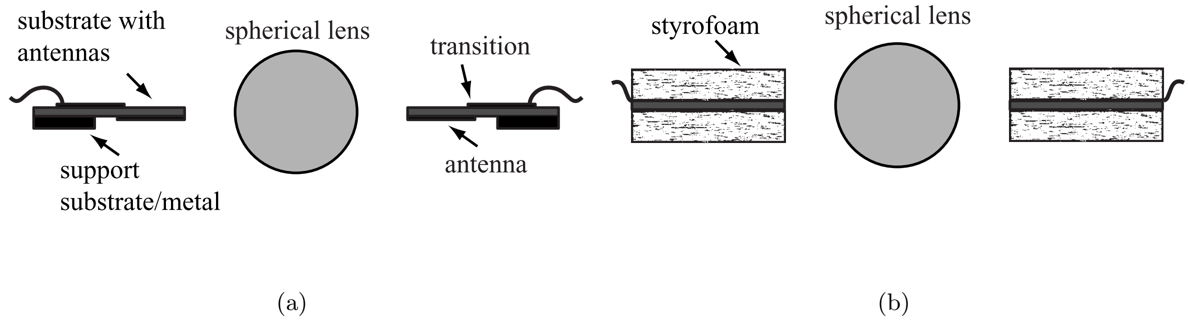


**Figure 3.19: Different ways of mounting a) the 33-beam and b) the 23-beam arrays.**

on another piece of RT/Duroid substrate with a thickness of 381 μm and copper on both sides (Fig. 3.19(a)). The support layer is attached to the side of the circuit with the TSAs, leaving enough space so as not to disturb the antennas.

The measured E-plane radiation patterns are shown in Fig. 3.20. The patterns are actually measured from 0 to 90° for a total of 17 patterns and the data is reflected about 0° to show the ±90° coverage. The peak detected powers are within ±1.5 dB from each other up to the ±75° scan angle, and are all normalized to 0 dB. This is acceptable since different Schottky-diodes are used at each antenna. However, there is a distinct drop in the measured power level for the three edge elements on either side of the array as shown in Fig. 3.20. This is due to the way the array is mounted: the supporting substrate results in a lot of scattering for scan angles greater than 75°. The cross-over of adjacent elements occurs at −3.5 dB and the sidelobe level is below −16 dB up to the ±80° scan angle, which is an increase of 4 dB compared to an antenna-lens system with only 1 feed antenna. This stems from reflections due to the mounting layer, from mutual coupling due to the close proximity of the feed antennas, and also from coupling through substrate waves which are launched at a specific bend in the microstrip feedline (see Chapter 2.6). The coupling through substrate waves is increased in the measurement setup due to the fact that the diode detector is not well matched to the incoming signal, which creates a standing wave on the microstrip line. Therefore, when implemented in a real application, the sidelobe-level is believed to be below −17 dB.

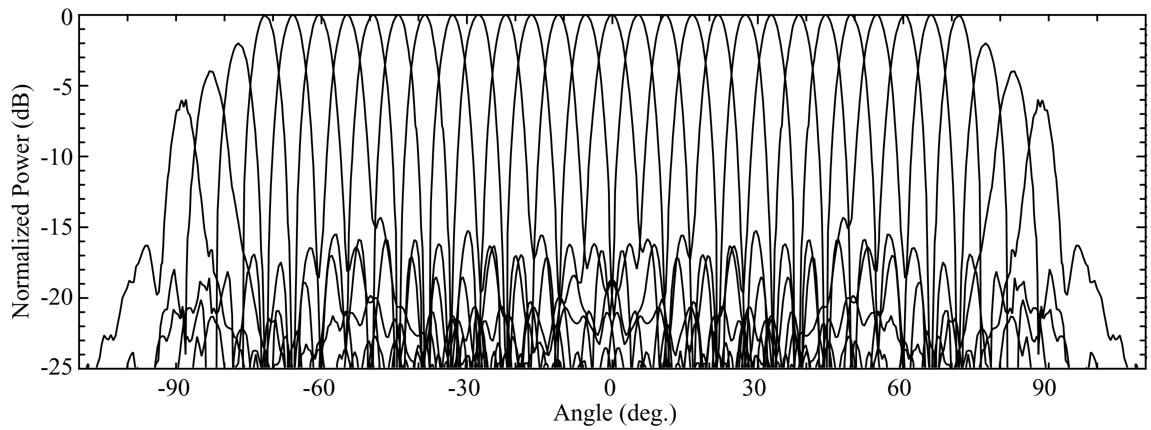


**Figure 3.20: Measured E-plane patterns of the 33-beam array with a cross-over of −3.5 dB. The drop in signal for the last 3 antennas is due to the mounting setup.**

### 3.3.2 −6 dB Overlap Array with 180° coverage at 77 GHz

Another array with a cross-over at −6 dB of adjacent beams is developed, also at 77 GHz, and with a 180° coverage angle (Fig. 3.21). Again, the FTSAs from Chapter 2.5.1 are used as the feed antennas and are placed around a spherical Teflon lens with radius $R = 25$ mm in a semicircular fashion with $d = 13$ mm ($d/R = 0.52$). The center-to-center spacing of the apertures is 5.2 mm or 8°, which results in a total of 23 antennas, all fabricated on a single piece of RT/Duroid 5880 substrate with thickness of $t = 127$ µm. In this case, the substrate is mounted between two layers of Styrofoam ($\varepsilon_r = 1.05$) (Figs. 3.19(b) and 3.22). The Styrofoam structure allows the entire substrate to be supported, and additional reflections and scattering from metal layers is completely avoided.

The E-plane radiation patterns are measured from 0 to 90° (12 beams) and ”reflected” about 0° for ±90° coverage (Fig. 3.23). The detected signal varies by ±1.5 dB randomly up to the 90°-scan antenna. That means that the antennas do not scatter even if looking straight at each other. This is because once the power is radiated from antenna #1 (Fig. 3.23) through the lens, the electromagnetic field is almost like a plane wave and only a very small portion couples to antenna #23. The cross-over occurs at the −6 dB level and the sidelobe level is −19 dB. Compared to the previously presented array with 33 an-

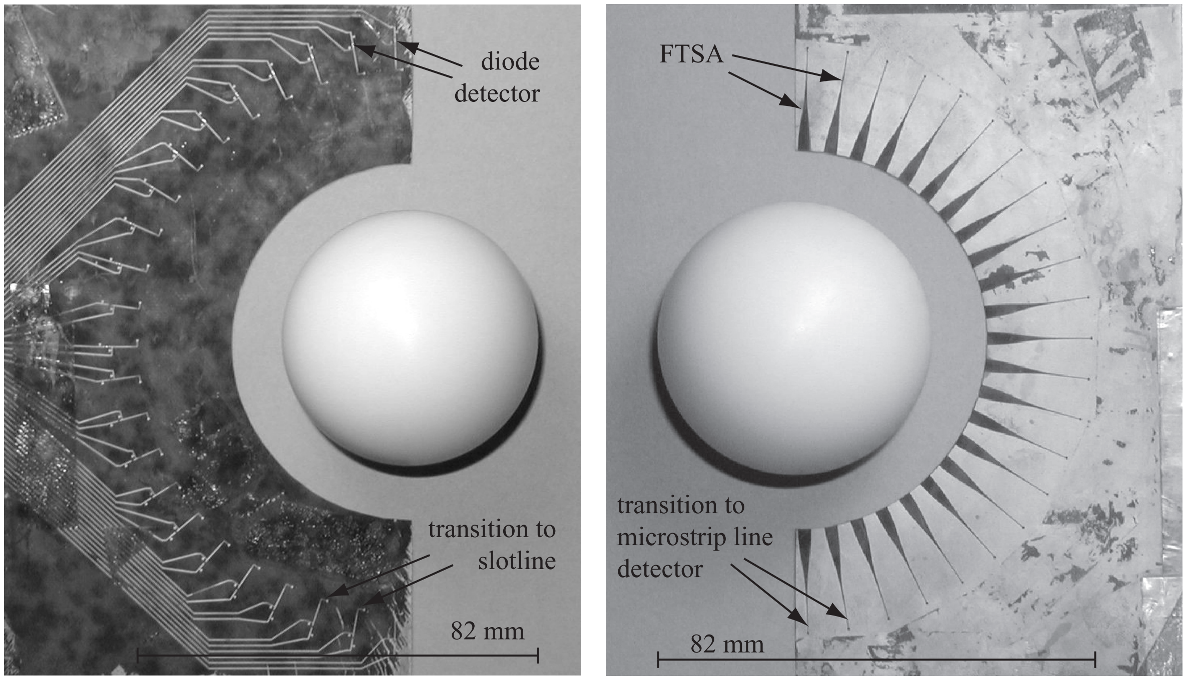


(a) (b)

**Figure 3.21: Photograph of the 23-beam array with Teflon spherical lens resulting in a −6 dB cross-over of adjacent beams: (a) frontside with microstrip feed lines and (b) backside with FTSAs.**

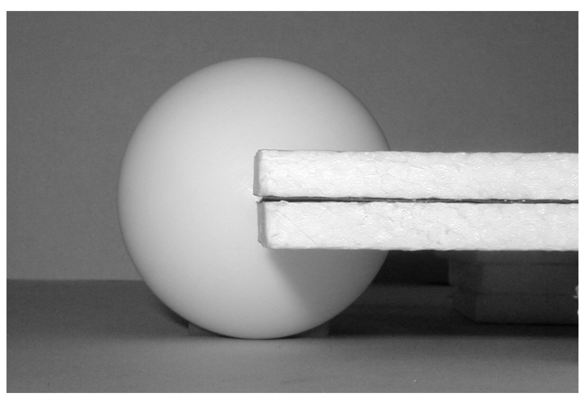

**Figure 3.22: Sideview of the 23-beam antenna array (photograph), mounted between two styrofoam layers.**

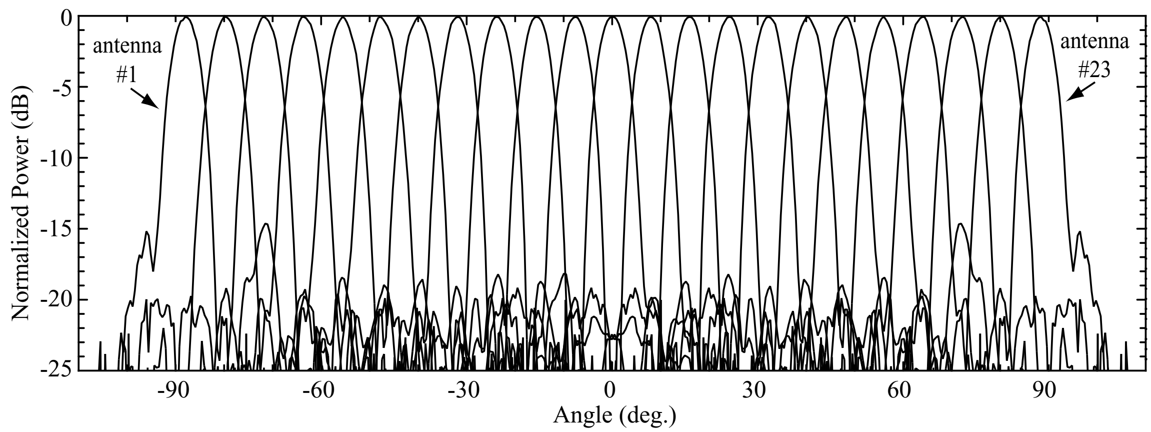


**Figure 3.23: Measured E-plane patterns of the 23 beam array with a cross-over of $-6$ dB.**

tenna beams, this means an improvement of 3 dB. It is explained by the reduced mutual coupling of adjacent antennas and reduced coupling through substrate waves due to larger separation.

The size of this circuit as well as the array with the $-3$ dB cross-over in the previous section is $82 \times 115 \times 50$ mm$^3$ (L×W×H). This includes the feed antennas and the lens only, and omits the microstrip feed lines as well as any housing that is needed for operation in a real application.

### 3.3.3 $-3$ dB Overlap Array with 144° coverage at 24 GHz

*Pattern Measurements:* An array with 8 beams which are located 18° apart and resulting in a field of view of 144° is designed at 24 GHz. The spherical Teflon lens has a radius of 23 mm. The array is realized in two different ways: with FTSAs of length $l = 5\lambda_0$ and $a = 0.7\lambda_0$ and with shortened FTSAs with $l = 2.5\lambda_0$ and $a = 0.7\lambda_0$. Both versions use RT/Duroid 5880 as substrate with a thickness of $t = 381$ µm (Fig. 3.24). The sizes of the array with the long and the short feed antennas are $118 \times 180 \times 46$ mm$^3$ and $87 \times 120 \times 46$ mm$^3$ (L×W×H), respectively. The shorter antennas result in an area reduction by a factor of 2 (and also in volume, since the height is unchanged).

The E-plane radiation patterns are measured for both arrays and are virtually the same

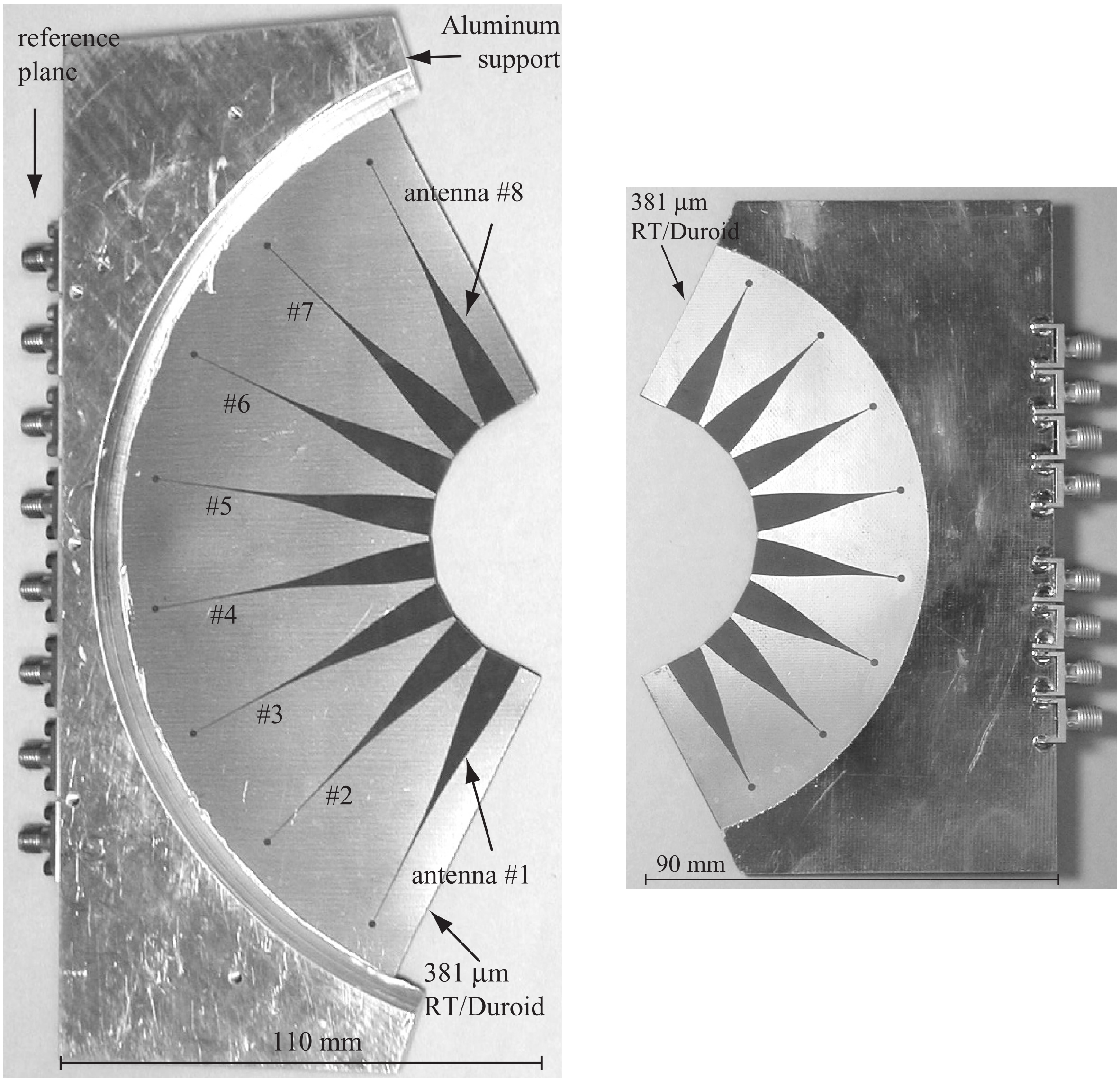


(a) (b)

**Figure 3.24: Photograph of the 8 beam array at 24 GHz with 144° field coverage: size comparison between arrays with (a) long ($5\lambda_0$ FTSA) and (b) short ($2.5\lambda_0$ shortened FTSA) TSAs.**

(Fig. 3.25). The −3 dB beamwidth is 18° and the sidelobe level is around −18 dB with the exception of one prominent sidelobe of −14 dB in each of the two middle beams. This sidelobe is caused by coupling through substrate waves which are launched by sharp bends

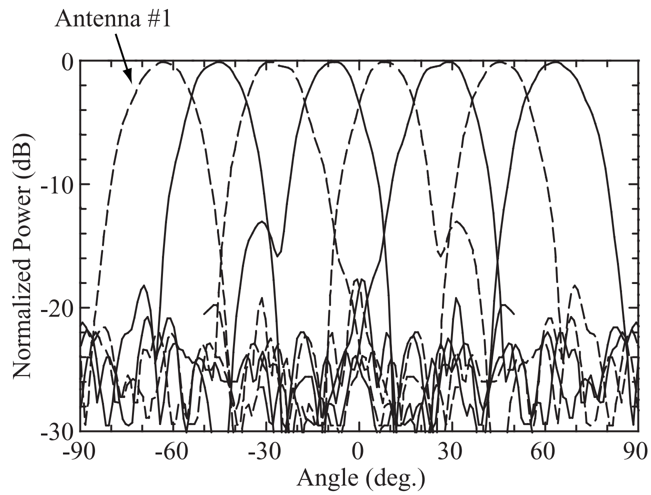


**Figure 3.25: Measured E-plane patterns at 24 GHz of the 8 beam array with a cross-over of −3 dB.**

of the microstrip feedlines which occur only in these antennas. More careful design of the microstrip feedlines will reduce this sidelobe level. Even the outer most antenna beams do not suffer from increased scattering which ensures good performance over the whole scan angle of 144°.

*S-Parameter Measurements:* It is possible to build well-matched transitions from microstrip line-to-coaxial cable at 24 GHz, and therefore full S-parameter measurements can be accurately done on the array. The array is composed of 8 FTSAs ($l = 5\lambda_0$) and connected using Anritsu K110-3 connectors. The reflection coefficient of antenna #1 (Fig.3.24(a)) is shown in Fig. 3.26. All other antennas show similar behavior. The reference plane is at the coax-to-microstrip connector, and the calibration is done with Short-Open-Load (SOL) standards using 3.5 mm coaxial calibration standards. The reflection coefficient is below $-8$ dB between 21.5 and 26.5 GHz. In order to identify the reflection points, the same measurement is done in time domain with the same bandwidth. Clearly, 3 main scatterers can be identified: the coaxial cable-to-microstrip line transition, the microstrip line-to-slotline transition, and the aperture of the FTSA.

For the measurement of the transmission coefficients ($S_{nm}$), a Short-Open-Load-Through (SOLT) calibration is done to shift the reference plane to the ends of the coaxial cables that

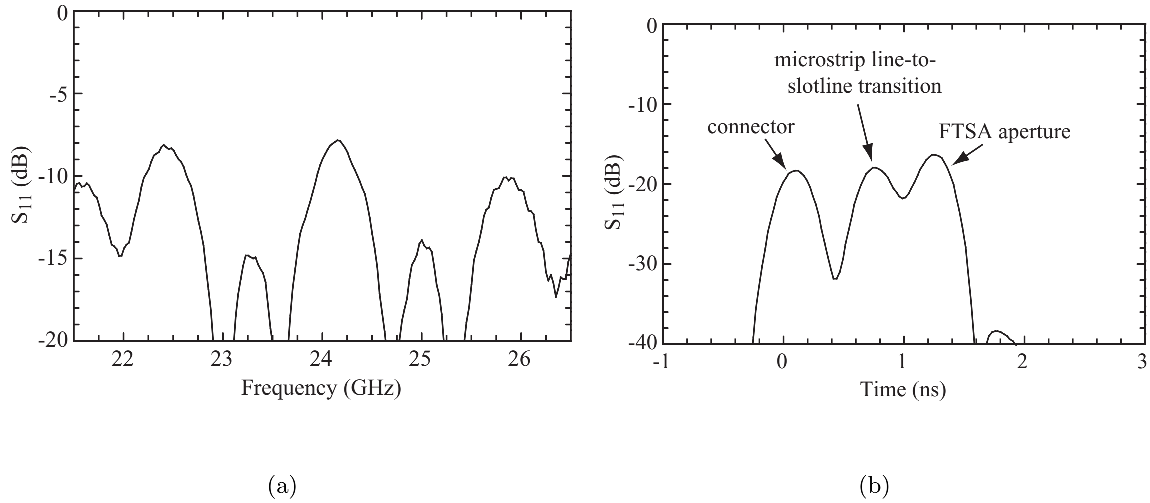


**Figure 3.26: Measured reflection coefficients of beam 1 of the 8 beam array at 24 GHz without a Teflon lens: (a) in frequency domain and (b) in time domain (21.5 to 26.5 GHz).**

are attached to the connectors. The transmission coefficients between antenna #1 and all other antennas with and without lens are shown in Fig. 3.27. The highest coupling occurs between two adjacent antennas with around −20 dB ($S_{21}$) at 24 GHz. The lens slightly increases the coupling by about 0.5 dB due to the reflection at the lens-air interface. The second highest coupling occurs between antennas that are furthest apart ($S_{81}$). This is because of the power which is transmitted had a near direct path between these antennas. These observations are seen to hold for the cases with and without a lens.

For the other antennas in the array, and for the case without a lens, the transmission coefficient is −30 dB at 24 GHz and it becomes gradually less (−33 dB, −35 dB, etc.) the closer the antennas are located until it is at an indistinguishable level around −40 dB for $S_{51}$, $S_{41}$, and $S_{31}$. For the case with a lens, the overall gain is much higher and therefore, this effect is less dominant. The coupling is generally lower and only $S_{81}$ can be identified, and the other transmission coefficients are very low. Similar observations are made for all other transmission coefficients which are not presented in Fig. 3.27. The coupling between the antennas is low enough that it can be neglected in all subsequent analysis (impedance, pattern, etc.), and as presented before, the coupling between the microstrip feedlines may

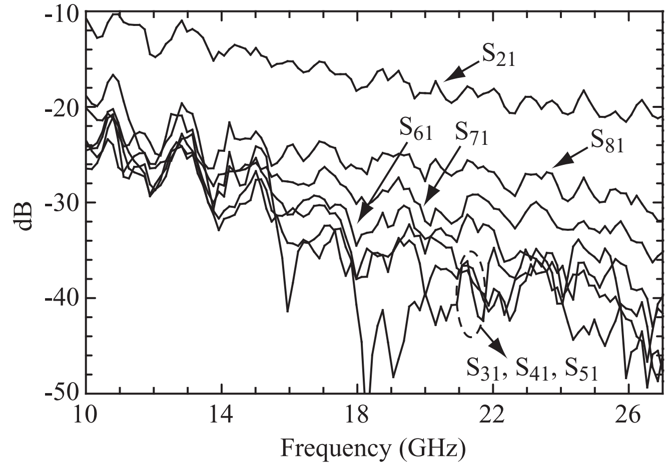


(a)

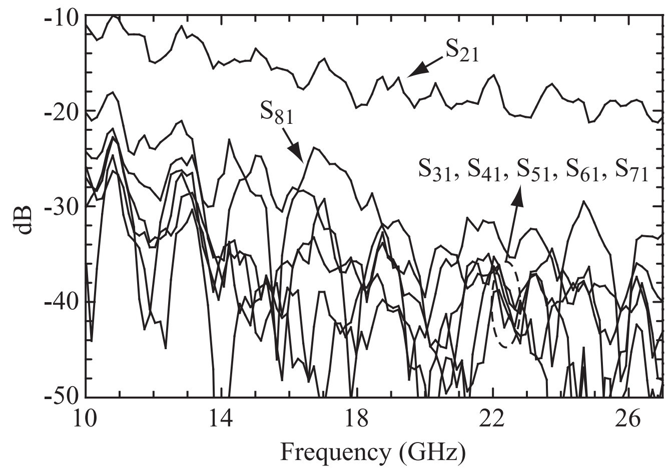


(b)

**Figure 3.27: Measured transmission coefficients of the 8 beam array at 24 GHz: (a) without and (b) with $R = 23$ mm lens.**

be the limiting factor in the array design.

# CHAPTER 4

# Dual-Band Wide-Scan Angle Spherical Lens Antennas

In Chapters 2 and 3, a wide scan-angle antenna-lens system composed of planar endfire tapered-slot antennas and a homogeneous spherical Teflon lens was developed. These antennas are excellent solutions for automotive radar systems due to the good performance, reliability, and low cost of production.

In this chapter, the antenna system is made more compact by altering the lens and implementing 24 and 77 GHz feed antennas in a single system using the same aperture.

## 4.1 Hemispherical Lens Array

### 4.1.1 Concept and Design Considerations

In certain applications, a full 180° scan-angle is not needed. Especially for systems working at 77 GHz, a field of view of $\pm 20°$ is sufficient in many cases. In order to meet this requirement, the number of beams can be reduced to 8 in the case of a $-3$ dB cross-over, each of the beams covering 5.5°. Also, the spherical lens can be replaced by a hemispherical lens with backside metallization, reducing the depth of the system by 25 mm. The concept of such an array is shown in Fig. 4.1. For a feed antenna placed at $\phi = 0$, which means with incidence normal to the backside metallization, the hemispherical lens acts like a spherical lens with the only difference that the feed antenna itself is now a (small) scatterer in the main direction of the beam. For decreasing values of $\phi$, the scattering decreases, but the hemispherical lens becomes less like a spherical lens.

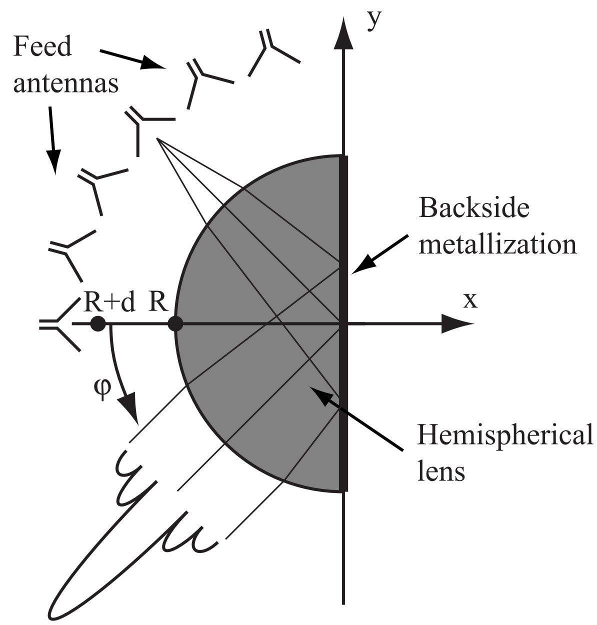


**Figure 4.1: Layout of the hemispherical lens antenna system with a backing reflector.**

### 4.1.2 Radiation Pattern

Using the same feed antennas as in Section 3.3.1 and 3.3.2, an array with a cross-over at −6 dB of adjacent beams is designed (Fig. 4.2). The frequency of operation is 77 GHz. The radius $R$ of the hemispherical lens is 25 mm. The feed antennas are placed in a semicircular fashion around the lens 8° apart from each other, starting at $\phi = 0°$ towards negative values of $\phi$. All feed antennas are fabricated on a single piece of RT/Duroid substrate 5880 ($\varepsilon_r = 2.2$) with thickness $t = 381$ μm and are mounted between 2 layers of Styrofoam.

Fig. 4.3 shows the measured and normalized E-plane radiation pattern for $\phi = -24°$, which is the optimum angle of incidence. The sidelobe level is −20 dB and the cross-polarization level is below −19 dB. The −3 dB beamwidth is 5.5° and the −10 dB beamwidth is 9.5°.

The measured and normalized E-plane patterns for $\phi = 0°$ to $-64°$ (9 beams) are shown in Figure 4.4. The beam patterns cross over at −6 dB and the optimum performance is achieved at an arc-angle between $\phi = -8°$ and $-48°$ with a sidelobe level below −18 dB.

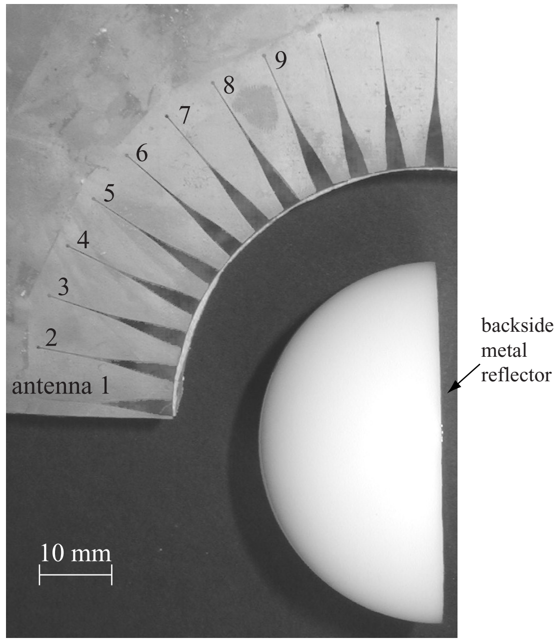


**Figure 4.2: Photograph of the antenna system at 77 GHz with hemispherical Teflon lens with backside metallization and different feed antennas, resulting in a −6 dB crossover of adjacent beams.**

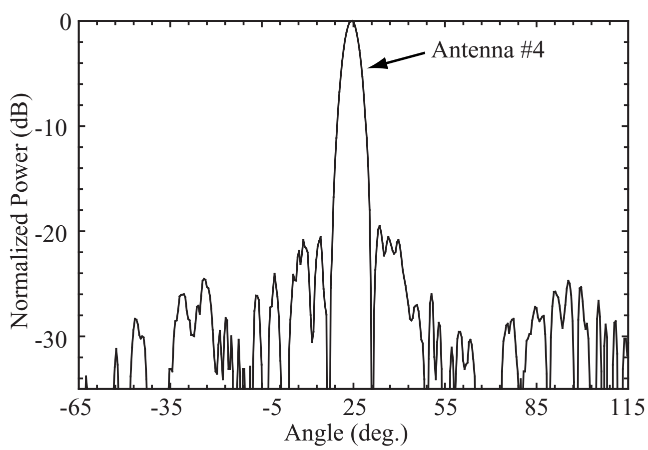


**Figure 4.3: Measured E-plane patterns at 77 GHz for an incidence angle of $\phi = -25°$.**

For angles greater than −8°, scattering from the feed results in −14 dB sidelobes. At angles smaller than −48°, the power is scattered by the edge of the ground-plane. Also, there is a substantial amount of spill-over loss. For angles of incidence smaller than −48° (antenna

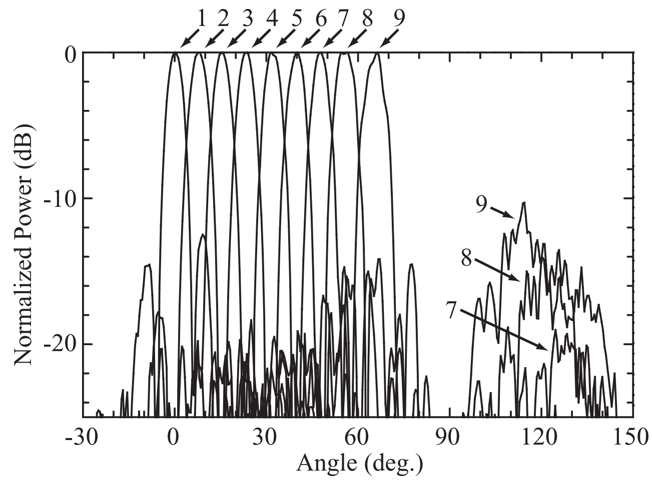


**Figure 4.4: Measured and normalized E-plane patterns at 77 GHz for incident angles of $\phi = 0°$ to $\phi = -64°$. The cross-over is $-6$ dB.**

#7 in Fig. 4.4), the power which is received on the direct path through the lens without reflection at the backside metallization becomes noticeable. It shows up as a sidelobe at an angle of $180° + \phi$ and is $-20$ dB for $\phi = -48°$ and becomes greater than $-10$ dB for angles smaller than $\phi = -64°$. This means that a hemispherical system with $R = 25$ mm at 77 GHz is suitable for a maximum of 6 beams ($\pm 20°$ coverage) with a $-6$ dB cross-over.

### 4.1.3 Absolute Gain Comparison versus Angle

The measured spill-over efficiency due to the angle tilt is shown in Figure 4.5. The gain of a single antenna is measured at different incident angles and is compared to $\phi = 0°$, which is normalized to 1. Any loss in gain is due to the increased spill-over at incident angles $\phi < 0°$. It is seen that the spill-over efficiency is greater than 90% up to antenna #6.

## 4.2 Dual Frequency Array

There are different applications for automotive radar systems operating at 24 and 77 GHz and both systems may be implemented in one vehicle. Therefore, it is useful to integrate 24 and 77 GHz in one antenna system to achieve greater compactness.

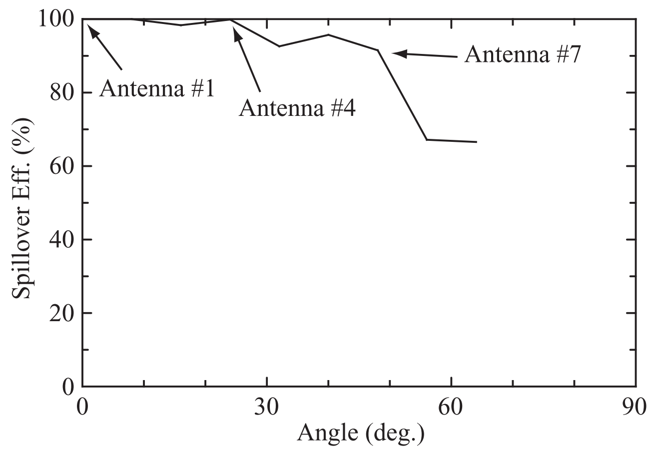


**Figure 4.5: Measured spill-over efficiency versus incident angle normalized to $\phi = 0°$ for the hemispherical-lens system.**

### 4.2.1 Concept

Fig. 4.6 shows the schematic of a dual-frequency antenna system. It is comprised of feed antennas at 24 and 77 GHz and two hemispherical lenses with a frequency-selective surface (FSS) layer in between. There are two possibilities: the FSS can be reflective at 24 GHz and transparent at 77 GHz or it can be transparent at 24 GHz and reflective at 77 GHz. In the following, the former case will be referred to as "version 1" and the latter as "version 2".

In version 1, the 77 GHz feed antennas are placed in a semicircular fashion around the lens with the center feed antenna at $\phi = 180°$. The two hemispherical lenses with FSS act like a spherical lens because the FSS is transparent at 77 GHz, and the center beam is focused in the main direction of incidence ($\phi = 0°$). At 24 GHz, the FSS is reflective and acts as a ground plane. The lens functions as a hemispherical lens with backside metallization. The FSS is tilted by $\phi = 25°$ with respect to the main plane of incidence in order to allow for a maximum scan angle for both, 24 and 77 GHz antennas. Therefore, the 24 GHz feed antennas are placed in a semicircular fashion around the lens with the center feed antenna at $\phi = 50°$. This allows the focussed beams to point in the main direction of incidence and also, it avoids scattering of the 77 GHz signal by the 24 GHz feed antennas.

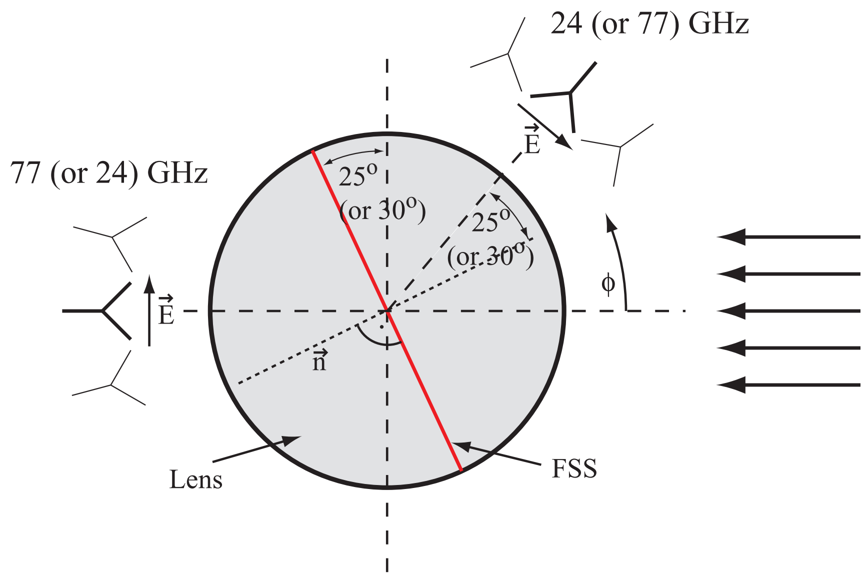


**Figure 4.6: Schematic of a dual-frequency antenna system using 2 hemispherical Teflon lenses and an FSS-layer.**

Version 2 is the dual of version 1. The 24 GHz feed antennas are placed about $\phi = 180°$ and the lens acts like a spherical lens. Since most automotive radar applications operating at 24 GHz require a wider scan-angle than at 77 GHz, the FSS is tilted by $\phi = 30°$ off the main plane of incidence to ensure a maximum scan angle at 24 GHz. It is reflective at 77 GHz and works as a hemispherical lens with backside metallization. The 77 GHz feed antennas are placed around $\phi = 60°$ so as the center beam to point in the main direction of incidence.

### 4.2.2 FSS

The filter function of an FSS with resonant elements can either be a band-stop type or a band-pass type. The fundamental resonance frequency of the FSS is either at 24 or 77 GHz depending on the FSS design and the implementation of version 1 or version 2. The better solution in all cases is a 77 GHz resonance frequency. With a resonance frequency of 77 GHz, the size of a unit cell is much smaller than at 24 GHz which eliminates the problem of grating lobes at 77 GHz. Also, if a fundamental resonance frequency of 24 GHz is used, then higher order resonance frequencies can be a problem especially when taking into account that there is a large range of angles of incidence.

The design constraints for the FSSs are not very hard. The transmission coefficient and the reflection coefficient in version 1 and version 2, respectively, has to be maximum at 77 GHz for a wide range of angles of incidence around the tilt angle of the FSS (25° for version 1 and 30° for version 2). The reflection coefficient and the transmission coefficient for version 1 and version 2, respectively, has to be high at 24 GHz for a wide range of angles of incidence around the tilt angle of the FSS. Since 24 and 77 GHz is separated by more than a factor of 3, this can be achieved by an FSS with only one layer.

The unit elements of the FSS need to be polarization independent. The resonance frequency will shift somewhat versus the angle of incidence and therefore, the bandwidth of the transmission/reflection coefficient should not be very small. A large bandwidth will also allow for small fabrication tolerances. At the same time, the bandwidth should not be very wide because the FSS needs to provide a sharp enough roll-off to achieve the desired properties at 24 GHz. The interelement spacing should be small to avoid the onset of grating lobes for large angles of incidence.

The four-legged loaded element is an element that fits this criteria well. As a band-pass type element, it is a slot in a ground plane that forms a loop with four "legs" (Fig. 4.7(a)). The circumference of the element is about $\lambda_g$ at resonance frequency which makes the element quite small: in the range of $\lambda_0/4$. Hence, the interelement spacing can be small and grating lobes are of no concern in the frequency range of interest. The four-legged loaded element repeats itself with a rotation of 90° and therefore, it is polarization independent for normal incidence. An almost unique feature of the four-legged loaded element is the possibility to control the bandwidth not only by the choice of interelement spacing but by the shape of the element. When reducing the width of the "legs" the bandwidth is decreased as well. Its dual element is a wire replacing the slot and no ground plane as shown in Fig. 4.7(b). This is a band-stop type element with otherwise similar properties to the previous one.

The simulated (Method of Moments) S-parameters for FSSs using four-legged loaded elements with the dimensions given in Figs. 4.7(a) and 4.7(b) are shown in Figs. 4.8 and 4.9. The graphs show reflection and transmission coefficients of parallel and orthogonal polarized

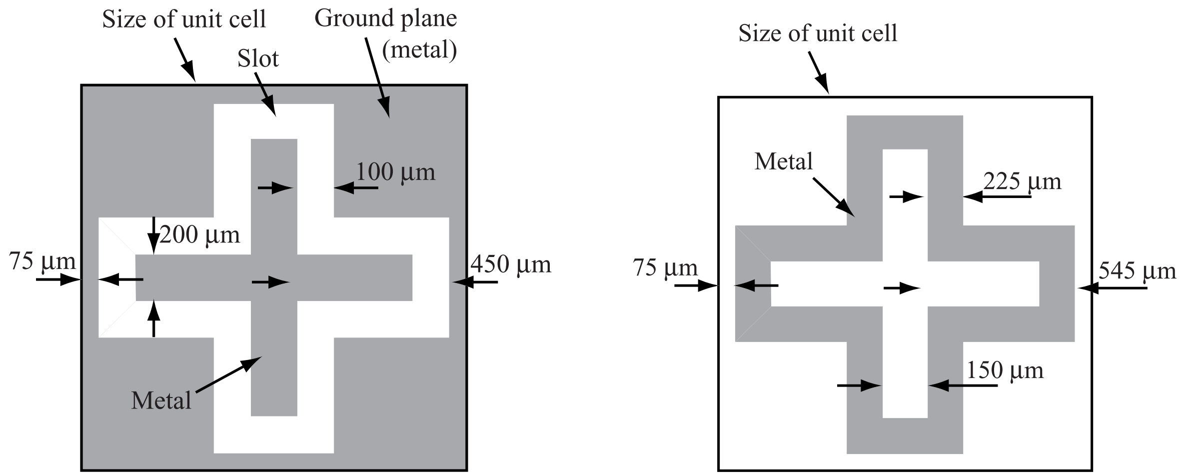


(a) (b)

**Figure 4.7: The unit cell of the FSS of the dual-frequency antenna system: (a) version 1, and (b) version 2.**

E-field for incidence with an angle of $\phi = 25°$ and $\phi = 30°$, respectively. For parallel polarization, which is the relevant case in this work, the $-1$ dB bandwidth of transmission of the FSS of version 1 is from 71 to 81 GHz which is wide enough to ensure low transmission losses even for oblique angles of incidence and with small fabrication tolerances. At 24 GHz, the transmission coefficient of the FSS of version 1 is about $-17$ dB and the reflection coefficient is almost 0 dB.

The $-1$ dB bandwidth of the reflection coefficient of the FSS of version 2 for an angle of incidence of 30° is from about 65 to 86 GHz. The reflection coefficient at 24 GHz is about $-8$ dB and the transmission loss is about $-1$ dB. Therefore, in an effort to reduce the transmission losses at 24 GHz and also the specular reflection at the FSS for high angles of incidence, an FSS with 2 metallic layers and a dielectric slab in between is designed. The metallic layers are periodic structures composed of the same unit cell as the FSS in version 2 (Fig. 4.7(b)) and the dielectric slab is a layer of RT/Duroid 5880 substrate with $\varepsilon_r = 2.2$ with a thickness of 2.4 mm. This corresponds to $\lambda_d/4$ at 24 GHz and functions as an impedance converter as it is used in filter design. The simulated S-parameters are

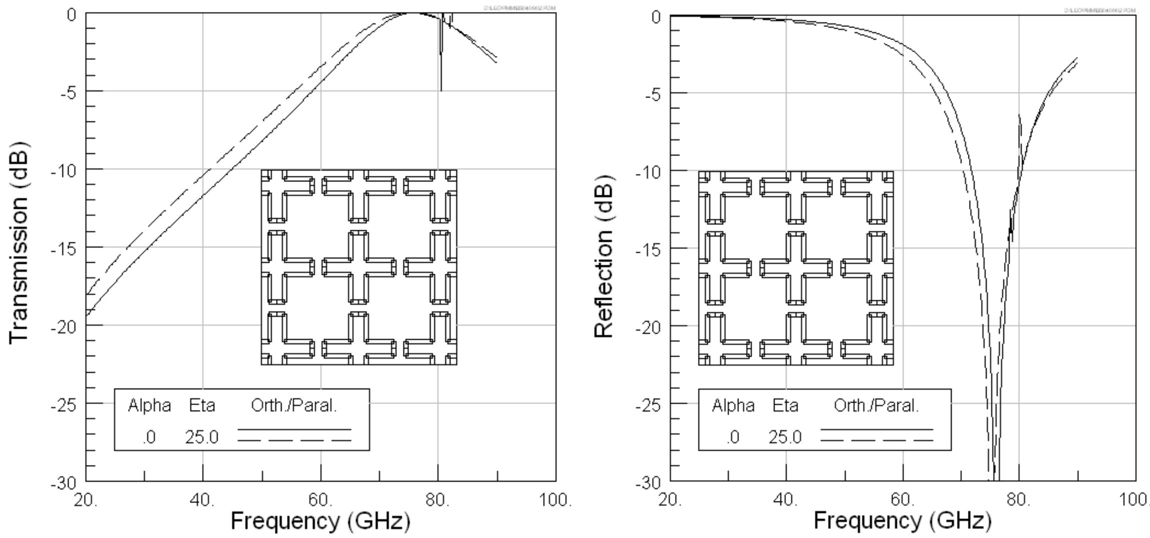


**Figure 4.8: Simulated S-parameters of the FSS, version 1, versus frequency for an angle of incidence of 25° for orthogonal (solid line) and parallel (dashed line) polarization.**

shown in Fig. 4.10 for an angle of incidence of 30°. Clearly, the two-pole filter characteristic can be seen with a maximum in reflection at 77 GHz and a maximum in transmission at 24 GHz. However, the −1 dB transmission bandwidth at 24 GHz is rather small and good performance of the dual-frequency antenna system is likely to be degraded due to fabrication and mounting tolerances as well as shifts in resonance frequency for different angles of incidence.

The simulation is done using a code which combines the method of moments and plane wave expansion [33]. In the simulation, it is assumed that the FSS is an infinite plane and is embedded between two halfspaces with $\varepsilon_r = 2.1$. This is a good approximation of the finite FSS placed between the two hemispherical Teflon lenses.

The FSSs are fabricated on a 127 µm thick RT/5880 substrate with $\varepsilon_r = 2.2$ (Fig. 4.11). The copper layer is 9 µm thick. The properties of the FSSs alone are not investigated in detail. However, the performance of the dual-frequency antennas which are presented in the following section indicates that the properties of the FSSs are as predicted.

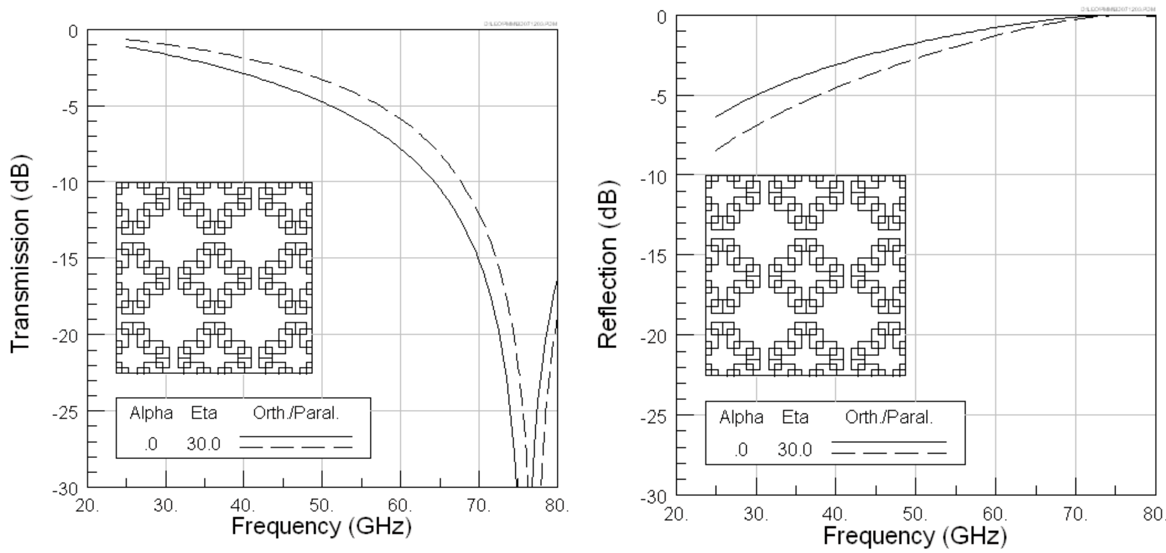


**Figure 4.9: Simulated S-parameters of the FSS, version 2, versus frequency for normal incidence and an angle of incidence of 30° for orthogonal (solid line) and parallel (dashed line) polarization.**

### 4.2.3 Radiation Pattern Measurements

**Dual-Frequency Antenna Version 1**

Fig. 4.12 shows the fabricated circuit of version 1 of the dual-frequency antenna system with $R = 25$ mm Teflon lens. Eleven 77 GHz feed antennas can be seen in the left side of the photograph. They are $5\lambda_0$ long FTSAs and are placed 5.5° apart from each other about $\phi = 180°$, covering 60.5° (55° center to center) field of view. The 24 GHz antennas are shortened FTSAs with length of $2.5\lambda_0$ (upper right corner). Three feed antennas are placed with an angular distance of 16.5° from each other about $\phi = 50°$, covering 49.5° (33° center to center) field of view. The separation between the lens and the feed antennas is 8 and 11 mm for 24 and 77 GHz, respectively. This is because of the location of the phase center which does not coincide with the aperture of the TSAs, as explained in Section 3.2.1. All feed antennas are fabricated on one piece of RT/Duroid 5880 with thickness 254 μm. The FSS is placed between two hemispherical Teflon lenses with a diameter of 50 mm and is tilted by 25° in the E-plane off the plane of main incidence. The size of the system,

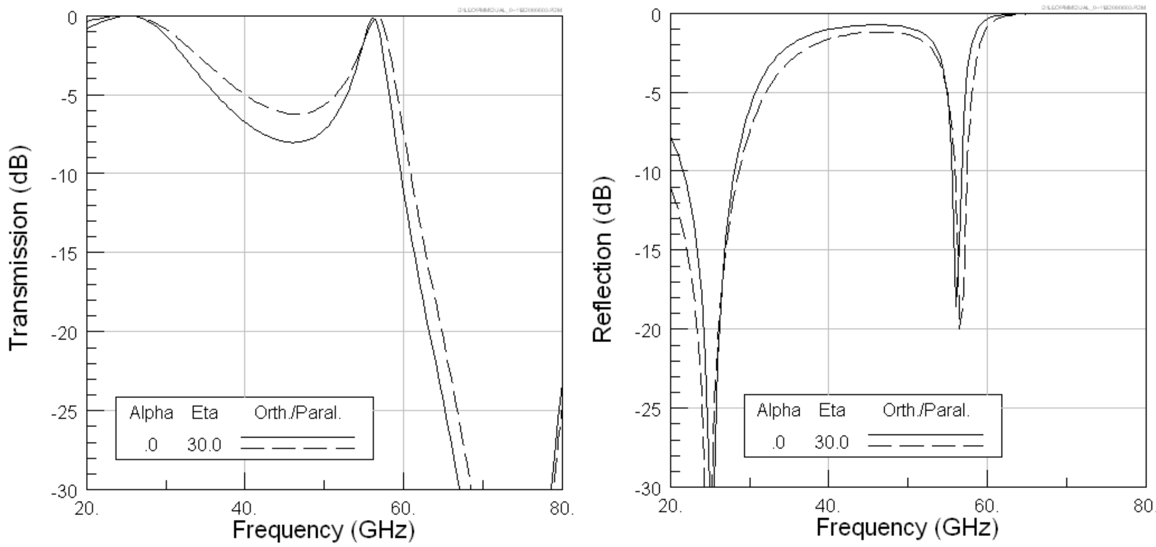


**Figure 4.10: Simulated S-parameters of the double layer FSS versus frequency for an angle of incidence of 30° for orthogonal (solid line) and parallel (dashed line) polarization.**

including the TSAs and the lens but not the microstrip feed lines, is 105 × 104 × 50 mm$^3$ (L×W×H).

The measured E-plane patterns at 24 and 77 GHz are shown in Figs. 4.13 and 4.14. At 24 GHz, the −3 dB beamwidth is 16.5° with a sidelobe level of −14 dB. At 77 GHz, the −3 dB beamwidth is about 5.5° and the sidelobe level is mostly below −18 dB with the exception of several sidelobes up to −15 dB. The radiation patterns at 24 and 77 GHz result in a cross-over at −3 dB. When comparing the gain of a feed antenna using the lens with FSS and without FSS, the difference is less than 5% at 24 GHz as well as at 77 GHz. This shows that the FSS has very little transmission losses at 77 GHz and very little reflection losses at 24 GHz.

An interesting observation at 77 GHz is that for increasing tilt angle of the FSS with respect to the main beam of the feed antenna, the −3 dB beamwidth decreases slightly whereas the gain remains about constant. This can be explained with a negative phase shift due to the FSS. For increasing angles of incidence, only the electromagnetic signal

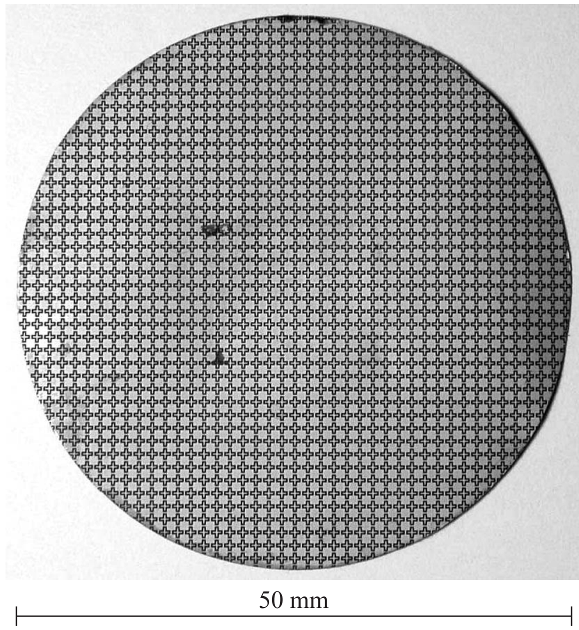


(a)

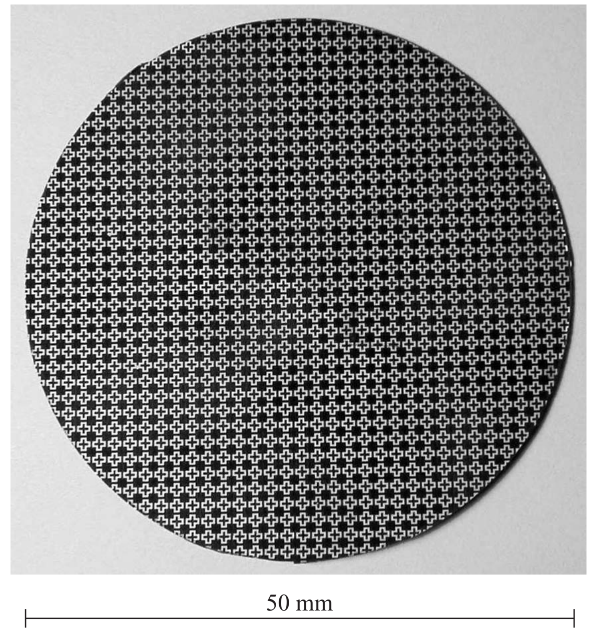


(b)

**Figure 4.11: Photographs of the FSSs of the dual-frequency antenna system: (a) version 1, and (b) version 2.**

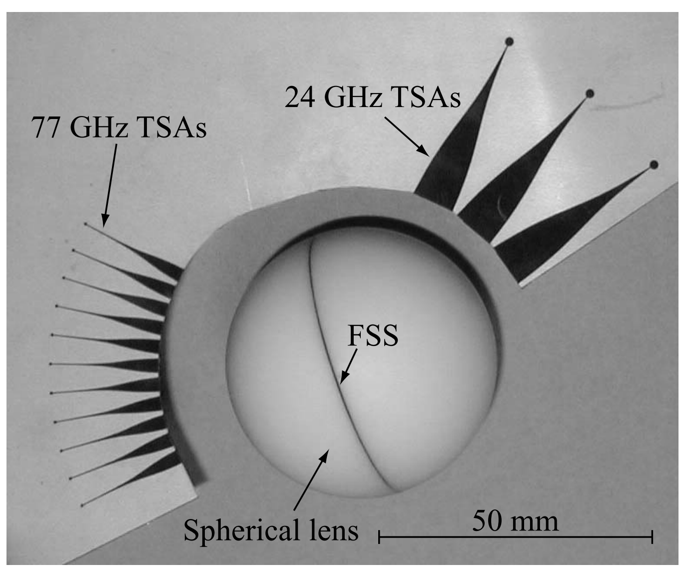


**Figure 4.12: Photograph of the dual-frequency antenna, version 1.**

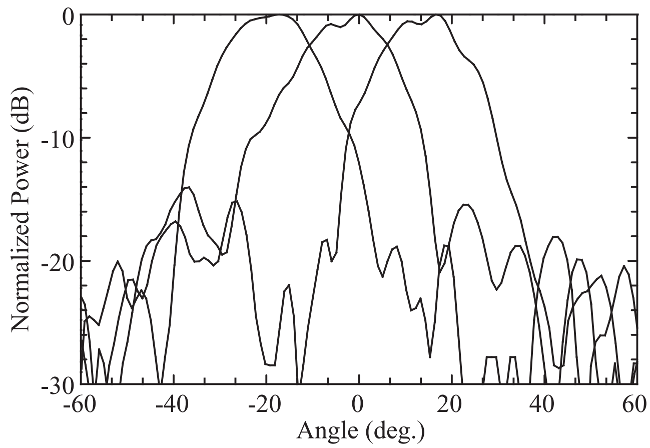


**Figure 4.13: Measured and normalized E-plane radiation patterns at 24 GHz of the dual-frequency antenna, version 1.**

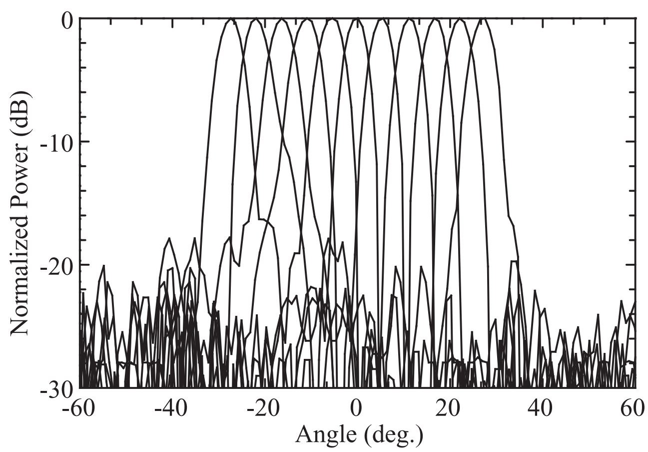


**Figure 4.14: Measured and normalized E-plane radiation patterns at 77 GHz of the dual-frequency antenna, version 1.**

that passes through the center part of the lens passes also through the FSS. The negative phase shift with respect to the signal that passes through the periphery of the lens corrects to a certain extent for the imperfect focusing properties of a homogeneous lens. The fact that the gain remains constant can be explained by the increasing losses in the FSS.

In order to confirm the good performance of the FSS, a 24 GHz feed antenna is placed behind the lens with FSS (normal incidence) which is reflective at that frequency and the

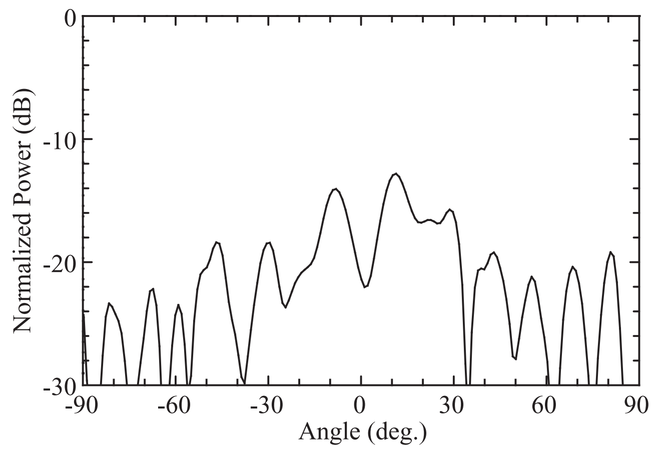


**Figure 4.15: Measured E-plane radiation pattern of a 24 GHz feed antenna through the reflective FSS of version 1.**

E-plane radiation pattern through the FSS is measured and normalized to the case with a spherical lens (Fig. 4.15). The isolation is $-13$ dB. This measurement shows that most of the power is indeed reflected by the FSS. Isolation between 24 and 77 GHz is not an issue in the design of this dual-frequency antenna because none of the two frequencies or any of its harmonics lies close to each other, and interference with spurious signals or increase in the noise level is not a concern. Also, other circuitry like the transitions from slotline-to-microstrip line, which are not so wideband in nature to operate concurrently at 24 and 77 GHz, will increase the isolation.

**Version 2**

Version 2 of the dual-frequency antenna is the dual of version 1 and a photograph is shown in Fig. 4.16. There are 7 feed antennas at 24 GHz placed about $\phi = 180°$ (left part of the picture), 16.5° apart from each other and also 7 feed antennas at 77 GHz (upper right part of the picture) located around $\phi = 60°$ with $\phi = 5.5°$ angular distance between each other. This results in a field of view of 115.5° (99° center to center) at 24 GHz and 38.5° (33° center to center) at 77 GHz. The feed antennas are separated from the lens by 8 and 11 mm for 24 and 77 GHz, respectively. The feed antennas are shortened FTSAs with length of $2.5\lambda_0$ at 24 GHz and $5\lambda_0$ long FTSAs at 77 GHz. All feed antennas are

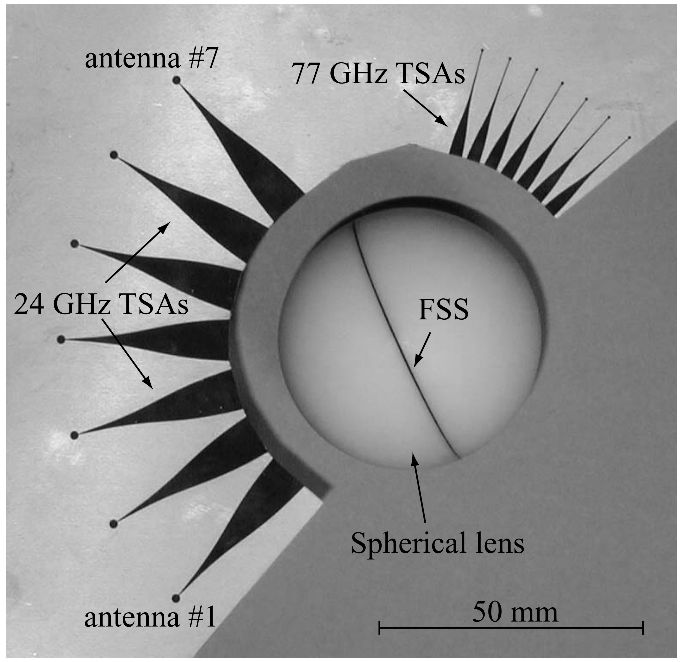


**Figure 4.16: Photograph of the dual-frequency antenna, version 2.**

fabricated on one piece of RT/Duroid 5880 with thickness 254 µm. The FSS is placed between two hemispherical Teflon lenses and is tilted by 30° in the E-plane off the plane of main incidence. The size of the system is 110 × 85 × 50 mm$^3$ (L×W×H).

The measured E-plane radiation patterns at 24 and 77 GHz are shown in Figs. 4.17 and 4.18. At 24 GHz, the −3 dB beamwidth is 16.5° and the sidelobe level is −14 dB. However, the −14 dB sidelobes can be attributed to 2 feed antennas. All sidelobes in Fig. 4.17 but the leftmost one belong to antenna #1. This antenna has increased scattering by the substrate which extends into the main direction of radiation. Also, when the measurement was performed, bondwires were coming off the backside of the substrate and the scattering was increased even more. The leftmost −14 dB sidelobe is part of the radiation pattern of antenna #7. It is caused by specular reflection off the FSS of the signal which is incident from $\phi = -70.5°$ (in Fig. 4.16 almost straight from the bottom). Without antennas #1 and #7, the sidelobe level is below −18 dB and the field of view is 82.5° (66° center to center). It is also possible to use 6 feed antennas at 24 GHz instead of 7 and achieve a scan angle of 99° (82.5° center to center). Such a case has not been measured but the sidelobe level has to be anywhere between −14 and −18 dB. At 77 GHz, the −3 dB beamwidth is

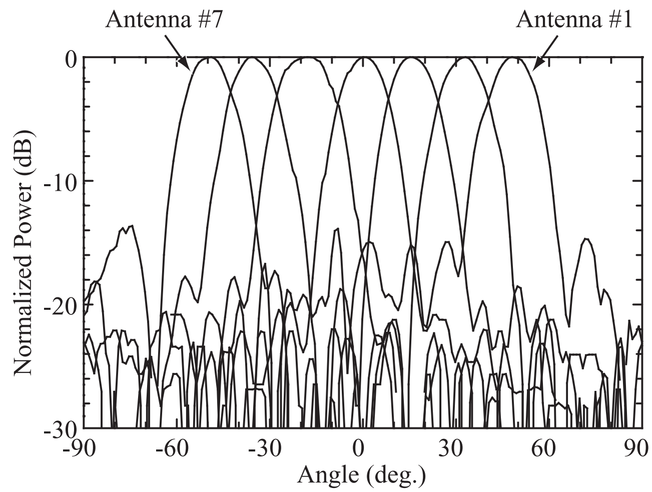


**Figure 4.17: Measured E-plane radiation patterns at 24 GHz of the dual-frequency antenna, version 2.**

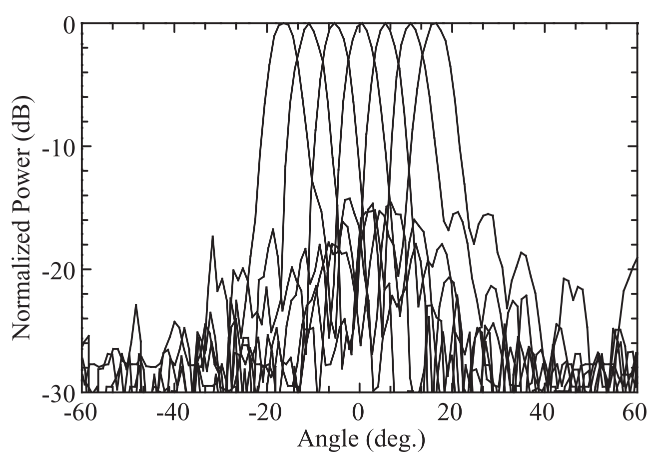


**Figure 4.18: Measured E-plane radiation patterns at 77 GHz of the dual-frequency antenna, version 2.**

5.5° and the sidelobe level is $-15$ dB. For both, 24 and 77 GHz, the cross-over of adjacent antenna beams occurs at the $-3$ dB level. When comparing the gain of a feed antenna using the lens with FSS and without FSS, the difference is 10% at 24 GHz and less than 5% at 77 GHz. This shows that the FSS is a good reflector at 77 GHz but has about $-10$ dB of transmission loss at 24 GHz, as predicted by the simulation.

In order to reduce the transmission losses at 24 GHz, the FSS is replaced by the double-

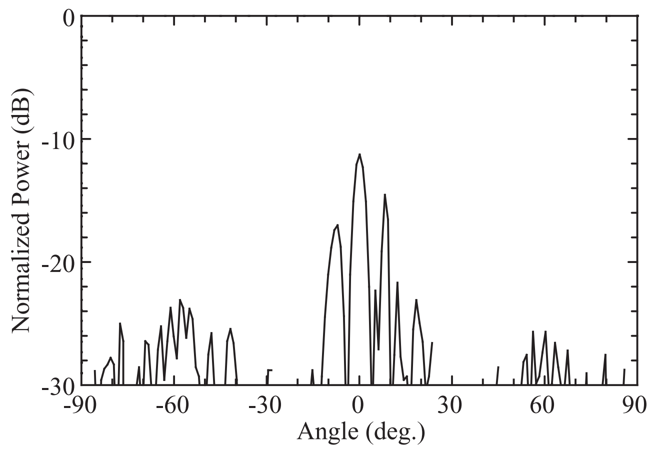


**Figure 4.19: Measured E-plane radiation pattern of a 77 GHz feed antenna through the reflective FSS of version 2.**

layer FSS presented Section 4.2.2. However, measurements do not exhibit any improvement in the transmission losses and specular reflection for high angles of incidence at 24 GHz. This may be due to the limited bandwidth of the double-layer FSS and the fabrication and assembling tolerances. Also, the shape of the two hemispherical Teflon lenses with a thick dual-layer FSS in-between deviates somewhat from a sphere and this may cause degradations in the radiation patterns.

As for version 1, a 77 GHz feed antenna is placed behind the lens with the FSS of version 2 at normal incidence (which is reflective at that frequency) and the E-plane radiation pattern is measured (Fig. 4.19). The measured isolation is $-11$ dB.

## 4.3 Concluding Remarks

It is shown that the FSS can be designed to allow for 2-frequency operation using the same aperture, operates well over a very wide angle of incidence, and does not result in high additional losses (0.5 dB maximum) as compared to an antenna-lens system without an FSS. In automotive radar systems, version 2 of the dual-frequency antenna is more likely to be used because 24 GHz applications usually require a wider scan-angle than 77 GHz systems. Also, such a system will not result in an independent control of the beamwidth at

24 and 77 GHz since both frequencies share the same aperture.

# CHAPTER 5

## Switchable Frequency-Selective Surface

Frequency-Selective Surfaces (FSSs) have found applications in multiband reflector antennas and radomes, especially in communications and defense applications. FSSs have been designed for a fixed frequency. However, for certain applications, it is desirable to be able to change the frequency behavior over time. This is done using a ferrite substrate, when the relative permeability ($\mu_r$) is tuned with a bias magnetic field [35, 97]. The properties of the resonating elements themselves can also be changed using varactor diodes [36–38] or Microelectromechanical Systems (MEMS) such as rotating dipoles [39]. However, these methods have many disadvantages such as high losses (ferrite substrate), high bias currents (varactor or PIN diodes), or high cost (ferrite substrate, varactor diodes).

The following chapter describes the design, simulation, fabrication, and measurement of a switchable FSS using RF MEMS as tuning elements.

## 5.1 Choice of the Unit Element

There are many possible unit elements and many have been studied in literature. Some typical elements are shown in Fig. 5.1. They have different properties regarding type of filter function (band-pass, band-stop, low-pass, high-pass), independence of polarization, independence of angle of incidence, bandwidth, location of higher resonance frequencies, onset of grating lobes, possibility of bandwidth tuning, possibility of close packing, and possibility of frequency tuning with loading elements.

In this work, the four-legged loaded element is chosen, implemented as a slot in a ground

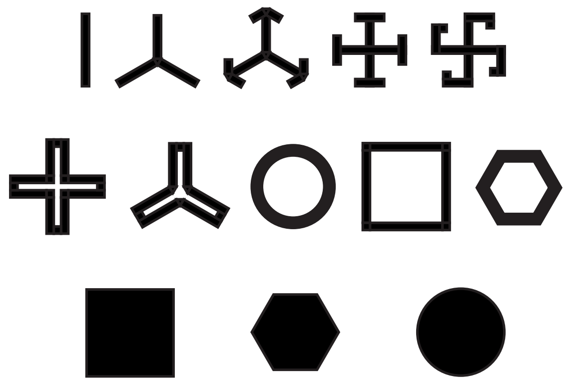

**Figure 5.1: Different types of unit cells for FSS circuits.**

plane (Fig. 5.2). It is an electrically small element with a typical size of $0.3\lambda_0$ in the x- (or y-) direction. This ensures that the elements can be densely packed and therefore, the resonance frequency is quite stable with angle of incidence [33] and the grating lobes are of no concern in the frequency range of interest. The four-legged loaded element is polarization independent due to its 90°-rotational symmetry, and its bandwidth is average compared to other typical unit elements. A special feature of the four-legged loaded element (as well as the three-legged loaded element) is the possibility of bandwidth control not only by the interelement spacing but also by the shape of the element. This is especially interesting for more complicated FSS designs with multiple layers for a multipole filter response. Also, the first transmission null above the fundamental resonance frequency is the same for parallel and orthogonal polarization as opposed to elements of the center-connected family [33]. The four-legged loaded element can be implemented in CPW form, which is compatible with capacitive switches and results in a relatively easy bias arrangement.

At resonance, the length of the slot loop is $1\lambda$. For a vertically polarized incident field, the maxima of the electric fields (open circuit) in the slot are in the tips of the vertical "legs", and the electric field in the tips of the horizontal "legs" is zero (short circuit) (Fig. 5.3(a)). This can be explained considering the symmetry of the circuit (Fig. 5.3(b)). The symmetry planes which are normal to the incident electric field can be replaced by a perfect electric conductor (PEC), and the symmetry planes parallel to the incident electric fields can be replaced by perfect magnetic conductors (PMC) without changing the properties of the circuit. These symmetry planes explain also the fact that the electric field in the slot

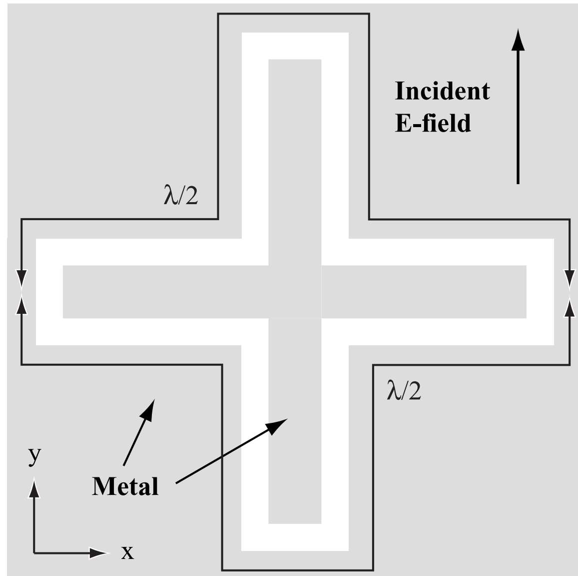


**Figure 5.2: Schematic of the four-legged loaded element.**

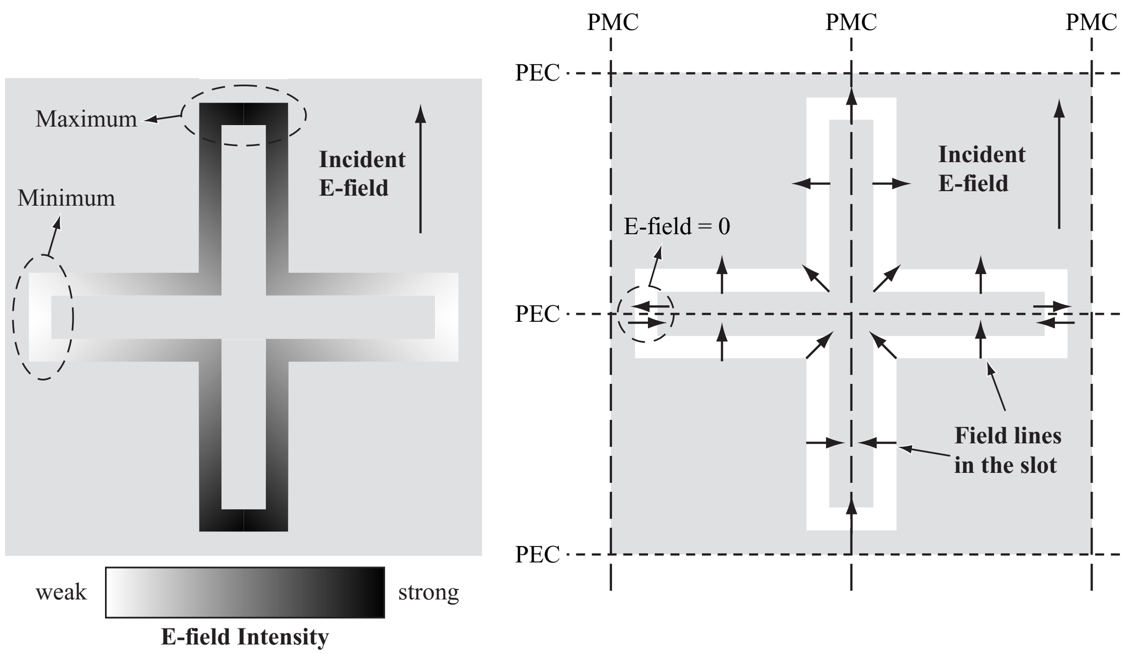


(a) (b)

**Figure 5.3: (a) E-field intensity and (b) orientation in the slot of the four-legged loaded element at a certain instant of time.**

resonates in an odd mode (CPW mode) in the vertical "legs" and in an even mode (slotline mode) in the horizontal "legs" for an incident field in the y-direction (Fig. 5.3(b)).

## 5.2 RF-MEMS Varactors as Tuning Elements

The FSS is a filter which can also be represented by a parallel LC-resonant circuit with a resonance frequency of:

$$f_0 = \frac{1}{2\pi\sqrt{LC}}. \tag{5.1}$$

A frequency shift can be achieved by changing the value of the resonator capacitance using RF MEMS. A simple model for an RF MEMS bridge is a variable capacitance ($C_{up}$ and $C_{down}$), and when implemented correctly, the capacitances add to the overall capacitance of the resonant circuit, resulting in new fundamental resonance frequencies:

$$f_{0,up} = \frac{1}{2\pi\sqrt{L(C + C_{up})}} \tag{5.2}$$

$$f_{0,down} = \frac{1}{2\pi\sqrt{L(C + C_{down})}}. \tag{5.3}$$

Equations 5.2 and 5.3 are only correct for lumped-element resonators. For distributed resonators, the location of the MEMS bridge is very important and the relevant equations are not easy to write [98]. Several advantages make the use of RF MEMS as tuning elements very attractive. The tuning element loss is very low because the quality factor, $Q$, for standard RF MEMS is greater than 200 at 30 GHz and the switching speed is reasonably fast (in the order of 10 μs). The DC power consumption is extremely low (in the order of 3 pJ per bridge per cycle). This is a great advantage over FSSs using PIN-diodes as tuning elements where each diode requires 2-3 mA of bias current. Also, the cost of fabrication does not increase with the number of elements since it is done using standard lithography.

## 5.3 Bias Circuitry and Model for RF MEMS Control

In order to actuate the RF MEMS bridges, the inner part of every single unit cell must be contacted. This can be done with high resistivity bias lines which run underneath the ground plane and are electrically isolated through a SiN-layer [99]. However, this may

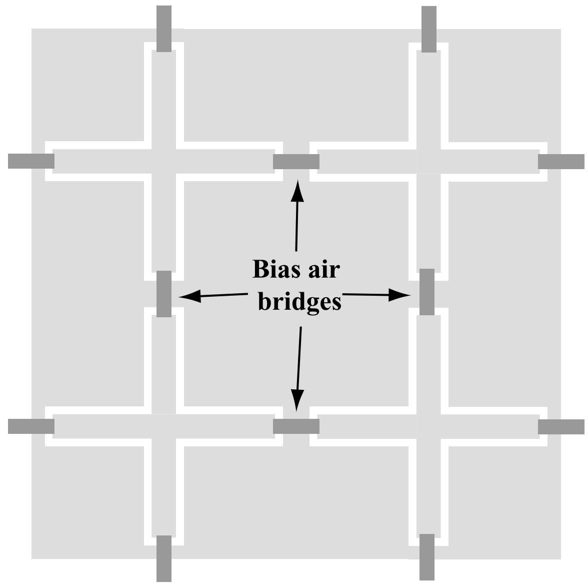


**Figure 5.4: DC-biasing of the four-legged loaded element using air bridges.**

create asymmetry in the elements and degrades the performance. Moreover, for an array with thousands of unit cells, it is likely that due to fabrication errors there is at some point an electrical contact between a bias line and the ground plane which results in a DC short circuit and a catastrophic failure of the tunable FSS.

A better solution is to arrange the unit cells as shown in Fig. 5.4 and to connect the tips of neighboring unit cells with air bridges (*bias bridges*). This way, the inner parts of all unit cells are DC-connected, and an electric potential can be applied by contacting only one unit cell, preferably at the edge of the FSS. Also, if an air bridge fails, the element is still DC-connected, using a multitude of other DC paths.

The choice of bias circuitry has substantial impact on the FSS design. One could erroneously think that the bias bridges act as variable capacitances. However, when examining the electric field distribution in the slots without bias bridges (Fig. 5.5(a)), it is observed that the field vectors at the location of the bias bridges point in the same direction. By adding an air bridge across the ground plane, the anchors of the bridge are at opposite potential with respect to the ground plane and a virtual ground is created at the center of the MEMS bridge. This means that instead of loading capacitors, the bias bridges function as virtual RF-short circuits to ground. Another explanation for the same phenomenon is

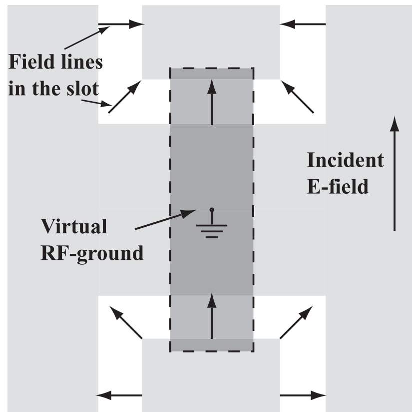


(a)

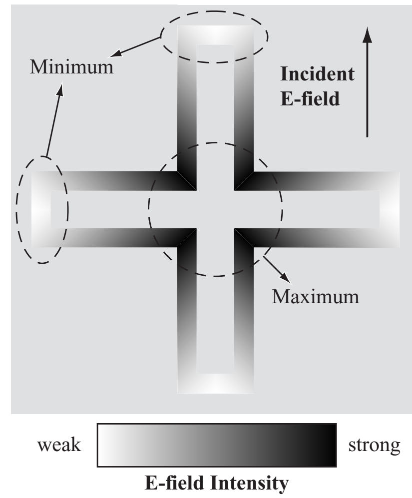


(b)

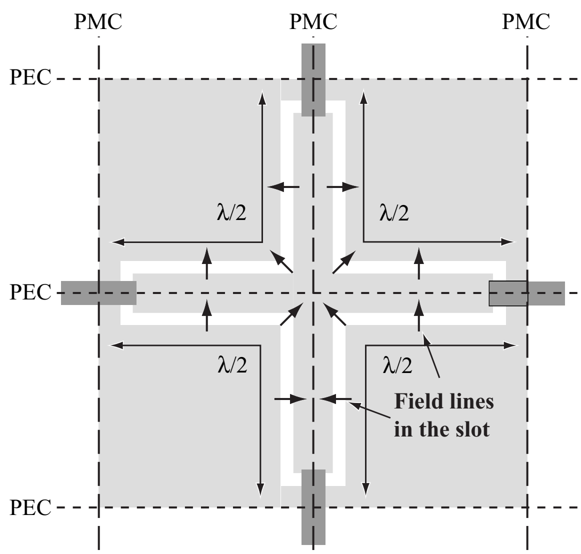


(c)

**Figure 5.5: The effect of the bias bridges on the design of the FSS: (a) electric field lines in the slot at the location of the bias bridges, (b) intensity of the electric field of the fundamental resonant mode and (c) PEC and PMC-symmetry planes and the resulting E-field orientation.**

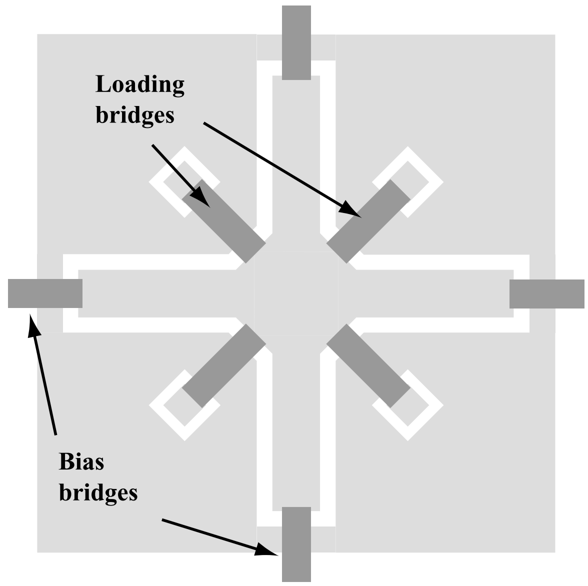


**Figure 5.6: Unit cell of the switchable FSS with bridges for DC-voltage bias and capacitive loading.**

found by considering again the symmetry planes of the circuit. Through the bias bridges, all four tips are connected to ground and a short circuit (no electric field) is established at the four tips (Fig. 5.5(b)). As a consequence, the four-legged loaded element is transformed from a double-$\lambda/2$ resonator to a quadruple-$\lambda/2$ resonator (Fig. 5.5(c)) with about twice the resonance frequency.

## 5.4 Placement of the MEMS Bridges

To achieve the highest capacitive loading, 4 RF MEMS varactors per unit cell (*loading bridges*) are placed at the location of the highest electric field intensity in the slot (Fig. 5.6). One could use cantilever beams, but for better uniformity, fixed-fixed beams are used with one of their anchors connected to the center of the FSS-element. The other anchor rests on an island which is electrically isolated from the ground plane. The membrane spans over a stretch of ground plane which establishes the variable capacitance necessary to tune the frequency response of the element.

## 5.5 Design of the Switchable FSS

Two different FSSs are designed, one with fixed frequency response and one switchable FSS using RF MEMS.

### 5.5.1 FSS with Fixed Frequency Response

The first design is a circuit with fixed frequency response without RF MEMS bridges. The effect of the bias bridges is taken into account using a physical short circuit across the slot at the tip of each leg. The FSS is built on a glass wafer (Pyrex Borosilicate glass, $\varepsilon_r = 4.6$, $\tan(\delta) = 0.01$ at 30 GHz) with a thickness of 0.5 mm. The slot and metal width of the "legs" is chosen to be 80 and 160 µm, respectively, because these are convenient dimensions for fabrication and the ratio of 1:2 results in the minimum CPW resonator loss [77]. Since this FSS design serves as a comparison to the switchable FSS with RF MEMS, the spacing between the unit cells is set from the length of the bias bridges and is 140 µm. The only remaining parameter, the length of the "legs", is determined by a 3-D full-wave simulation using the commercial FEM simulator HFSS [100]. A single unit cell is placed in a waveguide with PEC and PMC-walls, which ensures a plane wave excitation of the circuit.

For a resonance frequency of 31 GHz, the length of the "legs" is 1290 µm (Fig. 5.7) which results in a cell size of $l_c = 3$ mm. The simulated transmission and reflection coefficients are presented in Fig. 5.8. The mid-band insertion loss is 0.91 dB. Of that, 0.30 dB is contributed by the reflection ($S_{11} = -11.7$ dB), 0.24 dB by the ohmic losses in the slot/CPW resonator, and 0.37 dB by the glass dielectric losses. Losses due to metal roughness are not considered. The $-1$ dB bandwidth is 2.8 GHz and the $-3$ dB bandwidth is 5.4 GHz.

### 5.5.2 Switchable FSS

The second design is a switchable FSS with bias and loading bridges (Fig. 5.9). The substrate and line width dimensions are the same as in the first design. The bias bridges are 80 µm wide and 300 µm long. This sets the interelement spacing to 140 µm, which is also used for the first design. The loading bridges are implemented across a tilted section of

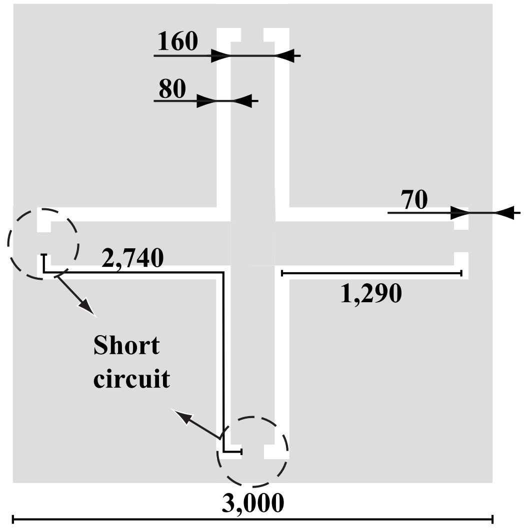


**Figure 5.7: The dimensions of the unit cell of the FSS with fixed frequency response in µm.**

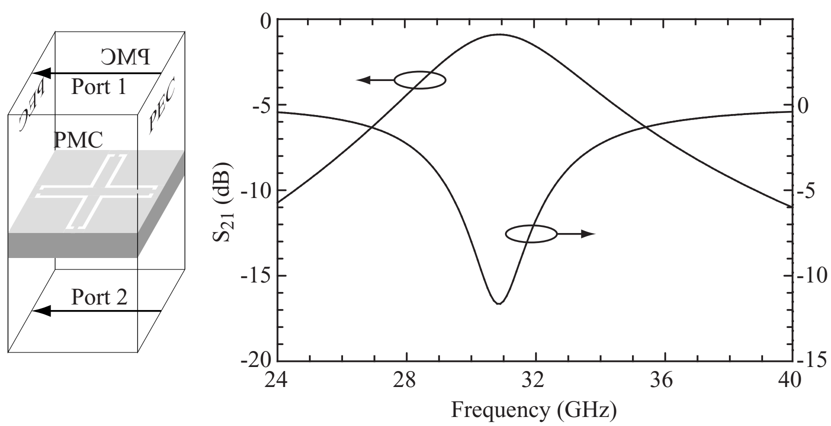


**Figure 5.8: The simulated (HFSS) transmission and reflection coefficients of the FSS with fixed frequency response.**

the slot near the center of the element. The bridges are 50 µm wide and 280 µm long and span over a ground plane of 140 µm width. The "islands" are $100 \times 100$ µm in size and are separated from the ground plane by a 50 µm wide slot. The resulting up-state capacitance $C_u$ of this geometry for a certain bridge height is found using full-wave simulation [101] and the calculated S-parameters are fitted in ADS [102] using a simple series $RLC$ circuit model

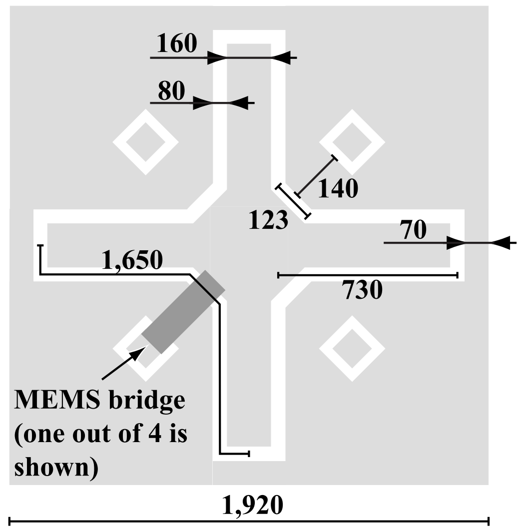


**Figure 5.9: The dimensions of the unit cell of the switchable FSS in μm.**

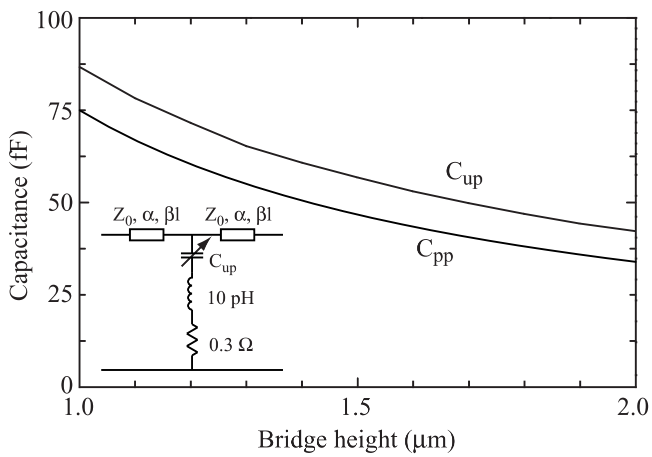


**Figure 5.10: Simulated up-state capacitance ($C_u$) and parallel-plate capacitance ($\varepsilon A/d$) of a 50 μm wide MEMS bridge over a 140 μm wide ground plane versus bridge height.**

for the bridge with $L = 10$ pH and $R = 0.3\ \Omega$ (Fig. 5.10).

The design frequency of the FSS is 32 GHz. However, the average bridge height on the fabricated switchable circuit is around 1.7 μm instead of an originally assumed value of 2.0 μm. Therefore, the simulations of the switchable FSS are retrofitted for the new bridge height. For a bridge height of 1.7 μm, the up-state capacitance of the loading bridges is

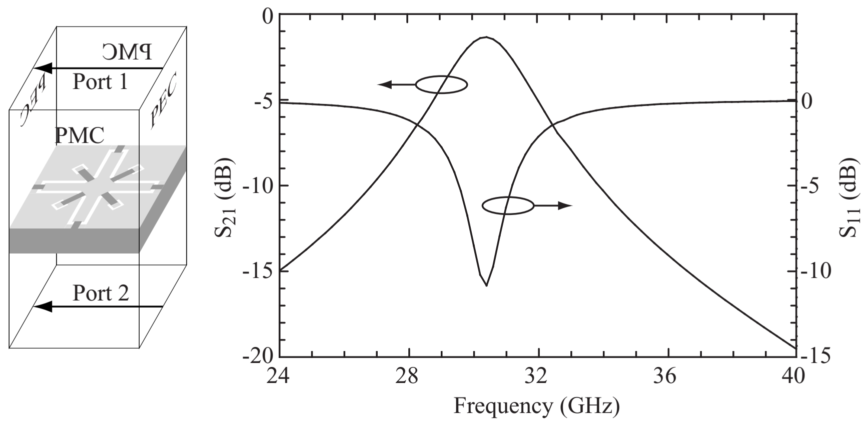


**Figure 5.11: The simulated (HFSS) transmission and reflection coefficient of the switchable FSS.**

50 fF (Fig. 5.10).

Once the geometry of the bridge is set, the length of the "legs" is determined by a 3-D full-wave simulation using HFSS (Fig. 5.9). Due to the capacitive loading of the MEMS bridges, the cell size $l_c$ is shrunk from 3 mm to 1.92 mm compared to the previous design with a fixed frequency response. This is advantageous, because periodic structures excite grating lobes and are prone to carrying substrate modes. This creates strong transmission zeros, and their occurrence near the pass-band can result in a distorted frequency response.

The overall simulated transmission loss using HFSS in the transmit mode at 30.4 GHz is 1.35 dB, not taking into account losses due to metal roughness (Fig. 5.11). The ohmic loss due to finite metal resistance contributes 0.68 dB, the loss tangent of the substrate ($\tan(\delta) = 0.01$) accounts for 0.31 dB, and the reflection loss accounts for 0.36 dB ($S_{11} = -11.0$ dB). The simulated $-1$ dB bandwidth is 1.4 GHz and the $-3$ dB bandwidth is 2.8 GHz.

The difference in the bandwidth of the two FSSs can be explained using (5.1). The admittance $Y$ of a parallel $LC$ circuit disappears at resonance:

$$Y\Big|_{f_0} = j2\pi fC + \frac{1}{j2\pi fL} = 0 \tag{5.4}$$

and its derivative with respect to the frequency is given by:

$$\frac{\mathrm{d}Y}{\mathrm{d}f}\Big|_{f_0} = j4\pi C. \tag{5.5}$$

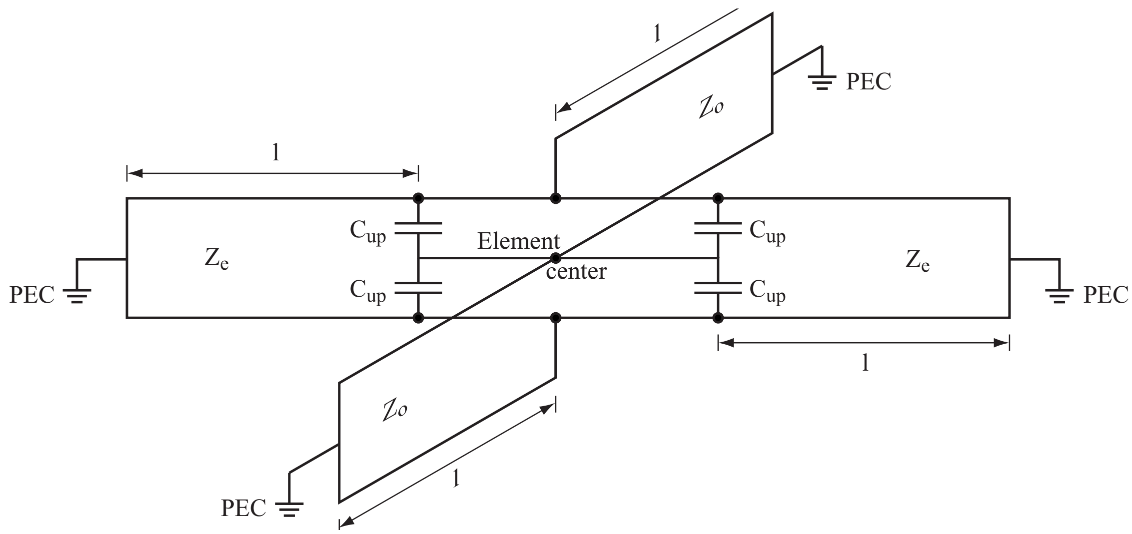


**Figure 5.12: Transmission line schematic of a single unit cell.**

The capacitance of the switchable FSS is larger than the capacitance of the FSS with fixed frequency response due to the loading of the MEMS membranes. Therefore, the admittance around resonance changes faster and the transmission bandwidth is reduced.

### 5.5.3 Equivalent Circuit Model

Using the schematic shown in Fig. 5.12 which represents the transmission lines and the bridge capacitances of a single unit cell, equivalent circuit models for the designed FSSs are derived (Fig. 5.13). The input and output ports are connected to the center of the element via a transformer. The transformer ratios for the FSS with fixed frequency response, $n_1$, and the switchable FSS, $n_2$, can be determined using the method introduced in Section 5.9.1 or by curve fitting and are 0.59 and 2.1, respectively. The four transmission line sections ("legs") are connected to the center of the element on one side and to ground on the other side due to the PEC symmetry planes. The two "legs" which carry the even mode are at the same potential which means they are in parallel and are represented as a single transmission line section with half of the impedance of a single transmission line stub, $Z_e \tanh \gamma l$. The two "legs" which carry the odd mode are connected in series because the outer conductors are at opposite potential with respect to the element center and are represented as a single

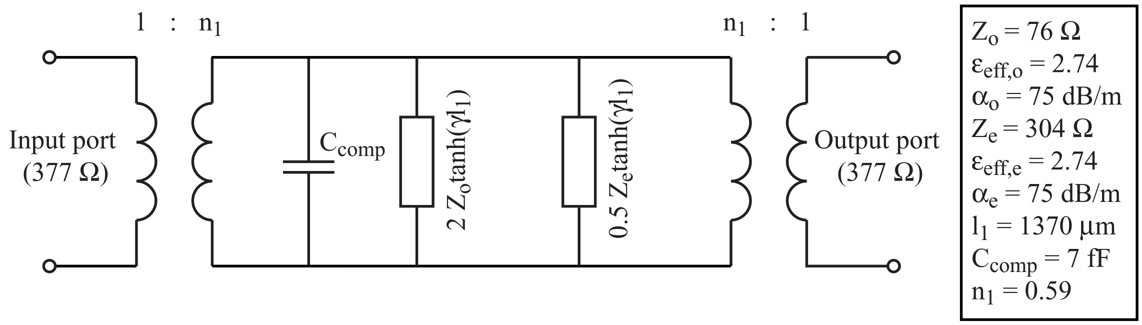


(a)

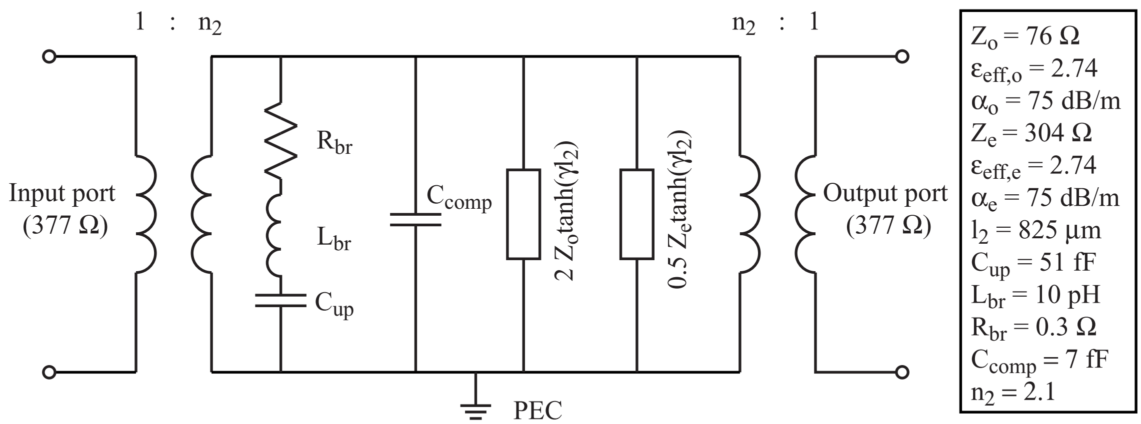


(b)

**Figure 5.13: The equivalent circuit models of (a) the FSS with fixed frequency response and (b) the switchable FSS.**

transmission line with twice the corresponding impedance, $Z_o \tanh \gamma l$. In the case of the switchable FSS, two of the four loading bridges are connected in series and two in parallel. They are therefore represented as a single MEMS bridge with a resistance of $R_{br} = 0.3\ \Omega$, an inductance of $L_{br} = 10$ pH, and a capacitance of $C_{up} = 51$ fF in series. The lengths of the legs, $l_1$ and $l_2$, are 1,370 µm in the case with the fixed frequency response and 825 µm in the case of the switchable FSS, respectively. $Z_o$ can be determined using ADS and is 76 Ω. $Z_e$ cannot be determined with an approximate closed form expression because the

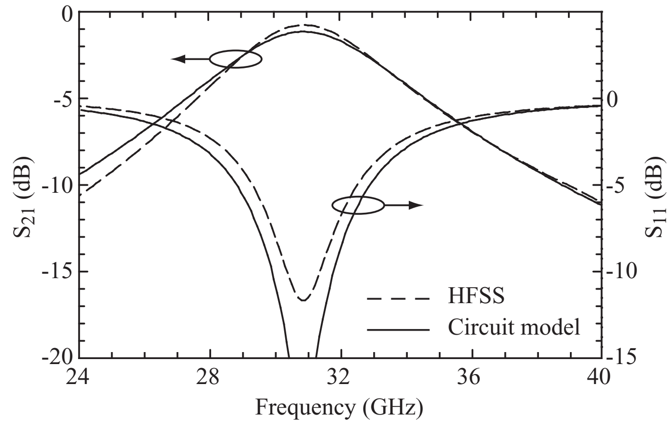


(a)

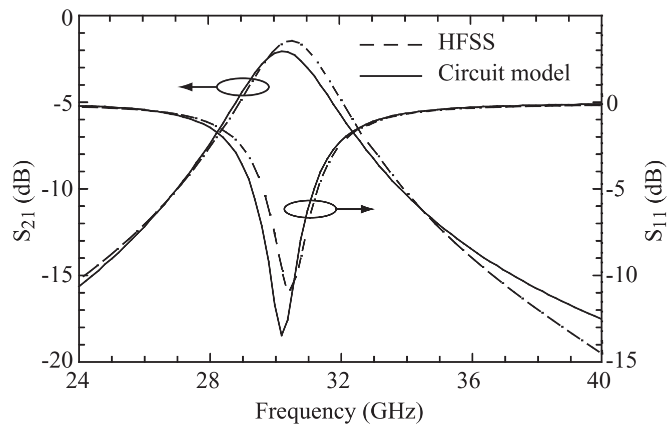


(b)

**Figure 5.14: The simulated S-parameters of (a) the FSS with fixed frequency response and (b) the switchable FSS with bridges in the up-state position using the equivalent circuit model in comparison with the HFSS simulation.**

current density on the outer conductors of the transmission line does in general not decay fast enough to converge. However, at a distance of 800 μm from the transmission line the current density is zero because of the PEC symmetry. Therefore, the current is concentrated close to the edges of the conductor and the capacitance between the outer conductors is very small. This leads to a characteristic impedance which is approximately 4 $\times$ greater than $Z_o$. The attenuation of the transmission line in odd mode was measured in [103] at 21 GHz and is 70 dB/m. For the FSS at 30 GHz, the attenuation for even and odd mode is approximated with 75 dB/m. The discontinuity of the transmission line close to the center of the element is accounted for with a capacitance, $C_{comp}$, of 7 fF. Fig. 5.14 shows the resulting transmission and reflection coefficient for both FSSs in comparison with the HFSS simulation.

## 5.6 Fabrication

The FSSs presented in this work are fabricated in a class 100 clean room (less than 100 particles larger than 1µm per cubic feet of air) at The University of Michigan. The FSSs are fabricated on a glass wafer with a dielectric constant $\varepsilon_r = 4.6$ and a loss tangent $\tan(\delta) = 0.01$ at 30 GHz. The diameter is $d = 76.4$ mm and the thickness is $t = 0.5$ mm. The fabrication procedure is illustrated in Fig. 5.15. First, the ground plane, bridge islands, and inner elements are defined by a lift-off process of evaporated Ti/Au/Ti = 500/5000/500Å. Then, the dielectric layer underneath the bridges is deposited in a Plasma Enhanced Chemical Vapor Deposition (PECVD) process. The material is Silicon Nitride ($Si_3N_4$) with $\varepsilon_r = 7.6$ and a thickness of 2000 Å. It is patterned using Reactive Ion Etching (RIE). The sacrificial layer is Polymethylmethacrylate (PMMA) with a thickness of 2 µm. The patterning of the PMMA layer is done with RIE using a Ti masking layer. Then the metal layer for the bridge membrane is deposited in a sputter process (Ti/Au/Ti = 100/8000/500Å). Using this layer as a seed layer, the anchors of the loading bridges, all of the bias bridges as well as the ground plane (excluding the parts underneath bridges) are electroplated with 3 µm-thick gold. For better uniformity of the loading bridges, the circuit undergoes a heating and cooling cycle from 100°C to 170°C to 100°C. This releases some stress in the membrane and also forms a very thin layer of Au-Ti alloy at the 2 Ti-Au interfaces with a thickness in the order of 50 Å. This alloy is considerably stiffer than either Au or Ti. Finally, the bridges are defined in a wet etching process, the sacrificial layer is desolved in PRS-2000, and the bridges are released in a Critical Point Dryer system.

The advantage of PMMA over Photoresist as a sacrificial layer is that it reflows after spinning and therefore does not create abrupt changes on the top profile. This helps making the bridge flatter and decreases mechanical instability due to thin vertical sections in the metal membrane. Also, after 30 min of baking at 170°C, all solvents are gone and no further out-gassing occurs in the following process steps which would damage the metal membranes. Furthermore, when removing the sacrificial layer, no etchant is needed which would eventually attack the Ti and the Silicon Nitride, as it happens when using PECVD $SiO_2$.

The purpose of the gold electroplating is threefold. First, the anchors of the loading bridges are reinforced. This ensures that the twin membrane, when released, stays flat and this increases the lifetime of the bridge. Second, the electroplating makes the bias bridges very stiff and prevents pulling down when applying DC-bias voltage (the entire bias bridge is electroplated). Third, the thickness of the ground plane is increased which reduces ohmic losses in the slots, and the losses due to the skin effect.

The fabrication process is listed in detail in Appendix E. For further information about the fabrication process, the reader is referred to [104–106].

The fabricated circuit of the FSS with fixed frequency response includes 409 unit cells (Fig. 5.16), each $3 \times 3$ mm$^2$. The switchable FSS (Figs. 5.17, 5.18, and 5.19) consists of 909 unit cells, each $1.92 \times 1.92$ mm$^2$, with 3,636 loading bridges and 1,686 bias bridges. Three unit cells each are tapped on opposite sides of the circuit to apply the DC-bias voltage.

### 5.6.1 Post-Fabrication Process

The 50 and 80 μm wide slots on the switchable FSS have an overall length of more than 8 m over the entire wafer. It is therefore likely that after fabrication, unwanted DC-connections remain on the circuit which can be caused by impurities in the photoresist used for the last metal etching step or by adhesion problems of the photoresist during the gold electroplating. Even a single unwanted short circuit would prevent the actuation of the loading bridges. Therefore, a post-fabrication process becomes necessary to remove any residual DC-shorts. Some faulty DC-connections can be found under the microscope and

(a) Lift-off metal layer to define ground planes, inner elements, and islands.

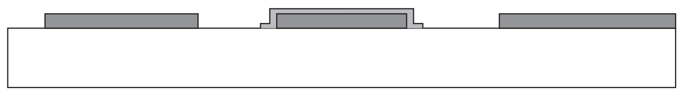

(b) Deposit PECVD SiN, pattern it using RIE.

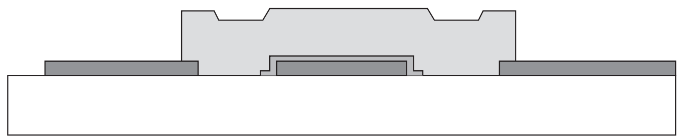

(c) Deposit sacrificial layer PMMA, pattern it using RIE.

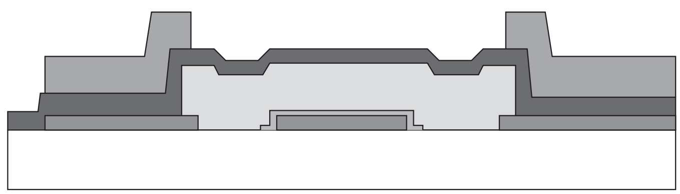

(d) Deposit the MEMS bridge layer using sputtered Ti/Au/Ti and electroplate anchors and ground plane.

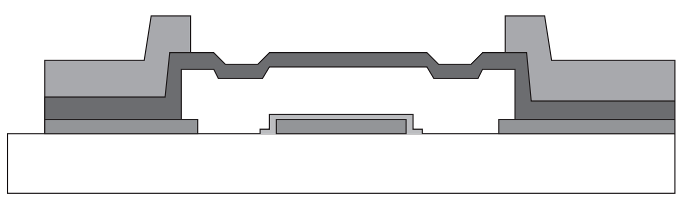

(e) Pattern the bridges using wet etching. Etch the sacrificial layer using PRS-2000. Release the membranes using a Critical Point Dryer system.

**Figure 5.15: The fabrication procedure of a MEMS bridge.**

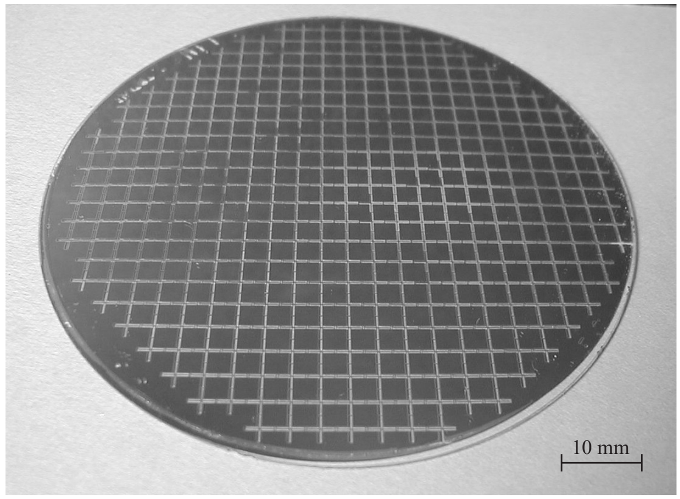


**Figure 5.16: Photograph of the FSS with fixed frequency response with 409 unit cells, each 3 mm in period.**

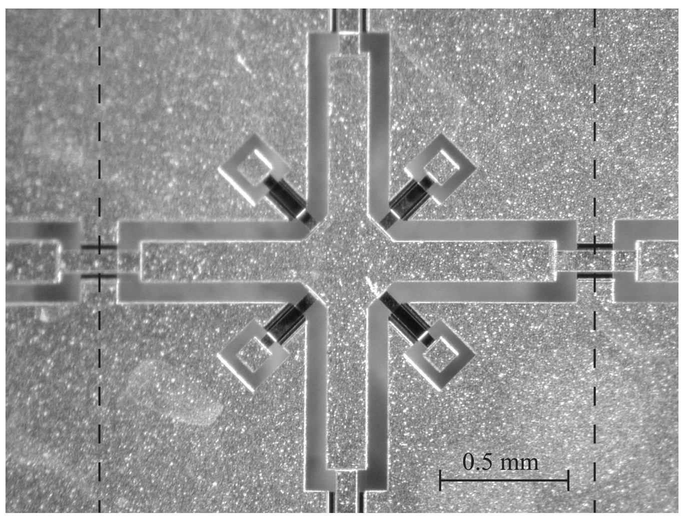


**Figure 5.17: Photograph of a unit cell of the switchable FSS of dimensions of $1.92 \times 1.92$ mm$^2$ and with four RF MEMS bridges at the center.**

manually scraped, but only a small number falls under this category. A way to find the remaining short circuits is to apply a DC-current between the tapped unit cells and ground. The current spreads evenly throughout all the unit cells and the high current density in the short circuits causes the unwanted short circuits to heat up. Hot spots of the size of about

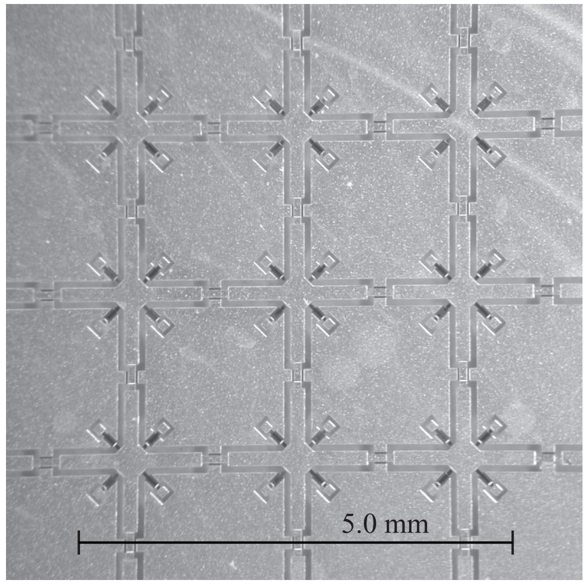


**Figure 5.18: Photograph of 3 × 3 unit cells of the switchable FSS.**

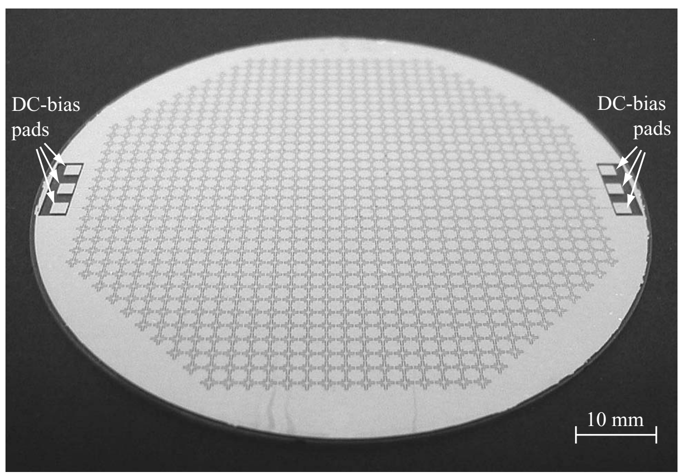


**Figure 5.19: Photograph of the switchable FSS on a 3" wafer with 909 unit cells, 3,636 loading bridges, and 1,686 bias bridges.**

2 mm (Fig. 5.20) are created which can be located at the backside of the circuit using an infrared camera (Fig. 5.21). Once located, the short circuits can be removed with a sharp strong metal tip under the microscope.

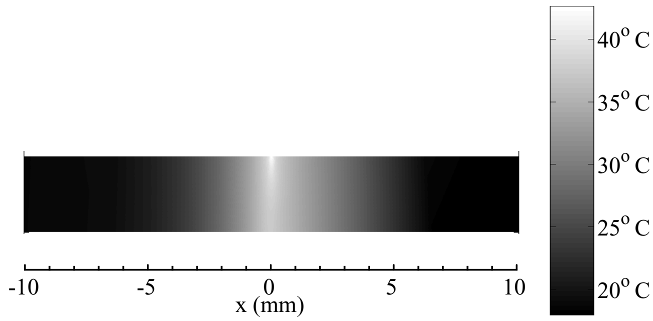


**Figure 5.20: The simulated temperature distribution using Matlab in the glass substrate after 10 s with a heat source of 50 mW [107]**

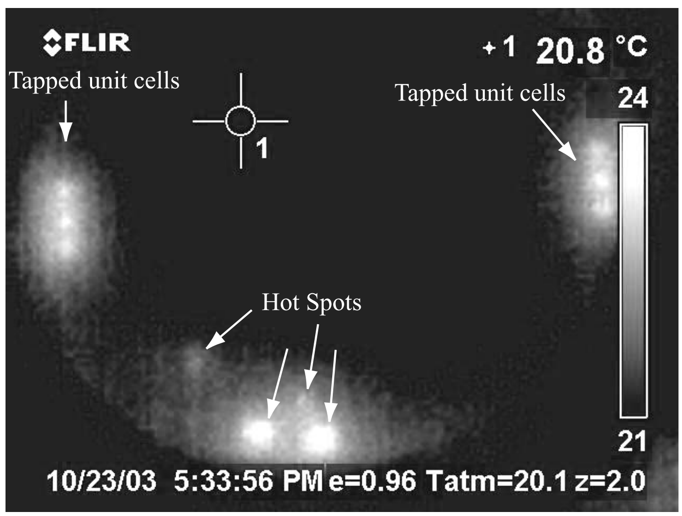


**Figure 5.21: Photograph of the FSS with an infrared camera with applied DC-current. Unwanted DC-connections between ground plane and inner elements are visible as warm spots.**

## 5.7 Measurement Setup

FSSs are generally measured either by illuminating a large sample with a plane wave in an anechoic chamber, or by placing a small sample in a waveguide and measuring the S-parameters. The first method obviously requires a large sample, and normally does not provide a way to measure the reflection coefficient. The waveguide technique can measure reflection, but it has two disadvantages. The cross-sectional dimensions of a standard waveguide are not generally integer multiples of the FSS grid period $l_c$. Also, as the full metallic waveguide cannot carry a TEM mode, it cannot be used to measure the sample at normal or arbitrary angles of incidence.

An alternative approach is to use a free space measurement setup that simulates the guided system. Quasi-optical measurement systems have been used for this purpose by a number of researchers at 60-300 GHz [108,109]. But the required lens/mirror size and focal length prove impractical in the the $Ka$-band. Based on the hard-horns developed by Ali *et al.* [110], a guided measurement system can be developed to simulate an oversized parallel-plate waveguide. Hard-horns are antennas with nearly uniform aperture distribution, which are formed by dielectric loading of the metallic pyramidal horns. A specially designed dielectric lens is used at the aperture to compensate the spherical phase error across the aperture. The hard-horns act as a matched transition between the coaxial terminals and the oversized TEM waveguide ports. The sample under test can be sandwiched between two of these waveguide ports, to form a guided system with coaxial ports. This system has been successfully used for excitation and measurement of $Ka$-band quasi-optical amplifier arrays [111]. Although for this application it is impractical to sandwich the FSS sample between the two hard-horns, due to the loading effect of the dielectric lenses, still the hard-horns can be used to form a quasi-guided system. In the modified system (Figs. 5.22 and 5.23), the hard horns form two parallel TEM ports that are separated by an air gap of 80 mm, and the sample under test is placed in the middle of the two ports. Due to their high directivity, the hard-horns are expected to generate a good approximation of the plane wave in the near-field, as is required for the FSS measurements. As the sample can be freely reoriented in the air gap, the quasi-guided system proves convenient for performing measurements at arbitrary angles of incidence.

Since the electromagnetic field in the gap region is assumed to be predominantly TEM, the air gaps between the hard-horn apertures and the surface of the sample can be treated as transmission-line sections. This allows for a standard TRL (Thru-Reflect-Line) calibration of the measurement setup, which simultaneously de-embeds the connecting cables, hard horns, and the air gaps from the measurement [112]. Also, a time-gating process with a gate width of 2 ns is applied to filter out the residual error due to the multiple reflections of the high-order modes.

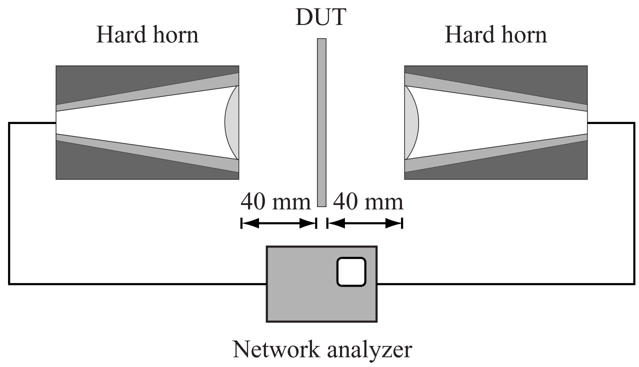


**Figure 5.22: The free-space measurement system using hard horns [110].**

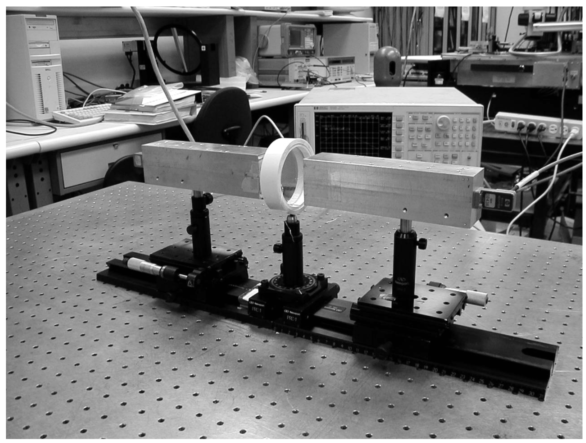

**Figure 5.23: Photograph of the quasi-optical measurement setup.**

## 5.8 Measurement Results

Due to the scattering at the edge of an actual circuit, an FSS is only an approximation of an infinite periodic structure. Therefore, the S-parameter measurements of the FSSs are specific to the size of the circuits and the measurement setup. With the method described above, edge effects are minimized and the scenario of an incident plane wave is reasonably well approximated. However, for large angles of incidence, the effective area of the FSSs is reduced and the results are somewhat qualitative. The dynamic range of the measurement using TRL-calibration is better than 40 dB for both, co- and cross-polarized components, at 30 GHz.

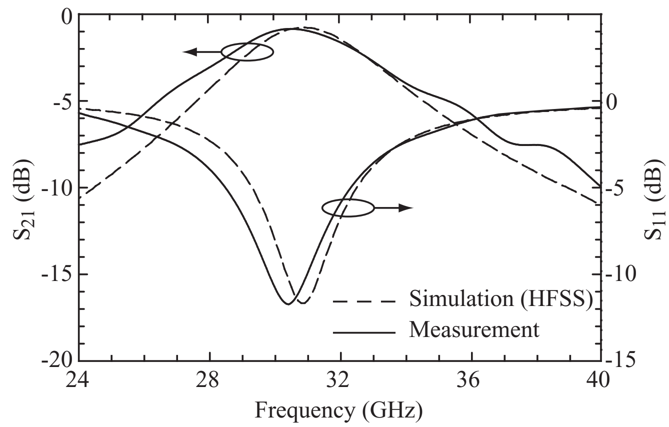


**Figure 5.24: The measured and simulated S-parameters (HFSS) of the FSS with fixed frequency response for normal incidence.**

### 5.8.1 FSS with Fixed Frequency Response

The measured S-parameters of the FSS with fixed frequency response in comparison with the simulated (HFSS) results are shown in Fig. 5.24. The resonance frequency is 30.5 GHz with an insertion loss of 0.83 dB and a reflection coefficient of −11.7 dB. The −1 dB bandwidth is 3.2 GHz and the −3 dB bandwidth is 6.6 GHz and agrees well with simulations. The deviation of 0.5 GHz in resonance frequency can partly be explained by an inaccuracy in the dielectric constant of the substrate which is introduced either by the available data or by the simulation tool [113].

The insertion loss is also measured for oblique angles of incidence. The transmission coefficient for incident TE-waves is shown in Fig. 5.25(a). It is seen that the resonance frequency and the −3 dB bandwidth do not change versus the angle of incidence. For large angles of incidence, the insertion loss increases by 3.3 dB (at 50°) and is partly explained by the decreased effective area of the FSS. With incident TM-waves (Fig. 5.25(b)), the frequency response essentially remains constant. The resonance frequency and the −3 dB bandwidth are unchanged, and only at an angle of incidence of 50° does the insertion loss increase by about 1.5 dB. The measured cross-polarization for different angles of incidence is excellent for all angles of incidence (Fig. 5.26).

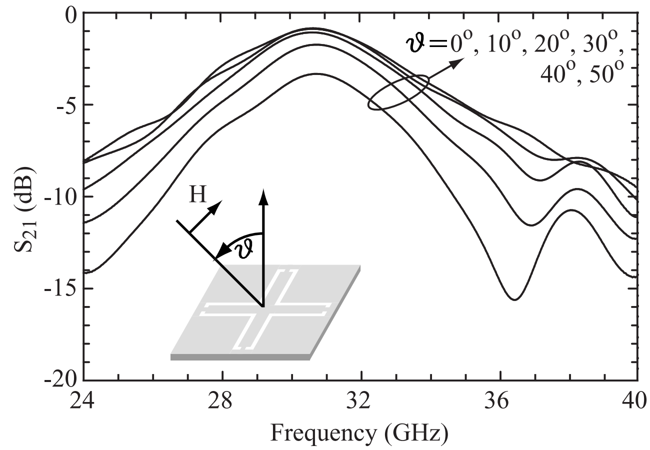


(a)

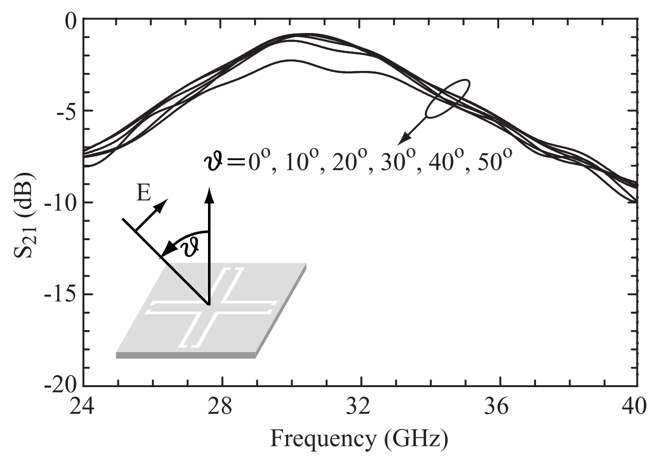


(b)

**Figure 5.25: The measured transmission coefficient of the FSS with fixed frequency response for oblique incidence: (a) TE-waves and (b) TM-waves.**

### 5.8.2 Switchable RF MEMS FSS

The transmission and reflection coefficients of the switchable FSS with bridges in the up-state position for normal incidence are presented in Fig. 5.27. The resonance frequency is 30.2 GHz with an insertion loss of 2.0 dB and a reflection of −11.5 dB. The −3 dB bandwidth

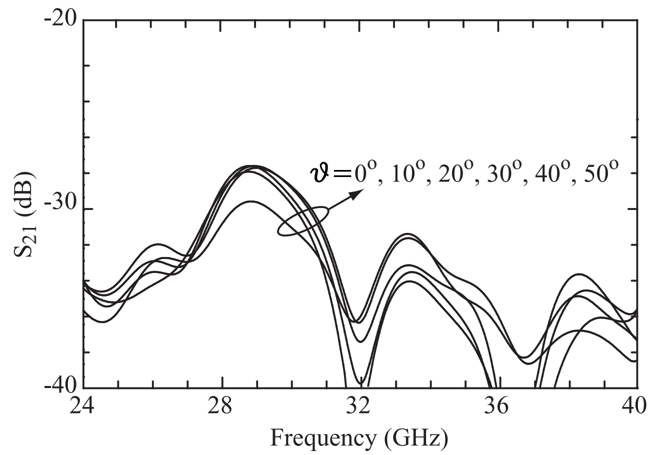


**Figure 5.26: The measured transmission coefficient for the cross-polarized component of the FSS with a fixed frequency response for normal and for oblique incidence.**

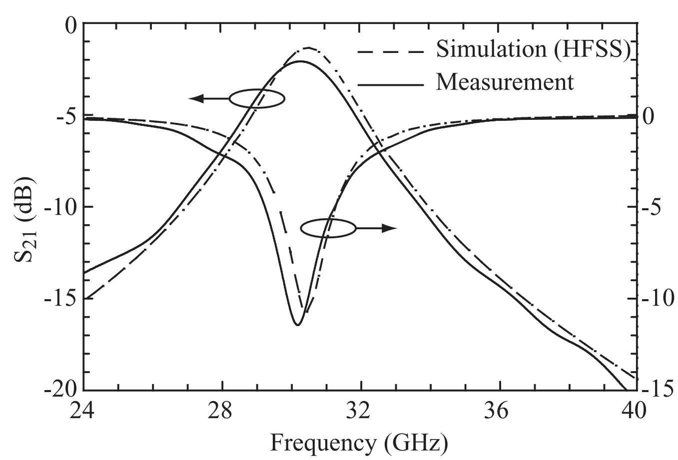


**Figure 5.27: The measured and simulated S-parameters (HFSS) of the switchable FSS versus frequency, with no applied voltage.**

is 3.2 GHz. The increase in insertion loss compared to simulation can be explained by increased losses due to surface roughness and non-uniformity of the MEMS bridges over the whole circuit, which can cause a deviation in the resonance frequency of the single resonators. The latter is also likely to be the reason for the slightly increased $-3$ dB bandwidth. When applying a DC-bias voltage between 0 and 13 V, the resonance frequency

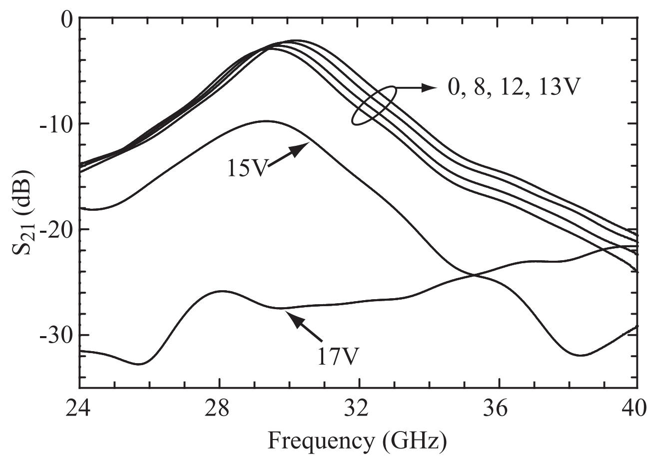


**Figure 5.28: The measured transmission coefficient of the switchable FSS versus frequency with different applied DC-bias voltage levels.**

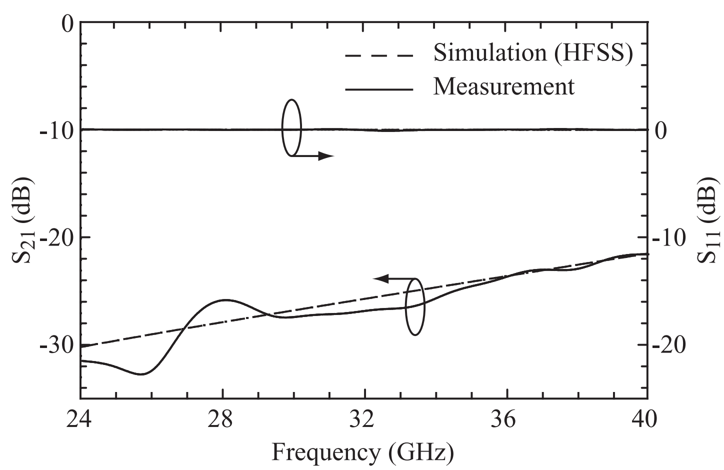


**Figure 5.29: The measured and simulated (HFSS) reflection coefficient of the switchable FSS versus frequency with applied DC-bias voltage of 17 V.**

is shifted to 29.4 GHz due to the increased capacitance of the loading bridges (Fig. 5.28). The corresponding transmission loss is increased to 2.9 dB while the −3 dB bandwidth remains constant. When the bridges are in the down-state position, which requires a DC-bias voltage of 17 V, the measured transmission coefficient is −27.5 dB at 30.2 GHz and the reflection is close to 0 dB, which agrees well with simulation (Fig. 5.29).

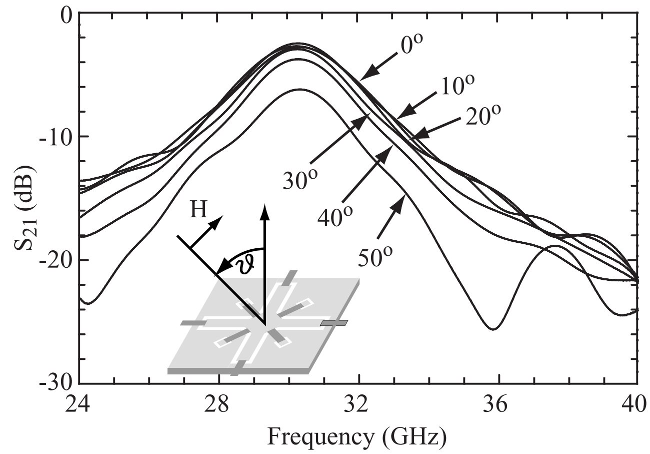


(a)

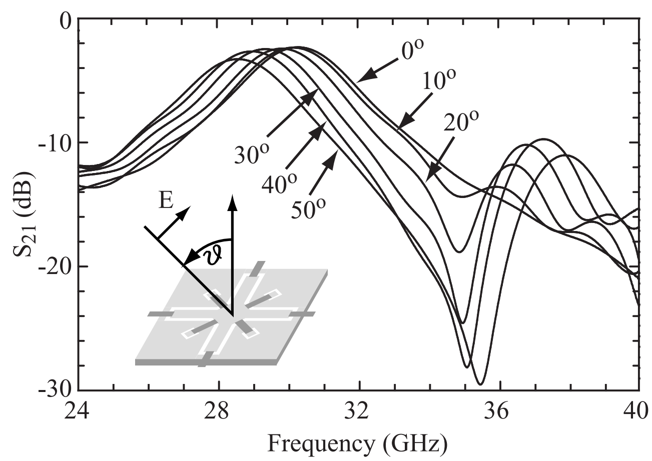


(b)

**Figure 5.30: The measured transmission coefficient of the switchable FSS versus frequency for different angles of incidence: (a) TE-waves and (b) TM-waves.**

The transmission coefficient for different angles of incidence is shown in Figs. 5.30(a) and 5.30(b). For orthogonal polarization of the electric field (TE-wave), the resonance frequency is stable versus angle of incidence and the $-3$ dB bandwidth is reduced only slightly to 2.9 GHz at an angle of incidence of $50°$. The measured transmission loss increases

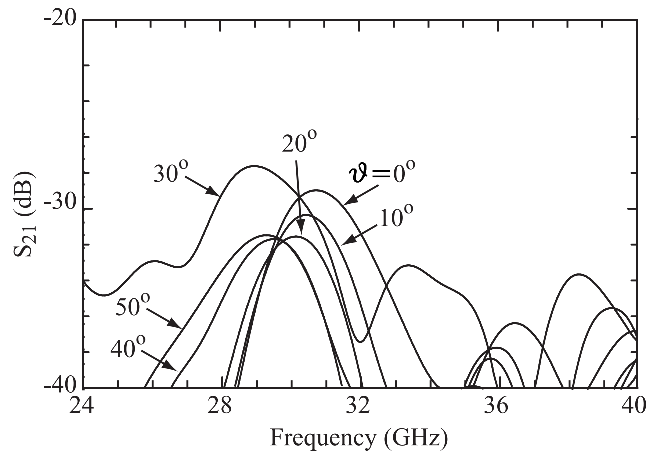


**Figure 5.31: The measured transmission coefficient for the cross-polarized component of the switchable FSS for normal and for oblique incidence.**

to 3.7 dB and 6.2 dB at an angle of incidence of 40° and 50°, respectively. For parallel polarization (TM-waves), the resonance frequency is shifted to 28.6 GHz at an angle of incidence of 50° and the transmission loss is increased to 3.3 dB, while maintaining a −3 dB bandwidth of 3.2 GHz. The reason for the shift in frequency is a transmission minimum at 35 GHz which becomes more prominent with increasing angle of incidence. The measured cross-polarization level for normal incidence is below −29 dB and is below −27 dB for all measured angles of incidence from 24 to 40 GHz (Fig. 5.31).

As a measure of the uniformity of the RF MEMS and a proof of the independence of polarization, the transmission coefficient for normal incidence is measured for different angular orientation of the FSS. It is observed that the transmission coefficient changes only by ±0.05 dB for a full 360° turn of the FSS.

### 5.8.3 Transmission Null for TM-Waves

The transmission zero for oblique angles of incidence for TM-waves is only observed in the switchable FSS and not in the FSS with fixed frequency response. Due to the small unit cell size compared to the wavelength and because the transmission zero is stable in frequency versus angle of incidence, it can neither be explained by substrate modes nor by

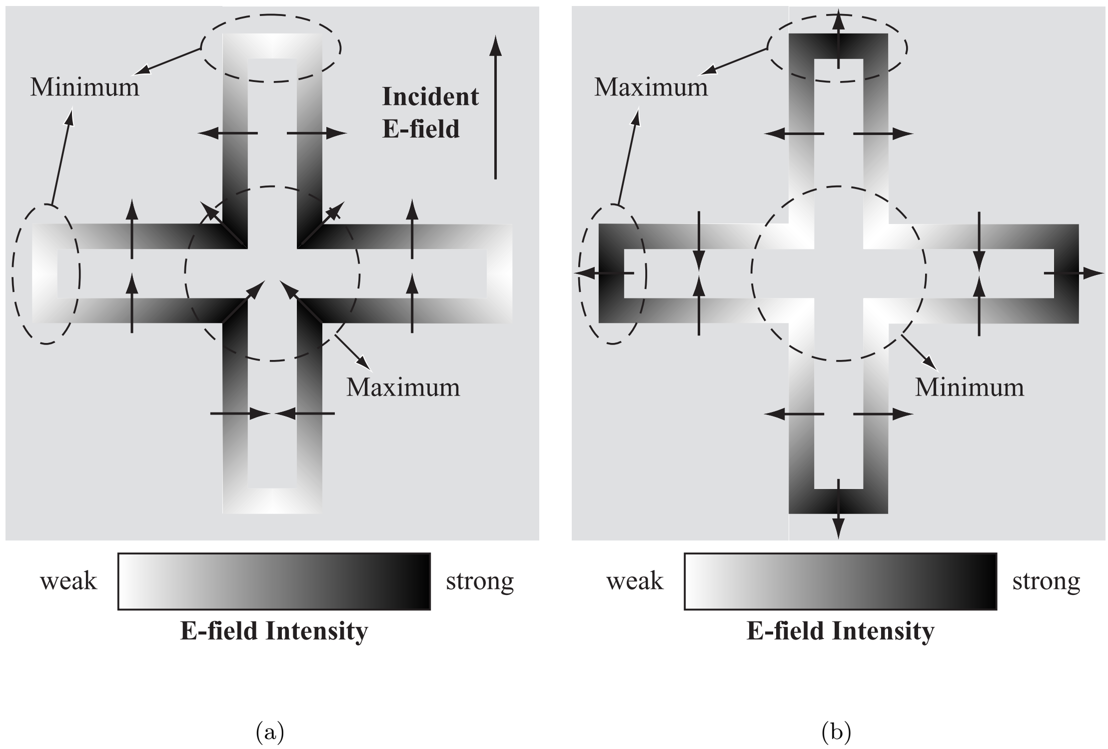


**Figure 5.32: The fundamental modes in the switchable FSS: (a) the single excited mode for normal incidence, (b) a second mode which is excited for oblique angles of incidence and TM-polarization.**

grating lobes.

The reason can be found when considering the modes in a unit cell of the switchable FSS. For normal incidence, PEC and PMC-walls force virtual grounds at the location of the bias bridges. The only fundamental mode that can exist is the mode with a voltage maximum at the location of the loading bridges and a voltage minimum at the location of the bias bridges (Fig. 5.32(a)). For vertical polarization, the electric fields in the horizontal "legs" are in even mode and cause radiation/transmission whereas in the vertical "legs", the electric fields are in a non-radiating odd mode. However, at oblique angles of incidence with parallel (TM-) polarization, no PEC-walls exist and a different mode shown in Fig. 5.32(b) can also propagate. This mode has a voltage maximum at the location of the bias bridges and a voltage zero at the location of the loading bridges. It does not radiate since the

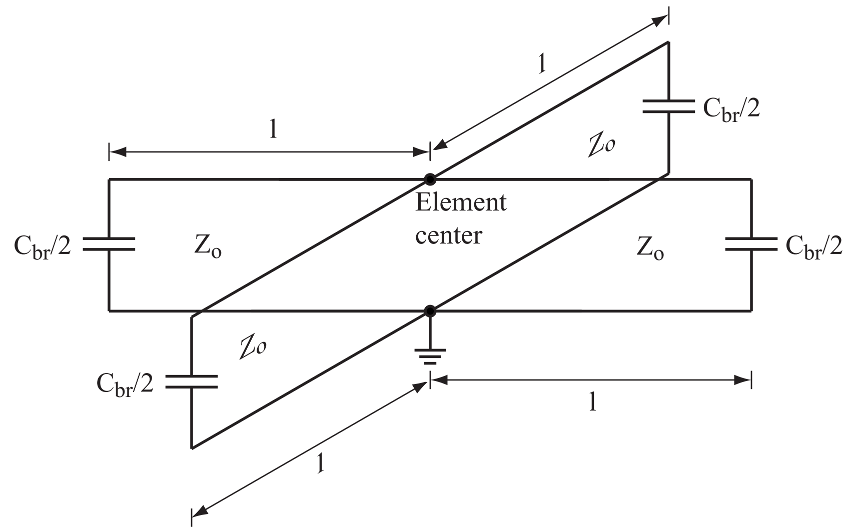


**Figure 5.33: Transmission line schematic of a single unit cell for the second propagating mode for oblique angles of incidence (TM-polarization).**

electric fields in the slot propagate in an odd mode in all "legs" and cancel each other in the far-field.

Based on the transmission line schematic of Fig. 5.33, the equivalent circuit model is extended to account for the additional propagating mode (Fig. 5.34). For the second mode, all four "legs" carry odd mode and are connected in parallel. This is represented by a single transmission line with a quarter of the corresponding impedance of a single transmission line stub. The PEC symmetries do not hold for this mode. Therefore, the transmission lines are connected to ground through the capacitance of the bias bridges, $C_{bias} = 75$ fF. For symmetry reasons, only half of $C_{bias}$ is effective for each transmission line. The bridge capacitances, $C_{up}$, and the compensation capacitance, $C_{comp}$, have no effect because they are connected across a voltage minimum. The transformer ratio for the new mode, $n_3$, depends on the angle of incidence, and is 0.14 to match the measurement for 30° (Fig. 5.35).

An easy way to avoid the existence of the unwanted mode close to the mid-band frequency is to avoid the air gap of the bias circuitry and design the bias bridges as MIM (metal-insulator-metal) capacitors. This will have no effect on the fundamental transmitting mode, but will increase the capacitive loading of the unwanted mode and will shift the

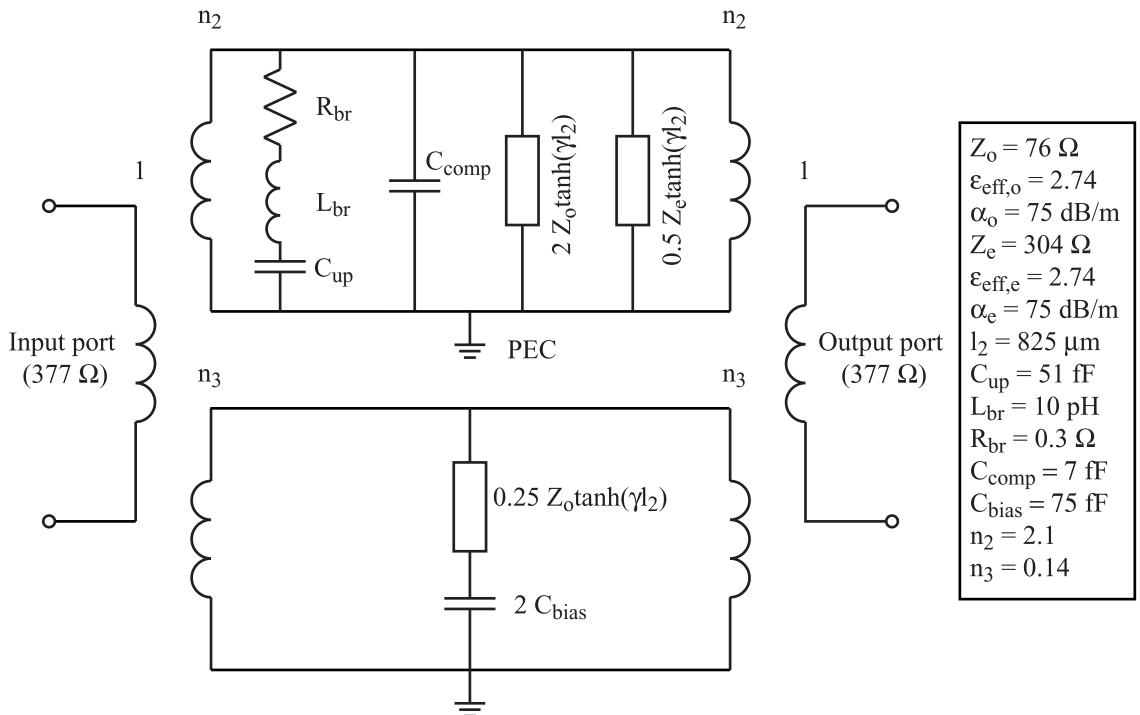


**Figure 5.34: The equivalent circuit model of the switchable FSS for oblique angles of incidence (TM-polarization).**

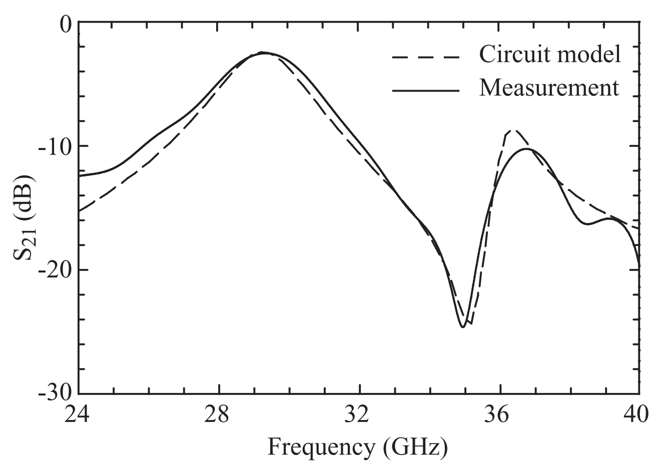


**Figure 5.35: The measured and simulated (circuit model) transmission coefficient of the switchable FSS for an angle of incidence of 30° (TM-polarization) using the model of Fig. 5.34.**

resonance frequency below 10 GHz.

## 5.9 High Power Considerations

As a distributed circuit, the FSS has the potential of handling high RF powers. However, simply multiplying the power handling capabilities of a single MEMS switch in a transmission line by the number of switches implemented in the FSS will lead to wrong results, since this is a resonant structure and not a bridge in a 50 Ω transmission line.

### 5.9.1 Failure Mechanisms due to High RF Power

There are different failure mechanisms due to high incident RF-power. The RF-power can cause actuation of the MEMS bridges when they are in the up-state position or hold the MEMS bridges permanently in the down-state position and prevent release. The current density in the bridges can also be too high in either the up-state or down-state position. Thermal destruction can occur due to the finite thermal conductivity in the membranes. The transmission loss in transmit-mode can cause thermal destruction of the overall circuit. In the following, each single failure mechanism is treated individually.

Pull-down due to RF-power: The FSS is a filter and therefore, a standing wave in the resonator leads to higher voltage levels than in a 50 Ω transmission line circuit. A one-pole filter equivalent circuit with a parallel $RLC$ resonator is shown in Fig. 5.36. The external loading impedances $R_s$ and $R_l$ are the characteristic impedance of free space, $120\pi$ Ω, and $R_r$ is the parallel resistance of the resonator. The transformer ratio, $n$, at the input and output port is assumed equal because the thickness of the FSS is much smaller than a wavelength. The loaded quality factor, $Q_l$, is given by:

$$Q_l = \frac{\omega_0}{\omega_{-3dB}} \tag{5.6}$$

and is 9.4. The unloaded quality factor, $Q_u$, is then 44.8 using:

$$Q_u = Q_l(1 - S_{21}) \tag{5.7}$$

and the external quality factor, $Q_{ext}$, is determined using:

$$\frac{1}{Q_l} = \frac{1}{Q_u} + \frac{1}{Q_{ext}} \tag{5.8}$$

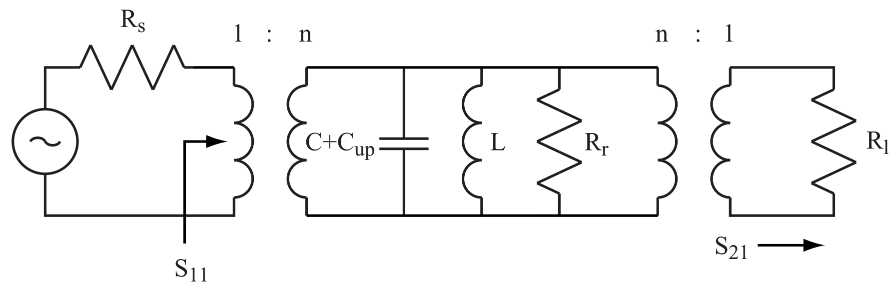


**Figure 5.36: One-pole RLC band-pass filter configuration with external loading.**

and is 11.9. Knowing that $C_{up}$ = 50 fF, the values for $L$ and $C$ can be found using (5.1) and (5.2) where $f_0$ is determined through HFSS simulations to be 52 GHz. This results in $L = 369$ pH and $C = 25.4$ fF. $R_r$ is found using:

$$Q_u = \omega_0 R_r (C + C_{up}) \tag{5.9}$$

and is 3.13 kΩ. The transformer ratio can be found using:

$$Q_l = \omega_0 R_{tot} (C + C_{up}) \tag{5.10}$$

with $R_{tot}$ being defined by:

$$R_{tot} = n^2 R_l \| R_r \| n^2 R_l \tag{5.11}$$

and is 2.1. With a maximum allowable RF voltage in the slotline of $V_{rms} = V_{pull-down}$ before self-actuation occurs, the input voltage, $V_{in}$, is limited to $V_{rms}/n$. Using:

$$P_{inc,max} = \frac{V_{in}^2}{R_s} = \frac{V_{rms}^2}{n^2 R_s}, \tag{5.12}$$

where $V_{pull-down}$ = 13 V, the maximum incident power per bridge, $P_{inc,max}$, is 102 mW, which results in an overall maximum input power of 370 W.

Hold-down due to RF-power: The hold-down voltage for MEMS bridges is considerably lower than the pull-down voltage (2-5 V). However, when the bridges are in the down-state position, no standing wave is induced in the resonator at $f_0$, and (5.12) does not apply in this case. Also, when the MEMS bridges are in the transition from the down-state to the up-state position, the capacitive loading due to the membrane is reduced quickly which leads to an increased voltage level across the bridge which tends to pull the bridge back to the down-state position. An equilibrium height will be achieved, which balances the mechanical pull-up force and the pull-down force due to the RF voltage at the bridge. For a thorough investigation an exact electromechanical model is necessary. An estimation of the maximum input power before hold-down occurs is found experimentally (Section 5.9.2).

<u>Current density on the RF MEMS bridge</u>: Current in MEMS shunt bridges is mostly carried on the edges as shown in [114]. This leads to current densities which can exceed the value for the critical DC-current density (0.5-1 MA/cm$^2$ for gold). However, no reliable data is available for the critical AC-current at microwave frequencies. According to observations made at the University of Michigan, 8,000 Å thick MEMS bridges can easily carry more than 400 mA of AC-current at 10-50 GHz. Based on this finding and according to [68], the induced current density in the MEMS bridges in the up or down-state position is not a limiting factor for the power handling of the switchable FSS and is not investigated further.

<u>Thermal destruction of the MEMS membrane due to series resistance</u>: Heat generation in the membranes is due to the finite conductivity of the gold membrane. In [68,98], however, it was found that this is not a predominant effect and it is not investigated further.

<u>Thermal destruction due to transmission loss</u>: The maximum allowable temperature for the FSS is about 80°C since for higher temperatures, the membranes start to deform and the performance of the circuit is affected. In the up-state position, the measured transmission coefficient is $-2.0$ dB or 63% of the power is transmitted. With a reflection coefficient of $-11.5$ dB (7% is reflected), this means that 30% of the incoming power is absorbed by the FSS, and leads directly to an increase of the overall temperature of the FSS.

Since the aspect ratio of the circuit is very high (76.4 mm wide, 0.5 mm thick), the FSS can be treated using a one-dimensional thermal model as shown in Fig. 5.37. The temperature gradient across the thickness of the glass wafer is very small because of the thin wafer used, and therefore it can be accurately assumed that the power is dissipated uniformly over the whole substrate. If the substrate is not thermally grounded at the edges, the governing equation is (steady state analysis):

$$\frac{Q_a}{2} = h\Delta T \tag{5.13}$$

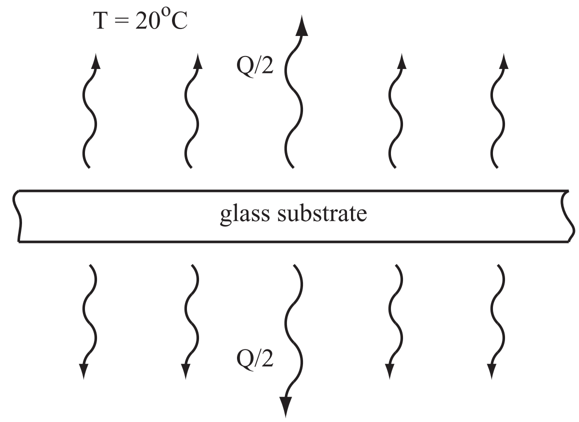


**Figure 5.37: One-dimensional heat transfer model for the switchable FSS.**

where $Q_a$ is the dissipated power per unit area [W/m$^2$], $h$ is the convective heat transfer coefficient per unit area [W/(K m$^2$)], and $\Delta T$ is the temperature difference between the circuit and the environment. Values for $h$ are empirical and range from 2 to 25 for natural airflow and from 25 to 250 for forced airflow [115]. Fig. 5.38 shows the relationship between $h$ and the maximum incident power on the FSS for a maximum temperature of 80°C ($\Delta T =$ 60°C) and an ambient temperature of 20°C. For an incident power of 25 W, the total dissipated power in the FSS is 7.5 W, $Q_a = 1.64$ mW/mm$^2$ and $h$ needs to be greater than 15. For a heat transfer coefficient of 100, which requires active air cooling, the incident power cannot exceed 180 W (54 W absorbed power).

The validity of the one-dimensional model is confirmed with a two-dimensional simulation using Matlab [107]. Fig. 5.39 shows a cross-section of the FSS and the temperature distribution with and without heat sink at the edge. The convective heat coefficient is 15 and the incident power is 25 W (7.5 W absorbed power). As predicted, the maximum temperature in the center of the circuit is close to 80°C in both cases. This means that for the fabricated circuit, a heat sink at the edge of the FSS does not improve the power handling capabilities.

If the applied incident power is only for a short period of time $t$, the thermal behavior can be approximated with:

$$\Delta T = \frac{Q_v t}{c\rho} \tag{5.14}$$

where $c = 0.81$ J g$^{-1}$ K$^{-1}$ is the specific heat capacity of glass, $\rho = 2.23$ g cm$^{-3}$ is the

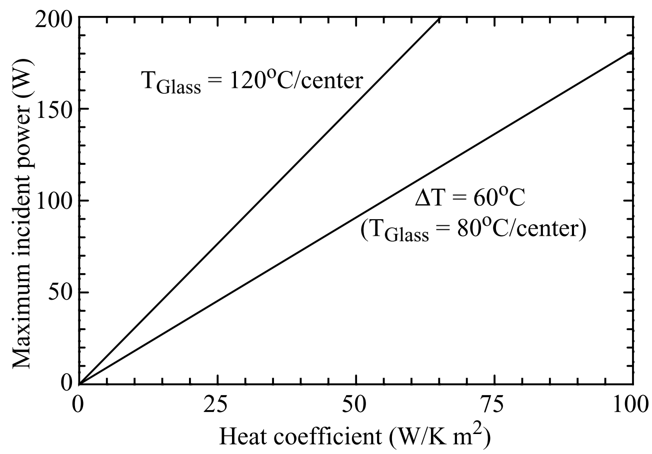


**Figure 5.38: Maximum incident power on the switchable FSS versus heat coefficient for an ambient temperature of 20°C.**

density of glass, and $Q_v$ is the dissipated power per volume. The maximum incident power is inverse proportional with time and for an exposure time of 1 s, it is 819 W (246 W absorbed power).

Summary: For a continuous wave operation, the power handling of the fabricated FSS is limited by the increased temperature of the overall circuit due to absorbtion and is about 25 W if no air cooling is available. For short pulses of incident power, the power limit is set by the self-actuation due to RF power and is 370 W. In these considerations it is assumed that the incident power is distributed evenly across the FSS.

### 5.9.2 High Power Experiment

The high power measurement setup is shown in Fig. 5.40. A 30.2 GHz signal is amplified and the power level is controlled by a tunable attenuator. The amplifier is a travelling-wave tube amplifier with a maximum output power of 50 W continuous wave. The same hard horns as for the S-parameter measurements are used to illuminate the FSS and receive the transmitted signal. The FSS is tilted by 15° to prevent the reflected signal from being fed back into the power amplifier but to direct it onto a large foam absorber, thus eliminating the need of a high power circulator. A −20 dB coupler is used in the transmit path to send part of the input power to a spectrum analyzer. The through port of the coupler is matched

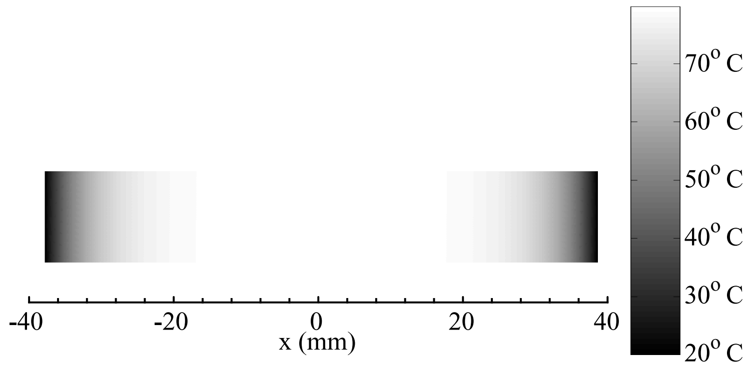


(a)

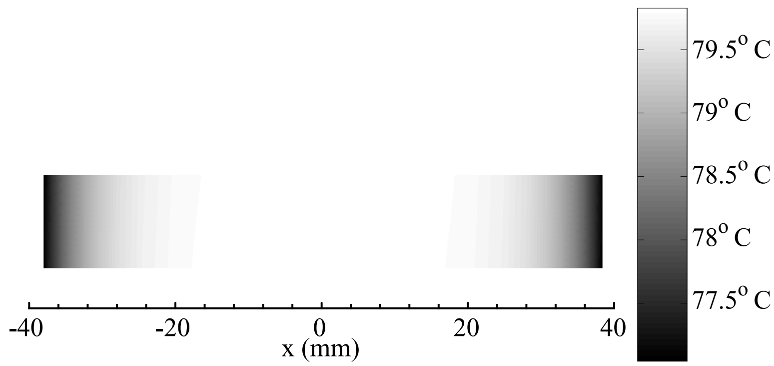


(b)

**Figure 5.39: Simulated (Matlab) heat distribution in a cross-section of the FSS with a convective heat coefficient of 15 W/(K m$^2$) and an incident power of 25 W (absorbed power of 7.5 W) (a) with and (b) without heat sink.**

with a horn antenna and the signal is radiated and absorbed by a large foam absorber, thus avoiding the need of a high power attenuator. Active air cooling for the FSS is provided by a fan.

The conducted experiment showed that for the fabricated switchable FSS, the maximum input power is 5 W for hot switching. With an input power of 10 W, some of the MEMS bridges are held in the down-state position, and for input levels greater than 20 W, self-actuation of some of the membranes due to RF power is observed. No destruction of the

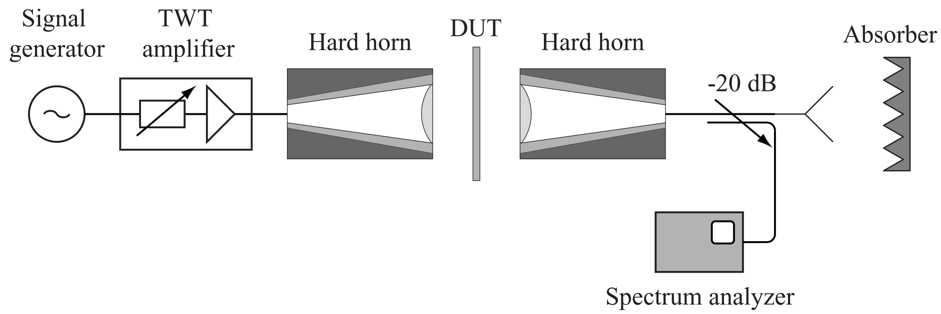


**Figure 5.40: The setup for the high power measurement.**

circuit is observed even for the maximum available input power of 50 W.

The difference between the measured (20 W) and calculated (370 W) power level for self-actuation can partly be explained by the non-uniform illumination of the FSS. The aperture of the hard horns is about half in area as the switchable FSS. This results in a power density in the center of the FSS which is 4 times as high as with uniform illumination. Combined with the field variation across the aperture of the horn antennas of $\pm 1$ dB, this leads to local power densities of roughly 5 times compared to uniform illumination. The self actuation of MEMS bridges at an input power of 20 W, however, can only be explained assuming that the pull-down voltage was decreased due to thermal expansion of the membranes.

The experiment shows that for the measured switchable FSS the power limit for hot switching is set by the hold-down voltage and is about half of the self-actuation level when the bridges are in the up-state position.

# CHAPTER 6

# Conclusions and Future Work

## 6.1 Antennas for Automotive Radars

The objective of this thesis is to develop antenna systems for automotive radar applications at 24 and 77 GHz which combine good performance (in particular a sidelobe level of below $-14$ to $-20$ dB) with wide scan-angle (up to 180°), compactness, and low cost of production.

Tapered-slot antennas (TSAs) are used as feed antennas to a single homogeneous spherical Teflon lens. This is a comparably low-cost solution and due to the small physical cross-section of the feed antennas, a very wide field of view is possible. A homogeneous sphere does not have a uniform focal point for center and off-axis rays. However, for a diameter of up to 30 - $40\lambda_0$, a Teflon sphere is well suited as a lens at microwave and millimeter wave frequencies.

The design of TSAs on RT/Duroid 5880 substrate which are suitable for such an antenna lens system is presented in Chapter 2. For close spacing around the spherical lens, the aperture is $0.7\lambda_0$ and for compactness, the length is minimized modifying a design first demonstrated by Sugawara *et al.*. To feed the TSAs, microstrip line-to-slotline transitions for different substrate thicknesses at 24 and 77 GHz are developed. With the designed TSAs, an array with low gain and no lens is demonstrated with the potential of 360° field of view.

In Chapter 3, the dependence of sidelobe level, directivity, and efficiency on the feed location is investigated in simulation (in collaboration with X. Wu and G.V. Eleftheriades at the University of Toronto, Canada) and experiment. For a Teflon lens, the best feed point lies 0.4-0.52$R$ outside the sphere. The maximum achievable gain is around 38 dB. Using a lens with a radius of $6.42\lambda_0$ at 77 GHz (25 mm), a sidelobe level of $-20$ dB and a gain of 29.4 dB is demonstrated which corresponds to an efficiency of 49%, not taking the losses in the TSA into account Also, antenna arrays using a spherical Teflon lens are designed at 24 and 77 GHz with a scan-angle of up to 180° while maintaining a low sidelobe level of $-16$ to $-20$ dB. The size of this multibeam antenna design is reduced using a hemispherical Teflon lens with backside metallization instead of a sphere (Chapter 4). Furthermore, the feed antennas for 24 and 77 GHz are integrated into a single aperture, using frequency-selective surfaces (FFSs), thus increasing further the compactness.

## 6.2 Switchable FSS

*In a related project, this thesis demonstrates the first RF MEMS switchable frequency-selective surface.* A polarization independent FSS using four-legged loaded elements is designed using 2.5 and 3-dimensional electromagnetic solvers and equivalent circuit models. High resistivity bias lines are avoided by connecting the elements through air bridges. The impact of the bias circuitry for normal and oblique incidence is explained and the loading MEMS bridges are placed accordingly.

An FSS consisting of 909 unit cells with 3,636 movable membranes is built on a 3" glass wafer using standard micromachining processes. The measured insertion loss at 30.2 GHz in midband is 2.0 dB in transmit mode (bridges up) and 27 dB in reflection mode (bridges down). For parallel polarization and at large angles of incidence, a transmission null close to the resonance frequency for oblique angles of incidence is observed, explained by a circuit model, and an easy solution to avoid this undesired behavior is proposed. The FSS can also be tuned in an analog fashion with a pass-band center frequency of 30.2 to 29.4 GHz. The power handling of the switchable FSS is estimated to be >60 - 100 W before any of the bridges is actuated by the RF power for $V_p$ = 20 - 30 V, or before any thermal limits are reached at the center of the array with active air cooling provided.

## 6.3 Antennas for Automotive Radars: Future Work

### 6.3.1 Low-Gain 360° Array without Lens

The presented measurements of a 180° TSA array without lens indicate that a compact, low-cost, reliable array with 360° field of view can be built (Section 2.6). The coupling of the closely spaced feedlines near a SPNT switch could not be measured since no SPNT switch was available at the time, and this should be investigated in the future. Permitting a suitable fabrication process, a way to keep the coupling near the switch to a minimum is to use CPW feedlines. The electric fields in CPW lines are much more confined than in microstrip lines and the line dimensions can be made significantly smaller. Also, for a transition from CPW line-to-slotline, a 90° bend in the CPW line is not necessary [116]. This reduces coupling through substrate waves and allows for an even more compact design of the array. It should be investigated if the size of the circuit and the coupling through the substrate waves can be reduced in a similar way by using a uniplanar microstrip line-to-slotline transition [117].

### 6.3.2 Ellipsoid of Revolution as Lens

In automotive radars, often, especially for long range applications, different beamwidths are desired in azimuth and elevation. The azimuth beamwidth limits the angular resolution for obstacles on the ground. The choice of elevation beamwidth is important for changes in the slope of the surface or to avoid false alarms which are caused e. g. by holes in the surface of the road.

In general, the beamwidth of an antenna in a certain plane is determined by its physical dimension in that plane. For different beamwidths in the azimuth and elevation, the spherical lens has to be replaced by an ellipsoid of revolution. However, the optimal feed location has to be maintained for both, azimuth and elevation. For a $-10$ dB beamwidth of the feed pattern, the optimum radiation patterns are achieved for a distance of $d = 0.40$ - $0.52R$ between the feed antenna and the Teflon lens. Therefore, it is clear that the ratio between the radii of the ellipsoid lens cannot be more than 1.3. The half-power beamwidth is indirectly proportional to the aperture dimension, and therefore, as an example, for a

$-3$ dB beamwidth in azimuth of 2.8°, the $-3$ dB beamwidth in elevation has to be within 2.2 and 3.6°. Moreover, the shape of the lens for the H-plane pattern is not a circle anymore. Therefore, it has to be investigated how well an ellipsoid lens is suited as a microwave and millimeter wave lens.

## 6.4 Switchable FSS: Future Work

### 6.4.1 Analog Frequency Tuning

For bias voltages less than the pull-down voltage, the height of an RF MEMS bridge is decreased and the capacitance is increased. This can be used for analog frequency tuning of an FSS (Section 5.8.2). However, due to the instability point at 2/3 of the original bridge height, the theoretically achievable capacitance ratio is only 1.5 and practically 1.2 - 1.25 [118]. The bridge capacitance is part of the resonant LC-circuit and in order to achieve highest frequency tuning, the bridge capacitance has to be as much of the overall capacitance as possible. This means that the up-state capacitance has to be large which makes the unit cell small. Still, the tuning range is limited to $\sqrt{1.2}$ - $\sqrt{1.25}$ which is around 10 - 14%.

To achieve higher tuning range, varactors with high tuning ratio are needed. In the recent years, tuning ratios of more than 300% have been demonstrated [119–121]. However, all of the presented designs require separate electrodes for actuation. These additional electrodes can be addressed only by an additional bias network with bias lines running underneath or on top of the ground metal, and the probability of DC-shorts and thus failure of the tunable FSS is greatly increased.

### 6.4.2 Digital Frequency Tuning Using Series Capacitances

The tuning between 2 discrete resonance frequencies can be achieved with RF MEMS bridges with small (2-3) capacitance ratio between up and down-state position, as opposed to the design presented in Chapter 5 with a capacitance ratio of around 1:20. This could be achieved with small bridge height and a thick dielectric layer with small $\varepsilon_r$ underneath the membrane. However, the capacitance in the down-state position is highly dependent

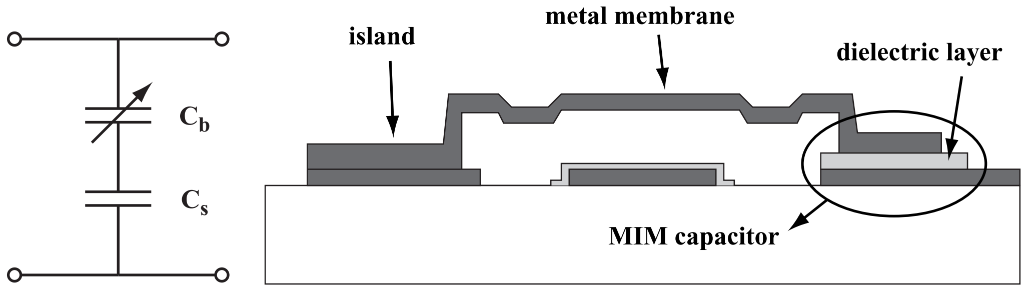


(a) (b)

**Figure 6.1: Circuit model (a) and realization of an MIM-capacitor in series with an RF MEMS bridge (b).**

on the surface roughness of the dielectric layer as well as the metal membrane and is very hard to control. Therefore, a better solution is the use of a lumped capacitance in series with each bridge (Fig. 6.1(a)) . The total load capacitance ($C_l$) is the series combination of the switch capacitance ($C_b$) and the lumped capacitance ($C_s$) and is:

$$C_l = \frac{C_s C_b}{C_s + C_b}. \tag{6.1}$$

If any of $C_s$ and $C_b$ is much larger than the other, $C_l$ is approximately equal to the smaller of $C_s$ and $C_b$. If well designed, the resulting capacitance is approximately $C_u$ when the bridge is in the up-state position and $C_s$ in the down-state position. $C_s$ can be realized as MAM (metal-air-metal) or MIM (metal-insulator-metal) capacitance which is easy to control (Fig. 6.1(b)).

### 6.4.3 Digital Frequency Tuning Using Different Spring Constants

The pull-in voltage for a fixed-fixed beam is dependent on the spring constant $k$ and is given by [118]:

$$V_p = \sqrt{\frac{8k}{27\varepsilon_r W w} h_0^3} \tag{6.2}$$

with $h_0$ being the original bridge height and $W$ and $w$ the dimensions of the pull-down electrodes. Fig. 6.2(a) shows different bridge configurations with different $k$. By imple-

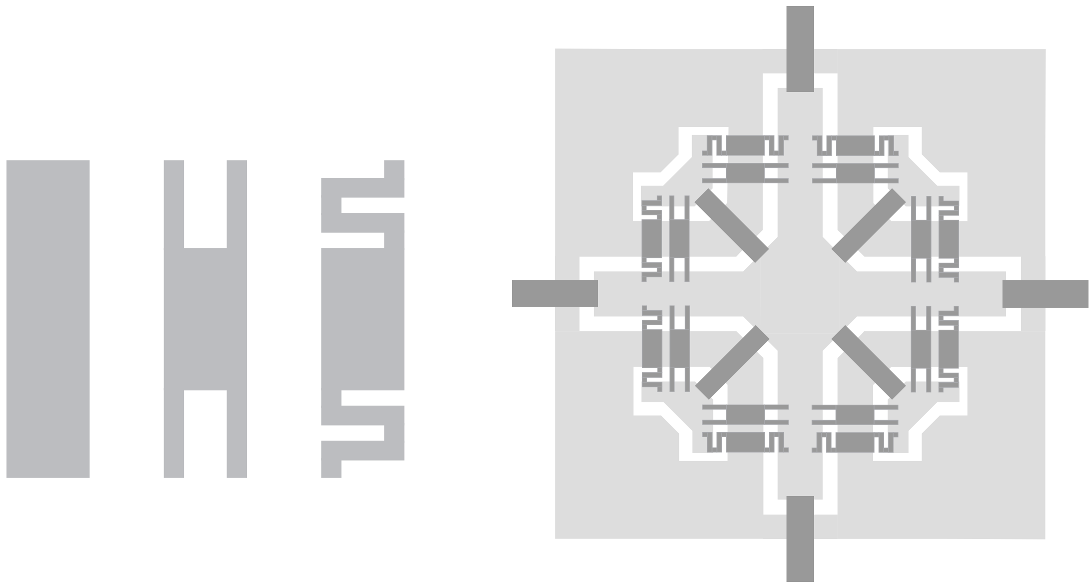

(a) (b)

**Figure 6.2: RF MEMS bridges with different spring constant $k$ (a) and an example of an FSS unit cell using membranes with different $k$ for digital frequency tuning (b).**

menting loading membranes with different $k$ in one unit cell, e. g. as shown in Fig. 6.2(b), the loading of the element can be controlled by the amount of bias voltage applied. With increasing bias voltage, first the membranes with low $k$ will be actuated, thus increasing the capacitive loading of the element, and then successively the ones with higher $k$. The amount of capacitive loading can be controlled by the location and the dimensions of the membranes and a series MIM or MAM capacitance as described in Chapter 6.4.2.

With this method, however, the power handling capability of the FSS is considerably reduced due to the decreased pull-down and hold-down voltages for lower spring constant.

### 6.4.4 Switchable Multilayer FSS

Often, FSSs are designed as multilayer structures to improve independence of angle of incidence and to achieve a multipole filter response with flat pass-band and steeper roll-off. The FSS presented in Chapter 5 can easily be extended to a multilayer circuit with switching capabilities. One possibility is to build all periodic layers with identical switching capabilities. Special care has to be taken for the layers that are included between dielectric layers in a circuit with more than 2 layers. A cavity of at least a few micrometers in height has to ensure that the RF MEMS bridges are freely moveable. Another way is to implement in only 1 periodic layer tuning elements and all other layers have a fixed frequency response. With actuated MEMS bridges, the entire circuit will be reflective, even if all other layers are still transparent. However, for a good filter design, special care has to be taken because the external loading of the switchable layer is changed by the RF MEMS.

### 6.4.5 Tunable Multilayer FSS

Multilayer FSSs are spatial multipole filters. In multipole filters, the resonators are connected through (K or J) impedance inverters which can be realized with lumped capacitances or inductances, or like in FSSs with $\lambda_g/4$ transmission lines. The $\lambda_g/4$ transmission line is realized by the dielectric layers which separate the periodic layers. However, the inverter properties of a $\lambda_g/4$ transmission line are rather narrow-band in nature and therefore, the tuning range of multilayer FSSs is limited. For a wide tuning range, a compromise in the performance has to be found. Fig. 6.3 shows the simulated (Method of Moments) transmission coefficient of a 2-pole tunable FSS which can be tuned from 30 to 44 GHz. The two FSS layers are similar to the switchable FSS in Chapter 5. The length of the "legs" is 600 μm and the loading capacitance is 108 fF and 40 fF for a resonance frequency at 30 and 44 GHz, respectively. In a digital design, this can be realized with an up-state capacitance of 60 fF and a series capacitance of 120 fF. Using (6.1), for an error of the loading capacitance of $\pm 2\%$, the down-state capacitance of the membrane has to be between 897 and 1343 fF. The periodic layers are separated by a glass substrate ($\varepsilon_r = 4.6$) of thickness 1 mm which corresponds to $\lambda_g/4$ at 35 GHz. Due to the narrow-band nature of the $\lambda_g/4$ transmission line, the ripples in the pass-band are not less than 2 dB.

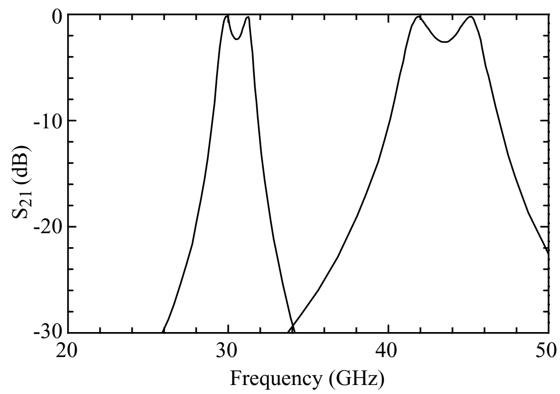


**Figure 6.3: Simulated transmission coefficient of a double-layer tunable FSS (not well tuned).**

### 6.4.6 Increasing the Power Handling

The power handling of the presented switchable FSS is limited by the self-actuation of the membranes in the up-state position (cold switching) or in the down-state position (hot switching). The power level for self-actuation in the up-state position depends on the pull-down voltage, $V_p$, which can be increased by increasing the bridge height, $h_0$, and with shorter and thicker membranes, thus increasing the spring constant, $k$. A pull-in voltage of 40 V is easily achievable. Moreover, when implementing series capacitances for digital frequency tuning, the pull-in voltage increases again because of the series division of the applied voltage. Therefore, the power limit due to self-actuation in the up-state position can easily be increased by a factor of 10.

The hold-down voltage depends on the spring constant of the MEMS membrane and the thickness of the dielectric layer, as well as its roughness. In practice, voltages up to 8 V are common [98]. Again, with series capacitances the hold-down voltage is increased due to the series division of the applied voltage.

# APPENDICES

# APPENDIX A

## Slotline and Microstrip Design Equations

Slotline design formulas [77]:

$$\begin{aligned}
Z_0 &= 60 + 3.69\,\sin\left(\frac{\varepsilon_r - 2.22\pi}{2.36}\right) + 133.5\,\ln(10\varepsilon_r)\sqrt{\frac{W}{\lambda_0}} \\
&+ 2.81\left[1 - 0.011\,\varepsilon_r\,(4.48 + \ln\varepsilon_r)\right]\frac{W}{t}\,\ln\left(\frac{100t}{\lambda_0}\right) \\
&+ 131.1\,(1.028 - \ln\varepsilon_r)\sqrt{\frac{t}{\lambda_0}} \\
&+ 12.48\,(1 + 0.18\,\ln\varepsilon_r)\frac{\frac{W}{t}}{\sqrt{\varepsilon_r - 2.06 + 0.85\left(\frac{W}{t}\right)^2}}
\end{aligned} \tag{A.1}$$

Microstrip line design formulas [77]:

$$Z_0 = \begin{cases} \frac{60}{\sqrt{\varepsilon_{r,eff}}}\,\ln\left(\frac{8t}{W_e} + \frac{W_e}{4t}\right); & \frac{W}{t} \leq 1 \\ 120\pi\left(\sqrt{\varepsilon_{r,eff}}\left[\frac{W_e}{t} + 1.393 + 0.667\,\ln\left(\frac{W_e}{t} + 1.444\right)\right]\right)^{-1}; & \frac{W}{t} \geq 1 \end{cases} \tag{A.2}$$

$$Z_0(f) = Z_0\,\frac{\varepsilon_{r,eff}(f) - 1}{\varepsilon_{r,eff} - 1}\sqrt{\frac{\varepsilon_{r,eff}}{\varepsilon_{r,eff}(f)}} \tag{A.3}$$

$$\frac{W_e}{t} = \begin{cases} \frac{W}{t} + \frac{1.25t_m}{\pi t}\left(1 + \ln\frac{4\pi \mathrm{W}}{\mathrm{t_m}}\right); & \frac{W}{t} \leq \frac{1}{2\pi} \\ \frac{W}{t} + \frac{1.25t_m}{\pi t}\left(1 + \ln\frac{2\mathrm{t}}{\mathrm{t_m}}\right); & \frac{W}{t} \geq \frac{1}{2\pi} \end{cases} \tag{A.4}$$

$$F = \begin{cases} \left(1 + 12\frac{t}{W}\right)^{-0.5} + 0.04\left(1 - \frac{W}{t}\right)^2; & \frac{W}{t} \leq 1 \\ \left(1 + 12\frac{t}{W}\right)^{-0.5}; & \frac{W}{t} \geq 1 \end{cases} \tag{A.5}$$

$$\varepsilon_{r,eff} = \frac{\varepsilon_r + 1}{2} + \frac{\varepsilon_r - 1}{2} F - \frac{\varepsilon_r - 1}{4.6} \frac{\frac{t_m}{t}}{\sqrt{\frac{W}{t}}} \tag{A.6}$$

$$\varepsilon_{r,eff}(f) = \varepsilon_r - \frac{\varepsilon_r - \varepsilon_{r,eff}}{1 + \left(\frac{f}{f_{50}}\right)^m} \tag{A.7}$$

$$f_{50} = \frac{f_{k,TM_0}}{0.75 + \left[0.75 - \left(\frac{0.332}{\varepsilon_r^{1.73}}\right)\right] \frac{W}{t}} \tag{A.8}$$

$$f_{k,TM_0} = \frac{c \tan^{-1}\left(\varepsilon_r \sqrt{\frac{\varepsilon_{r,eff} - 1}{\varepsilon_r - \varepsilon_{r,eff}}}\right)}{2\pi t \sqrt{\varepsilon_r - \varepsilon_{r,eff}}} \tag{A.9}$$

$$m = m_0 \, m_c \tag{A.10}$$

$$m_0 = 1 + \frac{1}{1 + \sqrt{\frac{W}{t}}} + 0.32 \left(\frac{1}{1 + \sqrt{\frac{W}{t}}}\right)^3 \tag{A.11}$$

$$m_c = \begin{cases} 1 + \frac{1.4}{1 + \frac{W}{t}} \left[0.15 - 0.235^{\left(\frac{-0.45 f}{f_{50}}\right)}\right]; & \frac{W}{t} \leq 0.7 \\ 1; & \frac{W}{t} \geq 0.7 \end{cases} \tag{A.12}$$

With:

$t$ = substrate thickness

$t_m$ = metal thickness

$W$ = width of slotline/microstrip line

$\varepsilon_r$ = relative permittivity

# APPENDIX B

## Microstrip Line-to-Waveguide Transition

At 24 GHz, microstrip line-to-coax transitions are relatively easy and inexpensive, and a prototype antenna can be easily connected to the rest of the radar module for testing. At 77 GHz, such a transition is not available and a transition to waveguide is necessary to connect a prototype antenna with MMICs.

Microstrip line-to-waveguide transitions have been studied extensively [122–124]. At W-band, transitions with insertion losses of better than 0.4 dB have been reported covering the whole frequency band.

Since the microstrip line-to-waveguide transition for this work is only to test a prototype antenna, it should be easy to build and to mount. The design is taken from [125] and modified such that the substrate does not have to be cut. Fig. B.1 shows a schematic of the microstrip line-to-waveguide transition. The microstrip line reaches into the waveguide and couples to the waveguide mode. The substrate is supported by a brass block which has a waveguide feed through and which holds positioning pins in order to align the waveguide on one side and the substrate and the waveguide cap on the other side. The brass block and the waveguide cap are connected using via holes in order to provide electric connection. The via holes are holes in the substrate which are filled with electric conductive glue, and screws (not shown in the schematic) provide mechanical pressure and therefore good electric contact. Dimensions are given in Fig. B.2.

The microstrip line-to-waveguide transition is measured in a back-to-back configuration for easy calibration to the ends of waveguides using SLLT (Short-Line-Load-Through) as

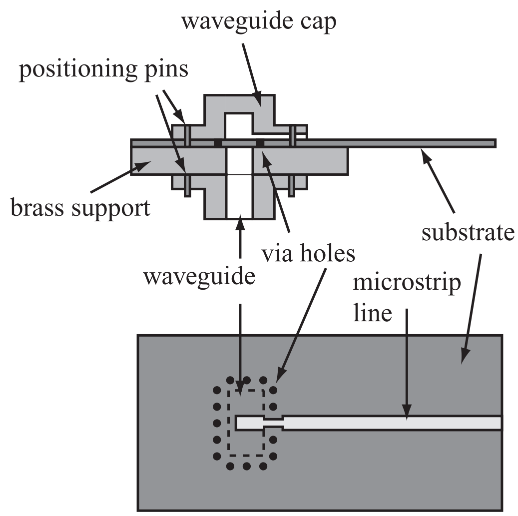


**Figure B.1: Cross-section and topview of the microstrip line-to-waveguide transition.**

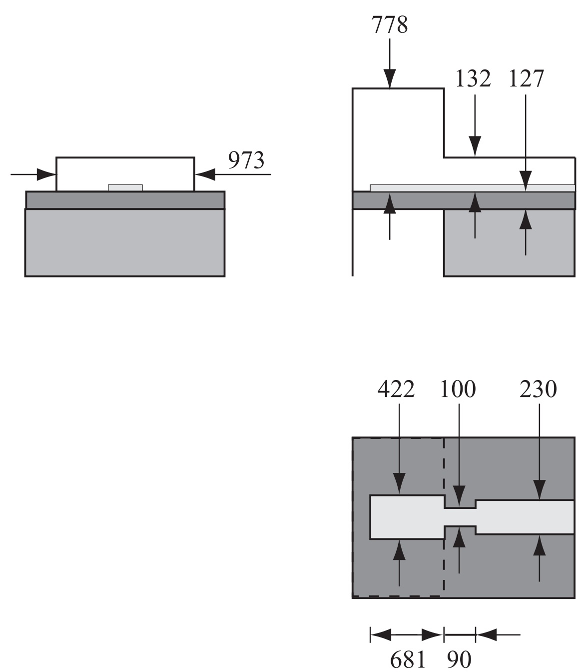


**Figure B.2: Dimensions of the microstrip line-to-waveguide transition in μm.**

standards. The length of the microstrip line between the 2 transitions is 40 mm. With a loss of 0.06 dB/mm (2.4 dB total microstrip line loss), the loss per transition is around 1.0 dB at 77 GHz. A critical issue is the placement of the via holes. Any distance from the

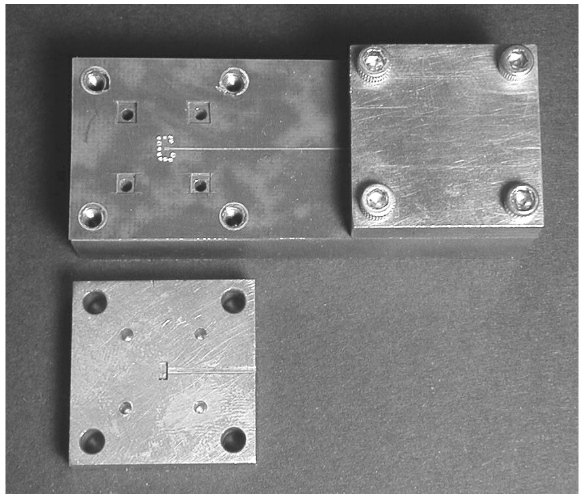

**Figure B.3: Photograph of the back-to-back microstrip line-to-waveguide transition.**

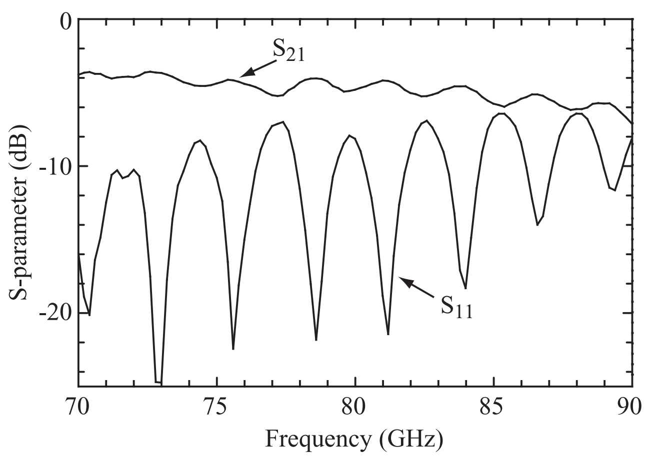


**Figure B.4: Measured S-parameters of a back-to-back microstrip line-to-waveguide transition.**

circumference of the waveguide means an additional current path and therefore unwanted reflections, and clearly, a better match is needed. The periodic nature of the measured $S_{11}$ is due to the presence of two transitions, each with a reflection coefficient around $-12$ dB and a 40 mm line in between them. This design being far from optimized nevertheless shows the possibility to build microstrip line-to-slotline transitions in a relatively easy fashion.

# APPENDIX C

# Radiometric Technique for Antenna Efficiency Measurement

## C.1 Description of Method

The radiometric technique is an accurate method to measure radiation efficiencies of antennas. The antenna efficiency is determined using a calibrated low-noise RF system with a measured gain $G_S$. The gain, $G_S$, of the RF system is determined using a hot/cold load placed in front of a horn antenna connected to the system. A horn antenna has very low losses, is well matched to 50 Ω, and results in an efficiency of about 98%. The system gain is calculated using:

$$G_s = \frac{P_H - P_C}{kB(T_H - T_C)} \tag{C.1}$$

where $T_H = 293$ K and $T_C = 77$ K. $B$ is the final resolution bandwidth of the RF system and $k$ the Boltzmann constant ($K = 1.8 \times 10^{-23}\mathrm{JK}^{-1}$. $P_H$ and $P_C$ are the measured (amplified) RF powers with the hot and cold load, respectively. This equation is the ratio between the measured (amplified) power difference with hot and cold load and the (not amplified) power difference in front of the horn antenna. The load is a black body absorber held at room temperature for the hot load and immersed in liquid nitrogen ($T = 77\ K$) for the cold load.

Using the same equations and the same measurement technique with the antenna-lens system instead of the horn antenna by itself connected to the system, $G_S{}'$, the gain of the RF system with the lossy antenna-lens system, is obtained. The measured loss is then:

$$\frac{G_A}{\mathrm{dB}} = \frac{G_S{}'}{\mathrm{dB}} - \frac{G_S}{\mathrm{dB}} \tag{C.2}$$

which is a negative number, and the expression as efficiency is:

$$\eta = \frac{P_H{}' - P_C{}'}{P_H - P_C} \tag{C.3}$$

The parameters of the RF system such as the noise temperature of the IF chain and the noise temperature of the whole RF system are determined using a standard coaxial hot/cold load measurement. By measuring output powers of the system when connected to a hot or cold 50 Ω load, the noise figure is given in [126] as:

$$F_r = \frac{T_H - T_C}{T_H \left(1 - \frac{1}{Y_r}\right)} \tag{C.4}$$

$$Y_r = \frac{P_H}{P_C} \tag{C.5}$$

where $Y_r$ is the measured power ratio and $T_H = 293$ K and $T_C = 77$ K are the temperatures for hot and cold load, respectively. The noise temperature $T_S$ of the RF system is then derived using:

$$F_r = 1 + \frac{T_S}{T_E} \tag{C.6}$$

where $T_E$ is the reference temperature of 293 K.

## C.2 RF Chain Design and Calibration

A detailed view of the measurement systems used to measure the efficiency of the antenna system is shown in Fig. C.1. The conversion loss of the balanced waveguide mixer is around 6 dB at 77 GHz. There is no bandpass filter used before the mixer which results in a double side band measurement. The intermediate frequency is 1.4 GHz with a bandwidth of 200 MHz. The power is averaged over the bandwidth and so is the efficiency. This is acceptable since the measured antenna-lens system is very wideband and the impedance is well match over the frequency range of interest (3 GHz). The noise temperature and gain of the whole measurement system are $T_S = 900$ K and $G_S = 73.6$ dB, respectively.

With this method values in the order of 100 µW are measured. The resulting radiation efficiency is 82% for the antenna-lens system.

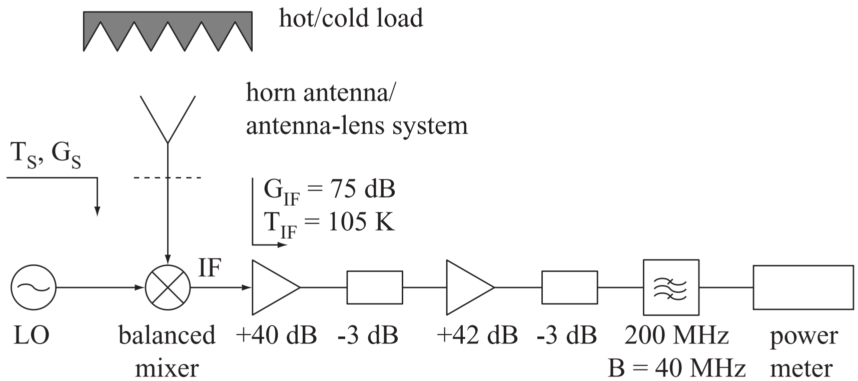


**Figure C.1: The RF chain for efficiency measurements for the antenna-lens system.**

# APPENDIX D

## Fabrication Processes: Circuits on RT/Duroid 5880

This Appendix presents the detailed fabrication process for the TSAs and the FSSs of the dual-frequency antenna system. The processing is done using RT/Duroid 5880 substrates of various thicknesses with a copper layer of 17 μm on both sides. The processing is done in a fabrication laboratory at the University of Michigan.

## D.1 Description of Terms

1. Photo-lithographic patterning:

   (a) **Photo-mask**: A patterned layer of material that is opaque to light and is used to pattern photo-sensitive material on the surface of a wafer. A typical photo-mask consists of a quartz plate with a reflective chrome surface and coated with photoresist.

   (b) **Photoresist**: A light sensitive material that is deposited on the surface of a wafer. Depending on the polarity of the photoresist, when an area of the photoresist is exposed to UV light, it can either be removed or preserved while the unexposed areas are either preserved or removed, respectively, during the developing process. Positive photoresist is removed after exposure and negative photoresist remains after exposure.

   (c) **Mask aligner**: A device which aligns a photo-mask to an existing pattern on a wafer. It then exposes the aligned mask and wafer with UV light, transferring the pattern from the mask to the photoresist.

(d) **Developer**: A chemical solution that will selectively remove exposed or unexposed areas of photoresist, depending on the polarity of the resist. These developers are often matched to a specific type and brand of photoresist.

(e) **Soft bake**: Heating step to partially remove solvent from photoresist before aligning and exposing a wafer. It reduces stickiness of the photoresist layer, which is necessary for contact alignment.

(f) **Hard bake**: Heating step to solidify photoresist after it has been developed. This process makes the photoresist more resistant to chemical etchants and increases adhesion.

2. Chemicals used:

   (a) **Acetone**: A strong chemical solvent capable of completely removing or stripping most photoresist materials from a wafer or mask.

   (b) **IPA** (isopropyl alcohol): A solvent used to clean the surface of a wafer. It is often used to remove traces of acetone and photoresist.

   (c) **PR 1827**: Positive photoresist.

   (d) **MF 351**: Developer.

   (e) **Sodium Persulfate** ($Na_2S_2O_8$): Cu etchant.

## D.2 Specific Processes

1. Wafer clean

   (a) Spray and swap with acetone.

   (b) Spray and swap with IPA.

   (c) Dry with $N_2$ air gun.

   (d) Wet etch in 90°C hot $Na_2S_2O_8$ for 10 seconds to remove copper oxide from the surface.

2. Photo-lithography

    (a) Spin photoresist 1827 on frontside for 30 seconds at 3 krpm.

    (b) Soft bake at 80°C for 15 minutes.

    (c) If necessary: Spin photoresist 1827 on backside for 30 seconds at 3 krpm.

    (d) If necessary: Soft bake at 80°C for 15 minutes.

    (e) Align to mask and expose for 15 seconds at 20 $mW/cm^2$.

    (f) Develop in MF 351 (diluted with DI: 1:5) developer for 1.5 minutes.

    (g) Rinse in DI water for 4 minutes.

    (h) Examine edge profile under microscope.

    (i) Hard bake at 110°C for 15 minutes.

3. Copper etching

    (a) Wet etch Cu in $Na_2S_2O_8$ for around 5 minutes.

    (b) Rinse in DI water for 2 minutes.

    (c) Remove photoresist in Acetone.

    (d) Spray and swap with IPA.

    (e) Dry with $N_2$ air gun.

# APPENDIX E

## Fabrication Processes: RF MEMS Circuits

This appendix presents detailed fabrication processes for the switchable FSS. The processing is done on 500 μm thick, double-side polished glass wafers with a surface roughness of ±15 Å and a diameter of 76.4 mm. The processing is done in a class 100 clean room at the University of Michigan. The specifics of the development of stress balanced membranes for MEMS switches are covered in the work of Joseph Hayden [104].

## E.1 Description of Terms

While there are numerous techniques and processes involved in micro-fabrication and micro-machining, only the most common techniques used in the fabrication of RF MEMS devices will be outlined here. The following is a list of common terms and techniques, taken from the thesis of Jeremy Muldavin [127] with minor changes.

1. Photo-lithographic patterning:
   (a) **Mask maker**: A device which selectively exposes small apertures onto the surface of photo-sensitive masking plates.
   (b) **Photo-mask**: A patterned layer of material that is opaque to light and is used to pattern photo-sensitive material on the surface of a wafer. A typical photo-mask consists of a quartz plate with a reflective chrome surface and coated with photoresist.
   (c) **Photoresist**: A light sensitive material that is deposited on the surface of a

wafer. Depending on the polarity of the photoresist, when an area of the photoresist is exposed to UV light, it can either be removed or preserved while the unexposed areas are either preserved or removed, respectively, during the developing process. Positive photoresist is removed after exposure and negative photoresist remains after exposure.

(d) **Image reversal photoresist**: A special type of negative photoresist that reverses its polarity after a second exposure. This process creates a special profile or lip at the edge of the resist pattern that is advantageous for use in lift-off techniques.

(e) **Mask aligner**: A device which aligns a photo-mask to an existing pattern on a wafer. It then exposes the aligned mask and wafer with UV light, transferring the pattern from the mask to the photoresist.

(f) **Developer**: A chemical solution that will selectively remove exposed or unexposed areas of photoresist, depending on the polarity of the resist. These developers are often matched to a specific type and brand of photoresist.

(g) **Soft bake**: Heating step to partially remove solvent from photoresist before aligning and exposing a wafer. It reduces stickiness of the photoresist layer, which is necessary for contact alignment.

(h) **Hard bake**: Heating step to solidify photoresist after it has been developed. This process makes the photoresist more resistant to chemical etchants and increases adhesion.

2. Material deposition:

(a) **Electron beam evaporator**: A device which uses a high energy beam to evaporate materials form a source crucible. The evaporated materials are ejected from the surface of the crucible and deposited unidirectionally in a thin film of the surface of a wafer. Common source materials include: Au, Al, Ti, Cr, Ag, Pt, NiCr, and Cu. These materials are often deposited in a lift-off process where photoresist protects areas of the wafer from direct deposition. The metal deposited on the photoresist is then removed when the photoresist is stripped from the wafer in PRS-2000.

(b) **Sputtering tool**: A device which uses a high energy plasma to etch particles from a source target and then redeposit the particles on the surface of a wafer. The source particles are ejected from the plasma in random directions, ensuring a conformal coating of a surface. The plasma, a mixture of charged particles and electrons, can be excited using a direct current (DC) or a radio frequency (RF) source. DC plasmas are often used to deposit metals such as Au, Al, Ti, Cr, and Cu. RF plasmas are used to deposit metal and dielectric materials such as Si, $SiO_2$, SiN, SiCr, and TaN.

(c) **PECVD (plasma enhanced chemical vapor deposition)**: A technique that uses an RF plasma with specific gaseous mixtures to deposit materials on the surface of a wafer. This process is often used to deposit dielectric films such as $SiO_2$ and SiN.

3. Etching techniques:

(a) **Wet chemical etching**: The use of wet chemical agents to selectively etch a material from the surface of a wafer. Common etchants include Au etchant, copper etchant, Ti etchant, Al etchant, HF and BHF to etch oxide and Ti films.

(b) **Plasma etching, RIE (reactive ion etching**: A technique that uses an RF plasma and chemical etching to remove materials from the surface of a wafer. This technique is often used to etch $SiO_2$, SiN, or organic layers, such as PMMA.

4. Release:

(a) **Sacrificial layer**: A layer of material that separates a deposited layer from underlying layers to create vertical gaps between the layers. The sacrificial layer is then removed to release portions of the top layer from the underlying layers.

(b) **CPD (critical point dryer)**: A device which allows the release of MEMS devices from their sacrificial layers without collapse due to surface tension. This device consists of a cooled chamber that fills with liquid $CO_2$ which mixes with and purges the wet chemicals from around the MEMS devices. The liquid $CO_2$ filled chamber is then pressurized and heated to the critical point of $CO_2$, in which $CO_2$ exists as a liquid and a vapor state simultaneously. The pressure is then lowered slowly, drying the MEMS wafer without passing through a liquid phase. This eliminates the collapse of the devices due to liquid surface tension.

5. Chemicals used:

   (a) **Acetone**: A strong chemical solvent capable of completely removing or stripping most photoresist materials from a wafer or mask.

   (b) **IPA** (Isopropyl alcohol): A solvent used to clean the surface of a wafer. It is often used to remove traces of acetone and photoresist.

   (c) **PMMA** (Polymethylmethacrylate: 950K, 9% in anisole solvent): An organic photoresist for e-beam lithography.

   (d) **PRS-2000**: A proprietary photoresist solvent.

   (e) **HF**: Hydrofluoric acid.

   (f) **TFA**: Au etchant.

   (g) **PR 1813**: Positive photoresist.

   (h) **PR 1827**: Positive photoresist.

   (i) **AZ 5214**: Image reversal photoresist.

   (j) **MF 351**: Developer.

   (k) **AZ 327**: Developer.

   (l) **HMDS** (Hexamethyldisilizane): Material improving adhesion of photoresist to the surface of a wafer.

## E.2 Specific Processes

1. Wafer clean

   (a) Spray and swap with acetone.

(b) Spray and swap with IPA.

(c) Dry with $N_2$ air gun.

2. First Metallization layer (lift-off)

   (a) Spin adhesion promoter HMDS for 30 seconds at 2.5 krpm.

   (b) Spin image reversal photoresist AZ 5214 for 30 seconds at 2.5 krpm.

   (c) Soft bake for 2 minutes on a 105°C hot plate.

   (d) Align to mask and expose for 2.0 seconds at 20 $mW/cm^2$.

   (e) Image reversal bake at 130°C for 2 minutes.

   (f) Flood expose (no mask) for 45 seconds at 20 $mW/cm^2$.

   (g) Develop in AZ 327 developer for 1.5 minutes.

   (h) Rinse in DI water for 4 minutes.

   (i) Dry with $N_2$ air gun.

   (j) Examine edge profile under microscope.

   (k) Evaporate Ti/Au/Ti (500/5000/500 Å).

   (l) Soak sample in hot PRS-2000 overnight for metallization lift-off.

   (m) Rinse in DI water for 15 minutes.

   (n) Dry with $N_2$ air gun.

3. Silicon-Nitride Deposition and Etch

   (a) PECVD deposit SiN for 13 minutes for a 2,000 Å thick layer ($SiH_4$ (100 sccm), $NH_3$ (10 sccm), He (900 sccm), $N_2$ (990 sccm), 400°C, 700 mT, 100 W.

   (b) Spin adhesion promoter HMDS for 30 seconds at 3 krpm.

   (c) Spin photoresist 1827 for 30 seconds at 3 krpm.

   (d) Soft bake 2 minutes on a 105°C hot plate.

   (e) Align to mask and expose for 15 seconds at 20 $mW/cm^2$.

   (f) Develop in MF 351 (diluted with DI: 1:5) for 1.5 minutes.

(g) Rinse in DI water for 4 minutes.

(h) Dry with ($N_2$) air gun.

(i) Examine circuit pattern under microscope.

(j) Hard bake for 2 minutes on a 130°C hot plate.

(k) RIE etch dielectric in $CF_4$ (40 sccm) and $O_2$ (1 sccm) plasma at 100 mT and 100 W for 6 minutes.

(l) Strip photoresist in hot PRS-2000. Swap lightly.

(m) Rinse in DI water.

(n) Dry with $N_2$ air gun.

4. Sacrificial Layer Deposition

(a) Spin adhesion promoter HMDS for 45 seconds at 2.5 krpm.

(b) Spin PMMA (950K, 9% in anisole solvent) for 45 seconds at 1.45 krpm for a thickness of $2.0\mu$m.

(c) Bake PMMA for 30 minutes in a 170°C oven to remove all the solvent.

(d) Evaporate 500 Å of Ti.

(e) Spin photoresist 1827 for 30 seconds at 3 krpm.

(f) Soft bake for 2 minutes on a 105°C hot plate.

(g) Align to mask and expose for 15 seconds at 20 mW/cm$^2$.

(h) Develop in MF 351 (diluted with DI: 1:5) for 1.5 minutes.

(i) Rinse in DI water for 4 minutes.

(j) Dry with ($N_2$) air gun.

(k) Examine circuit pattern under microscope.

(l) Skip hard bake.

(m) Etch Ti in 1:20 HF:DI (a quick dip etch).

(n) Rinse in DI water for 4 minutes.

(o) Dry with $N_2$ air gun.

(p) Flood expose for 30 seconds at 20 mW/cm$^2$.

(q) Develop in MF 351 (diluted with DI: 1:5) for 1.5 minutes.

(r) Rinse in DI water for 4 minutes.

(s) Dry with $N_2$ air gun.

(t) Etch PMMA in 100 mT, $O_2$ (100 sccm), 250 W plasma for 8 minutes, turning plasma RF power on and off in 1.5 and 1 minutes cycles, respectively, to prevent elevated temperatures of the wafer.

(u) Wet etch Ti in 1:20 HF:DI (a quick dip etch).

(v) Rinse in DI water for 4 minutes.

(w) Dry with $N_2$ air gun.

5. MEMS Membrane Sputtering

(a) DC sputter from Ti target, Argon environment, 7 mT, 550 W, 2 minutes, rotation of 20 rpm, for a 100 Å thick layer.

(b) DC sputter from Au target, Argon environment, 10 mT, 0.5 A, 30 minutes, rotation of 20 rpm, for a 8,000 Å thick layer.

(c) DC sputter from Ti target, Argon environment, 7 mT, 550 W, 10 minutes, rotation of 20 rpm, for a 500 Å thick layer.

6. Electroplating

(a) Spin adhesion promoter HMDS for 30 seconds at 3 krpm.

(b) Spin photoresist 1827 for 30 seconds at 2 krpm for a 3.8 $\mu$m thick layer.

(c) Soft bake 2 minutes on a 105°C hot plate.

(d) Align to mask and expose for 20 seconds at 20 mW/cm$^2$.

(e) Develop in MF 351 (diluted with DI: 1:5) for 1.5 minutes.

(f) Rinse in DI water for 4 minutes.

(g) Dry with $N_2$ air gun.

(h) Examine circuit pattern under microscope.

(i) Hard bake for 2 minutes on a 130°C hot plate.

(j) Electroplate gold on exposed 4.5 $cm^2$ area of wafer at 18 mA for 80 minutes, resulting in 2.5 μm thick layer.

7. Stress Release in Bridge Membrane

   (a) Flood expose for 90 seconds at 20 $mW/cm^2$.

   (b) Develop in MF 351 (diluted with DI: 1:5) for 2 minutes.

   (c) Rinse in DI water for 4 minutes.

   (d) Dry with $N_2$ air gun.

   (e) Bake for 2 minutes on a 100° C hot plate.

   (f) Increase the hot plate temperature linearly from 100°C to 170°C over 10 minutes.

   (g) Decrease the hot plate temperature linearly from 170°C to 100°C over 10 minutes.

8. MEMS Membrane Etch and Sacrificial Layer Removal

   (a) Spin adhesion promoter HMDS for 30 seconds at 2.5 krpm.

   (b) Spin photoresist 1827 for 30 seconds at 3 krpm.

   (c) Soft bake for 2 minutes on a 105°C hot plate.

   (d) Align to mask and expose for 18 seconds at 20 $mW/cm^2$.

   (e) Develop in MF 351 (diluted with DI: 1:5) for 1.5 minutes.

   (f) Rinse in DI water for 4 minutes.

   (g) Dry with $N_2$ air gun.

   (h) Examine circuit pattern under microscope.

   (i) Hard bake for 2 minutes on a 130°C hot plate.

   (j) Wet etch Ti in 1:20 HF:DI.

   (k) Rinse in DI water for 4 minutes.

   (l) Wet etch Au in TFA Au etchant for 1.5 minutes.

   (m) Rinse in DI water for 4 minutes.

(n) Flood expose for 90 seconds at 20 $mW/cm^2$.

(o) Develop in MF 351 (diluted with DI: 1:5) for 2 minutes.

(p) Rinse in DI water for 4 minutes.

(q) Dry with $N_2$ air gun.

(r) Wet etch Ti in 1:20 HF:DI.

(s) Rinse in DI water for 4 minutes.

(t) Release membranes in hot PRS-2000, overnight.

(u) Rinse in DI water for 15 minutes.

(v) Rinse in IPA for 5 minutes.

(w) Dry wafer in CPD.

# BIBLIOGRAPHY

# BIBLIOGRAPHY


[1] H.H. Meinel, "Commercial applications of millimeterwaves: history, present status, and future trends," in *IEEE Transactions on Microwave Theory and Techniques*, Jul 1995, vol. 43, no. 7, pp. 1639–1653.

[2] L. Hahn, "Advances in the development of headway radar using pulse techniques," in *IEE Automotive Electronics*, Oct 1979, pp. 189–192.

[3] T.O. Jones, D.M. Grimes, "Automotive station keeping and braking radars: a review," in *Microwave Journal*, Oct 1975, pp. 49–53.

[4] K. Lindner, W. Wiesbeck, "35-GHz-Impulsradarsensor zur Verwendung in Abstandswarngeraeten fuer Kraftfahrzeuge," "(35-GHz pulse radar for car distance warning applications,)" in *Nachrichtentechnische Zeitung,*, Z29, H9, Sep 1976, pp. 667–672.

[5] G. Neininger, "An FM/CW radar with high resolution in range and doppler; aplication for anti-collision radar for vehicles," in *IEE Conference*, London, UK, Oct 1977, pp. 526–530.

[6] H.P. Groll, J. Detlefsen, "History of automotive anticollision radars and final experimental results of a mm-wave car radar developed by the Technical University of Munich," in *IEEE AES Systems Magazine*, Aug 1997, pp. 15–18.

[7] T. v. Kerssenbrock, P. Heide, "Novel 77 GHz flip-chip sensor modules for automotive radar applications," in *IEEE MTT-S International Microwave Symposium Digest*, Jun 1999, vol. 1, pp. 289–292.

[8] J.F. Lamberg, M.J. Gawronski, J.J. Geddes, W.R. Carlyon, R.A. Hart, G.S. Dow, E.W. Holmes, M.Y.Huang, "A compact high performance W-band FMCW radar front-end based on MMIC technology," in *IEEE MTT-S International Microwave Symposium Digest*, Jun 1999, vol. 4, pp. 1797–1800.

[9] I. Gresham, N. Jain, T. Budka, A. Alexanian, N. Kinayman, B. Ziegner, S. Brown, P. Staecker, "A 76-77 GHz pulsed-Doppler radar module for autonomous cruise control applicaitons," in *IEEE MTT-S International Microwave Symposium Digest*, Jun 2000, pp. 1551–1554.

[10] T. Hancock, I. Gresham, G.M. Reibeiz, "Compack low phase-noise 23 GHz VCO fabricated in a commercial SiGe bipolar process," in *33rd European Microwave Conference*, Oct 2003, pp. 575–578.

[11] I. Gresham, A. Jenkins, "A fast switching, high isolation absorptive SPST SiGe switch for 24 GHz automotive applications," in *6th European Conference on Wireless Technology*, Oct 2003, pp. 37–40.

[12] F. Demmerle, W. Wiesbeck, "A biconical multibeam antenna for space-division multiple access," in *IEEE Transactions on Antennas and Propagation*, Jun 1998, pp. 782–787.

[13] W. Menzel, D. Pilz, M. Al-Tikriti, "Milimeter-wave folded reflector antennas with high gain, low loss, and low profile," in *IEEE Antennas and Propagation Magazine*, Jun 2002, vol. 44, pp. 24–29.

[14] W. Menzel, M. Al-Tikriti, R. Leberer, "A 76 GHz multiple-beam planar reflector antenna," in *32nd European Microwave Conference*, Sep 2002, vol. 3, pp. 977–980.

[15] M.A. Mitchell, J.R. Sanford, L.E. Corey, R.A. Moore, V.P. Pusateri, "A multiple-beam multiple-frequency spherical lens antenna system providing hemispherical coverage," in *6th International Conference on Antennas and Propagation*, Apr 1989, vol. 1, pp. 394–398.

[16] Y.-J. Park, A. Herschlein, W. Wiesbeck, "A photonic bandgap (PBG) structure for guiding and suppressing surface waves in millimeter-wave antennas," in *IEEE Transactions on Microwave Theory and Techniques*, Oct 2001, pp. 1854–1859.

[17] Y.-J. Park, W. Wiesbeck, "Offset cylindrical reflector antenna fed by a parallel-plate Luneburg lens for automotive radar applications in milimeter-wave," in *IEEE Transactions on Antennas and Propagation*, Sep 2003, no. 9, pp. 2481–2483.

[18] R.K. Luneburg, "The mathematical theory of optics," *Brown University Press*, Providence, R.I., 1994.

[19] H. Mosallaei, Yahya Rahmat-Samii, "Nonuniform luneburg and two-shell lens antennas: radiation characteristics and design optimization," *IEEE Trans. on Antennas and Propagation*, Jan 2001, vol. 49, no. 1, pp. 60–68.

[20] Q.M. Tang, K.K. Chan, G.A. Morin, S.K. Rao, "EHF multiple beam dielectric lens antenna," *Antennas and Propagation International Symposium*, Jun 1995, vol. 1, pp. 674–677.

[21] K.K. Chan, S.K. Ral, G.A. Morin, and M.Q. Tang, "Triangular ray-tube analysis of dielectric lens antennas," *IEEE Transactions on Antennas and Propagation*, Aug 1997, vol. 45, no. 8, pp. 1277–1285.

[22] J. Richter, A. Hofmann, L.-P. Schmidt, "Dielectric wide angle lenses for millimeter-wave focal plane imaging," *31st European Microwave Conference*, Oct 2001, vol. 1, pp. 674–677.

[23] C.L. Goldsmith, Z. Yao, S. Eshelman, D. Denniston, "Performance of low-loss RF MEMS capacitive switches," in *IEEE Microwave Guided Wave Letters*, Aug 1998, vol. 8, pp. 269–271.

[24] J.Y. Park, G.H. Kim, K.W. Chung, J.U. Bong, "Fully integrated micro-machined capacitive switches for RF applications," in *2000 IEEE MTT-S International Microwave Symposium*, Jun 2000, Boston, MA, pp. 283–286.

[25] J.B. Muldavin, G.M. Rebeiz, "High-isolation CPW MEMS shunt switches; part1: Modeling," in *IEEE Trans. Microwave Theory Tech.*, Jun 2000, vol. 48, pp. 1045–1052.

[26] J.B. Muldavin, G.M. Rebeiz, "High-isolation CPW MEMS shunt switches; part2: Design," in *IEEE Trans. Microwave Theory Tech.*, Jun 2000, vol. 48, pp. 1053–1056.

[27] D. Peroulis, S. Pacheco, L.P.B. Katehi, "MEMS devices for high isolation switching and tunable filtering," in *2000 IEEE MTT-S Int. Microwave Symp. Dig.*, Jun 2000, Boston, MA, pp. 1217–1220.

[28] G.L. Tan, G.M. Rebeiz, "DC-26 GHz MEMS series-shunt absorptive switches," in *2001 IEEE MTT-S Int. Microwave Symp. Dig.*, May 2001, Phoenix, AZ, pp. 325–328.

[29] G.M. Rebeiz, J.B. Muldavin, "RF MEMS switches and switch circuits," in *IEEE Microwave Magazine*, Dec 2001, vol. 2, pp. 59–71.

[30] M. Reimann, M. Ulm, "RF MEMS and packaging strategies," *IEEE Microwave Theory and Techniques Workshop*, Jun 2003.

[31] M.B. Cohn, "RF MEMS: packaging and integration techniques," *IEEE Microwave Theory and Techniques Workshop*, Jun 2003.

[32] Y.C. Lee, K.C. Gupta, V.M. Bright, S.M. George, N. Hoivik, H. Zhang, R. Ramadoss, C.H. Abell, F. Faheem, K. Harsh, A. Laws, S. Lee, "MEMS packaging for integration and reliability," *IEEE Microwave Theory and Techniques Workshop*, Jun 2003.

[33] B.A. Munk, "Frequency selective surfaces," John Wiley & Sons, 2000.

[34] A.C. de C. Lima, E.A. Parker, R.J. Langley, "Tunable frequency selective surface using lequid substrates," in *Electronics Letters*, Feb. 1994, no. 4, pp. 281–282.

[35] T.K. Chang, R.J. Langley, E.A. Parker, "Frequency selective surfaces on biased ferrite substrates," in *Electronics Letters*, Jul. 1994, no. 15, pp. 1193–1194.

[36] T.K. Chang, R.J. Langley, E.A. Parker, "Active frequency-selective surfaces," in *1999 IEE Proc. Microwave Antennas Propag.*, Feb. 1996, vol. 143, no. 1, pp. 62–66.

[37] K.D. Stephan, F.H. Spooner, P.F. Goldsmith, "Quasioptical millimeter-wave hybrid and monolithic PIN diode switches," in *IEEE Transactions on Microwave Theory and Techniques*, Oct. 1993, vol. 41, no. 10, pp. 1791–1798.

[38] C. Mias, "Frequency selective surfaces loaded with surface-mount reactive components," in *Electronics Letters*, May 2003, vol. 39, no. 9, pp. 724–726.

[39] J.P. Gianvittorio, J. Zendejas, Y. Rahmat-Samii, "MEMS enabled reconfigurable frequency selective surfaces: design, simulation, fabrication, and measurement," in *IEEE Antennas and Propagation Society International Symposium*, Jun. 2002, vol. 2, pp. 404–407.

[40] D. Lockyer, R. Seager, J.C. Vardaxoglou, "Reconfigurable FSS using multilayer conducting and slotted array structures," in *IEE Colloquium on Advances in Electromagnetic Screens, Radomes and Materials*, Oct. 1996, Digest no. 270, pp. 6/1–6/6.

[41] G.A. Deschamps, "Microstrip microwave antennas," in *3rd USAF Symposium an Antennas*, 1953.

[42] M. Kominami, D. Pozar, D. Schaubert, "Dipole and slot elements and arrays on semi-infinite substrates," in *IEEE Transactions on Antennas and Propagation*, Jun 1985, vol. 33, no. 6, pp. 600–607.

[43] D.B. Ruthledge, D.P. Neikirk, D.P. Kasilingam, "Integrated-circuit antennas," in *Infrared and Millimeter Waves*, 1983, vol. 10, New York: Academic, chap.1.

[44] Y.Yoshimura, "A Microstripline Slot Antenna," in *IEEE Transactions on Microwave Theory and Techniques*, Nov 1972, vol. 20, no. 9, pp. 760–762.

[45] T.M. Weller, L.P.B. Katehi, G.M. Rebeiz, "Single and double folded-slot antennas on semi-infinite substrates," in *IEEE Transactions on Antennas and Propagation*, Dez 1995, vol. 43, no. 12, pp. 1423–1428.

[46] K.A.S. Qassim, N.J. McEwan, "Printed Yagi antennas as a focal plane array in an imaging system," in *IEE 7th International Conference on Antennas and Propagation*, Apr 91, vol. 1, pp. 193–196.

[47] W.R. Deal, N. Kaneda, J. Sor, Y. Qian, T. Itoh, "A new quasi-Yagi antenna for planar active antenna arrays," in *IEEE Transactions on Microwave Theory and Techniques*, Jun. 2000, vol. 48, no. 6, pp. 910–918.

[48] P.R. Grajek, B. Schoenlinner, G.M. Rebeiz, "A 24-GHz High-Gain Yagi-Uda Antenna Array," in *IEEE Transactions on Antennas and Propagation*, appear in Jul. 2004.

[49] K.S. Yngvesson, T.L. Korzeniowski, Y.-S. Kim, E.L. Kollberg, J.F. Johansson, "The tapered slot antenna - a new integrated element for millimeter-wave applications," in *IEEE Transactions on Microwave Theory and Techniques*, Feb. 1989, vol. 37, no. 2, pp. 365–374.

[50] C.H. Walter, "Traveling Wave Antennas," New York: McGraw-Hill, 1965.

[51] H. Jasik, Ed., "Antenna Engineering Handbook," in *McGraw-Hill*, 1961.

[52] K.S. Yngvesson, D.H. Schaubert, T.L. Korzeniowski, E.L. Kollberg, T. Thungren, J.F. Johansson, "Endfire tapered slot antennas on dielectric substrates," in *IEEE Transactions on Antennas and Propagation*, Dec. 1985, vol. 33, no. 12, pp. 1392–1400.

[53] P.J. Gibson, "A novel mic slot-line aerial," in *9th European Microwave Conference*, 1979, pp. 120–124.

[54] D.H. Schaubert, "Radiation characteristics of linearly tapered slot antennas," in *IEEE Antennas and Propagation Symposium Digest*, Jun 1989, pp. 1324–1327.

[55] R.N. Simons, R.Q. Lee, "Linearly tapered slot antenna radiation characteristics at millimeter-wave frequencies," in *IEEE Antennas and Propagation Symposium Digest*, Jun 1998, vol. 2, pp. 1168–1171.

[56] J.B. Muldavin, G.M. Rebeiz, "Millimeter-wave tapered-slot antennas on synthesized low permittivity substrates," in *IEEE Transactions on Antennas and Propagation*, Aug 1999, vol. 8, pp. 1276–1280.

[57] P.J. Gibson, "The Vivaldi aerial," in *9th European Microwave Conference*, 1979, pp. 101–105.

[58] E.J. Kolberg, J. Johnason, T. Thungren, T.L. Korzeniowski, K.S. Yngvesson, "New results on tapered slot endfire antennas on dielectric substrate," in *IEEE 8th International Conference on Infrared and Millimeter Waves*, USA, 1983, pp. F3.6/1-2.

[59] D.A. Burrell, J.T. Aberle, "Characterization of Vivaldi antennas utilizing a microstrip-to-slotline transition," in *IEEE Antennas and Propagation Symposium Digest*, Jun 1993, vol. 3, pp. 1212–1215.

[60] J.J. Lee, S. Livingston, "Wide band bunny-ear radiating element," in *IEEE Antennas and Propagation Symposium Digest*, Jun 1993, pp. 1604–1607.

[61] M.C. Greenberg, K.L. Virga, "Characterization and design methodology for the dual exponentially tapered slot antenna," in *IEEE Antennas and Propagation Symposium Digest*, Jul 1999, no. 1, pp. 88–91.

[62] M.C. Greenberg, K.L. Virga, C.L. Hammond, "Performance characteristics of the dual exponentially tapered slot antenna (DETSA) for wireless communications applications," in *IEEE Transactions on Vehicular Technbology*, Mar 2003, vol. 52, no. 2, pp. 305–312.

[63] U. Kotthaus, B. Vowinkel, "Investigation of planar antennas for submillimeter receivers," in *IEEE Transactions on Microwave Theory and Techniques*, Feb 1989, vol. 37, no. 8, pp. 375–380.

[64] P.R. Acharya, J.F. Johansson, E.J. Kolberg, "Slotline antennas for millimeter and submillimeter waves," in *Proc. 20th European Microwave Conference*, Budapest, Hungary, 1990, pp. 353–358.

[65] P.R. Acharya, H. Ekstrom, S.S. Gearhart, S. Jacobsson, J.F. Johansson, E.L. Kollberg, G.M. Rebeiz, "Tapered slotline antennas at 802 GHz," in *IEEE Transactions on Microwave Theory and Techniques*, Oct 1993, vol. 41, no. 10, pp. 1715–1719.

[66] S. I. Svechnikov,O.V. Okunev, P.A. Yagoubov, G.N. Gol'tsman, B.M. Voronov, S.I. Cherednichenko, E.M. Gershenzon, E. Gerecht, E.F. Musante, Z. Wang, K.S. Yngvesson, "2.5 THz NbN hot electron mixer with integrated tapered slot antenna," in *IEEE Transactions on Applied Superconductivity*, Jun 1997, vol. 7, no. 2, pp. 3548–3551.

[67] S. Sugawara, Y. Maita, K. Adachi, K. Mori, and K. Mizuno, "A mm-wave tapered slot antenna with improved radiation pattern," in *1999 IEEE MTT-S Int. Microwave Symp. Dig.*, Anaheim, CA, June 1997, pp. 1151–1154.

[68] J.B. Rizk, G.M. Rebeiz, "Millimeter-wave Fermi tapered slot antennas on micromachined silicon substrates," in *IEEE Transactions on Antennas and Propagation*, Mar 2002, vol. 50, no. 3, pp. 379–383.

[69] R. Janaswamy, D.H. Schaubert, "Analysis of the tapered slot antenna," in *IEEE Transactions on Antennas and Propagation*, Sep. 1987, vol. 35, no. 9, pp. 1058–1065.

[70] S.-S. Zhong, H. Zhang, "Analysis of the tapered slotline antenna on a dielectric substrate," in *Antennas and Propagation Society International Symposium*, Jun. 1988, vol. 3, pp. 1174–1177.

[71] R. Janaswamy, “An accurate Moment Method model for the tapered slot antenna,” in *IEEE Transactions on Antennas and Propagation*, Dec. 1989, vol. 37, no. 12, pp. 1523–1528.

[72] A. Koksal, F. Kauffman, “Moment method analysis of linearly tapered slot antennas,” in *IEEE Antennas and Propagation Symposium Digest*, Jun 1991, vol.1, pp.314–317.

[73] E. Thiele, A. Taflove, “FD-TD analysis of vivaldi flared horn antennas and arrays,” in *IEEE Transactions on Antennas and Propagation*, May 1994, vol. 42, no. 5, pp. 633–641.

[74] E. Topsakal, R. Kindt, K. Sertel, J. Volakis, “Evaluation of the BICGSTAB(l) algorithm for the finite-element/boundary-integral method,” in *IEEE Antennas and Propagation Magazine*, Dec 2001, vol. 43, no. 6, pp. 124–131.

[75] S.B. Cohn, “Slotline on a dielectric substrate,” in *IEEE Transactions*, vol. MTT-17, pp. 768–778, 1968.

[76] H. Meinke, F.W. Gundlach, “Taschenbuch der Hochfrequenztechnik,” in *Springer-Verlag*, 5th edition, 1992.

[77] K.C. Gupta, R. Garg, I. Bahl, P. Bhartia, “Microstrip lines and slotlines,” in *Artech House*, 2nd edition, 1996.

[78] G.D. Vendelin, “Limitations on stripline Q,” in *Microwave Journal*, vol. 13, pp. 63–69, 1970.

[79] G.H. Robinson, J.L. Allen, “Slotline application to miniature ferrite devices,” in *IEEE Transactions*, vol. MTT-17, pp. 1097–1101, 1969.

[80] J. Chramiec, “Reactances of slotline short and open circuits on alumina substrate,” in *IEEE Transactions*, vol. MTT-37, pp. 1638–1641, 1989.

[81] H.-Y. Yang, N.G. Alexopoulos, “A dynamic model for microstrip-slotline transition and related structures,” in *IEEE Transactions on Microwave Theory and Techniques*, Feb 1988, vol. 36, no. 2, pp. 286–293.

[82] W. Schwab, W. Menzel, “On the design of planar microwave components using multilayer structures,” in *IEEE Transactions on Microwave Theory and Techniques*, Jan 1992, vol. 40, no. 1, pp. 67–72.

[83] Y.M.M. Antar, A.K. Bhattcharyya, A. Ittipiboon, “Microstrip-slotline transition analysis using the spectral domain technique,” in *IEEE Transactions on Microwave Theory and Techniques*, Mar 1992, vol. 40, no. 3, pp. 515–523.

[84] N.K. Das, “Generalized multipoert reciprocity analysis of surface-to-surface transitions between multiple printed transmission lines,” in *IEEE Transactions on Microwave Theory and Techniques*, Jun/Jul 1993, vol. 41, no. 6/7, pp. 1164–1177.

[85] B. Schuppert, “Microstrip/slotline transitions: modeling and experimental investigation,” in *IEEE Transactions on Microwave Theory and Techniques*, Aug 1988, vol. 36, no. 8, pp. 1272–1282.

[86] D. Chambers, S.B. Cohn, E.H. Cristol, F. Young, "Microwave active network synthesis," Stanford Research Institute, Menlo Park, California, Semiannual Report, contract DAAB07-C-0044, SRI Project 8254, Jun 1970.

[87] R. Marks, D. Williams, "Multical," Ph.D. thesis, National Institute of Standards and Technology (NIST), Boulder CO, 2000.

[88] M.J. Vaughan, R.C. Compton, "Improved radiation pattern for 28 GHz omnidirectional quasi-optical oscillator array," in *IEEE Antennas and Propagation Society International Symposium*, Jun. 1995, vol. 3, pp. 1372–1375.

[89] M.J. Vaughan, R.C. Compton, K.Y. Hur, R.A. McTaggart, "InP-based 28 GHz integrated antennas for point-to-multipoint distribution," in *IEEE Proc. Advanced Concepts in High Speed Semiconductor Devices and Circuits*, Aug 1995, pp. 75–84.

[90] W.L. Barrow, L.J. Chu, J.J. Jansen, "Biconical electromagnetic horns," in *Proceedings IRE*, Dec 1939, vol. 27, pp. 769–779.

[91] G. Bekefi, and G. W. Farnell, "A homogenous dielectric sphere as a microwave lens," *Canadian Journal of Physics*, vol. 34, pp. 790–803, 1956.

[92] S. Lee, M. S. Sheshadri, V. Jamnejad, and R. Mittra, "Refraction at a curved dielectric interface: geometrical optics solution," *IEEE Trans. on Microwave Theory and Techniques*, Vol. 30, no. 1, pp. 12–19, Jan 1982.

[93] Xidong Wu, "Millimeter-wave lens antennas for broadband wireless communications and automobile collision avoidance," Ph.D. thesis, University of Toronto, 2001.

[94] M. N. Afsar, "Dielectric measurements of common polymers at millimeter wavelength range," in *IEEE MTT-S Digest*, pp. 439–442, 1985.

[95] J. Ahkenazy, E. Levine, and D. Treves, "Radiometric measurement of antenna efficiency," in *Electron. Lett.*, vol. 21, no. 3, Jan 1985.

[96] G.P. Gauthier, A. Courtay, G.M. Rebeiz, "Microstrip antennas on synthesized low dielectric-constant substrates," *IEEE Trans. on Antennas and Propagation*, Vol. 45, no. 8, pp. 1310–1314, Aug 1997.

[97] D.M. Pozar, "Radiation and scattering characteristics of microstrip substrates on normally biased ferrite substrates," in *IEEE Transactions on Antennas and Propagation*, Sep 1992, vol. 40, no. 9, pp. 1084–1092.

[98] G.M. Rebeiz, "RF MEMS: theory, design, and thechnology," John Wiley & Sons, Inc., 2003.

[99] J.S. Hayden, G.M. Rebeiz, "Very low-loss distributed X-band and Ka-band MEMS phase shifters using metal-air-metal capacitors," in *IEEE Transactions on Microwave Theory and Techniques*, Jan 2003, vol. 51, no. 1, pp. 309–314.

[100] High Frequency Structure Simulator (HFSS), Ansoft Corporation, Pittsburg, PA, 2002.

[101] Sonnet em Suite, Sonnet Software, Inc., Liverpool, NY, 2002.

[102] Advanced design system 2002, Agilent Technologies, Santa Clara, CA, 2002.

[103] A. Abbaspour-Tamijani, L. Dussopt, G.M. Rebeiz, "Miniature and tunable filters using MEMS capacitors," in *IEEE Transactions on Microwave Theory and Techniques*, Jul 2003, vol. 51, no. 7, pp. 1878–1885.

[104] J.S. Hayden, "High-performance digital X-band and Ka-band distributed MEMS phase shifters," Ph.D. dissertation, University of Michigan, Ann Arbor, MI, USA, 2002.

[105] G.-L. Tan, "High performance RF-MEMS circuits and phase shifters," Ph.D. dissertation, University of Michigan, Ann Arbor, MI, USA, 2002.

[106] J.B. Rizk, "W-band RF-MEMS switches, phase shifters and antennas," Ph.D. dissertation, University of Michigan, Ann Arbor, MI, USA, 2003.

[107] Matlab, The Mathworks, Inc., 2002.

[108] B. C. Deckman, *Active quasi-optics and measurements*, Ph.D. dissertation, California Institute of Technology, Pasadena, CA, USA, 2000.

[109] N. Gagnon, J. Shaker, P. Berini, L. Roy, A. Petosa, "Material characterization using a quasi-optical measurement system," *IEEE Transactions on Instrumentation and Measurement*, Apr 2003, vol. 52, no. 4, pp. 333–336.

[110] M.A. Ali, S.C. Oritz, T. Ivanov, A. Mortazawi, "Analysis and measurement of hardhorn feeds for the excitation of quasi-optical amplifiers," *IEEE Transactions on Microwave Theory and Techniques*, Apr 1999, vol. 47, no. 4, pp. 479–487.

[111] S.C. Oritz, J. Hubert, E. Schlecht, A. Mortazawi, "A high-power Ka-band quasi-optical amplifier array," *IEEE Transactions on Microwave Theory and Techniques*, Feb 2002, vol. 50, no. 2, pp. 487–494.

[112] G.F. Engen, C.A. Hoer, "Thru-Reflect-Line: an improved technique for calibrating the dual six-port automatic network analyzer," *IEEE Transactions on Microwave Theory and Techniques*, Dez 2002 vol. 27, no. 12, pp. 987–993.

[113] A. Abbaspour-Tamijani, "Novel Components for Integrated Millimeter-Wave Front-Ends," Ph.D. dissertation, University of Michigan, Ann Arbor, MI, USA, 2003.

[114] J.B. Muldavin, G.M. Rebeiz, "High-isolation CPW MEMS shunt switches - part 1: modeling," in *IEEE Transactions on Microwave Theory and Techniques*, Jun 2000, vol. 48, no. 6, pp. 1045–1052.

[115] Conventorware, Manual, Coventor, Inc., 2003.

[116] M. Kuang-Ping, T. Itoh, "A new broadband coplanar waveguide to slotline transition," in *IEEE International Conference on Microwave Theory and Techniques*, Jun 1997, vol. 3, pp. 1627–1630.

[117] N.I. Dib, R.N. Simons, L.P.B. Katehi, "Broadband uniplanar microstrip to slot-line transitions," in *IEEE International Conference on Microwave Theory and Techniques*, May 1995, vol. 2, pp. 683–686.

[118] S. Barker, G.M. Rebeiz, "Distributed MEMS true-time delay phase shifters and wideband switches," in *IEEE Transactions on Microwave Theory and Techniques*, Nov 1998, vol. 46, no. 11, part 2, pp. 1881–1890.

[119] J. Zou, C. Liu, J. Schutt-Aine, "Development of a wide trunin-range two-parallel-plate tunable capacitor for integrated wireless communication systems," in *International Journal of RF and Microwave CAE*, Sep 2001, vol. 11, pp. 322–329.

[120] L. Dussopt, G.M. Rebeiz, "High-Q millimeter-wave MEMS varactors: extended tuning range and discrete-position designs," in *IEEE Transactions on Microwave Theory and Techniques Symposium*, Jun 2002, vol. 2, pp. 1205–1208.

[121] D. Peroulis, L.P.B. Katehi, "Electrostatically-tunable analog RF MEMS varactors with measured capacitance range of 300%," in *IEEE Transactions on Microwave Theory and Techniques Symposium*, Jun 2003, vol. 3, pp. 1793–1796.

[122] J.H.C. van Heuven, "A new integrated waveguide-microstrip transition," in *IEEE Transactions on Microwave Theory and Techniques*, Mar 1976, vol. 24, pp. 144–147.

[123] Y-C. Shih, T-N. Ton, L.Q. Bui, "Waveguide-to-microstrip transitions for millimeter-wave applications," in *IEEE Microwave Theory and Techniques International Symposium*, 1988, pp. 473–475.

[124] H-W. Yao, A. Abdelmonem, J-J. Liang, K.A. Zaki, "Analysis and design of microstrip-to-waveguide transitions," in *IEEE Transactions on Microwave Theory and Techniques*, Dec 1994, vol. 42, pp. 2371–2380.

[125] Y-C. Leong, S. Weinreb, "Full band waveguide-to-microstrip probe transitions," in *IEEE Microwave Theory and Techniques International Symposium*, Jun 1999, vol. 4, pp. 1435–1438.

[126] D.M. Pozar, "Microwave Engineering," in *John Wiley & Sons, Inc.*, 1998.

[127] J.B. Muldavin, "Design and analysis of series and shunt MEMS switches," Ph.D. dissertation, University of Michigan, Ann Arbor, MI, USA, 2001.